Sensitivity Analysis for Aeroacoustic and Aeroelastic Design of Turbomachinery Blades

Christopher B. Lorence
Graduate Research Assistant

and

Kenneth C. Hall
Principal Investigator

Department of Mechanical Engineering and Materials Science
School of Engineering
Duke University
Durham, NC 27708-0300

A Final Technical Report on Research Conducted Under
NASA Grant NAG3-1433
(Grant Title: Aeroacoustic Sensitivity Analysis and Optimal Aeroacoustic Design of Turbomachinery Blades)

Submitted to NASA Lewis Research Center
May 1995

Abstract

A new method for computing the effect that small changes in the airfoil shape and cascade geometry have on the aeroacoustic and aeroelastic behavior of turbomachinery cascades is presented. The nonlinear unsteady flow is assumed to be composed of a nonlinear steady flow plus a small perturbation unsteady flow that is harmonic in time. First, the full potential equation is used to describe the behavior of the nonlinear mean (steady) flow through a two-dimensional cascade. The small disturbance unsteady flow through the cascade is described by the linearized Euler equations. Using rapid distortion theory, the unsteady velocity is split into a rotational part that contains the vorticity and an irrotational part described by a scalar potential. The unsteady vorticity transport is described analytically in terms of the drift and stream functions computed from the steady flow. Hence, the solution of the linearized Euler equations may be reduced to a single inhomogeneous equation for the unsteady potential. The steady flow and small disturbance unsteady flow equations are discretized using bilinear quadrilateral isoparametric finite elements. The nonlinear mean flow solution and streamline computational grid are computed simultaneously using Newton iteration. At each step of the Newton iteration, LU decomposition is used to solve the resulting set of linear equations. The unsteady flow problem is linear, and is also solved using LU decomposition. Next, a sensitivity analysis is performed to determine the effect small changes in cascade and airfoil geometry have on the mean and unsteady flow fields. The sensitivity analysis makes use of the nominal steady and unsteady flow LU decompositions so that no additional matrices need to be factored. Hence, the present method is computationally very efficient. To demonstrate how the sensitivity analysis may be used to redesign cascades, a compressor is redesigned for improved aeroelastic stability and two different fan exit guide vanes are redesigned for reduced downstream radiated noise. In addition, a framework detailing how the two-dimensional version of the method may be used to redesign three-dimensional geometries is presented.

Contents

List of Figures

List of Tables

Chapter 1

Introduction

1.1 Statement of the Problem

As the efficiency of modern aircraft engines continues to increase, aeroacoustic and aeroelastic considerations will play an increasingly important role in the design of turbomachinery blading. Government regulations and community standards demand reduced levels of noise from aircraft, while competitive pressures require increased efficiency and reliability from modern designs. Unfortunately, aeroacoustic and aeroelastic performance can be very difficult to predict, due primarily to the complexity of the unsteady aerodynamic flowfield. In recent years, however, the computational modeling of these unsteady flows has substantially improved.

Although current unsteady aerodynamic computational methods may improve the prediction of aeroelastic phenomena, they provide very little insight to the designer as to how to improve the aeroelastic behavior. As a result, the steady aerodynamic design and aeroelastic design phases during the development of fan, compressor, and turbine blading remain largely decoupled. After the airfoil shapes have been designed to satisfy their steady aerodynamic requirements, detailed aeroelastic studies are performed to determine whether the blades will meet design standards for flutter stability and fatigue. These studies can be very computationally expensive, particularly because of the expense of determining the unsteady aerodynamic flowfield. If the blade fails to meet these requirements, the blade is redesigned, and the process is repeated. This redesign process increases the time and expense necessary to design a blade and misses an opportunity to design for steady and unsteady aerodynamic performance simultaneously.

In current aeroacoustic analyses, the primary emphasis has been on the choice of the number of blades and vanes so that the so-called lower order modes do not propagate [1]. Furthermore, steady blade loading, thickness, and camber effects are only approximated, if they are considered at all [2]. Hence, improved steady and unsteady aerodynamic modeling, particularly through the use of computational fluid dynamic (CFD) techniques, will lead to more accurate predictions of blade row response to incoming gusts, and help to illustrate the relationship between the blade shape and the radiated noise.

The goal of this research is to provide a framework for development and a realistic implementation of useful design tools (as opposed to analysis tools) for designing turbomachinery blading for improved aeroacoustic and aeroelastic performance. These tools should be very computationally efficient, yet still model the dominant flow physics. In addition, these tools should provide physical insight that will lead to guidelines for future blade designs.

1.1.1 Aeroelastic Problems in Turbomachines

Aeroelastic phenomena arise from the interaction between inertial, elastic, and aerodynamic forces [3]. For turbomachinery applications, this interaction may be illustrated by examining a simplified version of the equation of motion for an airfoil

$$m\ddot{x} + c\dot{x} + kx = F_{\text{motion}}(x, \dot{x}, \ddot{x}) + F_{\text{gust}}(t) \tag{1.1}$$

On the left-hand side of Eq. (1.1), x is the displacement, the dots represent time derivatives, m is the mass of the blade, c represents the structural damping, and k is the blade stiffness.

The right-hand side consists of two forces. The first force is due to self-induced oscillations and is a function of the displacement, velocity, and acceleration of the blade. If this force increases the energy of the vibration, the amplitude of the vibration increases, and blade failure may occur. Such an unstable self-induced vibration is referred to as flutter. The second force on the right-hand side is due to an externally excited oscillating motion (gust) where the force is independent of the blade displacement. The external forcing induces a response which in some cases may lead to high cycle fatigue failure of the blade, and is referred to as forced response [4].

These two aeroelastic phenomena, flutter and forced response, are two major types of aeroelastic problems encountered in modern aircraft engines. Both of these phenomena can lead to fatigue failure of one or more of the blades, and therefore are of great interest to aircraft engine designers.

Flutter

Self-excited blade vibrations that are sustained by the unsteady aerodynamic forces are of great concern to engine designers. If the aerodynamic forces produced by the blade vibration add energy to the blade motion, the vibration will grow exponentially until a limit cycle is reached or the blade fails. This aeroelastic phenomena is known as flutter. Flutter tends to occur near one of the lower natural frequencies of the blades. In modern engines, flutter may be encountered in a wide range of operating conditions. As a result, there are significant constraints on the design of fan, compressor, and turbine blading. Figure 1.1 shows the operating map for a typical fan or compressor, showing the boundaries for the most common types of flutter [3]. This figure illustrates the complexity of the design problem for a compressor. Deviations from the operating line can easily lead to one of the indicated types of flutter. Because the structural damping of the blades is usually small, the aerodynamic damping is of primary interest. The unsteady aerodynamics problem is to determine whether the

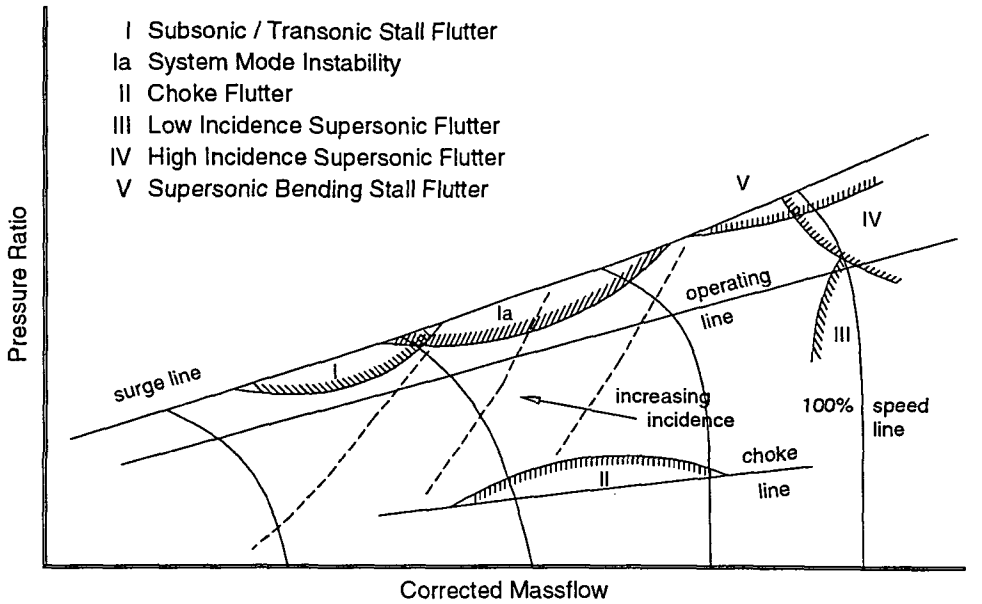

Figure 1.1: Axial compressor or fan characteristic map showing principal types of flutter and regions of occurrence (adapted from [3]).

aerodynamic damping is positive (stabilizing) or negative (destabilizing) for a given blade motion and flow condition. If the system is unstable, then the blades must be redesigned.

Forced Response

Forced vibration is also a significant problem in the design of turbomachines. Forced vibrations may occur in fan, compressor, and turbine blades when a periodic aerodynamic forcing function acts on the blades in a given row. These forced vibrations may be destructive if the frequency of the forcing is near a resonant frequency of the blade. The forcing functions are generated at integer multiples of the engine rotational frequency and may arise from a number of different sources, the most common being aerodynamic interaction between adjacent blade rows. Specifically, unsteady aerodynamic forces often arise from the wakes of upstream blade rows impinging on the blade surface. Unlike the flutter problem, the aerodynamic forcing is independent of the blade motion, as indicated in Eq. (1.1).

The frequencies at which these vibrations may occur can be predicted using a Campbell diagram [5]. Figure 1.2 shows a typical Campbell diagram for an axial-flow compressor, which displays the natural frequency of each blade vibration mode and the possible forcing function frequencies as functions of rotor speed. In this figure, the dashed lines indicate the natural frequencies of the first two bending and torsion vibratory modes of the rotor blades. Note that these curves increase somewhat with rotor speed due to centrifugal stiffening of the rotor. The solid lines are simply multiples of the rotor speed (so-called engine orders). It is at the crossing of these

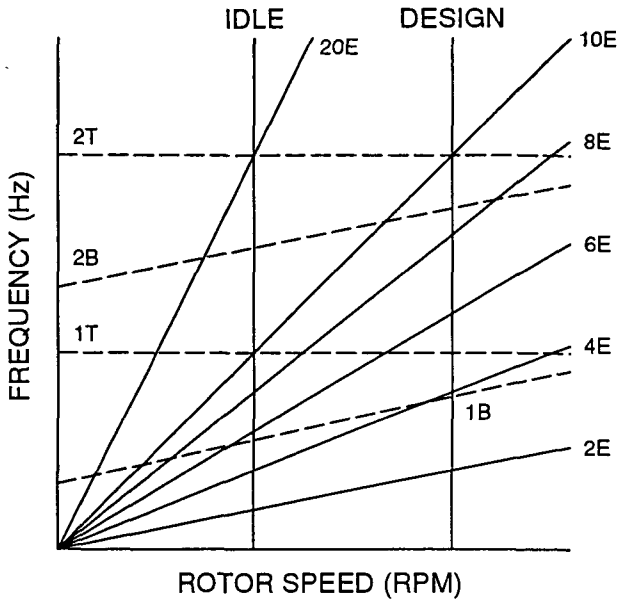

Figure 1.2: Typical compressor resonance (or Campbell) diagram (adapted from [5]).

two types of curves in the operating region that the possibility of destructive forced vibrations exists, because the forcing frequency corresponds to the resonant frequency of the blade. Hence, due to the small structural damping, large amplitude vibrations may be induced.

Clearly, it is not possible to eliminate all sources of forced vibration from the operating range of a turbomachine, but designers need to either avoid these points or ensure that their effect is minimal. For the forced response problem, an unsteady aerodynamic analysis is performed to determine the unsteady forces on the blades due to an incoming gust from the upstream blade row at the points where the curves cross on the Campbell diagram. If the unsteady aerodynamic forces induce large amplitude vibration at one or more of these points, the blade must be redesigned.

1.1.2 Aeroacoustic Problems in Turbomachines

Noise radiation continues to be an obstacle to the design and development of modern aircraft engines. Engine noise can be classified as either broadband noise (occurring over a continuous range of frequencies) or tonal noise (occurring at discrete frequencies). The relative magnitude of these two types of noise is primarily determined by the bypass ratio of the engine, i.e., the ratio of the amount of air flowing through the fan outside of the engine core to the amount of air flowing through the fan into the core. To increase the propulsive efficiency of engines, higher bypass ratios are desirable. As the bypass ratio of the engine increases, tonal noise becomes the more important contributor to the total engine noise signature [2]. Furthermore, broadband noise is a very complicated problem since it is usually caused by the interaction of random disturbances with blade surfaces and jet exhaust mixing. Because tonal noise is the larger contributor to the engine noise signature, broadband noise will not

be considered in this report.

The source of tonal noise is nonuniformities in the flowfield such as inlet distortion, inlet angle of attack, or convected wakes from upstream blade rows. The noise is produced by an interaction between the flow nonuniformity (or "gust"), the blade row, and the duct surrounding the blade row coupling to produce propagating acoustic modes. Currently, most tonal noise reduction methods are aimed at either reducing the strength of the gust by increasing the distance between blade rows, or by modifying the duct through the use of casing treatment. In addition, blade counts are carefully chosen. Pressure waves that decay as they propagate are referred to as "cut-off." Propagating pressure waves are referred to as "cut-on," and it is these waves which result in audible noise. Acousticians use analytical models of the duct to choose blade and vane counts to prevent lower order pressure modes from propagating [1]. All three of these noise reduction techniques, increasing blade row spacing, casing treatment, and modifying blade/vane counts are not desirable because these methods add weight and expense to the finished engine.

The unsteady aerodynamics problem is to determine the response of a blade row to an incoming gust, determine the pressure field generated by the wake-blade interaction and determine whether these pressure waves will propagate outside of the engine. Most unsteady aerodynamic methods, however, are best viewed as *analysis* tools rather than design tools. They are capable of solving the direct problem where the shape of the airfoil as well as the flow conditions are specified. Unfortunately, except through trial and error or extensive parametric studies, these analyses do not provide physical insight into how, for example, to design blade shapes to reduce their acoustic response without compromising their aerodynamic efficiency. An additional complication is that the frequencies associated with aeroacoustic analysis are approximately an order of magnitude higher than those found in aeroelastic problems, requiring finer discretization of the governing equations of the unsteady flowfield and increased computational expense.

1.2 Previous Work

1.2.1 Unsteady Aerodynamic Models

The first unsteady aerodynamic analyses were semi-analytical methods that were designed to determine the unsteady surface pressure on a cascade of two-dimensional flat plates due to bending or torsional vibration. In the semi-analytical approach, a number of point singularities are placed on the blade surface, and an appropriate kernel function is used to calculate the unsteady flowfield. One of the first such analyses was performed by Whitehead [6], who considered uniform, incompressible, undeflected flow over the plates. Because the flow is not deflected, however, there is no steady loading on the blade, and the model failed to predict experimentally observed bending flutter. To include the effect of steady loading, Whitehead later allowed the blades to deflect the mean flow, resulting in steady loading on the blades [7], and bending flutter was predicted. This provided numerical evidence that steady blade

loading (and therefore the blade shape design) had an important effect on flutter in aircraft engines. Later, Atassi and Akai [8] distributed point singularities along the surface of an airfoil with finite camber and thickness. This model allowed them to analyze incompressible flows through more realistic cascades, also showing the importance of steady loading and blade shape on flutter.

Both Whitehead [9] and Smith [10] investigated subsonic compressible flows over flat plate airfoils. Smith's approach was developed primarily for noise analysis in an attempt to determine the propagation characteristics of acoustic modes generated by a cascade of airfoils. Smith also measured the acoustic waves experimentally, and found that the theory and experiment agreed well for the unloaded blade case, but the theory was inadequate to deal with the extra sound sources introduced by steady blade loading, and underestimated the generated wave amplitude in this case. Both Whitehead and Smith found that steady loading is extremely important to predict correctly the amplitudes of the outgoing pressure waves.

Advanced designs required researchers to analyze transonic and supersonic flows. Adamczyk and Goldstein [11] and others [12, 13, 14] investigated vibrating flat plates in supersonic flow which is axially subsonic. Unfortunately, these models did not predict flutter at the experimentally observed frequencies and Mach numbers. More sophisticated models, such as the in-passage shock model developed by Goldstein, Braun, and Adamczyk [15], analyzed supersonic cascades with finite strength shocks. The in-passage shock model predicted experimentally observed supersonic bending flutter, at least for low reduced frequencies. The design problem was also beginning to be considered. Bendiksen [16] used a perturbation analysis to include effects due to steady loading, thickness, camber, angle of attack, and shock motion, showing that these effects are important in flutter prediction.

Finally, some three-dimensional problems have been considered using a semi-analytical approach. Namba [17] has developed a lifting surface analysis to determine the unsteady flow over vibrating three-dimensional flat plate cascades in the subsonic, transonic, and supersonic regimes. Although his approach demonstrates the importance of three-dimensional effects, its application is primarily limited to lightly loaded fan blades.

Although these semi-analytical methods have developed greatly over the years, they are insufficient to analyze most unsteady aerodynamic problems in modern engines, especially at off-design conditions. The blades in modern designs are heavily loaded, and violate a number of the assumptions used in the semi-analytical approach.

As computers became more powerful, so-called field methods became an important research area. Using this approach, a set of governing equations (i.e., potential, Euler, or Navier-Stokes) is solved using computational fluid dynamics techniques. This approach has the advantage that many of the effects not included in the analytical models may be easily incorporated, e.g., arbitrary blade geometries, complicated shock structures, and various flow models.

In the area of field methods, two main approaches have emerged. These are referred to as time-marching and time-linearized methods. Using the time-marching approach, the unsteady governing equations of the fluid motion are time-accurately marched subject to some appropriate set of unsteady boundary conditions. For ex-

ample, to analyze a flutter problem, the airfoils are prescribed to vibrate at some fixed frequency and interblade phase angle. Once the initial transients have decayed, the unsteady flowfield is found to be periodic in time. The advantage to this approach is that nonlinear flow effects are incorporated, and finite blade motions may be considered.

Two-dimensional, time-accurate Euler solution methods have been developed by Giles [18] and others. Three-dimensional unsteady flow problems have been investigated by Ni and Sharma [19] using a time-accurate Euler method, but their results require several hours of supercomputer time to obtain a solution. Other three-dimensional methods have been developed to investigate rotor-stator interaction. Saxer and Giles [20] used an Euler method and Rai [21] used a Navier-Stokes analysis. Although these methods model many of the important physical mechanisms of the unsteady flow problem, the massive amount of time required to march these equations time-accurately will prevent this type of analysis from being used for design purposes for many years to come, especially for three-dimensional problems.

The second approach in field methods is the use of linearized analyses to investigate small perturbation unsteady flows. Using this approach, the flow is assumed to be composed of a nonlinear mean or steady flow plus a small unsteady perturbation flow. The linearized equations which describe the unsteady perturbation are linear variable coefficient equations in the unknown complex amplitude of the harmonic motion of the flow.

Verdon and Caspar [22] determined the mean flow through a subsonic cascade using a steady full potential method. They then linearized the potential equation about the mean flow to solve for the small disturbance unsteady flow. Whitehead and Grant [23] and Hall [24] used a similar approach but used finite elements instead of finite differences to discretize the linearized equations. Verdon and Caspar later extended their model to transonic flows using shock fitting to model the shock motion [25]. Although these potential methods work well for subsonic flutter problems, their use for forced response and aeroacoustic applications has been limited because the model does not in general include unsteady vorticity, as would have to be included to determine the response of a blade row to an incoming vortical gust.

Within a linearized potential framework, Goldstein [26] developed a velocity splitting technique that includes unsteady vorticity and entropy. Goldstein assumed an isentropic and irrotational mean flow, and split the unsteady velocity into rotational and irrotational parts. The rotational unsteady velocity, which contains the unsteady vorticity, is expressed analytically using the drift and stream functions from the steady flow solution. The rotational velocity appears in an inhomogeneous source term in the linearized potential equation. Hence, unsteady flows with vorticity could be analyzed without having to numerically solve the Euler equations. Unfortunately, this analysis could only be applied to flat plate airfoils. Atassi and Grzedzinski [27] developed a modification to this method that allowed real airfoils to be analyzed. Hall and Verdon [28] implemented this technique and showed that vortical gust effects could be modeled accurately without the computational expense of solving the Euler equations.

Even with vortical gust extensions, the linearized potential formulation has its

limits. For transonic flows with strong shocks, the Euler equations must be solved. Also, the potential formulation does not translate well to three-dimensional applications due to the assumption of irrotational steady flow. For these and other reasons, linearized methods continue to advance.

Hall and Crawley [29] originally solved the linearized Euler equations using a Newton iteration technique to solve the nonlinear steady Euler equations and a direct method to solve the unsteady linearized Euler equations. This approach also used shock fitting to model the shock motion. There were some problems with this method, however. For example, the direct solution method prevented fine computational grids from being used on typical workstation computers, particularly if the analysis were to be extended to three dimensions. To circumvent this and other problems, Hall and Clark [30] and Holmes and Chuang [31] implemented linearized Euler methods using an iterative solution method rather than a direct solution. In addition, Hall, Clark, and Lorence [32] and Lindquist and Giles [33] showed that transonic aeroelastic problems can be modeled appropriately within a linearized framework using shock capturing. Using a similar technique, Clark and Hall [34] have implemented a method for solving the linearized Navier-Stokes equations so that stall flutter problems may be analyzed. Finally, Hall and Lorence [35] extended the linearized Euler analysis to three dimensions and showed the importance of three-dimensionality on the unsteady flow in fans.

Linearized methods require significantly less computational time than their time-marching counterparts. For most unsteady aerodynamic flows of interest, the linearized approach requires one to two orders of magnitude less computational time than an equivalent time-marching calculation. Although for some complex applications, time-accurate time-marching methods may be employed, in most cases, a linearized analysis is sufficient to model the unsteady flowfield.

1.2.2 Design Methods and Optimization

A substantial body of work exists on the inverse design and optimal design of airfoils. Most of this work, however, is directed at achieving desirable *steady* flow properties. In an inverse method, a pressure distribution is specified and the analysis produces an airfoil shape (if possible) that will produce the desired distribution. For example, Lighthill [36] developed an inverse design method based on conformal mapping techniques. More recently, a number of investigators have proposed inverse design techniques based on modern computational fluid dynamic algorithms (e.g., [37]).

More popular are optimal design techniques, where an initial airfoil shape is specified, and the analysis attempts to minimize some quantity (e.g., steady aerodynamic losses) while satisfying some appropriate constraints (e.g., the blade maintains the correct turning). A number of investigators have used nonlinear programming techniques to solve this problem (e.g., [38]), and Jameson has suggested that this problem may be viewed as an optimal control problem [39].

Researchers have also developed some optimization techniques for aeroelastic problems in turbomachinery. For example, Crawley and Hall [40] developed a method to calculate an optimal distribution of "mistuning" for a blade row. These techniques,

however, have focused on structural optimization rather than optimization of the unsteady aerodynamic behavior.

One of the key ingredients in optimization algorithms is the evaluation of the sensitivity of the quantity to be optimized (for example, the flutter stability or efficiency of a cascade) to a small change in a physical parameter (such as the airfoil shape). Sensitivity analysis of structures has been an active area of research for the past decade [41, 42]. Recently, researchers have begun to develop similar sensitivity analysis techniques for steady aerodynamic problems. For example, Taylor *et al* [43] and Baysal and Eleshaky [44] have computed the effect of modifying the shape of a nozzle on the flow in the nozzle. Their work was based on a sensitivity analysis of the discretized Euler equations. Most recently, such techniques have been applied to airfoil design [45]. Despite these advances, only a few unsteady sensitivity analyses have been reported, for example the semi-analytical panel method of Murthy and Kaza [46]. Other unsteady sensitivity analyses have been computed by differencing two slightly different nominal unsteady solutions. The use of these types of finite differences, as opposed to analytical perturbations, are not as desirable because of their increased computational expense and susceptibility to truncation error.

1.3 Present Method

In this report, strategies for efficient aeroacoustic and aeroelastic design of turbomachinery blades will be examined. An essential part of these strategies is a new method for computing the sensitivity of unsteady flows in cascades due to small changes in blade geometry. The approach is general in nature and may be applied to different governing equations and numerical schemes. Consequently, an appropriate equation set must be chosen. For many aeroacoustic and aeroelastic problems in turbomachinery, an inviscid flow analysis is sufficient to model the dominant physical mechanisms of the unsteady flowfield. Hence, a linearized potential or linearized Euler framework would be applicable. Since vortical gusts must be analyzed, however, the traditional linearized potential method is not appropriate. The linearized Euler approach, while incorporating complete inviscid physics, is still computationally expensive to solve directly, as the present method requires. Therefore, a linearized potential model with vortical gust extensions is the logical choice. This is the method that will be used in this report to demonstrate the sensitivity analysis procedure.

Specifically, the nominal analysis used here is a linearized harmonic unsteady potential method based on a deforming grid variational principle and finite element method by Hall [24] extended using rapid distortion theory to include the effect of incident vortical gusts due to wake interaction. The sensitivity analysis procedure is as follows. First, the nominal flow equations are discretized and solved using a finite element procedure. Next, a perturbation analysis is performed on the discretized equations from the nominal finite element analysis. This leads to a set of linear equations for the sensitivity of the unsteady potential due to small changes in the airfoil shape. If the nominal unsteady analysis is computed with LU decomposition, the sensitivities may then be computed by back-substitution. Consequently, the sensitivity

of the unsteady potential may be computed very efficiently.

Once the sensitivities have been calculated, a range of approaches exist for improving the aeroacoustic and aeroelastic performance of the cascade. For example, the calculated sensitivities may be used by themselves as a guide to redesign the airfoil. A more thorough approach would be to perform an optimization on the aeroacoustic or aeroelastic behavior of the cascade, subject to appropriate constraints. The radiated noise, for example, could be minimized subject to the constraint that the desired steady flow turning is achieved. The results shown in this report will essentially be a compromise between these two methods, where the calculated sensitivities are post-processed such that design changes satisfy steady aerodynamic constraints. The framework for the use of this technique in more complicated design situations will also be discussed.

1.4 Outline of Report

In Chapter 2, the governing equations and basic theory of the nominal flow analysis will be presented. This includes both the steady flow potential equation and the linearized potential equation and the vortical gust extension. Use of a deforming computational grid will be discussed, as will the theoretical description of the steady and unsteady boundary conditions.

Chapter 3 contains a discussion of the basic numerical discretization scheme, based on Hall's finite element method. The grid generation procedure will be discussed, as will the implementation of the boundary conditions, with particular emphasis on the nonreflecting far-field boundary conditions. Finally, the matrix assembly and solution will be described.

In Chapter 4, the sensitivity analysis procedure will be examined in detail for both the steady and unsteady flow equations. Although the procedure will be applied to the present potential method, this chapter should clarify how the sensitivity analysis would be performed on other governing equations and discretization schemes.

In Chapter 5, results of the sensitivity analysis will be presented, demonstrating how the analysis may be used to redesign blade rows for improved aeroelastic and aeroacoustic performance. Also, the computational efficiency of the method will be discussed, as will its range of effectiveness.

In Chapter 6, three-dimensional flow considerations will be examined. Specifically, application of the analysis in an actual design environment will be discussed , with particular emphasis on how three-dimensional problems could be analyzed using the present method.

Finally, in Chapter 7, some conclusions from the present analysis will be presented as well as some recommendations for future work in this area.

Chapter 2

Nominal Flow Field Description

In this chapter, the equations and boundary conditions governing the steady and small disturbance unsteady flow through a two-dimensional cascade of airfoils are introduced. Section 2.1 contains a description of the rapid distortion theory used so that unsteady vortical flows may be modeled within a potential flow framework. This theory results in a set of sequentially coupled partial differential equations that must be solved numerically to obtain the unsteady flow. In Section 2.2, an extension of a variational principle originally developed by Bateman [47] is described. This variational principle has as its Euler-Lagrange equation the potential flow equation developed in Section 2.1. This variational principle will be used in Chapter 3 to construct a finite element description of the steady and unsteady flow. Finally, in Sections 2.3 and 2.4, the steady flow and small disturbance unsteady flow boundary conditions will be discussed, including the far-field nonreflecting boundary conditions.

2.1 Euler Equations

The equations governing the fluid motion through a cascade of airfoils may be derived from the integral conservation laws of mass, momentum, and energy, along with the equation of state for an ideal gas. For this analysis, the flow is assumed to be inviscid and compressible, and the fluid is assumed to be a perfect gas with specific heat ratio $\gamma = c_p/c_v$ (a complete list of symbols used in this report is given in Appendix A). Consequently, the governing equations of the fluid are the Euler equations, which in conservation form are

$$\frac{\partial \hat{\rho}}{\partial t} + \nabla \cdot (\hat{\rho}\hat{\mathbf{v}}) = 0 \tag{2.1}$$

$$\frac{\partial \hat{\rho}\hat{\mathbf{v}}}{\partial t} + \nabla \cdot \hat{\rho}\hat{\mathbf{v}}\hat{\mathbf{v}} + \nabla \hat{p} = 0 \tag{2.2}$$

$$\frac{\partial}{\partial t}\left(\frac{\hat{p}}{\gamma - 1} + \frac{1}{2}\hat{\rho}\hat{\mathbf{v}} \cdot \hat{\mathbf{v}}\right) + \nabla \cdot \left(\frac{\gamma}{\gamma - 1}\hat{p} + \frac{1}{2}\hat{\rho}\hat{\mathbf{v}} \cdot \hat{\mathbf{v}}\right)\hat{\mathbf{v}} = 0 \tag{2.3}$$

where $\hat{\rho}$ is the density, $\hat{\mathbf{v}}$ is the velocity, and $\hat{p}$ is the pressure. These quantities are related by the state equation for a perfect gas

$$\hat{p} = \hat{\rho} R_u \hat{T}_f \tag{2.4}$$

where R_u is the universal gas constant and $\hat{T}_f$ is the temperature. The superscript "^" indicates that the quantity is unsteady. For this discussion, it is useful to define the entropy of the fluid, $\hat{s}_f$. This is most easily accomplished using the thermodynamic relation defined by Gibbs,

$$\hat{T}_f \, d\hat{s}_f = c_p \, d\hat{T}_f - \frac{1}{\hat{\rho}} \, d\hat{p} \tag{2.5}$$

The temperature dependence may be removed through the use of the state equation, Eq. (2.4), resulting in

$$d\hat{s}_f = c_v \frac{d\hat{p}}{\hat{p}} - c_p \frac{d\hat{\rho}}{\hat{\rho}} \tag{2.6}$$

Equation (2.6) may then be integrated to obtain the entropy change between two fluid states.

It is further assumed that the nonlinear time-varying flow may be split into two parts: a nonlinear mean or steady flow and a small unsteady perturbation flow that is harmonic in time. In other words, each of the variables in the above equations may be expanded in a perturbation series. Furthermore, it is assumed that the steady flow is irrotational and homentropic, so that the steady velocity may be written as the gradient of a scalar velocity potential, Φ. Under these assumptions, the perturbation series for the flow variables may be written as

$$\begin{array}{lcccl}
\hat{\rho}(x,y,t) & = & R(x,y) & + & \rho(x,y)e^{j\omega t} \\
\hat{\mathbf{v}}(x,y,t) & = & \nabla\Phi(x,y) & + & \mathbf{v}(x,y)e^{j\omega t} \\
\hat{p}(x,y,t) & = & P(x,y) & + & p(x,y)e^{j\omega t} \\
\underbrace{\hat{s}_f(x,y,t)} & = & \underbrace{\qquad} & & \underbrace{s_f(x,y)e^{j\omega t}} \\
\text{total flow} & & \begin{array}{c}\text{nonlinear} \\ \text{mean}\end{array} & & \begin{array}{c}\text{small harmonic} \\ \text{disturbance}\end{array}
\end{array} \tag{2.7}$$

To obtain the steady and unsteady flow equations, these expansions are substituted into the governing equations, Eqs. (2.1)–(2.6), collecting terms of equal order. The zeroth-order terms result in the steady flow equations, while the first-order terms describe the unsteady flow. The zeroth-order continuity equation is

$$\nabla \cdot (R\nabla\Phi) = 0 \tag{2.8}$$

The zeroth-order momentum equation and equation of state may be integrated and combined to obtain the steady form of Bernoulli's Equation, i.e.,

$$R = \rho_T \left[1 - \frac{\gamma - 1}{2{C_T}^2} (\nabla\Phi)^2 \right]^{\frac{1}{\gamma - 1}} \tag{2.9}$$

or

$$P = p_T \left[1 - \frac{\gamma - 1}{2{C_T}^2} (\nabla\Phi)^2 \right]^{\frac{\gamma}{\gamma - 1}} \tag{2.10}$$

where p_T and ρ_T are the total pressure and density, respectively, and C_T is the total speed of sound. Substituting Eq. (2.9) into Eq. (2.8) results in an equation for the mean flow that is only a function of the potential and the steady speed of sound,

$$\nabla^2\Phi = \frac{1}{C^2}\left[\frac{1}{2}\nabla\Phi\cdot\nabla(\nabla\Phi)^2\right] \tag{2.11}$$

where

$$C^2 = C_T^2 - \frac{\gamma-1}{2}(\nabla\Phi)^2 \tag{2.12}$$

Note that the steady flow is completely described by a single equation for the scalar potential Φ. It is indeed nonlinear, as was noted earlier.

Having described the equation governing the steady flow, we now consider the unsteady small disturbance equations. Collection of the first-order terms results in the following set of equations describing the behavior of the small disturbance unsteady flow

$$\frac{Ds_f}{Dt} = 0 \tag{2.13}$$

$$\frac{D}{Dt}(\mathbf{v} - s_f\nabla\Phi/2) + [(\mathbf{v} - s_f\nabla\Phi/2)\cdot\nabla]\nabla\Phi + \nabla\left(\frac{p}{R}\right) = 0 \tag{2.14}$$

$$\frac{D}{Dt}\left(\frac{p}{RC^2}\right) + \frac{1}{R}\nabla\cdot(R\mathbf{v}) = 0 \tag{2.15}$$

where $D/Dt = \partial/\partial t + \nabla\Phi\cdot\nabla$ is the convective derivative. Note that while the steady flow may be described using a single equation, the unsteady flow is governed by a system of four simultaneously coupled equations. Computationally, this description of the unsteady flow would result in a very large system of equations to solve. Hence, a more compact description of the unsteady flow is desired.

2.1.1 Goldstein Decomposition

Equations (2.14) and (2.15) may be simplified further using the Goldstein velocity decomposition [26]. The unsteady velocity, $\mathbf{v}$, is split into a rotational part, $\mathbf{v}^R$, and an irrotational part that is written as the gradient of a scalar velocity potential, ϕ, so that

$$\mathbf{v} = \nabla\phi + \mathbf{v}^R \tag{2.16}$$

It should be noted that there is no unique choice for $\mathbf{v}^R$ and ϕ, since it is the combination of the two that results in the actual unsteady flow velocity. However, if $\mathbf{v}^R$ is chosen such that

$$\frac{D}{Dt}\mathbf{v}^R + \left[\mathbf{v}^R\cdot\nabla\right]\nabla\Phi + \nabla\left(\frac{p}{R}\right) = 0 \tag{2.17}$$

then the unsteady pressure is only a function of the unsteady potential, so that

$$p = -R\frac{D\phi}{Dt} \tag{2.18}$$

Substituting Eqs. (2.16) and (2.18) into the linearized momentum and continuity equations [Eqs. (2.14) and (2.15)] results in a system of equations for the unsteady entropy, rotational velocity, and velocity potential, i.e.,

$$\frac{Ds_f}{Dt} = 0 \tag{2.19}$$

$$\frac{D}{Dt}\left(\mathbf{v}^R - s_f \nabla\Phi/2\right) + \left[\left(\mathbf{v}^R - s_f \nabla\Phi/2\right) \cdot \nabla\right] \nabla\Phi = 0 \tag{2.20}$$

$$\frac{D}{Dt}\left(\frac{1}{C^2}\frac{D\phi}{Dt}\right) - \frac{1}{R}\nabla \cdot (R\nabla\phi) = \frac{1}{R}\nabla \cdot \left(R\mathbf{v}^R\right) \tag{2.21}$$

Note that the equations for entropy, rotational velocity, and velocity potential are now only sequentially coupled. Although four equations still must be solved, they need not be solved simultaneously. As a result, a numerical solution to these equations may be obtained for considerably less computational cost than the earlier set of simultaneously coupled equations. Furthermore, in this report, the effect of unsteady entropy will not be investigated, so it is assumed that $s_f = 0$. Consequently, only Eqs. (2.20) and (2.21) must be solved.

Goldstein [26] showed that Eq. (2.20) may be solved analytically for certain cases in terms of two functions. One is the well-known stream function, $\Psi(x, y)$. The other is the drift function, $\Delta(x, y)$, which is defined as the time it takes a mean flow fluid particle to move between two points on a streamline, i.e.,

$$\Delta(x, y) = \Delta(x_0, y_0) + \int_{(x_0,y_0)}^{(x,y)} \frac{1}{|\nabla\Phi|} d\psi \tag{2.22}$$

where the location (x_0, y_0) is a point upstream of (x, y) on the same steady streamline, $|\nabla\Phi|$ is the magnitude of the steady flow velocity, and the differential distance $d\psi$ is measured along the streamline. The drift and stream functions are often referred to as the Lagrangian coordinates of the fluid.

Figure 2.1 shows contours of the drift and stream functions for a typical fan exit guide vane. Note that upstream of the cascade, the drift function contours are aligned between the blade passages, while downstream of the airfoils the contours are no longer aligned. This indicates that there is circulation around the airfoil, i.e., the steady velocities are different on the two sides of the airfoil surface. Furthermore, note that the drift contours are well-behaved in the interior of the blade passages, but change rapidly near the blade and wake surfaces. This is due to the presence of a stagnation point at the leading edge of the airfoil. Examining Eq. (2.22) shows that if the steady velocity is zero at some point (i.e., a stagnation point), the drift function becomes infinite. This property of the drift function is problematic in the derivation of a general expression for the rotational velocity over airfoils, so a detailed analysis of the drift function behavior near a stagnation point is warranted.

Consider the steady flow field near a stagnation point. Sufficiently close to a solid boundary, the boundary appears to be a plane surface (unless the boundary happens

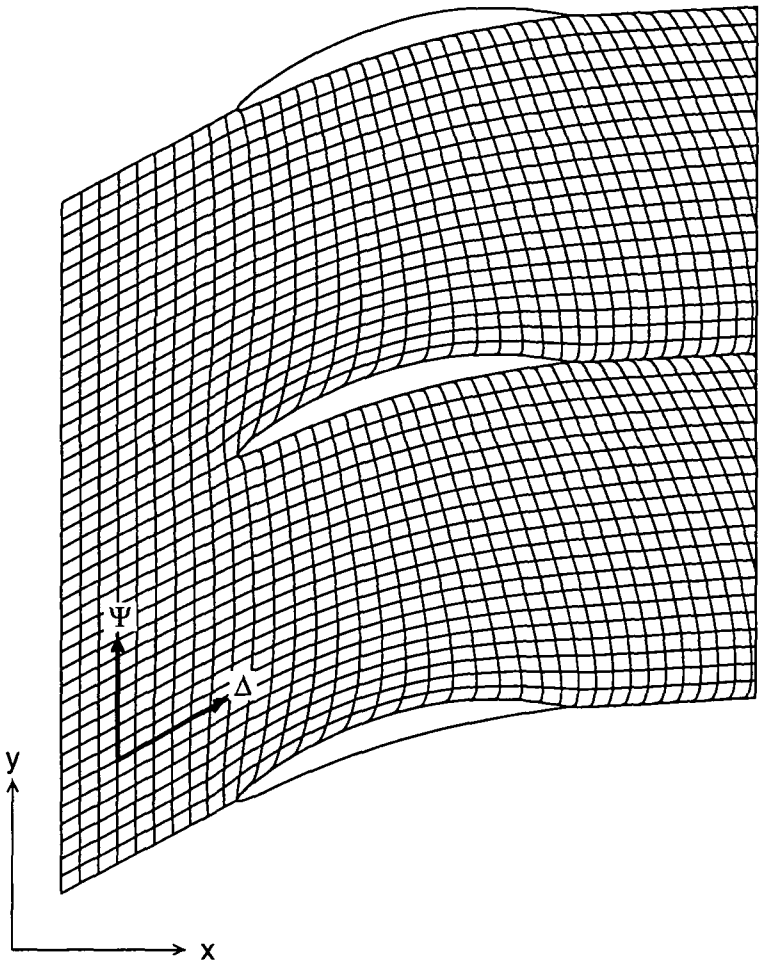

Figure 2.1: Contours of drift function, $\Delta(x, y)$, and stream function, $\Psi(x, y)$, for a typical fan exit guide vane.

to have a discontinuity of slope there) [48]. If the flow is incompressible, the governing equation for the steady potential is Laplace's equation, i.e.,

$$\nabla^2 \Phi = 0 \tag{2.23}$$

The solution that satisfies the boundary conditions is

$$\Phi = \frac{1}{2}\mathcal{A}(x^2 - y^2) \tag{2.24}$$

where $\mathcal{A}$ is some constant. Alternatively, the flow may be described in terms of the stream function by

$$\Psi = \mathcal{A}xy \tag{2.25}$$

Figure 2.2 shows contours of the drift and stream functions near a stagnation point. The stream function is shown near a plane boundary [i.e., a flow described by Eq. (2.25)], while the drift function is shown near the stagnation point of an actual airfoil.

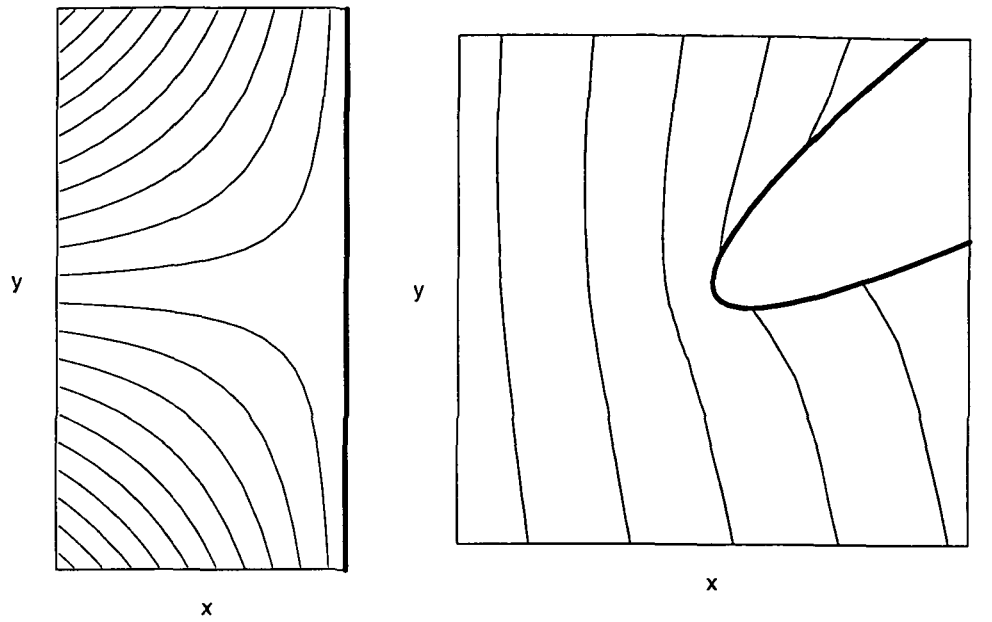

Figure 2.2: Left, contours of the stream function, Ψ, near a solid plane boundary. Right, contours of the drift function, Δ, near an airfoil stagnation point.

Returning to the flow near a plane boundary, it is clear from Eq. (2.24) that the velocity in the direction normal to the surface (the x-direction) is

$$\frac{\partial \Phi}{\partial n} = \mathcal{A}x \tag{2.26}$$

So the velocity is proportional to the distance from the boundary. Hence, using the definition of the drift function [Eq. (2.22)], near the surface

$$\Delta = \frac{1}{\mathcal{A}} \ln x \tag{2.27}$$

So there is a logarithmic singularity in the drift function near the stagnation point. In general, then, we may define a constant a_0 such that

$$a_0 = -\left(\frac{\partial |\nabla \Phi|}{\partial n}\right)^{-1}_{\text{SP}} \tag{2.28}$$

where $|\nabla \Phi|$ is the magnitude of the steady velocity, n is measured normal to the airfoil surface, and the derivative is evaluated at the stagnation point. Using this definition, from Eq. (2.27) it is apparent that to leading order

$$\frac{\partial \Delta}{\partial n} = \frac{a_0}{n} + \ldots \tag{2.29}$$

Furthermore, using Eq. (2.25), Eq. (2.29) may be rewritten in terms of the stream function, so that

$$\frac{\partial \Delta}{\partial \Psi} = \frac{a_0}{\Psi - \Psi_0} + \ldots \tag{2.30}$$

where Ψ_0 is the value of the stream function on the stagnation streamline. This result will prove to be useful shortly when a general expression for $\mathbf{v}^R$ will be derived. First, however, we will return to Goldstein's description of the rotational velocity.

Goldstein's paper did not explicitly address the singular nature of the drift function, so we will put this property aside for the moment. In general, the Goldstein rotational velocity, $\mathbf{v}^G$, may be written in terms of the drift and stream functions as

$$\mathbf{v}^G = (c_1 \nabla\Delta + c_2 \nabla\Psi) \exp[j(K_1\Delta + K_2\Psi)] \tag{2.31}$$

Here K_1 and K_2 are essentially wave numbers along drift and stream contours, and c_1 and c_2 are constants. Goldstein chose c_1 and c_2 so that the rotational velocity in the upstream far field is divergence-free, i.e.,

$$\nabla \cdot \mathbf{v}^G = 0 \tag{2.32}$$

or

$$c_1 K_1 + c_2 K_2 = 0 \tag{2.33}$$

The constants c_1 and c_2 may then be uniquely determined by specifying the magnitude and phase of the vorticity of the incoming gust.

With $\mathbf{v}^G$ defined, in principle all that remains is to solve Eq. (2.21) for the unsteady potential, ϕ. However, for flows over bodies that contain a stagnation point, this formulation leads to a singular rotational velocity on the blade and wake surfaces due to the logarithmic singularity in the drift function at the stagnation point described earlier. To avoid this singularity, one possible approach would be to set c_1 to zero in Eq. (2.31) to remove the terms that depend on the gradient of the drift function, and choose c_2 to match the specified vorticity. Unfortunately, although this modification produces a bounded rotational velocity, the rotational velocity has indeterminate phase along the blade and wake surfaces. As a result, the *divergence* of the rotational velocity still has a strong singularity at the airfoil and wake surfaces. Since the source term in Eq. (2.21) is dependent on the divergence of the rotational velocity, a modification to the description of the rotational velocity is necessary.

2.1.2 Atassi Decomposition

Atassi and Grzedzinski [27] developed a modified velocity splitting that is uniformly valid for flows around bodies. Shortly thereafter, Hall and Verdon [28] used this technique to study unsteady flows in cascades.

Atassi and Grzedzinski suggested adding the gradient of a convected, and therefore pressureless, scalar potential, $\tilde{\phi}$, to Goldstein's rotational velocity, so that

$$\mathbf{v}^R = \mathbf{v}^G + \nabla\tilde{\phi} \tag{2.34}$$

Since the curl of the gradient of a scalar is zero, this additional term does not change the unsteady vorticity in the flow.

This potential may not be simply chosen arbitrarily. First of all, this new form of $\mathbf{v}^R$ must satisfy Eq. (2.20). This is true if

$$\frac{D\tilde{\phi}}{Dt} = 0 \tag{2.35}$$

which implies that it has no pressure associated with it [see Eq. (2.18)]. Since it is convected, the potential propagates the same way as the Goldstein rotational velocity, i.e.,

$$\tilde{\phi} = \tilde{\Phi}(\Psi)\exp[j(K_1\Delta + K_2\Psi)] \tag{2.36}$$

where $\tilde{\Phi}$ is an as yet undetermined function. Using the form of $\tilde{\phi}$ given in Eq. (2.36), the rotational velocity may be written as

$$\mathbf{v}^R = \left[\left(c_1 + \frac{\partial\tilde{\phi}}{\partial\Delta}\right)\nabla\Delta + \left(c_2 + \frac{\partial\tilde{\phi}}{\partial\Psi}\right)\nabla\Psi\right]\exp[j(K_1\Delta + K_2\Psi)] \tag{2.37}$$

We wish to determine the potential $\tilde{\phi}$ such that $\mathbf{v}^R$ is zero on the blade and wake surfaces, which will produce the desired result that the normal and tangential components of the rotational velocity field are regular along the blade and wake surfaces. In terms of the unit surface tangent, $\mathbf{s}$, and the unit surface normal, $\mathbf{n}$, we want

$$\mathbf{v}^R \cdot \mathbf{s} = \left(\mathbf{v}^G + \nabla\tilde{\phi}\right)\cdot\mathbf{s} = 0 \tag{2.38}$$

and

$$\mathbf{v}^R \cdot \mathbf{n} = \left(\mathbf{v}^G + \nabla\tilde{\phi}\right)\cdot\mathbf{n} = 0 \tag{2.39}$$

The first condition, Eq. (2.38), is satisfied if $\tilde{\Phi}$ is a constant. To illustrate this, consider the tangential component of $\mathbf{v}^R$. Using Eq. (2.37), if $\tilde{\Phi}$ is constant, then

$$\left(c_1 + jK_1\tilde{\Phi}\right)\frac{\partial\Delta}{\partial s} + \left(c_2 + jK_2\tilde{\Phi}\right)\frac{\partial\Psi}{\partial s} = 0 \tag{2.40}$$

Since the airfoil surface and wake is a stagnation streamline, $\partial\Psi/\partial s$ is zero. Hence, if $\tilde{\Phi}$ is chosen such that

$$\tilde{\Phi} = \frac{jc_1}{K_1} \tag{2.41}$$

then Eq. (2.40) [and therefore Eq. (2.38)] is satisfied. This choice of $\tilde{\Phi}$ removes the dominant singularity in $\mathbf{v}^G$ which is on the order of $\nabla\Delta$. In fact, this is equivalent to setting c_1 to zero in Eq. (2.31) and choosing c_2 to match the specified vorticity, as suggested earlier.

Unfortunately, $\mathbf{v}^R$ may still have indeterminate phase. The singular behavior of the normal component of $\mathbf{v}^R$ is only completely eliminated when $\tilde{\phi}$ satisfies Eq. (2.39). To eliminate this singular behavior, we will proceed by splitting $\tilde{\phi}$ into two parts, so that

$$\tilde{\phi} = \tilde{\phi}_1 + \tilde{\phi}_2 \tag{2.42}$$

where, $\tilde{\phi}_1$ is the potential associated with the constant $\tilde{\Phi}$ given in Eq. (2.41), and $\tilde{\phi}_2$ is still to be determined. So as not to violate Eq. (2.38), $\tilde{\phi}_2$ will be chosen so that its

value will be zero on the blade and wake surfaces, while allowing $\tilde{\Phi}_2$ to be dependent on the stream function, Ψ.

Considering both parts of $\tilde{\phi}$, the normal component of $\mathbf{v}^R$ may be written as

$$\left(c_1 + \frac{\partial\tilde{\phi}_1}{\partial\Delta} + \frac{\partial\tilde{\phi}_2}{\partial\Delta}\right)\frac{\partial\Delta}{\partial n} + \left(c_2 + \frac{\partial\tilde{\phi}_1}{\partial\Psi} + \frac{\partial\tilde{\phi}_2}{\partial\Psi}\right)\frac{\partial\Psi}{\partial n} = 0 \tag{2.43}$$

In light of the choice of $\tilde{\phi}_1$, this reduces to

$$\frac{\partial\tilde{\phi}_2}{\partial\Delta}\frac{\partial\Delta}{\partial n} + \left(c_2 - \frac{c_1 K_2}{K_1} + \frac{\partial\tilde{\phi}_2}{\partial\Psi}\right)\frac{\partial\Psi}{\partial n} = 0 \tag{2.44}$$

or

$$\left(\frac{\partial\tilde{\phi}_2}{\partial\Delta}\frac{\partial\Delta}{\partial\Psi} + c_2 - \frac{c_1 K_2}{K_1} + \frac{\partial\tilde{\phi}_2}{\partial\Psi}\right)\frac{\partial\Psi}{\partial n} = 0 \tag{2.45}$$

Next, we wish to determine the behavior of the first term in Eq. (2.45) near the surface of the airfoil. Performing a Taylor expansion of $\partial\tilde{\phi}_2/\partial\Delta$ about the stagnation point gives

$$\frac{\partial\tilde{\phi}_2}{\partial\Delta} = \frac{\partial}{\partial\Psi}\left(\frac{\partial\tilde{\phi}_2}{\partial\Delta}\right)(\Psi - \Psi_0) + \ldots \tag{2.46}$$

This equation, combined with the expression for $\partial\Delta/\partial\Psi$ obtained in the earlier discussion of the behavior of the drift function near a stagnation point [Eq. (2.30)], leads to

$$\left[\frac{\partial}{\partial\Psi}\left(\frac{\partial\tilde{\phi}_2}{\partial\Delta}\right)a_0 + c_2 - \frac{c_1 K_2}{K_1} + \frac{\partial\tilde{\phi}_2}{\partial\Psi}\right]\frac{\partial\Psi}{\partial n} = 0 \tag{2.47}$$

As was shown earlier, $\tilde{\phi}_2$ has the form

$$\tilde{\phi}_2 = \tilde{\Phi}_2(\Psi)\exp[j(K_1\Delta + K_2\Psi)]$$

Substituting this expression into Eq. (2.47) gives

$$\left[(1 + ja_0K_1)\frac{\partial\tilde{\Phi}_2}{\partial\Psi} + c_2 - \frac{c_1 K_2}{K_1} + jK_2\tilde{\Phi}_2\right]\frac{\partial\Psi}{\partial n} = 0 \tag{2.48}$$

Also, because the cascade is periodic, a similar boundary condition must be applied on the next adjacent blade surface. Hence, the value of the stream function at this surface is required. The stream function may be computed by integrating the mass flux over the blade-to-blade gap

$$\Psi(G) = \Psi_0 + \int_0^G Q\,dy \tag{2.49}$$

where G is the blade-to-blade gap measured in the y-direction, and Q is the mass flux. Typically, the upstream steady density, $R_{-\infty}$, the upstream free stream velocity, $V_{-\infty}$, and the upstream flow angle, $\Omega_{-\infty}$, are specified. Using these values, the stream function may be written as

$$\Psi(x, y + G) = \Psi_0 + R_{-\infty}V_{-\infty}G\cos\Omega_{-\infty} \tag{2.50}$$

Consequently, since the potential should vanish at the blade and wake surfaces, we let $\tilde{\Phi}_2$ take the form

$$\tilde{\Phi}_2(\Psi) = \mathcal{B} \sin\left[\frac{2\pi(\Psi - \Psi_0)}{R_{-\infty} V_{-\infty} G \cos\Omega_{-\infty}}\right] \tag{2.51}$$

where $\mathcal{B}$ is a constant independent of Ψ. Substituting this functional form into the boundary condition [Eq. (2.48)] gives

$$\frac{2\pi\mathcal{B}(1 + ja_0K_1)}{R_{-\infty} V_{-\infty} G \cos\Omega_{-\infty}} \cos\left[\frac{2\pi(\Psi - \Psi_0)}{R_{-\infty} V_{-\infty} G \cos\Omega_{-\infty}}\right]_{\Psi=\Psi_0}$$

$$+ c_2 - \frac{c_1 K_2}{K_1} + jK_2\mathcal{B} \sin\left[\frac{2\pi(\Psi - \Psi_0)}{R_{-\infty} V_{-\infty} G \cos\Omega_{-\infty}}\right]_{\Psi=\Psi_0} = 0 \tag{2.52}$$

solving for $\mathcal{B}$ gives

$$\mathcal{B} = -\frac{R_{-\infty} V_{-\infty} G \cos\Omega_{-\infty}(c_2K_1 - c_1K_2)}{2\pi K_1(1 + ja_0K_1)} \tag{2.53}$$

After performing some algebra, the final expression for $\tilde{\phi}$ is obtained, i.e.,

$$\tilde{\phi} = \frac{j}{K_1}\left\{c_1 + \frac{jR_{-\infty} V_{-\infty} G \cos\Omega_{-\infty}(c_2K_1 - c_1K_2)}{2\pi(1 + ja_0K_1)} \sin\left[\frac{2\pi(\Psi - \Psi_0)}{R_{-\infty} V_{-\infty} G \cos\Omega_{-\infty}}\right]\right\}$$

$$\times \exp[j(K_1\Delta + K_2\Psi)] \tag{2.54}$$

This expression for $\tilde{\phi}$ results in a rotational velocity that is regular along the blade and wake surfaces, so that the divergence of the rotational velocity may be calculated despite the presence of a stagnation point. Note that the complete expression for $\mathbf{v}^R$ is relatively simple, and may be calculated once the steady flow has been computed and the desired magnitude and phase of the unsteady vorticity has been chosen. Now that a uniformly valid expression for $\mathbf{v}^R$ has been written, then, the next task is to calculate the unsteady velocity potential, ϕ, using Eq. (2.21).

2.2 Extension of Bateman's Variational Principle

Now that the governing equations have been developed, it is useful to consider how these equations will be solved numerically. Essentially there are two choices: finite differences and finite elements. Both of these methods have been used to solve the linearized potential equation for blade motion and pressure gust analyses [22, 23]. In addition, Hall and Verdon used finite differences to solve the linearized potential equation with rapid distortion theory to analyze vortical gusts [28]. For this report, a finite element discretization of the field equations is used. There are three main reasons for this approach. First, finite element techniques are versatile, elegant, and relatively easy to implement. Second, it is believed that a finite element approach will reduce the overall truncation error because the governing equation is solved in the

integral sense instead of the differential sense. Truncation errors tend to be higher in derivative evaluation than integral evaluation. Finally, a potential method for blade motion analyses developed by Hall [24] was readily available. The details of the finite element procedure will be given in Chapter 3. This section will describe the variational principle on which the finite element method is based and its application to the current work, including the effect of unsteady vorticity.

2.2.1 Nonlinear Full Variational Principle

First, consider irrotational and homentropic flow. Bateman [47] developed a variational principle that states that for a steady flow, the volume integral of the pressure must have an extreme value, and the associated Euler-Lagrange equation is the steady conservation of mass. Hall [24] later extended this principle for application to cascades by considering temporally periodic flow. In this case, the pressure integrated over a domain Σ and over a period Λ is extremized. In functional form,

$$\Pi = \frac{1}{\Lambda}\int_\Lambda \iint_\Sigma \hat{p}\; dx\; dy\; dt + \frac{1}{\Lambda}\int_\Lambda \oint_\Gamma \hat{Q}\hat{\phi}\; ds\; dt \tag{2.55}$$

where $\hat{Q}$ is the prescribed mass flux on the boundary and s is the distance along the boundary Γ. Taking the first variation of Π and setting to zero gives

$$\delta\Pi = \frac{1}{\Lambda}\int_\Lambda \iint_\Sigma \delta\hat{p}\; dx\; dy\; dt + \frac{1}{\Lambda}\int_\Lambda \oint_\Gamma \hat{Q}\;\delta\hat{\phi}\; ds\; dt = 0 \tag{2.56}$$

Bernoulli's Equation says that

$$\frac{\hat{p}}{\hat{\rho}} + \frac{1}{2}\left(\nabla\hat{\phi}\right)^2 + \frac{\partial\hat{\phi}}{\partial t} = \mathcal{C} \tag{2.57}$$

where $\mathcal{C}$ is a constant. Since we have assumed that the flow is homentropic, the variation of the pressure may be written as

$$\delta\hat{p} = -\hat{\rho}\left(\nabla\hat{\phi}\cdot\nabla\delta\hat{\phi} + \frac{\partial}{\partial t}\delta\hat{\phi}\right) \tag{2.58}$$

Substituting this expression into the equation for $\delta\Pi$, using the divergence theorem and integration by parts gives

$$\delta\Pi = \frac{1}{\Lambda}\int_\Lambda \iint_\Sigma \left[\nabla\cdot\left(\hat{\rho}\nabla\hat{\phi}\right) + \frac{\partial\hat{\rho}}{\partial t}\right]\;\delta\hat{\phi}\; dx\; dy\; dt$$

$$+ \frac{1}{\Lambda}\int_\Lambda \oint_\Gamma \left(\hat{Q} - \hat{\rho}\frac{\partial\hat{\phi}}{\partial n}\right)\;\delta\hat{\phi}\; ds\; dt = 0 \tag{2.59}$$

To extremize Π, $\delta\Pi$ must be zero for all permissible variations in $\hat{\phi}$. Therefore, Eq. (2.59) says that the conservation of mass must be satisfied in the domain Σ. On the boundary Γ, Dirichlet boundary conditions may be imposed, since then $\delta\hat{\phi}$ will be

zero, or the Neumann boundary condition may be used, so that $\hat{\rho}\partial\hat{\phi}/\partial n = \hat{Q}$. This is the so-called natural boundary condition.

Since the steady and unsteady flow is governed by the conservation of mass, this variational principle is the appropriate choice to be discretized and solved. For this principle to be used, however, the temporal integration must be removed. This may be accomplished through the use of the earlier assumption that the unsteady flow is harmonically varying with frequency ω. With the temporal behavior of the potential represented by assumed mode shapes, the resulting steady and unsteady variational principles for the spatial behavior of the flow may then be discretized and solved using traditional finite element techniques.

2.2.2 Steady Flow Variational Principle

For steady flows, the variational principle is quite simple. Since the pressure, P, the potential, Φ, and the density, R, are all independent of time, the functional Π becomes

$$\Pi_{\text{steady}} = \iint_{\Sigma} P \, dx \, dy + \oint_{\Gamma} Q\Phi \, ds \tag{2.60}$$

To extremize this equation, the first variation is set to zero, resulting in

$$\begin{aligned} \delta\Pi_{\text{steady}} &= \iint_{\Sigma} \delta P \, dx \, dy + \oint_{\Gamma} Q \, \delta\Phi \, ds \\ &= -\iint_{\Sigma} R\nabla\Phi \cdot \nabla\delta\Phi \, dx \, dy + \oint_{\Gamma} Q \, \delta\Phi \, ds = 0 \end{aligned} \tag{2.61}$$

Using the divergence theorem, this becomes

$$\delta\Pi_{\text{steady}} = \iint_{\Sigma} \left[\nabla \cdot (R\nabla\Phi)\right] \, \delta\Phi \, dx \, dy + \oint_{\Gamma} \left(Q - R\frac{\partial\Phi}{\partial n}\right) \, \delta\Phi \, ds \tag{2.62}$$

The Euler-Lagrange equation of this variational principle is the steady conservation of mass, Eq. (2.8). The natural boundary condition is the Neumann condition $R\partial\Phi/\partial n = Q$. Finally, it should be noted that the steady conservation of mass is nonlinear in the steady potential, Φ due to the dependence of R on Φ. Consequently, nonlinear finite element techniques will be required.

2.2.3 Unsteady Flow Variational Principle With Deforming Grid and Vorticity

The variational principle for the unsteady flow is considerably more complicated than its steady flow counterpart. Part of this complexity is due to the fact that the linearized potential equation is more complicated than the steady flow potential equation, as was shown earlier. In addition, we will see that an extension to the variational principle is useful for the analysis of blade motion problems.

Up to this point, the theoretical development in this chapter has been mainly concerned with the forced response (or gust) problem, i.e., how to include the effect

of unsteady vorticity within a linearized potential framework. There is an additional complication inherent in the flutter (blade vibration) problem, however. Previous methods for solving the potential equation have used grids that are fixed in space. While this is numerically convenient, the airfoil boundary conditions must be applied at the mean airfoil location instead of the instantaneous location. As a result, extrapolation terms must be added to the unsteady airfoil boundary conditions to transfer the boundary conditions from the instantaneous location of the airfoil to its mean position. These terms contain steady velocity gradients that are difficult to evaluate numerically. Consequently, the accuracy of numerical calculations using fixed grids is limited.

One way to eliminate these extrapolation terms is to use a computational grid that continuously deforms with the airfoil motion. This procedure has been shown to be an effective technique for improving the accuracy of linearized analyses [30, 31, 35].

In this report, it is assumed that the grid motion is a small harmonic perturbation about the mean grid location. We introduce computational coordinates (ξ, η, τ) so that the grid deforms in the physical coordinate system (x, y, t), but appears stationary in the computational coordinate system. Said another way, the computational coordinates are "attached" to the deforming grid. To illustrate, Figure 2.3 shows contours of the computational coordinate system for deformed and undeformed grids for a cascade of airfoils pitching about their midchords. Note that the computational coordinates do indeed "deform" with the blade motion. Mathematically, the two coordinate systems are related by the perturbation series

$$x(\xi, \eta, \tau) = \xi + f(\xi, \eta)e^{j\omega\tau} \tag{2.63}$$

$$y(\xi, \eta, \tau) = \eta + g(\xi, \eta)e^{j\omega\tau} \tag{2.64}$$

$$t(\xi, \eta, \tau) = \tau \tag{2.65}$$

Note that to zeroth order, the physical and computational coordinates are the same. The terms f and g are first-order perturbations that map the computational coordinate system to the moving physical system. The flow decomposition described earlier may be expressed in a similar fashion, i.e.,

$$\begin{array}{lcccl} \hat{\rho}(x,y,t) & = & R(\xi,\eta) & + & \rho(\xi,\eta)e^{j\omega\tau} \\ \hat{\mathbf{v}}(x,y,t) & = & \nabla\Phi(\xi,\eta) & + & \mathbf{v}(\xi,\eta)e^{j\omega\tau} \\ \hat{p}(x,y,t) & = & P(\xi,\eta) & + & p(\xi,\eta)e^{j\omega\tau} \\ \underbrace{\hat{s}_f(x,y,t)} & = & \underbrace{\qquad} & & \underbrace{s_f(\xi,\eta)e^{j\omega\tau}} \\ \text{total flow} & & \begin{array}{c}\text{nonlinear}\\ \text{mean}\end{array} & & \begin{array}{c}\text{small harmonic}\\ \text{disturbance}\end{array} \end{array} \tag{2.66}$$

To first order, the gradient operator, ∇, and time derivative operator, $\partial/\partial t$, operators may be expressed in terms of the computational coordinate operators ∇' and

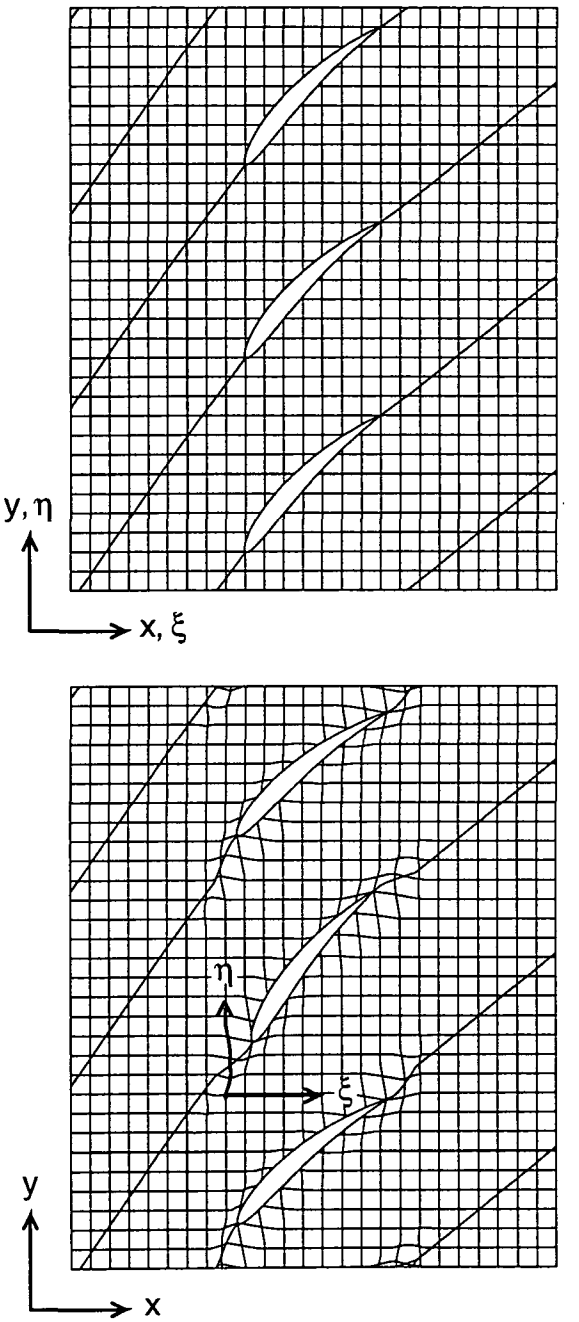

Figure 2.3: Contours of computational coordinates (ξ, η) for undeformed (top) and deformed (bottom) grids for a cascade of airfoils. Airfoils are pitching about their midchords with an interblade phase angle, σ, of 180°.

$\partial/\partial\tau$ as follows:

$$\nabla = \begin{pmatrix} \partial/\partial x \\ \partial/\partial y \end{pmatrix} = \begin{bmatrix} 1-f_\xi & -g_\xi \\ -f_\eta & 1-g_\eta \end{bmatrix} \begin{pmatrix} \partial/\partial\xi \\ \partial/\partial\eta \end{pmatrix} = [\mathbf{J}]\nabla' \tag{2.67}$$

and

$$\frac{\partial}{\partial t} = \frac{\partial}{\partial \tau} - \frac{\partial \mathbf{f}}{\partial \tau} \cdot \nabla' \tag{2.68}$$

where $\mathbf{f}$ is the vector of grid motion perturbation functions, $(f, g)^T$.

Now that the coordinate systems have been described, the unsteady variational principle may be expressed in the computational coordinate system. By assuming a harmonic time dependence, the temporal integration in the functional Π may be carried out. In the computational coordinate system, the unsteady functional is

$$\Pi_{\text{unsteady}} = \frac{1}{\Lambda}\int_\Lambda \iint_\Sigma \hat{p}\left|[\mathbf{J}]^{-1}\right| \, d\xi \, d\eta \, d\tau + \frac{1}{\Lambda}\int_\Lambda \oint_\Gamma \hat{Q}\hat{\phi}\left|[\mathbf{J}]^{-1}\right| \, ds \, d\tau \tag{2.69}$$

The expression for $\hat{p}$ in the computational coordinate system may be derived by substituting the coordinate transformation operators from Eqs. (2.67) and (2.68) into the unsteady nonlinear Bernoulli Equation, i.e.,

$$\hat{p} = p_T \left(1 - \frac{\gamma - 1}{{C_T}^2}\left[\frac{1}{2}\nabla'\hat{\phi}^T[\mathbf{J}]^T[\mathbf{J}]\nabla'\hat{\phi} + \frac{\partial\hat{\phi}}{\partial t} - \mathbf{f}_\tau \cdot \nabla'\hat{\phi}\right]\right)^{\frac{\gamma}{\gamma-1}} \tag{2.70}$$

Also, to first order, the inverse of the transformation matrix $[\mathbf{J}]$ may be written as

$$[\mathbf{J}]^{-1} = \begin{bmatrix} 1+f_\xi & g_\xi \\ f_\eta & 1+g_\eta \end{bmatrix} \tag{2.71}$$

To obtain an expression for the small disturbance unsteady flow, the functional in Eq. (2.69) is expanded in powers of ϕ, f, and g retaining up to quadratic terms. The first-order terms in the functional will result in the steady flow Euler-Lagrange equation. Because the steady flow Euler-Lagrange equation is satisfied by the mean flow potential Φ, these terms will not contribute to the unsteady flow functional. Therefore, only the second-order terms will contribute. Hence, the functional may be written as

$$\begin{aligned}\Pi_{\text{linear}} = {} & \frac{1}{\Lambda}\int_\Lambda \iint_\Sigma \frac{1}{2}R\left[-\nabla'\phi^T\nabla'\phi + \frac{1}{C^2}\left(\nabla'\Phi^T\nabla'\phi + \phi_\tau\right)^2\right] d\xi \, d\eta \, d\tau \\ & -\frac{1}{\Lambda}\int_\Lambda \iint_\Sigma R\left\{\left[\nabla'\Phi^T[\tilde{\mathbf{J}}]\nabla'\phi + \nabla'\cdot\mathbf{f}\left(\nabla'\Phi^T\nabla'\phi + \phi_\tau\right) - \mathbf{f}_\tau\cdot\nabla'\phi\right]\right. \\ & \left. -\frac{1}{C^2}\left[\left(\frac{1}{2}\nabla'\Phi^T[\tilde{\mathbf{J}}]\nabla'\Phi - \mathbf{f}_\tau\cdot\nabla'\Phi\right)\left(\nabla'\Phi^T\nabla'\phi + \phi_\tau\right)\right]\right\} d\xi \, d\eta \, d\tau\end{aligned} \tag{2.72}$$

Note that the surface integral terms have been omitted for the time being. Next, the time integral needs to be evaluated. As was stated earlier, it is assumed that the unsteady flow variables (and the blade motion, if any) vary harmonically. Hence, the unsteady flow may be represented as a Fourier series in time. These Fourier modes

may be analyzed individually and summed, since the governing equation is linear. Therefore, it may be assumed that, for example,

$$\phi(\xi,\eta,\tau) \rightarrow \mathrm{Re}\left[\phi(\xi,\eta)e^{j\omega t}\right] = \frac{1}{2}\left[\phi(\xi,\eta)e^{j\omega t} + \overline{\phi}(\xi,\eta)e^{-j\omega t}\right] \tag{2.73}$$

where $\phi(\xi,\eta)$ is now the complex amplitude of the unsteady potential, and $\overline{\phi}(\xi,\eta)$ is its complex conjugate. The other unsteady variables are represented in a similar fashion. Substitution of this assumption into the unsteady flow functional, Eq. (2.72), results in

$$\begin{aligned}
\Pi_{\text{linear}} = \frac{1}{2}\iint_\Sigma R\Big\{ & -\nabla'\overline{\phi}^T\nabla'\phi + \frac{1}{C^2}\Big[\nabla'\overline{\phi}^T\nabla'\Phi\nabla'\Phi^T\nabla'\phi \\
& + j\omega\left(\nabla'\overline{\phi}^T\nabla'\Phi\phi - \overline{\phi}\nabla'\Phi^T\nabla'\phi\right) + \omega^2\overline{\phi}\phi\Big]\Big\}\, d\xi\, d\eta \\
- \iint_\Sigma R\Big\{ & \nabla'\Phi^T[\tilde{\mathbf{J}}]\nabla'\overline{\phi} + \nabla'\cdot\mathbf{f}\left(\nabla'\Phi^T\nabla'\overline{\phi} - j\omega\overline{\phi}\right) - j\omega\mathbf{f}\cdot\nabla'\overline{\phi} \\
& - \frac{1}{C^2}\left[\left(\frac{1}{2}\nabla'\Phi^T[\tilde{\mathbf{J}}]\nabla'\Phi - j\omega\mathbf{f}\cdot\nabla'\Phi\right)\left(\nabla'\Phi^T\nabla'\overline{\phi} - j\omega\overline{\phi}\right)\right]\Big\}\, d\xi\, d\eta \\
& + \text{complex conjugate terms}
\end{aligned} \tag{2.74}$$

where $[\tilde{\mathbf{J}}] = [\mathbf{J}]^T[\mathbf{J}] - [\mathbf{I}]$. Note that none of the boundary conditions have been discussed as yet. Additional terms will be added to the variational principle in the next section to specify the boundary conditions.

At this point, it should be noted that no vorticity has been included in the unsteady functional. Although the grid motion and unsteady vorticity problems are usually analyzed separately in practice, the vortical terms will be added here for completeness.

The divergence theorem says that for any vector $\mathbf{V}$,

$$\iint_\Sigma \nabla\cdot\mathbf{V}\, dA - \oint_\Gamma \mathbf{V}\cdot\mathbf{n}\, ds = 0 \tag{2.75}$$

Consider the case where $\mathbf{V} = \overline{\phi}R\mathrm{v}^R$. The divergence theorem may be written as

$$\iint_\Sigma \nabla'\cdot R\mathrm{v}^R\overline{\phi}\, d\xi\, d\eta - \oint_\Gamma R\mathrm{v}^R\cdot\mathbf{n}\overline{\phi}\, ds = 0 \tag{2.76}$$

Note that because the rotational velocity and grid motion terms in the functional are both second order, there is no coupling between the two, i.e., there will be no terms in the functional that depend on both the rotational velocity and the grid motion. Consequently, Eq. (2.76) may be written in the computational coordinate system.

We wish to add terms to the unsteady functional Π so that the Euler-Lagrange equation will contain the appropriate rotational velocity terms appearing in Eq. (2.21). Because the terms in Eq. (2.76) sum to zero, Eq. (2.76) and its associated complex conjugate expression may be added to the functional given in Eq. (2.74). Leaving aside the boundary terms for the moment, taking the variation of Eq. (2.74) including the rotational velocity terms and applying the divergence theorem results in the

Euler-Lagrange equation for the unsteady flow. This linearized potential equation may be written as

$$\nabla' \cdot R\nabla'\phi - \nabla' \cdot \left[\frac{R}{C^2}\left(\nabla'\Phi^T\nabla'\phi + j\omega\phi\right)\nabla'\Phi\right] - \frac{R}{C^2}\left(j\omega\nabla'\Phi^T\nabla'\phi - \omega^2\phi\right)$$
$$= -\nabla' \cdot \left[R\left([\tilde{\mathbf{J}}]\nabla'\Phi + \nabla' \cdot \mathbf{f}\nabla'\Phi\right)\right] + j\omega\mathbf{f} \cdot \nabla' R$$
$$+\nabla' \cdot \left[\frac{R}{C^2}\left(\frac{1}{2}\nabla'\Phi^T[\tilde{\mathbf{J}}]\nabla'\Phi\nabla'\Phi - j\omega\mathbf{f} \cdot \nabla'\Phi\nabla'\Phi\right)\right]$$
$$+\frac{R}{C^2}\left[\frac{j\omega}{2}\nabla'\Phi[\tilde{\mathbf{J}}]\nabla'\Phi + \omega^2\mathbf{f} \cdot \nabla'\Phi\right] - \nabla' \cdot R\mathbf{v}^R \qquad (2.77)$$

Note that if there is no grid motion, Eq. (2.77) may be rearranged into the form of Eq. (2.21), the original equation to be solved.

In summary, then, Bateman's variational principle may be extended to include both the flutter and forced response problems typically encountered in turbomachinery. The next two sections will describe the boundary conditions required for cascades, and Chapter 3 will discuss how Eq. (2.77) and the boundary conditions are discretized and solved numerically.

2.3 Near-Field Boundary Conditions

Now that the governing equations have been developed, appropriate boundary conditions need to be imposed. Figure 2.4 shows the locations of the four types of boundary conditions for cascades. In this report, the periodic, airfoil surface, and wake conditions will be referred to as "near-field" boundary conditions and will be discussed in this section. The remaining "far-field" boundary conditions are somewhat more complicated and will be discussed in the next section.

2.3.1 Periodic Boundary Condition

Steady Flow

In this analysis, all of the airfoils in a given blade row are assumed to be identical. Hence, the steady flow over each blade is the same. The periodic boundary condition is that the difference in the steady potential between two adjacent periodic boundaries is a constant, i.e.,

$$\Phi(\xi, \eta + \kappa G) = \Phi(\xi, \eta) + \kappa G V_{-\infty} \qquad (2.78)$$

where G is the blade-to-blade gap, $V_{-\infty}$ is the specified upstream velocity in the y-direction, and κ is the blade number, where the reference blade number is zero. This boundary condition is applied on the periodic surfaces shown in Fig. 2.4.

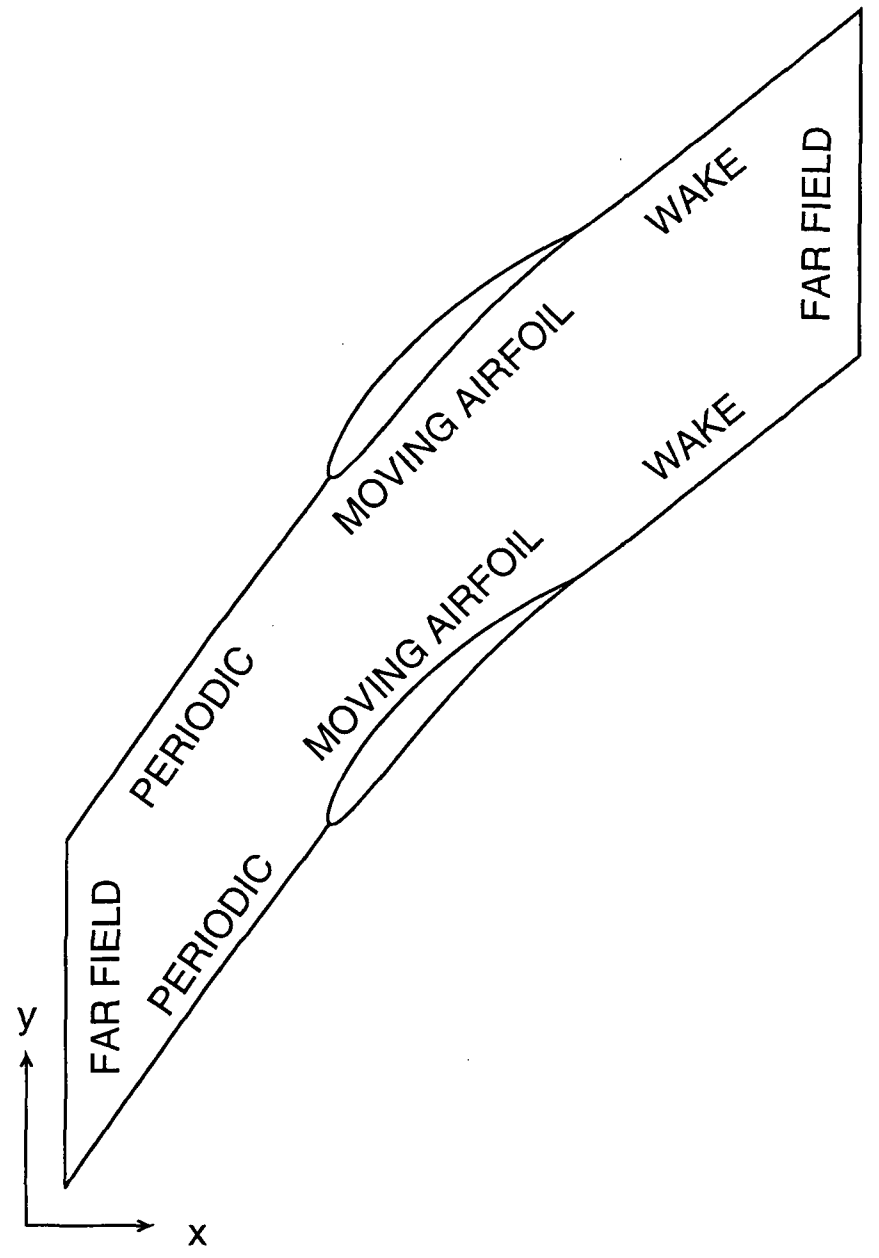

Figure 2.4: Locations of boundaries for a typical cascade.

Unsteady Flow

Clearly, computing the unsteady flow around every airfoil in a blade row would be a formidable computational task. Hence, we wish to reduce the size of the numerical calculation. Lane [49] showed that any vibration of the blades of a cascade may be decomposed into a sum of traveling waves with a fixed interblade phase angle. Accordingly, in this analysis, it is assumed that any incoming disturbance or blade motion may be decomposed into a sum of Fourier modes, i.e., the unsteady flow is periodic in the circumferential direction. Since the governing equation is linear, the flow solutions for each of the individual modes may be superposed to form the complete flow solution.

Hence, the flow around any blade may be computed by simply using the interblade phase angle (or circumferential wave number) to account for the distance between the blade to be analyzed and a reference blade. The periodic boundary condition may then be expressed as

$$\phi(\xi, \eta + \kappa G) = \phi(\xi, \eta) e^{j\kappa\sigma} \tag{2.79}$$

where σ is the interblade phase angle.

The periodic boundary condition is not included explicitly in the variational principle. Its application will be discussed in Chapter 3.

2.3.2 Airfoil Surface Boundary Condition

Steady Flow

On the surface of the blade, no flow must pass through the blade. For the steady flow analysis, there is no blade motion or incoming disturbance, so this condition is simply

$$\frac{\partial \Phi}{\partial n} = 0 \tag{2.80}$$

where n is measured normal to the airfoil surface. Note that this condition is the natural boundary condition from the steady flow variational principle [Eq. (2.62)]. Since it is a natural boundary condition, no boundary condition need actually be imposed here to obtain the correct solution.

Unsteady Flow

For unsteady flows, the airfoil surface boundary condition is also the natural boundary condition of the variational principle. The motion of the blades induces an upwash on the airfoil surface (which is the source of the unsteadiness for flutter problems). If $\mathbf{v}^R$ is nonzero on the blade surface (such as in the case of the original Goldstein formulation) then the upwash due to the rotational velocity must also be accounted for. The natural boundary condition from the variational principle is obtained from the first variation of the functional Π that includes the rotational velocity terms, i.e.,

$$\delta \Pi_{\text{linear}} = \iint_{\Sigma} \{\ldots\}\, \delta\overline{\phi}\, d\xi\, d\eta$$

$$+ \oint_\Gamma R \left(j\omega \mathbf{f} \cdot \mathbf{n} - [\tilde{\mathbf{J}}] \nabla \Phi \cdot \mathbf{n} + \mathbf{v}^R \cdot \mathbf{n} - \frac{\partial \phi}{\partial n} \right) \delta \overline{\phi} \, ds = 0 \tag{2.81}$$

So the boundary condition is

$$\frac{\partial \phi}{\partial n} = j\omega \mathbf{f} \cdot \mathbf{n} - [\tilde{\mathbf{J}}] \nabla \Phi \cdot \mathbf{n} + \mathbf{v}^R \cdot \mathbf{n} \tag{2.82}$$

The first term on the right hand side of Eq. (2.82) is the upwash due to the translation of the airfoil. The second term is an additional upwash required to counter a downwash produced by shearing motion of the grid and resulting shearing of the steady potential field in the vicinity of the airfoil surface. Note that there is no upwash due to local rotation of the airfoil, nor are there extrapolation terms due to the difference between the mean and instantaneous position of the blade surface. These are not required because the mean potential field moves with the grid due to the grid motion assumption imposed earlier. The last term on the right hand side of Eq. (2.82) is the upwash associated with a nonzero rotational velocity on the blade surface.

2.3.3 Wake Boundary Condition

Steady Flow

The wake boundary conditions have characteristics of both the periodic and airfoil surface boundary conditions described earlier. The first boundary condition is that the wake is considered to be an impermeable surface, so the steady no throughflow condition applies, Eq. (2.80). Second, there is a jump in potential at the trailing edge which is equal to the circulation around the blade. If the jump in potential across the wake is equal to the jump in potential at the trailing edge, the Kutta condition is automatically satisfied. The boundary condition is then

$$[\![\Phi]\!]_{\text{Wake}} = [\![\Phi]\!]_{\text{TE}} \tag{2.83}$$

where $[\![\Phi]\!]$ is the jump in the steady potential. An equivalent boundary condition is that the pressure is continuous across the wake. Hence, the steady pressure continuity condition is

$$[\![P]\!] = 0 \tag{2.84}$$

where $[\![P]\!]$ is the steady pressure jump across the wake. For the wake to coincide with the grid boundary, an additional equation will be required to enforce the pressure continuity condition.

Unsteady Flow

For unsteady flows, the wake oscillates harmonically about its mean position with an unknown displacement, r. Thus, as in the steady case, there is an auxiliary equation to enforce the unsteady pressure continuity. In one dimension, the unsteady pressure is linearly related to the unsteady potential, i.e.,

$$p = -R \left(j\omega + \frac{\partial \Phi}{\partial s} \frac{\partial}{\partial s} \right) \phi \tag{2.85}$$

The pressure continuity equation may then be written as

$$[\![p]\!] = -R\left(j\omega + \frac{\partial\Phi}{\partial s}\frac{\partial}{\partial s}\right)[\![\phi]\!] = 0 \tag{2.86}$$

where $[\![\ldots]\!]$ represents the jump across the wake. Specifically, the jump in potential is

$$[\![\phi]\!] = \phi^u e^{-j\sigma} - \phi^\ell \tag{2.87}$$

where ϕ^u is the potential on the upper wake surface of the computational domain (see Fig. 2.4), and ϕ^ℓ is the potential on the lower wake surface.

The other boundary condition applied on the wake is that conservation of mass must be satisfied. In particular, the upwash due to the wake displacement must be accounted for. This additional upwash may be written as

$$\frac{\partial\phi}{\partial n} = \frac{\partial\Phi}{\partial s}\frac{\partial r}{\partial s} + j\omega r \tag{2.88}$$

where $\partial\Phi/\partial s$ is the mean flow tangential velocity along the wake. The first term is a "ramp" effect due to a change in wake displacement along the wake. The second term is the upwash due to the translation of the wake. However, these effects are in addition to the grid deformation effects given by Eq. (2.82). Therefore, the complete upwash on the wake surface is

$$\frac{\partial\phi}{\partial n} = j\omega\mathbf{f}\cdot\mathbf{n} - [\tilde{\mathbf{J}}]\nabla\Phi\cdot\mathbf{n} + \mathbf{v}^R\cdot\mathbf{n} + \frac{\partial\Phi}{\partial s}\frac{\partial r}{\partial s} + j\omega r \tag{2.89}$$

Consequently, a term must be added to the variational principle to account for this additional upwash due to the motion of the wake. Taking the first variation of the modified variational principle and setting to zero gives

$$\delta\Pi_{\text{linear}} = [\text{Eq. (2.81)}] + \int_{\Gamma_{\text{WAKE}}} -R\left(\frac{\partial\Phi}{\partial s}\frac{\partial r}{\partial s} + j\omega r\right)\left(\delta\overline{\phi}^u e^{j\sigma} - \delta\overline{\phi}^\ell\right)\,ds = 0 \tag{2.90}$$

2.4 Far-Field Boundary Conditions

The boundary conditions at the far field are of a different nature than the near-field conditions, particularly for unsteady flows. Specifically, the far-field boundary conditions isolate the computational domain from influences outside the blade row being examined. Unsteady waves from the airfoil must pass out of the computational domain unreflected, so that the reflection of these waves does not corrupt the unsteady solution. For this reason, it is crucial to apply highly *nonreflective* far-field boundary conditions.

2.4.1 Steady Flow

First, the steady flow boundary conditions must be enforced at the far field of the computational domain, as shown in Fig. 2.4. The steady far-field boundary conditions

are specified using four parameters: the total pressure, p_T, the total density, ρ_T, the inflow circumferential velocity, $V_{-\infty}$, and the mass flux through the cascade, $Q_\infty = R_\infty U_\infty$. For a fluid with ratio of specific heats γ, these four quantities may be determined once the inflow Mach number and flow angle are known.

Upstream, the inflow circumferential velocity is used to specify the steady potential, Φ, at the far field, i.e.,

$$\Phi(y) = V_{-\infty} y \tag{2.91}$$

Note that since this is a Dirichlet boundary condition, the variation of the steady potential, $\delta\Phi$, is zero. Hence, the boundary integral in the first variation of the steady variational principle, Eq. (2.62), is zero.

Downstream, the steady mass flux is is specified, i.e.,

$$R\frac{\partial \Phi}{\partial n} = Q_\infty \tag{2.92}$$

In this case, a Neumann boundary condition is applied, which is the natural boundary condition of the steady variational principle. Note that because the governing equation is the steady conservation of mass, specifying the mass flux at the exit of the domain also fixes the mass flow at the cascade inlet.

2.4.2 Unsteady Flow

There are two main approaches for imposing nonreflecting boundary conditions at the far field. The first approach, developed by Verdon et al [50], matched an analytical description of the far-field behavior to the numerically calculated near-field solution. This approach was also applied to the linearized Euler equations by Hall and Crawley [29]. The advantage of this method is that the far-field solutions may be obtained with very little computational expense, since the far-field behavior may be described analytically. There are two main disadvantages to this approach, however. First, it does not lend itself well to three-dimensional problems. The annular geometry makes analytical solutions extremely difficult to obtain, except for special cases. Second, the assumption that the circumferential eigenmodes of the solution are Fourier modes is only exact if the computational grid is uniformly spaced in the circumferential direction in the far field. In addition, the method does not account for the truncation error associated with the field discretization scheme.

To alleviate these and other problems, Hall [24] and Hall, Lorence, and Clark [51] developed a numerically exact method for constructing nonreflecting far-field boundary conditions. In this approach, the eigenmodes of the unsteady fluid motion in the far field are obtained using the discretized governing equations. These eigenmodes are then used to construct nonreflecting boundary conditions. Although the numerically exact behavior is obtained using this method, it is much more computationally expensive than the analytical approach.

Initially, the numerically exact method was implemented in the present method. Unfortunately, the sensitivity analysis (to be described in Chapter 4) of this method becomes extremely computationally expensive due to the need to compute the sensitivities of the eigenvectors. To reduce the computational expense of the present

method, the analytical approach was chosen to demonstrate the present method. For the cases to be considered here, the error associated with this approach is actually quite small. In the future, particularly for three-dimensional applications, it would be useful to find a computationally efficient procedure to perform the sensitivity analysis on the exact approach.

In this section, the method for computing the analytical description of the unsteady potential in the far field is described. Only the homogeneous (i.e., the right-hand side of Eq. (2.77) is zero) problem will be described here. It should be noted that there is never any grid motion in the far field. If there is an incoming acoustic or vortical gust, the problem is inhomogeneous, and the particular solution is computed numerically. The computation of the particular solution will be described in Chapter 3.

Continuous Far-Field Potential

In the upstream far field, the unsteady potential is continuous in the circumferential direction. Downstream, the jump in potential associated with the wake requires an additional discontinuous part of the unsteady potential. The continuous part of the potential is derived in the same fashion upstream and downstream, and is described here.

In the far field, it is assumed that the steady flow is uniform and the unsteady flow is a small harmonic perturbation about the steady flow. Under these conditions, the unsteady flow is governed by the convective wave equation, i.e.,

$$\frac{D^2\phi_c}{Dt^2} - C^2\nabla^2\phi_c = 0 \tag{2.93}$$

where the total derivative is

$$\frac{D}{Dt} = \frac{\partial}{\partial t} + U\frac{\partial}{\partial x} + V\frac{\partial}{\partial y}$$

Here ϕ_c is the continuous unsteady potential, U and V are the steady flow velocities in the x- and y-directions, and C is the steady flow speed of sound. Next, it is assumed that the unsteady potential in the far field may be decomposed into a sum of Fourier modes, so that

$$\phi_c(x,y,t) = \sum_{m=-\infty}^{\infty} d_m \exp\left[j\omega t + j\alpha_m x + j\beta_m y\right] \tag{2.94}$$

where d_m are the Fourier coefficients, α_m are the as yet undetermined axial wave numbers, and $\beta_m = (\sigma + 2\pi m)/G$ are the specified circumferential wave numbers. The axial wave numbers may be obtained by substituting Eq. (2.94) into Eq. (2.93), which gives

$$\alpha_m = \frac{U(\omega + \beta_m V) \pm C\sqrt{\beta_m^2(U^2 + V^2 - C^2) + 2\beta_m\omega V + \omega^2}}{C^2 - U^2} \tag{2.95}$$

These wavenumbers correspond to upstream going and downstream going pressure waves. The direction of propagation may be determined as follows. If the α_m pair are complex, the direction may be determined on physical grounds by the direction of exponential decay. For example, at the upstream far field, the wave that decays in the positive x-direction must be a downstream going mode, since if it were an upstream going mode, that would imply that the wave generated in the computational domain would eventually have infinite amplitude, which is not physically possible. Waves that decay exponentially are referred to as "subresonant".

If the α_m pair are purely real, the waves propagate unattenuated. These are referred to as "superresonant" modes. Their direction of propagation may be determined by examining the group velocity [51], which is defined as

$$V_g = -\left(\frac{\partial \alpha}{\partial \omega}\right)^{-1} \tag{2.96}$$

The group velocity is the speed at which a packet of waves of a given wave number moves. If the group velocity is positive, there is a net flux of energy in the positive x-direction. Hence, the wave propagates in the positive x-direction.

Finally, the coefficients d_m may be determined from a Fourier transform of the unsteady potential in the far field, i.e.,

$$d_m = \frac{1}{G}\int_0^G \phi_c(x_{\text{ff}}, y)\exp(-j\beta_m y)\, dy \tag{2.97}$$

where x_{ff} is the x-coordinate at the far-field boundary being examined. Once all of the Fourier coefficients and wave numbers have been obtained, only the outgoing pressure waves are retained. All incoming modes are set to zero, since they come from outside of the computational domain. The outgoing modes are then summed using Eq. (2.94) to determine the new continuous unsteady potential, ϕ_c.

Discontinuous Far-Field Potential

Next, an expression for the discontinuous part of the downstream far-field potential due to the wake is required. The wake is modeled here as a vorticity wave that convects with the free stream. The geometry for this analysis is shown in Fig. 2.5. Here the x- and y-axes form the usual coordinate system, shifted so that the origin is at the downstream far-field boundary. The x_r- and y_r-axes are rotated through the angle θ to align with the wake boundary. The wake boundary is aligned with the steady free stream velocity, V_r. The conversion between the two coordinate systems is given by

$$x_r = x\cos\theta + y\sin\theta$$

$$y_r = -x\sin\theta + y\cos\theta$$

and

$$x = x_r\cos\theta - y_r\sin\theta$$

$$y = x_r\sin\theta + y_r\cos\theta$$

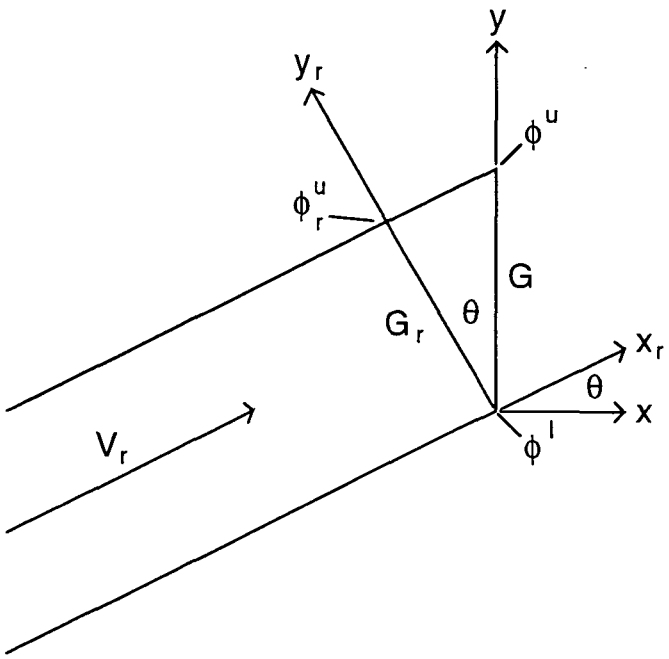

Figure 2.5: Coordinate systems for downstream far-field analysis.

Because there is no pressure associated with the wake vorticity, the discontinuous part of the potential satisfies Laplace's equation, i.e.,

$$\nabla^2 \phi_d = 0 \tag{2.98}$$

where ϕ_d is the discontinuous part of the unsteady potential.

It will be clearer to derive ϕ_d in the coordinate system aligned with the flow. The vorticity convects with the free stream, so the potential may be assumed to be of the form

$$\phi_d(x_r, y_r) = \phi_{r,d}(y_r) \exp(j\alpha_r x_r) \tag{2.99}$$

where $\alpha_r = -\omega/V_r$. Substituting this expression into Laplace's equation gives

$$\frac{d^2\phi_{r,d}(y_r)}{dy_r^2} - \alpha_r^2 \phi_{r,d}(y_r) = 0 \tag{2.100}$$

The solution to this ordinary differential equation has the form

$$\phi_{r,d}(y_r) = \mathcal{D} \exp(\alpha_r y_r) + \mathcal{E} \exp(-\alpha_r y_r) \tag{2.101}$$

There are two boundary conditions required to obtain the coefficients $\mathcal{D}$ and $\mathcal{E}$. The first is that there is a jump in potential across the wake, $[\![\phi_r]\!]$, which is defined as

$$[\![\phi_r]\!] = \phi_{r,d}(G_r) \exp(-j\beta_r G_r) - \phi_{r,d}(0) \tag{2.102}$$

where β_r may be determined from the interblade phase angle, σ, and the coordinate transformation

$$\beta_r = \frac{\sigma + \omega G \sin\theta / V_r}{G \cos\theta} \tag{2.103}$$

The second boundary condition is that the wake motion is periodic

$$\phi_{r,d}(0) = \phi_{r,d}(G_r)\exp(-j\beta_r G_r) \tag{2.104}$$

After using these two boundary conditions, some algebra results in the expression for $\phi_{r,d}$

$$\phi_{r,d}(y_r) = -\frac{1}{2}[\![\phi_r]\!]\left[\frac{\exp(\alpha_r y_r)}{1-\exp(\alpha_r G_r - j\beta_r G_r)} + \frac{\exp(-\alpha_r y_r)}{1-\exp(-\alpha_r G_r - j\beta_r G_r)}\right] \tag{2.105}$$

The next task is to determine $[\![\phi_r]\!]$. Using the notation of Figure 2.5, it is clear that

$$[\![\phi_r]\!] = \phi_r^u \exp(-j\beta_r G_r) - \phi^\ell \tag{2.106}$$

Since the behavior of ϕ_d is known in the x_r direction,

$$\phi_r^u = \phi^u \exp(j\alpha_r G \sin\theta) \tag{2.107}$$

Substituting this expression into Eq. (2.106) and simplifying results in

$$[\![\phi_r]\!] = \phi^u \exp(-j\sigma) - \phi^\ell \tag{2.108}$$

So the complete expression for the discontinuous unsteady potential is

$$\phi_d(x_r, y_r) = -\frac{1}{2}[\![\phi_r]\!]\exp(j\alpha_r x_r)$$

$$\times\left[\frac{\exp(\alpha_r y_r)}{1-\exp(\alpha_r G_r - j\beta_r G_r)} + \frac{\exp(-\alpha_r y_r)}{1-\exp(-\alpha_r G_r - j\beta_r G_r)}\right] \tag{2.109}$$

Finally, for this expression to be used in the present method, it must be converted to the original coordinate system, so that

$$\phi_d(x,y) = -\frac{1}{2}[\![\phi_r]\!]\exp[j\alpha_r(x\cos\theta + y\sin\theta)]$$

$$\times\left[\frac{\exp[\alpha_r(-x\sin\theta + y\cos\theta)]}{1-\exp(\alpha_r G_r - j\beta_r G_r)} + \frac{\exp[-\alpha_r(-x\sin\theta + y\cos\theta)]}{1-\exp(-\alpha_r G_r - j\beta_r G_r)}\right] \tag{2.110}$$

This expression is added to the continuous downstream unsteady potential to determine the complete solution at the downstream far field.

Chapter 3

Numerical Solution Method

In this chapter, the methods for numerical solution of the governing equations and boundary conditions described in Chapter 2 for the steady and small disturbance unsteady flow through a two-dimensional cascade of airfoils are presented. Section 3.1 contains a description of the steady solution procedure. The first step in the steady solution process is the choice of a computational grid upon which to discretize the governing equations and boundary conditions. After the equations governing the generation of the computational grid have been discussed, the finite element discretization of the steady flow variational principle and the associated boundary conditions will be presented. To complete the steady flow analysis, the matrix assembly and solution of the discretized equations and boundary conditions will be described. In Section 3.2, the unsteady solution procedure will be developed, beginning with the numerical calculation of the drift function and rotational velocity, as well as the generation of the grid deformation. Next, the unsteady finite element discretization of the field equations and boundary conditions is presented, with particular emphasis on the numerical discretization of the far-field boundary conditions. Finally, the assembly and solution procedure for the discretized unsteady flow equations is described.

3.1 Steady Flow Solution Procedure

3.1.1 Grid Generation

In any computational fluid dynamic analysis, the choice of a computational grid upon which to discretize the governing equations is crucial. Poor computational grids may reduce the accuracy of the discretization scheme or, in some cases, reduce the stability of the solution procedure. For cascade flows, the computational grids typically used are referred to as C, O, and H grids (or some combination thereof). The grid topology for each of these grids looks much like the letter used to identify them. In this investigation, H grids will be used. H grids, unlike their C and O counterparts, provide good resolution throughout the computational domain, not just near the airfoil. This is important because the accurate resolution of acoustic and vortical waves is critical to evaluating the aeroacoustic performance of a blade row. Another important reason for using an H grid is that the matrix containing

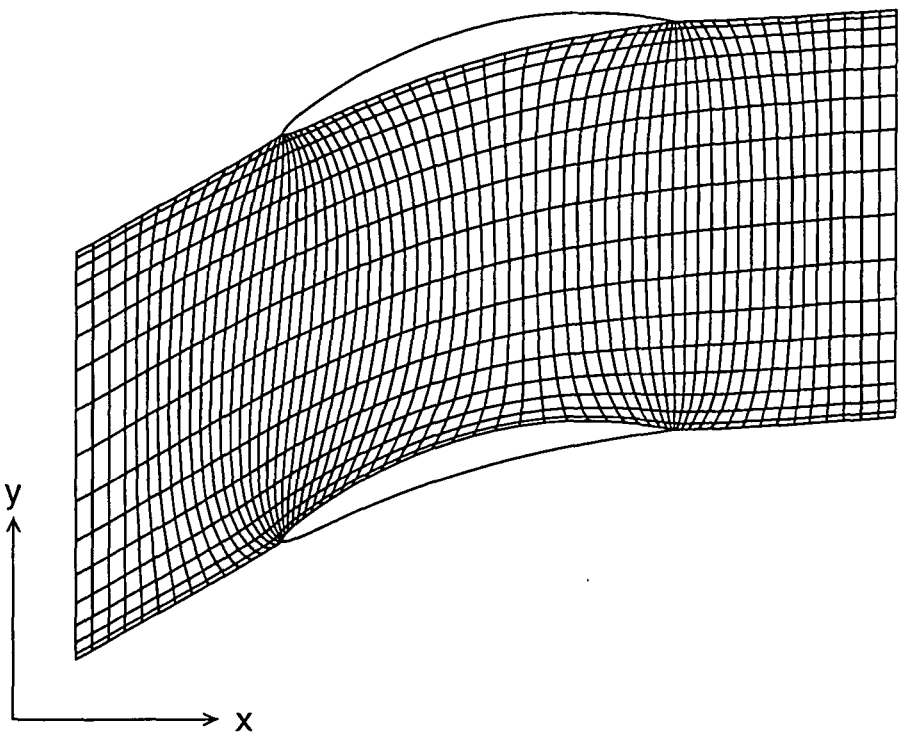

Figure 3.1: Typical computational grid for a fan exit guide vane.

the discretized flow equations will be block-tridiagonal. In addition to reducing the memory requirements for the method, block-tridiagonal matrix solvers are, in general, considerably faster than a general (i.e., fully populated) matrix solution. A typical H grid is shown in Figure 3.1.

There is an additional requirement of the computational grid. Recall from Chapter 2 that for aeroacoustic calculations, knowledge of the drift and stream functions is required. To facilitate the computation of these functions, one possible approach would be to solve for the steady flow on some initial computational grid, and afterwards calculate the streamlines based on the computed steady flow. Hall and Verdon [28] used this approach, finding the stagnation point and then calculating the stream function using a Runge-Kutta algorithm. Unfortunately, this procedure increases the overall truncation error of the solution procedure and does not lend itself well to a sensitivity analysis. A method that is better suited to a sensitivity analysis is to compute the grid nodes as part of the steady solution procedure. The final steady solution will then be on a computational grid that follows the streamlines. The latter procedure will be implemented here.

Thompson [52] has developed an elliptic grid generation technique that is well-suited for cascades. The (x, y) position of the grid nodes are defined by the partial differential equations

$$\nabla^2 \Xi = \mathcal{P} \tag{3.1}$$

$$\nabla^2 H = \mathcal{Q} \tag{3.2}$$

where $\mathcal{P}$ and $\mathcal{Q}$ are functions which are used to control the grid spacing. Lines of constant Ξ and H define the grid lines.

Equations (3.1) and (3.2) may be inverted to obtain partial differential equations for the unknown grid node locations in terms of the known computational coordinates Ξ and H, i.e.,

$$\overline{\alpha}\frac{\partial^2 x}{\partial \Xi^2} - 2\overline{\beta}\frac{\partial^2 x}{\partial \Xi \partial H} + \overline{\gamma}\frac{\partial^2 x}{\partial H^2} + \overline{\delta}^2 \mathcal{Q}\frac{\partial x}{\partial H} = 0 \tag{3.3}$$

and

$$\overline{\alpha}\frac{\partial^2 y}{\partial \Xi^2} - 2\overline{\beta}\frac{\partial^2 y}{\partial \Xi \partial H} + \overline{\gamma}\frac{\partial^2 y}{\partial H^2} + \overline{\delta}^2 \mathcal{Q}\frac{\partial y}{\partial H} = 0 \tag{3.4}$$

where

$$\overline{\alpha} = \left(\frac{\partial x}{\partial H}\right)^2 + \left(\frac{\partial y}{\partial H}\right)^2 \qquad \overline{\beta} = \frac{\partial x}{\partial \Xi}\frac{\partial x}{\partial H} + \frac{\partial y}{\partial \Xi}\frac{\partial y}{\partial H}$$

$$\overline{\gamma} = \left(\frac{\partial x}{\partial \Xi}\right)^2 + \left(\frac{\partial y}{\partial \Xi}\right)^2 \qquad \overline{\delta} = \frac{\partial x}{\partial \Xi}\frac{\partial y}{\partial H} - \frac{\partial x}{\partial H}\frac{\partial y}{\partial \Xi}$$

The next task is to choose the grid spacing functions $\mathcal{P}$ and $\mathcal{Q}$ so that the grid follows the flow streamlines. These functions may be obtained through the fluid dynamic definitions of the velocity potential and stream function. Consider an inviscid, irrotational, compressible flow. In terms of the stream function, Ψ, and the density, R, the steady conservation of mass may be written as

$$-\frac{\partial}{\partial x}\left(\frac{1}{R}\frac{\partial \Psi}{\partial x}\right) - \frac{\partial}{\partial y}\left(\frac{1}{R}\frac{\partial \Psi}{\partial y}\right) = 0 \tag{3.5}$$

which, after rearranging, may be written in the form

$$\nabla^2 \Psi = \frac{1}{R}\frac{\partial \Psi}{\partial x}\frac{\partial R}{\partial x} + \frac{1}{R}\frac{\partial \Psi}{\partial y}\frac{\partial R}{\partial y} \tag{3.6}$$

Finally, writing the right hand side of Eq. (3.6) in terms of the steady velocity potential, Φ, gives

$$\nabla^2 \Psi = |\nabla \Phi \times \nabla R| \tag{3.7}$$

Note the similarity between Eq. (3.7) and Eq. (3.2). If we choose $\mathcal{P} = 0$ and $\mathcal{Q} = |\nabla \Phi \times \nabla R|$, then lines of constant H will correspond to streamlines, provided the boundary conditions around the computational domain are consistent with the definition of the stream function. Furthermore, note that if the flow is incompressible, $|\nabla \Phi \times \nabla R| = 0$, and no grid spacing functions are necessary in the grid generation equations (i.e., $\mathcal{P} = \mathcal{Q} = 0$). Regardless of the compressibility of the flow, it should be noted that lines of constant Ξ do not correspond to contours of the drift function, Δ, nor is this a requirement of the computational grid. The drift function may be calculated after the steady flow solution has been obtained.

Figure 3.2 shows a typical computational grid in the (Ξ, Ψ) coordinate system. If the grid generation equations, Eqs. (3.3)–(3.4), were solved without the influence

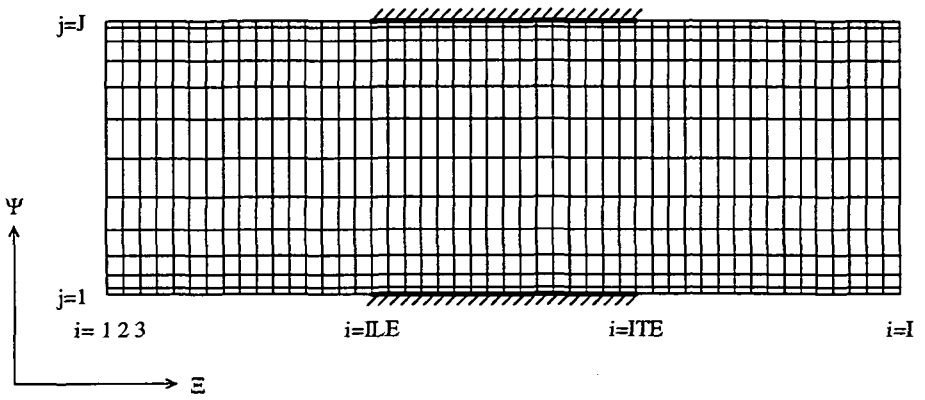

Figure 3.2: Typical computational grid in (Ξ, Ψ) coordinates. The computational node numbering convention is also illustrated.

of the grid spacing functions (i.e., $\mathcal{P} = \mathcal{Q} = 0$), an example of the resulting computational mesh is shown in Figure 3.1. Note that the area of the computational cells shown in Fig. 3.1 varies smoothly throughout the computational domain. The lack of large area changes from cell to cell is characteristic of elliptic grid generation algorithms, and is desirable because smoothly varying grids do not increase the overall truncation error of the numerical solution procedure.

The overall computational grid has I nodes in the axial direction and J nodes in the circumferential direction. The node numbering convention is illustrated in Figure 3.2. Any node on the computational grid may be referred to by its node number (i, j). The upstream far-field boundary is the first axial grid line, so $i = 1$ on this boundary. Similarly, $i = I$ on the downstream far-field boundary. The j-nodes are numbered from the lower boundary of the computational domain ($j = 1$) to the upper boundary of the domain ($j = J$).

In addition to the grid generation equations described above, boundary conditions must be imposed around the blade passage. Specifically, the distribution of grid nodes along the boundaries are specified. These locations are specified as a fraction of arc length on each boundary. There is no restriction on the grid distribution, although to minimize truncation error, it is best to increase the grid resolution near large steady flow gradients. A typical boundary distribution is shown in Figure 3.3. The arc length fraction for each boundary node i along the periodic, airfoil surface, and wake boundaries is denoted by F_i. The value is the same for both the upper and lower surfaces. The arc length fraction for each node j along the far-field boundaries is denoted by F_j. The values of F_i and F_j at the endpoints of each boundary type are also shown in Figure 3.3. The values of F_i and F_j at the intermediate nodes represents the fraction of the arc length between the endpoints at which the node is located.

The grid generation equations and associated boundary conditions are discretized

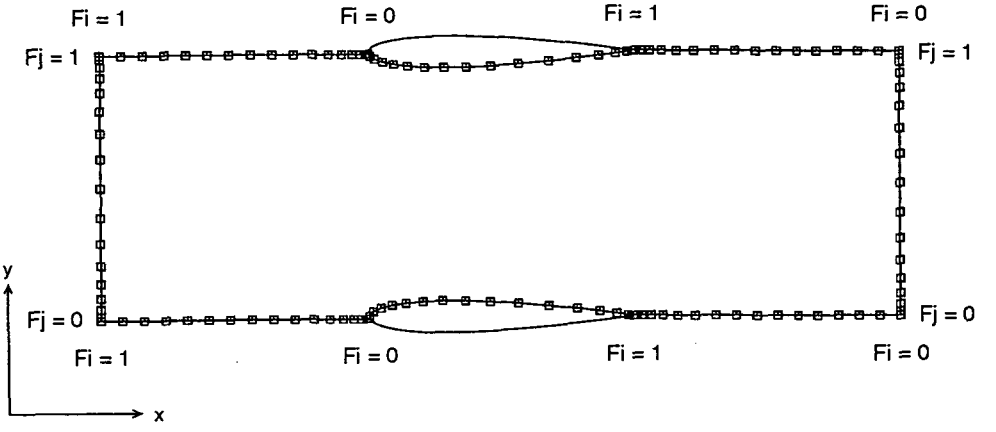

Figure 3.3: Typical distribution of boundary grid points.

using centered finite difference operators for nonuniform spacing in Ξ and Ψ. The resulting set of nonlinear equations is of the form

$$\mathbf{M}(\mathbf{\Phi}, \mathbf{x}; \mathbf{Z}) = \mathbf{0} \tag{3.8}$$

where $\mathbf{M}$ is a vector of nonlinear functions, $\mathbf{\Phi}$ is the vector containing the discrete approximation of the nominal steady potential Φ at all the computational nodes, $\mathbf{x}$ is the vector of the location of the computational nodes, and $\mathbf{Z}$ is a vector containing a set of parameters that define the airfoil shape and cascade geometry. The semicolon indicates that $\mathbf{\Phi}$ and $\mathbf{x}$ are the dependent variables to be computed during the solution procedure. The parameters contained in the $\mathbf{Z}$ vector are independent variables during the solution procedure, although they may change in the overall design process. The details of the parameters in the $\mathbf{Z}$ vector will be discussed in the next section.

3.1.2 Airfoil Definition and Spline Notation

Now that we have defined the computational grid, we consider how to represent the airfoil shape and cascade geometry using the vector $\mathbf{Z}$. Generally, airfoil shapes are defined using two distinct approaches. One approach is to define the airfoil analytically using some set of design variables such as thickness and camber. In this case, the vector $\mathbf{Z}$ may be considered to contain the magnitudes of each of these defining variables, in addition to the cascade parameters. A second, more general approach is to define the airfoil shape using a set of points on the airfoil surface. In this case, the vector $\mathbf{Z}$ will contain the x- and y-coordinates of the defining points as well as the cascade parameters. It should be noted that this second approach is more general because any analytical airfoil definition may be discretized to obtain a set of defining points. Furthermore, it may be argued that each defining point is actually a design variable of the airfoil shape. Hence, for the most part, the discussion of the airfoil shape in this report will assume that the blade has been defined by a set of points on the surface.

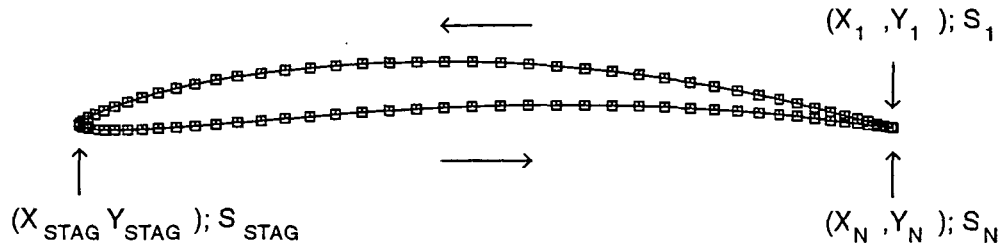

Figure 3.4: Detail of airfoil spline definition. Arrows indicate direction of airfoil spline.

The cascade parameters are design variables that are independent of the airfoil shape. For example, the blade-to-blade gap, G, and the stagger angle, Θ, are both parameters that would be included in the vector $\mathbf{Z}$. In general, any parameter that defines the cascade and is considered to be a design variable (i.e., the parameter is allowed to change during the design process) is included in $\mathbf{Z}$. This may include parameters that define the computational grid, such as the fractional arc length arrays F_i and F_j defined in the previous section, and parameters that define the steady flow conditions, such as the inflow Mach number.

At this point, it is useful to explain the relationship between the vector containing the airfoil shape and cascade parameters, $\mathbf{Z}$, and the vector containing the nodes of the computational grid, $\mathbf{x}$. Consider a blade definition consisting of a number of defining points as shown in Figure 3.4. Each point defining the shape of the blade has a coordinate that will be denoted (X, Y). In the present analysis, it is assumed that the points begin at the trailing edge on the upper surface of the airfoil and end at the trailing edge on the lower airfoil surface. Note that in general these points are not points defined by the computational grid. The coordinates of the grid nodes (i.e., the vector $\mathbf{x}$) will be denoted using lower case letters, i.e., (x, y), to distinguish the nodes of the computational grid from the points defining the airfoil shape.

Figure 3.4 shows a schematic of an airfoil defined by some finite number of points, N. The points begin at (X_1, Y_1) and end at (X_N, Y_N). In addition, the initial estimate of the stagnation point is denoted by (X_{STAG}, Y_{STAG}). The arc length, S, of each of these points measured from the trailing edge of the upper airfoil surface is then calculated at each point based on its X and Y location. Once the arc length has been calculated, the X and Y locations are given a "functional" definition using a cubic spline. In this way, the X and Y location of the surface of the airfoil is defined to be a function of S.

Although the airfoil shown in Fig. 3.4 has a sharp trailing edge, it should be noted that this analysis is not restricted to airfoils with sharp trailing edges. Actual airfoils usually have rounded (or blunt) trailing edges. Unfortunately, the wake boundary condition is difficult to apply near rounded trailing edges. In such cases, it is useful to "cut off" the airfoil near the trailing edge so that there is a space between the first

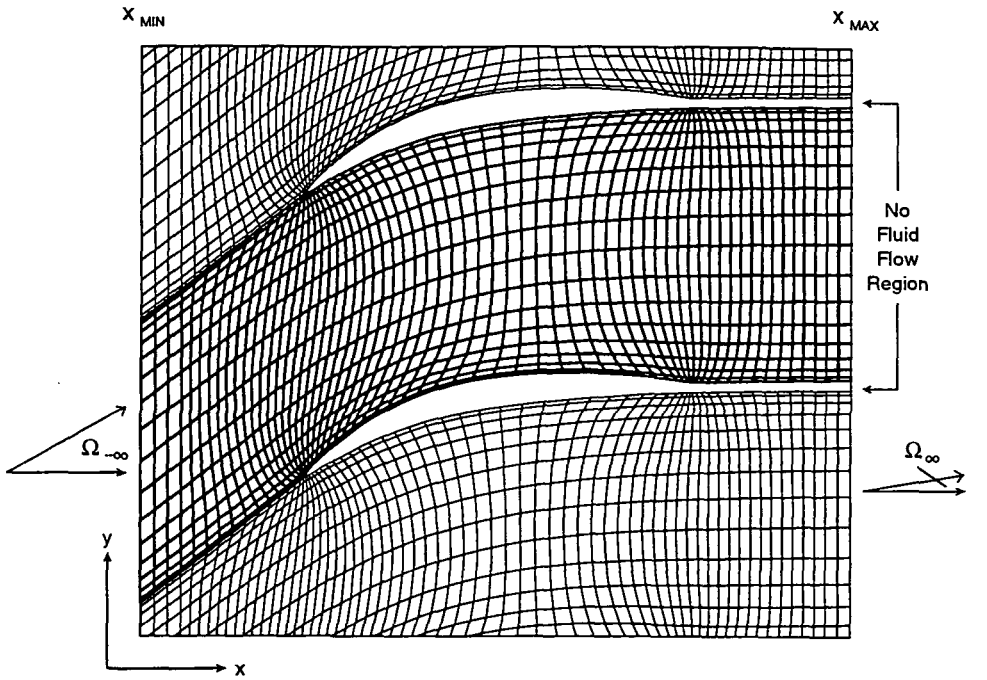

Figure 3.5: Typical computational grid illustrating modifications for airfoils with blunt trailing edges. Multiple passages shown for clarity. The highlighted lines define the actual computational grid.

and last point of the airfoil definition. The resulting computational grid around such an airfoil is shown in Figure 3.5. Note that there is constant spacing between adjacent blade passages from the trailing edge to the downstream far field of the computational grid. This space is intended to model the flow deficit due to a viscous wake. Placing the grid boundaries on either side of this space is analogous to representing the displacement thickness of a viscous boundary layer by a solid surface in an inviscid analysis. Although no displacement thickness modification has been applied to the airfoil surface, the space in the wake represents an estimate of the actual viscous wake region. Inside the space between the grids there is no fluid flow. The wake boundary conditions are then applied in the usual fashion, on either side of the space. Previous researchers [35, 24] have shown that modeling a blunt trailing edge through a space in the computational grid results in a solution that satisfies the Kutta condition, and hence no spurious stagnation points arise along the wake boundary.

Finally, there are four other parameters that define the computational grid. The first two are the x-location of the upstream far field, x_{MIN}, and the inflow angle $\Omega_{-\infty}$. The other two are the x-location of the downstream far field, x_{MAX}, and the flow exit angle, Ω_{∞}. Although the inflow and exit flow angles may change during the course of the steady solution procedure, x_{MIN} and x_{MAX} remain fixed. These four parameters are shown in Fig. 3.5, and they complete the specification of the computational grid.

3.1.3 Finite Element Discretization

The next step in the analysis is to calculate the steady flow. As was shown in Chapter 2, the governing equation is the steady version of the full potential equation, Eq. (2.11). Following the notation in the previous section, the discretized set of steady flow equations has the form

$$\mathbf{N}(\mathbf{\Phi}, \mathbf{x}; \mathbf{Z}) = \mathbf{0} \tag{3.9}$$

where $\mathbf{N}$ is a vector of nonlinear functions. Note that Eqs. (3.8) and (3.9) are both nonlinear in $\mathbf{\Phi}$ and $\mathbf{x}$. Since the objective given earlier is to solve the equations simultaneously, Newton iteration will be used to solve the grid and flow equations. Consequently, it will be useful to discretize the steady flow equations in a manner consistent with Newton iteration.

From the functional given in Eq. (2.62), it is clear that a perturbation expression for the steady pressure is required. To do this, consider the steady Bernoulli equation, Eq. (2.10). If the current estimate of the steady pressure is P and the current current estimate of the steady potential is Φ, then to compute the new value of the steady pressure, we expand Eq. (2.10) in a Taylor series about the current value of P, retaining terms to second order. In terms of the perturbation potential, Φ', the new estimate of the steady pressure may be written as

$$P_{\text{NEW}} = P - R\nabla\Phi \cdot \nabla\Phi' - \frac{R}{2}\nabla\Phi' \cdot \nabla\Phi' + \frac{R}{2C^2}(\nabla\Phi \cdot \nabla\Phi')^2 + \mathcal{O}(\Phi'^3) \tag{3.10}$$

where P_{NEW} is the new estimate of the steady pressure. In Chapter 2, it was noted that Taylor expansions within variational principles must be carried out to second order if a first-order result is desired. This is because taking the variation will reduce these second-order terms to first order. Since first-order terms are required in a perturbation expression for the pressure, the Taylor expansion in Eq. (3.10) is carried out to include terms of second order.

Now, rewriting the steady flow functional given in Eq. (2.62) to second order results in

$$\Pi_{\text{steady}} = \iint_{\Sigma} \left[P - R\nabla\Phi \cdot \nabla\Phi' - \frac{R}{2}\nabla\Phi' \cdot \nabla\Phi' + \frac{R}{2C^2}(\nabla\Phi \cdot \nabla\Phi')^2 \right] d\xi \, d\eta \tag{3.11}$$

where the boundary integral has been omitted for the time being. Taking the first variation and setting to zero gives

$$\delta\Pi_{\text{steady}} = \iint_{\Sigma} R\left[-\nabla\Phi \cdot \nabla\delta\Phi' - \nabla\Phi' \cdot \nabla\delta\Phi' + \frac{1}{C^2}\nabla\Phi \cdot \nabla\Phi'\nabla\Phi \cdot \nabla\delta\Phi' \right] d\xi \, d\eta = 0 \tag{3.12}$$

For Π_{steady} to be stationary, $\delta\Pi_{\text{steady}}$ must be zero for all admissible variations in Φ'. Since the area of the domain Σ is arbitrary, the expression inside the integral in Eq. (3.12) must be zero (i.e., it is the Euler-Lagrange equation of the variational principle). Hence, discretization of the functional given in Eq. (3.11) will result in a set of nonlinear equations of the form given in Eq. (3.9), which is the desired result.

The variational principle may be discretized using conventional finite element techniques. In the present work, a four node bilinear isoparametric element will be used. The values of the perturbation steady potential at the corners of a given element n may be interpolated into the interior of the element using an interpolation of the form

$$\Phi'(\xi,\eta) = \lfloor \mathbf{N} \rfloor_n \mathbf{\Phi'}_n \tag{3.13}$$

where

$$\lfloor \mathbf{N} \rfloor_n = \lfloor N_1, N_2, N_3, N_4 \rfloor_n \tag{3.14}$$

is a row vector of interpolation functions and $\mathbf{\Phi'}_n$ is the vector containing the corner values of the perturbation steady potential. Similarly, the gradient operator may be represented by the gradient of the interpolation functions, i.e.,

$$\nabla\Phi' = [\mathbf{N'}_n]\mathbf{\Phi'}_n \tag{3.15}$$

where

$$[\mathbf{N'}]_n = \left[\begin{array}{cccc} \frac{\partial N_1}{\partial \xi}, & \frac{\partial N_2}{\partial \xi}, & \frac{\partial N_3}{\partial \xi}, & \frac{\partial N_4}{\partial \xi} \\ \\ \frac{\partial N_1}{\partial \eta}, & \frac{\partial N_2}{\partial \eta}, & \frac{\partial N_3}{\partial \eta}, & \frac{\partial N_4}{\partial \eta} \end{array} \right]_n \tag{3.16}$$

Substituting these expressions into the functional given in Eq. (3.11) results in

$$\Pi_{\text{steady}} = \iint_{\Sigma_n} \left[P - R\mathbf{\Phi'}_n^T [\mathbf{N'}]_n^T \nabla\Phi - \frac{R}{2}\mathbf{\Phi'}_n^T [\mathbf{N'}]_n^T [\mathbf{N'}]_n \mathbf{\Phi'}_n \right.$$
$$\left. + \frac{R}{2C^2}\mathbf{\Phi'}_n^T [\mathbf{N'}]_n^T \nabla\Phi\nabla\Phi^T [\mathbf{N'}]_n \mathbf{\Phi'}_n \right] d\xi\, d\eta \tag{3.17}$$

Setting the first variation to zero results in the Newton iteration equation for the perturbation of the flow

$$\delta\Pi_{\text{steady}} = \iint_{\Sigma_n} \left[-[\mathbf{N'}]_n^T \nabla\Phi - [\mathbf{N'}]_n^T [\mathbf{N'}]_n \mathbf{\Phi'}_n \right.$$
$$\left. + \frac{1}{C^2}[\mathbf{N'}]_n^T \nabla\Phi\nabla\Phi^T [\mathbf{N'}]_n \mathbf{\Phi'}_n \right] R\, dx\, dy = 0 \tag{3.18}$$

Rearranging, this may be written as

$$\delta\Pi_{\text{steady}} = \iint_{\Sigma_n} \left[[\mathbf{N'}]_n^T \left(-[\mathbf{I}] + \frac{1}{C^2}\nabla\Phi\nabla\Phi^T \right) [\mathbf{N'}]_n \mathbf{\Phi'}_n \right.$$
$$\left. - [\mathbf{N'}]_n^T \nabla\Phi \right] R\, d\xi\, d\eta = 0 \tag{3.19}$$

In finite element notation, then, the steady flow equations for each element may be written in the form

$$[\mathbf{K}]_n \mathbf{\Phi'}_n - \mathbf{E}_n = 0 \tag{3.20}$$

where the elemental stiffness matrix, $[\mathbf{K}]_n$, is

$$[\mathbf{K}]_n = \iint_{\Sigma_n} [\mathbf{N'}]_n^T \left(-[\mathbf{I}] + \frac{1}{C^2}\nabla\Phi\nabla\Phi^T \right) [\mathbf{N'}]_n R\, d\xi\, d\eta \tag{3.21}$$

and the elemental force vector, $\mathbf{E}_n$, is

$$\mathbf{E}_n = \int\int_{\Sigma_n} [\mathrm{N}']_n^T \nabla\Phi R \, d\xi \, d\eta \tag{3.22}$$

The elemental stiffness matrix and force vector are computed for each cell in the computational domain. These elemental values are assembled into a global stiffness matrix and force vector so that the steady flow governing equation, Eq. (3.9), may be solved using Newton iteration. Also included in the global stiffness matrix and force vector are contributions from boundary integral terms resulting from the steady flow variational principle. The boundary conditions will be discussed in the next section, followed by a description of the global matrix assembly and solution procedure.

3.1.4 Near-Field Boundary Conditions

Periodic Boundary Condition

In Chapter 2, it was stated that the steady periodic boundary condition is that the difference in the steady potential between two adjacent periodic boundaries is a constant. In addition, it is clear from the discussion of the grid generation procedure that the periodic surfaces on the upper and lower boundaries of the computational domain must be separated by the specified blade-to-blade gap, G. There is an additional requirement of the steady flow solution on the periodic boundaries, however.

Earlier in this chapter, we stated that we wish to have the computational grid follow the flow streamlines. Because the periodic boundaries are attached to the airfoil, the periodic boundaries must be stagnation streamlines of the steady flow. Consequently, we wish to formulate boundary conditions to enforce this requirement.

The stagnation streamline condition may be enforced through the application of a "Kutta condition" requirement on the periodic boundaries. This may be accomplished by implementing two separate boundary conditions. First, there is a condition that is purely a function of the grid locations. In general, the shape of the stagnation streamline from the inlet to the leading edge of the airfoil is not known *a priori*. Often the boundary has some curvature, because the stagnation streamline must be normal to the surface of the airfoil at the stagnation point, which is not necessarily the same direction as the specified flow direction in the upstream far field. Hence, the grid locations on the periodic boundaries are not fixed, but are adjusted during the solution procedure, so that the same relative spacing along the boundaries is maintained. Specifically, on the lower ($j = 1$) periodic boundary of the computational domain, the boundary condition for the grid is that at grid station i, the x- and y-coordinates are the appropriate fractional arc length between the upstream far-field boundary and the airfoil surface, so that

$$\begin{aligned} M^x_{i,1} &= (F_{i+1} - F_i)^2 \left[(x_i - x_{i-1})^2 + (y_i - y_{i-1})^2\right] \\ &- (F_i - F_{i-1})^2 \left[(x_{i+1} - x_i)^2 + (y_{i+1} - y_i)^2\right] = 0 \end{aligned} \tag{3.23}$$

where the superscript x refers to the x grid equation for the computational node (i, j) indicated by the subscripts, and F_i refers to the fractional arc length array described

in the previous section. This boundary condition is applied from node $i = 2$ to node $i = ILE - 1$ (see Figure 3.2). At the inlet ($i = 1$) boundary, the x-location is prescribed. The y-location is permitted to change to satisfy Eq. (3.23).

On the upper ($j = J$) periodic boundary of the computational domain, the x-coordinate of the grid node is the same as the lower boundary, and the y-coordinate is one blade-to-blade gap larger than the lower boundary, i.e.,

$$M^x_{i,J} = x_{i,J} - x_{i,1} = 0 \tag{3.24}$$

and

$$M^y_{i,J} = y_{i,J} - y_{i,1} - G = 0 \tag{3.25}$$

The other boundary condition for closure is purely a function of the steady potential. In Chapter 2 during the discussion of the steady wake boundary condition, it was noted that if the jump in steady potential across the wake is the same as the jump in potential at the trailing edge, the Kutta condition is automatically satisfied. This condition may be applied in an analogous fashion on the upstream boundary. If the jump in potential across the periodic boundary is the same as the jump at the stagnation point (i.e., zero), then the periodic boundary is a stagnation streamline of the flow. This condition may be expressed as

$$M^y_{i,1} = (\Phi_{i+1,J} - \Phi_{i+1,1}) - (\Phi_{i,J} - \Phi_{i,1}) = 0 \tag{3.26}$$

The result of these boundary conditions is that the upstream periodic grid boundaries are stagnation streamlines of the converged solution.

Airfoil Surface

As was noted in Chapter 2, on the airfoil surface, the steady flow satisfies the natural Neumann boundary condition, i.e., no through flow. Since it is the natural boundary condition of the variational principle, no additional expressions are required to enforce this condition. The grid equations, however, are another matter. For each computational node on the airfoil surface, there are boundary conditions that must be satisfied.

The first set of boundary conditions requires that the computational nodes lie on the airfoil surface. For the lower ($j = 1$) boundary of the computational domain, this condition may be expressed by the equations

$$M^x_{i,1} = x_{i,1} - X_S(s_{i,1}) = 0 \tag{3.27}$$

and

$$M^y_{i,1} = y_{i,1} - Y_S(s_{i,1}) = 0 \tag{3.28}$$

where X_S and Y_S are cubic spline evaluations of the airfoil surface coordinate corresponding to the arc length $s_{i,1}$ for the computational node at the ith station on the $j = 1$ surface. Note that $s_{i,1}$ is a new variable that is stored only for the airfoil surface points (i.e., from $i = ILE$ to $i = ITE$). This new variable will require an additional boundary condition to close the system, which will be described shortly.

It should be clear now why the airfoil definition points (X, Y) are referred to separately from the grid nodes (x, y). At each iteration of the Newton solver, the nodes of the computational grid are permitted to "slide" along the surface specified by the airfoil defining points. The coordinates of the points containing the airfoil definition are fixed during the steady solution procedure. Hence, these points must be considered separately from the grid node locations.

On the upper $(j = J)$ surface of the computational domain, the grid nodes must also lie on the airfoil surface, so that

$$M^x_{i,J} = x_{i,J} - X_S(s_{i,J}) = 0 \tag{3.29}$$

and

$$M^y_{i,J} = y_{i,J} - Y_S(s_{i,J}) - G = 0 \tag{3.30}$$

where the latter equation also ensures that the blade-to-blade gap is constant along the blade, and $s_{i,J}$ refers to the arc length of the computational node i on the $j = J$ surface.

The other boundary condition for closure is that the arc length that the nodes on the airfoil surface "slide" is a specified value of the fractional arc length between the stagnation point and the spline endpoint. This condition is applied at all airfoil surface nodes except the stagnation point. Recall that earlier in this chapter, the arc length fraction F_i was defined. Using this definition, the arc length at station i and $(i-1)$ on the lower $(j = 1)$ airfoil surface of the computational domain may be expressed as a function of the arc length at the stagnation point and the arc length at the trailing edge, so that

$$M = -s_{i,1} + S_{SP} - F_i\,(S_{SP} - S_1) = 0 \tag{3.31}$$

$$M = -s_{i-1,1} + S_{SP} - F_{i-1}\,(S_{SP} - S_1) = 0 \tag{3.32}$$

where S_{SP} is the arc length at the stagnation point. Solving both of these equations for S_{SP} and setting them equal to each other results in an expression for $s_{i,1}$ that is only dependent on the specified fraction array F, the arc length at an adjacent node, $s_{i-1,1}$, and the arc length at the trailing edge, S_1 (see Fig. 3.4). Hence, the boundary condition that enforces the fractional arc length distribution on the $(j = 1)$ airfoil surface may be written as

$$M^x_{i,J+1} = s_{i,1} - \frac{1 - F_i}{1 - F_{i-1}}\, s_{i-1,j} - \frac{F_i - F_{i-1}}{1 - F_{i-1}}\, S_1 = 0 \tag{3.33}$$

Note that the $J+1$ designation on M indicates that this equation is solved in addition to the grid and flow equations for the J nodes at each i station. Hence, Eq. (3.33) is stored in the x grid equation for the "fictional node" $J+1$. This boundary condition is applied from node $i = ILE + 1$ to $i = ITE$ on the $j = 1$ surface.

In a similar fashion, the boundary condition on the $j = J$ airfoil surface may be written as

$$M^y_{i,J+1} = s_{i,J} - \frac{1 - F_i}{1 - F_{i-1}}\, s_{i-1,J} - \frac{F_i - F_{i-1}}{1 - F_{i-1}}\, S_N = 0 \tag{3.34}$$

This equation is stored in the y grid equation for the "fictional node" $J+1$. Like the $j=1$ surface, this boundary condition is applied from node $i = ILE+1$ to $i = ITE$ on the $j = J$ surface.

These last two boundary conditions essentially state that any change in position of the stagnation point will result in a proportional change in the position of the grid nodes on the airfoil surface.

Stagnation Point

Next, we consider the boundary condition at the stagnation point. This boundary condition is extremely important because the description of the unsteady vorticity given in Chapter 2 is only valid if the stagnation point is identified accurately. The boundary condition is that the steady potential, Φ, has a minimum value on the surface of the blade at the stagnation point. In other words, the derivative of the steady potential in the tangential direction (i.e., with respect to the arc length) is zero. Discretizing this derivative using a second-order finite difference operator allowing variable grid spacing results in

$$M^x_{ILE,J+1} = \frac{1}{s_{ILE+1,1} - s_{ILE+1,J}} \left[\frac{s_{ILE} - s_{ILE+1,J}}{s_{ILE+1,1} - s_{ILE}} \left(\Phi_{ILE+1,J} - V_{-\infty} G - \Phi_{ILE,1} \right) \right.$$

$$\left. + \frac{s_{ILE+1,1} - s_{ILE}}{s_{ILE} - s_{ILE+1,J}} \left(\Phi_{ILE,1} - \Phi_{ILE+1,1} \right) \right] = 0 \tag{3.35}$$

where ILE refers to the grid station i corresponding to the leading edge of the airfoil (see Fig. 3.2). The $i = ILE$ grid station is also the stagnation point. Note that the potential on the upper ($j = J$) surface of the computational domain must be evaluated on the reference airfoil, so the jump in potential between adjacent blades, $V_{-\infty}G$, must be subtracted from the value of the upper surface potential, $\Phi_{ILE+1,J}$. Furthermore, note that s only has a single subscript at the leading edge. This is because the arc length at the leading edge is the same for both airfoil surfaces. Hence, only one additional variable must be stored, which results in there being only one additional boundary condition at the leading edge stagnation point.

Downstream Wake Boundary

The last near-field boundary conditions are applied at the downstream wake boundary. Like the upstream periodic condition, the grid line attached to the trailing edge must be a stagnation streamline. Hence, the boundary conditions on the wake surfaces are nearly identical to those on the periodic surfaces. First, the boundary condition on the grid for the lower ($j = 1$) surface of the computational domain is

$$M^x_{i,1} = (F_{i+1} - F_i)^2 \left[(x_i - x_{i-1})^2 + (y_i - y_{i-1})^2 \right]$$

$$- (F_i - F_{i-1})^2 \left[(x_{i+1} - x_i)^2 + (y_{i+1} - y_i)^2 \right] = 0 \tag{3.36}$$

Also like the periodic boundary, the grid boundary conditions on the upper ($j = J$) surface are

$$M^x_{i,J} = x_{i,J} - x_{i,1} = 0 \tag{3.37}$$

and

$$M^y_{i,J} = y_{i,J} - y_{i,1} - [G - (Y_1 - Y_N)] = 0 \tag{3.38}$$

where the last two terms in Eq. (3.38) account for any space in the downstream wake due to a blunt trailing edge, as described earlier in this chapter.

Finally, similar to the upstream periodic boundary, the boundary condition that enforces the Kutta condition may be written as

$$M^y_{i,1} = (\Phi_{i,J} - \Phi_{i,1}) - (\Phi_{i-1,J} - \Phi_{i-1,1}) = 0 \tag{3.39}$$

there are two differences between the wake boundary condition expressed in Eq. (3.39) and the periodic boundary condition given in Eq. (3.26). First, the jump in the potential is measured at the i and $(i-1)$ points instead of the i and $(i+1)$ points. This is because the wake boundary conditions are applied from node $i = ITE + 1$ to $i = I$. Hence, so that a single condition may be used at all of these nodes, the difference is computed in the "upwind" (i.e., negative i) direction. Upstream, because the boundary condition is applied at the $i = 1$ node, the difference is computed in the "downwind" (i.e., positive i) direction. The second difference between the wake condition and the periodic condition is that there is a finite jump in potential across the wake if there is circulation around the airfoil.

All of the near-field boundary conditions necessary for the calculation of the steady flow have now been presented. The final step in the steady flow solution procedure is to examine the steady far-field boundary conditions.

3.1.5 Far-Field Boundary Conditions

Upstream Far-Field Boundary

There are three boundary conditions the grid and steady flow must satisfy on the upstream far-field boundary. The first is that the y-component of velocity must be equal to a specified value. This condition effectively specifies the steady potential at the upstream boundary, as shown in Eq. (2.91). Computationally, this may be accomplished using the finite element procedure known as the penalty method [53]. Using the penalty method, the boundary condition may be written as

$$N_{1,j} = [\mathbf{K}]_{1,j}\mathbf{\Phi}_1 - \mathbf{E}_{1,j} - k_p\,(\Phi_{1,j} - V_{-\infty}y_{1,j}) = 0 \tag{3.40}$$

where the matrix $[\mathbf{K}]$ and vector $\mathbf{E}$ are the stiffness matrix and force vector described earlier, and k_p is called a penalty number. As k_p approaches infinity, the condition $\Phi_{1,j} = V_{-\infty}y_{1,j}$ is exactly enforced. For computational purposes, it is sufficient to choose k_p to have a large finite value.

The other two conditions apply to the location of the grid nodes on the upstream far-field boundary. The boundary is a line of constant x-coordinate, while the y-coordinate is specified as a fraction of arc length through the F array described

earlier. The x-coordinate is computed through the equation

$$M^x_{1,j} = x_{1,j} - x_{1,1} = 0 \tag{3.41}$$

Note that the value of $x_{1,1}$ is computed as part of the periodic boundary conditions described in the previous section. The y-coordinate is computed in a similar fashion, i.e.,

$$M^y_{1,j} = y_{1,j} - y_{1,1} - F_j G = 0 \tag{3.42}$$

where F_j is the value of the far-field arc length fraction array corresponding to node j (see Fig. 3.3), and G is the blade-to-blade gap.

Downstream Far-Field Boundary

The downstream flow boundary condition specifies the mass flux through the computational domain. Because the governing equation of the steady flow is the conservation of mass, specifying the mass flux at the exit fixes the mass flux at the inlet. The circumferential grid lines are modeled as streamtubes, so that the flow through each tube is proportional to its fraction of the gap at the far-field boundary. It should be noted that the downstream gap is not necessarily the same as the blade-to-blade gap, G, due to the space left in the wake for airfoils with finite thickness trailing edges. To prescribe the mass flux at the boundary, the desired mass flux is added to the "force vector" computed from the finite element procedure, i.e.,

$$N_{I,j} = [\mathbf{K}]_{I,j}\mathbf{\Phi}_I - \mathbf{E}_{I,j} - \frac{1}{2}R_{-\infty}U_{-\infty}\frac{G}{G-(Y_1-Y_N)}(y_{I,j+1} - y_{I,j}) = 0 \tag{3.43}$$

and

$$N_{I,j+1} = [\mathbf{K}]_{I,j+1}\mathbf{\Phi}_I - \mathbf{E}_{I,j+1} - \frac{1}{2}R_{-\infty}U_{-\infty}\frac{G}{G-(Y_1-Y_N)}(y_{I,j+1} - y_{I,j}) = 0 \tag{3.44}$$

The last term in Eqs. (3.43) and (3.44) represents the mass flux through the streamtube defined by two adjacent streamlines (i.e., lines of constant j). The grid equations at the downstream far-field boundary are analogous to those at the upstream boundary, i.e.,

$$M^x_{I,j} = x_{I,j} - x_{I,1} = 0 \tag{3.45}$$

and

$$M^y_{I,j} = y_{I,j} - y_{I,1} - F_j[G - (Y_1 - Y_N)] = 0 \tag{3.46}$$

where again the blade-to-blade gap, G, is modified by the space left in the wake due to finite thickness trailing edges.

3.1.6 Assembly and Solution

The final step in describing the steady flow solution method is to explain how the equations given in the previous sections are actually assembled and solved. Earlier in this chapter, it was noted that the governing equations and boundary conditions for

the grid and steady flow could be expressed as two sets of nonlinear functions, $\mathbf{M}$ and $\mathbf{N}$ [see Eqs. (3.8) and (3.9)]. It was also noted that the equations would be solved simultaneously using Newton iteration. Schematically, the steady solution procedure may be written in the form

$$\begin{pmatrix} \mathbf{\Phi} \\ \mathbf{x} \end{pmatrix}^{n+1} = \begin{pmatrix} \mathbf{\Phi} \\ \mathbf{x} \end{pmatrix}^{n} - \begin{bmatrix} \frac{\partial \mathbf{N}}{\partial \mathbf{\Phi}} & \frac{\partial \mathbf{N}}{\partial \mathbf{x}} \\ \frac{\partial \mathbf{M}}{\partial \mathbf{\Phi}} & \frac{\partial \mathbf{M}}{\partial \mathbf{x}} \end{bmatrix}_n^{-1} \begin{pmatrix} \mathbf{N} \\ \mathbf{M} \end{pmatrix}^n \tag{3.47}$$

where n denotes the current estimate of the solution and $n+1$ denotes the new estimate. Literally structuring the equations in this way would result in a sparse matrix of extremely high bandwidth. Large bandwidth sparse matrices are not conducive to efficient solution. Fortunately, the bandwidth of the matrix may be substantially reduced by reordering the equations.

At each computational node, there are three equations to be solved, for variables Φ, x, and y. Examination of the equations derived in this chapter shows that the discretized form of the governing equations and boundary conditions at a grid station i are at most dependent on variables at the $(i-1)$, i, and $(i+1)$ stations. The boundary conditions may depend on variables at any j station, however. Hence, the equations may be reordered so that the global matrix is block-tridiagonal, where each block equation represents a single grid station i.

For a computational grid with I nodes in the axial direction and J nodes in the circumferential direction, the matrix to be solved at every iteration has the form

$$\begin{bmatrix} \mathbf{B}_1 & \mathbf{C}_1 & & & & & \\ \mathbf{A}_2 & \mathbf{B}_2 & \mathbf{C}_2 & & & & \\ & \ddots & \ddots & \ddots & & & \\ & & \mathbf{A}_i & \mathbf{B}_i & \mathbf{C}_i & & \\ & & & \ddots & \ddots & \ddots & \\ & & & & \mathbf{A}_{I-1} & \mathbf{B}_{I-1} & \mathbf{C}_{I-1} \\ & & & & & \mathbf{A}_I & \mathbf{B}_I \end{bmatrix} \tag{3.48}$$

where each block row corresponds to an axial grid line. For each i block equation, $\mathbf{A}_i$ contains terms that multiply variables at the $(i-1)$-station, $\mathbf{B}_i$ contains terms that multiply variables at the i-station, and $\mathbf{C}_i$ contains terms that multiply variables at the $(i+1)$-station, so that

$$\mathbf{A}_i \begin{pmatrix} \mathbf{\Phi}_{i-1}^{n+1} - \mathbf{\Phi}_{i-1}^{n} \\ \mathbf{x}_{i-1}^{n+1} - \mathbf{x}_{i-1}^{n} \end{pmatrix} + \mathbf{B}_i \begin{pmatrix} \mathbf{\Phi}_{i}^{n+1} - \mathbf{\Phi}_{i}^{n} \\ \mathbf{x}_{i}^{n+1} - \mathbf{x}_{i}^{n} \end{pmatrix} + \mathbf{C}_i \begin{pmatrix} \mathbf{\Phi}_{i+1}^{n+1} - \mathbf{\Phi}_{i+1}^{n} \\ \mathbf{x}_{i+1}^{n+1} - \mathbf{x}_{i+1}^{n} \end{pmatrix} = -\begin{pmatrix} \mathbf{M}_i \\ \mathbf{N}_i \end{pmatrix} \tag{3.49}$$

where $\lfloor \mathbf{\Phi}_i^{n+1} - \mathbf{\Phi}_i^n, \mathbf{x}_i^{n+1} - \mathbf{x}_i^n \rfloor^T$ is the change in the solution vector at the i-station, and $\lfloor \mathbf{M}_i, \mathbf{N}_i \rfloor^T$ is the residual at the i-station.

The sub-matrices $\mathbf{A}_i$, $\mathbf{B}_i$, and $\mathbf{C}_i$ are large sparse matrices. For all i stations except those on the airfoil surface (i.e., from $i = ILE$ to $i = ITE$) each of blocks are

of size $3J \times 3J$, because there are three equations per node, for variables Φ, x, and y. The variables are ordered so that

$$\begin{pmatrix} \Phi_i^{n+1} - \Phi_i^n \\ \mathbf{x}_i^{n+1} - \mathbf{x}_i^n \end{pmatrix} = \begin{pmatrix} \Phi_{i,1}^{n+1} - \Phi_{i,1}^n \\ x_{i,1}^{n+1} - x_{i,1}^n \\ y_{i,1}^{n+1} - y_{i,1}^n \\ \vdots \\ \Phi_{i,j}^{n+1} - \Phi_{i,j}^n \\ x_{i,j}^{n+1} - x_{i,j}^n \\ y_{i,j}^{n+1} - y_{i,j}^n \\ \vdots \\ \Phi_{i,J}^{n+1} - \Phi_{i,J}^n \\ x_{i,J}^{n+1} - x_{i,J}^n \\ y_{i,J}^{n+1} - y_{i,J}^n \end{pmatrix} \tag{3.50}$$

For i-stations on the airfoil surface, there are an additional two equations per node to compute the stagnation point location and grid movement along the airfoil surface, as described earlier. Hence, the blocks at these stations are formally of size $(3J+2) \times (3J+2)$ (although one of these equations is actually not necessary at the $i = ILE$ station, since there is only one additional equation at the stagnation point). The arc length variables $s_{i,1}$ and $s_{i,J}$ are stored at the end of the vector given in Eq. (3.50) at these stations.

The entries in the global matrix shown in Eq. (3.48) and its corresponding residual are computed in two ways. The terms due to the steady flow governing equation are assembled from the elemental stiffness matrix and force vector given in Eqs. (3.21) and (3.22), respectively. The stiffness matrix is evaluated at each computational cell, and its entries are assembled into the appropriate locations in the global matrix. The force vector is also evaluated at each computational cell, and its entries are assembled into the appropriate locations in the residual vector.

The entries due to the grid generation equations, Eqs. (3.3) and (3.4), and the boundary conditions described in the previous sections are computed by linearizing the grid discretized equations and boundary conditions with respect to the value of the steady potential and grid location at the current iteration. For example, earlier in this chapter [Eq. (3.25)] we said that the boundary condition on the y-coordinate on the upper ($j = J$) surface of the computational domain on the periodic boundary may be written as

$$M_{i,J}^y = y_{i,J} - y_{i,1} - G = 0 \tag{3.51}$$

To perform Newton iteration on this equation, we rewrite it in the form

$$\left(\frac{\partial M_{i,J}^y}{\partial y_{i,J}}\right)^n \left(y_{i,J}^{n+1} - y_{i,J}^n\right) + \left(\frac{\partial M_{i,J}^y}{\partial y_{i,1}}\right)^n \left(y_{i,1}^{n+1} - y_{i,1}^n\right) = -\left(M_{i,J}^y\right)^n \tag{3.52}$$

or

$$\left(y_{i,J}^{n+1} - y_{i,J}^n\right) - \left(y_{i,1}^{n+1} - y_{i,1}^n\right) = -\left(M_{i,J}^y\right)^n \tag{3.53}$$

where the right-hand side of Eqs. (3.52) and (3.53) is the residual of Eq. (3.51) evaluated at the current iteration. The remaining boundary conditions and the grid equations may be linearized with respect to these variables in a similar fashion. Once the linearization has been performed, the entries need only to be assembled into their proper locations. The resulting linear system of equations may then be solved very efficiently using LU decomposition.

After each Newton iteration, the grid locations and potential are updated to obtain a new estimate of the solution. This process is repeated until the error in the residual vector $[\mathbf{M}, \mathbf{N}]^T$ is less than a specified tolerance.

3.2 Unsteady Flow Solution Procedure

Now that the steady solution has been obtained on a streamline grid, the unsteady flow may be calculated. For unsteady flows with vorticity (i.e., the forced response problem), the drift function and rotational velocity must be calculated at the before the assembly of the unsteady field equations and boundary conditions. For unsteady flows due to blade motion (the flutter problem), the unsteady grid motion must be calculated before the unsteady field equations and boundary conditions.

3.2.1 Drift Function and Rotational Velocity Calculation

Drift Function Evaluation

The first step in the vortical analysis is to calculate the drift function, Δ, since the stream function, Ψ, is already known from the grid generation equations. Since the grid follows the flow streamlines, it is sufficient to define the stream function at each point along the inlet ($i = 1$) boundary. From the discussion in Chapter 2 [Eq. (2.49)], the stream function may be expressed as

$$\Psi_{i,j} = R_{-\infty} U_{-\infty} (y_{1,j} - y_{1,1}) = Q_\infty (y_{1,j} - y_{1,1}) \tag{3.54}$$

where $R_{-\infty}$ and $U_{-\infty}$ are the upstream steady density and x-velocity, the product of which is equal to the prescribed mass flux at the exit boundary of the computational domain, Q_∞. Note that the value of the stream function on the stagnation streamline on the lower boundary of the computational domain, Ψ_0, is assumed to be zero.

For this analysis, the drift function will be set to zero at the upstream far-field boundary. Because the drift function measures the relative time it takes a fluid particle to move along a streamline, the initial value may be any arbitrary constant. Zero has been used here for convenience. Since the steady solution procedure resulted in a streamline grid, the calculation of the drift function at each grid location is relatively straightforward. Using the definition from Chapter 2 [Eq. (2.22)], the drift function may be calculated using the compound expression

$$\Delta_{i,j} = \begin{cases} 0 & i = 1 \\ \Delta_{i-1,j} + \left[(x_{i,j} - x_{i-1,j})^2 + (y_{i,j} - y_{i-1,j})^2 \right] / \left(\Phi_{i,j} - \Phi_{i-1,j} \right) & i > 1 \end{cases} \tag{3.55}$$

The drift function is measured relative to the upstream far-field boundary, so the drift function at the $i = 1$ axial grid station is zero. Once the drift function has been calculated, the rotational velocity, $\mathbf{v}^R$, may be calculated.

Rotational Velocity Calculation

The calculation of the rotational velocity, $\mathbf{v}^R$, may be accomplished largely through Eqs. (2.37) and (2.54) described in Chapter 2, i.e.,

$$\mathbf{v}^R = \left[\left(c_1 + \frac{\partial\tilde{\phi}}{\partial\Delta}\right)\nabla\Delta + \left(c_2 + \frac{\partial\tilde{\phi}}{\partial\Psi}\right)\nabla\Psi\right]\exp[j(K_1\Delta + K_2\Psi)] \tag{3.56}$$

and

$$\tilde{\phi} = \frac{j}{K_1}\left\{c_1 + \frac{jR_{-\infty}V_{-\infty}G\cos\Omega_{-\infty}(c_2K_1 - c_1K_2)}{2\pi(1 + ja_0K_1)}\sin\left[\frac{2\pi(\Psi - \Psi_0)}{R_{-\infty}V_{-\infty}G\cos\Omega_{-\infty}}\right]\right\} \times \exp[j(K_1\Delta + K_2\Psi)] \tag{3.57}$$

Here the constants c_1 and c_2, and the "wave numbers" K_1 and K_2 may be calculated using the upstream divergence-free condition of $\mathbf{v}^R$ [Eq. (2.33)] and the choice of the magnitude and phase of the vorticity. The stream function, Ψ, may be determined as part of the grid generation procedure, and the description of the drift function calculation was given earlier. All of the upstream flow conditions are prescribed. Hence, the only remaining tasks to determine $\mathbf{v}^R$ are the calculation of the stagnation point constant a_0 and the gradients of the drift and stream functions.

Recall from Eq. (2.28) that the constant a_0 is defined as

$$a_0 = -\left(\frac{\partial|\nabla\Phi|}{\partial n}\right)^{-1}_{\text{SP}} \tag{3.58}$$

Numerically, a_0 may not be evaluated exactly at the stagnation point. Instead, we wish to calculate a_0 at the midpoint between the stagnation point ($i = ILE$) and the previous adjacent grid point ($i = ILE - 1$). Using a simple finite difference expression, a_0 may be written as

$$a_0 = -\left[\frac{\Phi_{ILE,1} - \Phi_{ILE-1,1}}{(s_{ILE} - s_{ILE-1})}\right]^{-1}\frac{(s_{ILE} - s_{ILE-1})}{2} \tag{3.59}$$

where

$$s_{ILE} - s_{ILE-1} = \sqrt{(x_{ILE,1} - x_{ILE-1,1})^2 + (y_{ILE,1} - y_{ILE-1,1})^2} \tag{3.60}$$

Numerical experiments have shown that $\mathbf{v}^R$ is relatively insensitive to the details of the numerical calculation of a_0, i.e., different numerical formulations of a_0 did not result in a measurable difference in the resulting unsteady potential.

Finally, the gradients of the drift and stream functions must be evaluated. A general and straightforward approach to numerically calculating the gradient of a

function is to use a generalized coordinate transformation [54]. Specifically, the gradient will be evaluated in the (Ξ, H) grid generation coordinate system. This may be accomplished by considering the derivatives with respect to x and y using the chain rule, i.e.,

$$\frac{\partial}{\partial x} = \frac{\partial \Xi}{\partial x}\frac{\partial}{\partial \Xi} + \frac{\partial H}{\partial x}\frac{\partial}{\partial H} \tag{3.61}$$

and

$$\frac{\partial}{\partial y} = \frac{\partial \Xi}{\partial y}\frac{\partial}{\partial \Xi} + \frac{\partial H}{\partial y}\frac{\partial}{\partial H} \tag{3.62}$$

Ideally, however, we only wish to evaluate derivatives with respect to Ξ and H. This may be accomplished using the transformation matrix [J], which is defined as

$$[\mathbf{J}] = \begin{bmatrix} \dfrac{\partial \Xi}{\partial x} & \dfrac{\partial \Xi}{\partial y} \\ \dfrac{\partial H}{\partial x} & \dfrac{\partial H}{\partial y} \end{bmatrix} \tag{3.63}$$

To obtain the derivatives we desire, the matrix [J] may be inverted, resulting in

$$\frac{\partial \Xi}{\partial x} = \frac{\partial y/\partial H}{|[\mathbf{J}]|} \qquad \frac{\partial H}{\partial x} = -\frac{\partial y/\partial \Xi}{|[\mathbf{J}]|} \tag{3.64}$$

$$\frac{\partial \Xi}{\partial y} = -\frac{\partial x/\partial H}{|[\mathbf{J}]|} \qquad \frac{\partial H}{\partial y} = \frac{\partial x/\partial \Xi}{|[\mathbf{J}]|} \tag{3.65}$$

where

$$|[\mathbf{J}]| = \left(\frac{\partial x}{\partial \Xi}\frac{\partial y}{\partial H} - \frac{\partial x}{\partial H}\frac{\partial y}{\partial \Xi}\right)^{-1} \tag{3.66}$$

Combining the above expressions, the derivatives in Eqs. (3.61) and (3.62) may be rewritten as

$$\frac{\partial}{\partial x} = |[\mathbf{J}]|\left(\frac{\partial y}{\partial H}\frac{\partial}{\partial \Xi} - \frac{\partial y}{\partial \Xi}\frac{\partial}{\partial H}\right) \tag{3.67}$$

and

$$\frac{\partial}{\partial y} = |[\mathbf{J}]|\left(-\frac{\partial x}{\partial H}\frac{\partial}{\partial \Xi} + \frac{\partial x}{\partial \Xi}\frac{\partial}{\partial H}\right) \tag{3.68}$$

Note that now all derivatives are with respect to Ξ and H. These derivatives may be computed using centered finite differences modified for variable spacing in Ξ and H. The gradients of the drift and stream functions (or any other scalar) may be evaluated using this approach. Once the gradients have been calculated, the rotational velocity may be determined at each computational node.

3.2.2 Unsteady Grid Generation

For flutter problems, the motion of the computational grid must be computed before the calculation of the unsteady flow. The motion of the grid boundaries is easily

specified. The motion of the grid on the airfoil surface is required to match the vibrational mode shape of the blade motion. There is no grid motion in the far field to simplify the implementation of the far-field boundary conditions. Finally, the periodic and wake boundaries must smoothly connect these specified boundaries.

Previous researchers have solved Laplace's equation to determine the grid motion throughout the computational domain [30, 35, 24]. Laplace's equation was used so that the grid motion varies smoothly throughout the computational domain. As a result, derivatives of the grid motion may be computed with minimal truncation error. Furthermore, in finite difference discretizations using centered differences, grid motion that does not vary smoothly may excite sawtooth modes in the unsteady solution.

In the present method, sawtooth modes are not admitted into the finite element solution, so the grid motion need not be as smooth as for centered finite difference schemes. The truncation error of the derivatives must still be kept to a minimum, however. In this report, the calculation of the grid motion will be performed using a linear distribution of the grid motion over a few adjacent grid lines. A linear distribution is quite simple to implement, results in a relatively smooth distribution of grid motion, and does not significantly increase the overall truncation error of the unsteady solution method. For most cases examined in the present work, approximately five grid nodes in each direction were sufficient to obtain the correct unsteady solution. Mathematically, this may be expressed as

$$\mathbf{f}_{i,j} = L_i \, L_j \, \mathbf{f}_{\text{AIR}} \tag{3.69}$$

where $\mathbf{f}_{\text{AIR}}$ is the grid motion at the nearest grid point on the airfoil surface, and L_i and L_j are functions that contain fractional values to distribute the grid motion smoothly.

3.2.3 Finite Element Discretization

The next step is to compute the stiffness matrix and force vector for the unsteady flow equations. The variational principle governing the unsteady flow was developed in Chapter 2 [Eq. (2.74)]. As for the steady flow, the variational principle is discretized using bilinear quadrilateral isoparametric elements. Since the unsteady flow problem is linear, however, the solution may be computed in one iteration. At each element n, the values of the unsteady potential at each of the corners are interpolated into the interior of the domain using the interpolation

$$\phi(\xi, \eta) = \lfloor \mathbf{N} \rfloor_n \boldsymbol{\phi}_n \tag{3.70}$$

Similarly, the gradient operator may be written as

$$\nabla' \phi = [\mathbf{N}']_n \boldsymbol{\phi}_n \tag{3.71}$$

Substituting these expressions into the unsteady functional given in Eq. (2.74), results in

$$\Pi_{\text{linear}} = \frac{1}{2} \int\int_{\Sigma_n} R \left\{ -\overline{\boldsymbol{\phi}}_n^T [\mathbf{N}']_n^T [\mathbf{N}']_n \boldsymbol{\phi}_n + \frac{1}{C^2} \left[\overline{\boldsymbol{\phi}}_n^T [\mathbf{N}']_n^T \nabla' \Phi \nabla' \Phi^T [\mathbf{N}']_n \boldsymbol{\phi}_n \right. \right.$$

$$+j\omega\left(\overline{\phi}_n^T[\mathbf{N}']_n^T\nabla'\Phi\lfloor\mathbf{N}\rfloor_n\phi_n - \overline{\phi}_n^T\lfloor\mathbf{N}\rfloor_n^T\nabla'\Phi^T[\mathbf{N}']_n\phi_n\right)$$
$$+\omega^2\overline{\phi}_n^T\lfloor\mathbf{N}\rfloor_n^T\lfloor\mathbf{N}\rfloor_n\phi_n\Big]\Big\}\ d\xi\ d\eta$$
$$-\int\!\!\int_{\Sigma_n} R\Big\{\nabla'\Phi^T[\tilde{\mathbf{J}}][\mathbf{N}']_n\overline{\phi}_n + \nabla'\cdot\mathbf{f}\nabla'\Phi^T[\mathbf{N}']_n\overline{\phi}_n - j\omega\nabla'\cdot\mathbf{f}\lfloor\mathbf{N}\rfloor_n\overline{\phi}_n$$
$$-j\omega\mathbf{f}^T[\mathbf{N}']_n\overline{\phi}_n - \frac{1}{2C^2}\nabla'\Phi^T[\tilde{\mathbf{J}}]\nabla'\Phi\nabla'\Phi^T[\mathbf{N}']_n\overline{\phi}_n + \frac{j\omega}{2C^2}\nabla'\Phi^T[\tilde{\mathbf{J}}]\nabla'\Phi\lfloor\mathbf{N}\rfloor_n\overline{\phi}_n$$
$$+\frac{j\omega}{C^2}\mathbf{f}\cdot\nabla'\Phi\nabla'\Phi^T[\mathbf{N}']_n\overline{\phi}_n + \frac{\omega^2}{C^2}\mathbf{f}\cdot\nabla'\Phi\lfloor\mathbf{N}\rfloor_n\overline{\phi}_n\Big\}\ d\xi\ d\eta$$
$$+\int\!\!\int_{\Sigma_n}\nabla\cdot R\mathbf{v}^R\lfloor\mathbf{N}\rfloor_n\overline{\phi}_n\ d\xi\ d\eta \tag{3.72}$$

Setting the first variation of this functional to zero results in the discretized governing equations for the unsteady flow

$$\delta\Pi_{\text{linear}} = \int\!\!\int_{\Sigma_n} R\Big\{-[\mathbf{N}']_n^T[\mathbf{N}']_n + \frac{1}{C^2}\Big[[\mathbf{N}']_n^T\nabla'\Phi\nabla'\Phi^T[\mathbf{N}']_n$$
$$+j\omega\left([\mathbf{N}']_n^T\nabla'\Phi\lfloor\mathbf{N}\rfloor_n - \lfloor\mathbf{N}\rfloor_n^T\nabla'\Phi^T[\mathbf{N}']_n\right) + \omega^2\lfloor\mathbf{N}\rfloor_n^T\lfloor\mathbf{N}\rfloor_n\Big]\Big\}\phi_n\ d\xi\ d\eta$$
$$+\int\!\!\int_{\Sigma_n} R\Big\{j\omega\mathbf{f}^T\left([\mathbf{I}] - \frac{1}{C^2}\nabla'\Phi\nabla'\Phi^T\right)[\mathbf{N}']_n - \frac{\omega^2}{C^2}\mathbf{f}\cdot\nabla'\Phi\lfloor\mathbf{N}\rfloor_n$$
$$-\left(\nabla'\Phi^T[\tilde{\mathbf{J}}] + \nabla'\cdot\mathbf{f}\nabla'\Phi^T - \frac{1}{2C^2}\nabla'\Phi^T[\tilde{\mathbf{J}}]\nabla'\Phi\nabla'\Phi^T\right)[\mathbf{N}']_n$$
$$+j\omega\left[\nabla'\cdot\mathbf{f} - \frac{1}{2C^2}\nabla'\Phi^T[\tilde{\mathbf{J}}]\nabla'\Phi\right]\lfloor\mathbf{N}\rfloor_n\Big\}\ d\xi\ d\eta$$
$$+\int\!\!\int_{\Sigma_n}\nabla\cdot R\mathbf{v}^R\lfloor\mathbf{N}\rfloor_n\ d\xi\ d\eta = 0 \tag{3.73}$$

From this form of the first variation, it is clear that the local stiffness matrix, $[\mathbf{k}]_n$, may be written as

$$[\mathbf{k}]_n = \int\!\!\int_{\Sigma_n} R\Big\{-[\mathbf{N}']_n^T[\mathbf{N}']_n + \frac{1}{C^2}\Big[[\mathbf{N}']_n^T\nabla'\Phi\nabla'\Phi^T[\mathbf{N}']_n$$
$$+j\omega\left([\mathbf{N}']_n^T\nabla'\Phi\lfloor\mathbf{N}\rfloor_n - \lfloor\mathbf{N}\rfloor_n^T\nabla'\Phi^T[\mathbf{N}']_n\right) + \omega^2\lfloor\mathbf{N}\rfloor_n^T\lfloor\mathbf{N}\rfloor_n\Big]\Big\}\ d\xi\ d\eta \tag{3.74}$$

and the corresponding unsteady force vector, $\mathbf{e}_n$, is

$$\mathbf{e}_n = \int\!\!\int_{\Sigma_n}\Big(R\Big\{j\omega\mathbf{f}^T\left([\mathbf{I}] - \frac{1}{C^2}\nabla'\Phi\nabla'\Phi^T\right)[\mathbf{N}']_n - \frac{\omega^2}{C^2}\mathbf{f}\cdot\nabla'\Phi\lfloor\mathbf{N}\rfloor_n$$
$$-\left(\nabla'\Phi^T[\tilde{\mathbf{J}}] + \nabla'\cdot\mathbf{f}\nabla'\Phi^T - \frac{1}{2C^2}\nabla'\Phi^T[\tilde{\mathbf{J}}]\nabla'\Phi\nabla'\Phi^T\right)[\mathbf{N}']_n$$
$$+j\omega\left[\nabla'\cdot\mathbf{f} - \frac{1}{2C^2}\nabla'\Phi^T[\tilde{\mathbf{J}}]\nabla'\Phi\right]\lfloor\mathbf{N}\rfloor_n\Big\} + \nabla\cdot R\mathbf{v}^R\lfloor\mathbf{N}\rfloor_n\Big)\ d\xi\ d\eta \tag{3.75}$$

As in the steady flow calculation, the elemental stiffness matrix and force vector are computed for each cell in the computational domain and assembled into a global stiffness matrix and force vector. The next section describes the unsteady boundary conditions which also contribute terms to the global stiffness matrix and force vector.

3.2.4 Near-Field Boundary Conditions

Periodic Boundary Condition

In Chapter 2, it was noted that the periodic boundary condition would be enforced as part of the numerical solution procedure. This is not the only way to apply this condition, however. In Hall's original linearized potential formulation [24], a Lagrange multiplier was used to enforce cascade periodicity on the upstream periodic boundary. Although this approach will result in the correct solution, it does not lend itself well to the sensitivity analysis procedure. Consequently, in this work a slightly different approach is used to enforce cascade periodicity.

Examining the periodic boundary condition, Eq. (2.79), shows that the unsteady potential on the upper and lower periodic surfaces of the computational domain are not independent. Hence, the value of the unsteady potential on one of the periodic boundaries need not be calculated explicitly. The number of equations at each axial station in the periodic region may then be reduced by one. This new vector of the discretized unsteady potential and the original vector are related by a simple linear relationship. If the original unsteady potential vector is denoted by ϕ, and the new reduced vector by $\tilde{\phi}$, then

$$\phi = [\tilde{\mathbf{I}}]\,\tilde{\phi} \tag{3.76}$$

where

$$[\tilde{\mathbf{I}}] = \begin{bmatrix} 1 & & & \\ & 1 & & \\ & & \ddots & \\ & & & 1 \\ \hline e^{j\sigma} & & & \end{bmatrix} \tag{3.77}$$

Note that the matrix $[\tilde{\mathbf{I}}]$ is rectangular, of size $J \times (J-1)$.

The variational principle describing the flow may be written as

$$\Pi = \frac{1}{2}\overline{\phi}^T[\mathbf{k}]\phi - \overline{\phi}^T\mathbf{e} = \min \tag{3.78}$$

where $[\mathbf{k}]$ is the global stiffness matrix and $\mathbf{e}$ is the force vector. Substituting the solution vector transformation equation, Eq. (3.76), results in

$$\Pi = \frac{1}{2}\overline{\tilde{\phi}}^T[\bar{\tilde{I}}]^T[\mathbf{k}][\tilde{I}]\tilde{\phi} - \overline{\tilde{\phi}}^T[\bar{\tilde{I}}]^T\mathbf{e} \tag{3.79}$$

where the overbars again denote the complex conjugate. Setting the first variation of this expression to zero gives

$$\delta\Pi = [\bar{\tilde{I}}]^T[\mathbf{k}][\tilde{I}]\tilde{\phi} - [\bar{\tilde{I}}]^T\mathbf{e} = 0 \tag{3.80}$$

This is the equation that must be computed. In practice, Eq. (3.80) means that the periodicity condition is enforced by pre- and/or post-multiplying the stiffness matrices and force vectors by $[\bar{\tilde{\mathbf{I}}}]^T$ and $[\mathbf{I}]$, respectively, once the block stiffness matrices and force vectors have been computed. Hence, the block stiffness matrices $[\mathbf{a}_i]$, $[\mathbf{b}_i]$, and $[\mathbf{c}_i]$ and block force vector $\mathbf{e}_i$ at each station i are replaced according to the following table

i =	1	2 → ILE-1	ILE	ILE+1	ILE+2 → ...
$[\mathbf{a}_i] \rightarrow$	—	$[\bar{\tilde{\mathbf{I}}}]^T[\mathbf{a}_i][\tilde{\mathbf{I}}]$	$[\bar{\tilde{\mathbf{I}}}]^T[\mathbf{a}_i][\tilde{\mathbf{I}}]$	$[\mathbf{a}_i][\tilde{\mathbf{I}}]$	$[\mathbf{a}_i]$
$[\mathbf{b}_i] \rightarrow$	$[\bar{\tilde{\mathbf{I}}}]^T[\mathbf{b}_i][\tilde{\mathbf{I}}]$	$[\bar{\tilde{\mathbf{I}}}]^T[\mathbf{b}_i][\tilde{\mathbf{I}}]$	$[\bar{\tilde{\mathbf{I}}}]^T[\mathbf{b}_i][\tilde{\mathbf{I}}]$	$[\mathbf{b}_i]$	$[\mathbf{b}_i]$
$[\mathbf{c}_i] \rightarrow$	$[\bar{\tilde{\mathbf{I}}}]^T[\mathbf{c}_i][\tilde{\mathbf{I}}]$	$[\bar{\tilde{\mathbf{I}}}]^T[\mathbf{c}_i][\tilde{\mathbf{I}}]$	$[\bar{\tilde{\mathbf{I}}}]^T[\mathbf{c}_i]$	$[\mathbf{c}_i]$	$[\mathbf{c}_i]$
$\mathbf{e}_i \rightarrow$	$[\bar{\tilde{\mathbf{I}}}]^T\mathbf{e}_i$	$[\bar{\tilde{\mathbf{I}}}]^T\mathbf{e}_i$	$[\bar{\tilde{\mathbf{I}}}]^T\mathbf{e}_i$	$\mathbf{e}_i$	$\mathbf{e}_i$

So, for example, from axial grid stations $i = 2$ to $i = ILE - 1$, the block equation to be solved is of the form

$$[\tilde{\mathbf{a}}_i]\tilde{\phi}_{i-1} + [\tilde{\mathbf{b}}_i]\tilde{\phi}_i + [\tilde{\mathbf{c}}_i]\tilde{\phi}_{i+1} = \tilde{\mathbf{e}}_i \tag{3.81}$$

where $[\tilde{\mathbf{a}}_i]$, $[\tilde{\mathbf{b}}_i]$, $[\tilde{\mathbf{c}}_i]$, and $\tilde{\mathbf{e}}_i$ are the block stiffness matrices and force vector, respectively, that have been modified according to the table given above. Although this may appear to be somewhat complicated, the sparseness of the transformation matrix actually results in very few changes to the computed stiffness matrices and force vector, and eliminates the need to use Lagrange multipliers.

Airfoil Surface

The boundary condition on the airfoil surface is that there is an upwash on the surface of the airfoil due to blade motion and if there is a nonzero rotational velocity on the blade surface. Recall from Chapter 2, that the boundary integral terms in the first variation of the unsteady variational principle may be written as

$$\delta\Pi_{\text{linear}} = \int\int_{\Sigma} \{\ldots\}\ \delta\bar{\phi}\ d\xi\ d\eta$$

$$+ \oint_{\Gamma} R\left(j\omega\mathbf{f}\cdot\mathbf{n} - [\tilde{\mathbf{J}}]\nabla\Phi\cdot\mathbf{n} + \mathbf{v}^R\cdot\mathbf{n} - \frac{\partial\phi}{\partial n}\right)\ \delta\bar{\phi}\ ds = 0 \tag{3.82}$$

The first two terms in the boundary integral arise as the natural boundary condition of the variational principle. The third term, however, was added separately to account for the upwash due to a nonzero rotational velocity on the airfoil surface. The integral of this third term is discretized using one-dimensional finite elements, and the result is added to the inhomogeneous term $\mathbf{e}$. On the $(j = 1)$ surface, the equation to be solved is

$$[\mathbf{k}]_{i,1}\phi_i = \mathbf{e}_{i,1} + \frac{R_{i-1,1}}{6}\left[-v^R_{x,i-1,1}(y_{i,1} - y_{i-1,1}) + v^R_{y,i-1,1}(x_{i,1} - x_{i-1,1})\right]$$

$$+\frac{R_{i,1}}{3}\left[-v^R_{x,i,1}(y_{i,1} - y_{i-1,1}) + v^R_{y,i,1}(x_{i,1} - x_{i-1,1})\right]$$

$$+\frac{R_{i,1}}{3}\left[-v^R_{x,i,1}(y_{i+1,1} - y_{i,1}) + v^R_{y,i,1}(x_{i+1,1} - x_{i,1})\right]$$

$$+\frac{R_{i+1,1}}{6}\left[-v^R_{x,i+1,1}(y_{i+1,1}-y_{i,1})+v^R_{y,i+1,1}(x_{i+1,1}-x_{i,1})\right] \tag{3.83}$$

where the x and y subscripts refer to the x- and y-components of the rotational velocity $\mathbf{v}^R$, respectively. On the $(j = J)$ surface,

$$\begin{aligned}[\mathrm{k}]_{i,J}\boldsymbol{\phi}_i = \mathbf{e}_{i,J} &- \frac{R_{i-1,1}}{6}\left[-v^R_{x,i-1,1}(y_{i,1}-y_{i-1,1})+v^R_{y,i-1,1}(x_{i,1}-x_{i-1,1})\right] \\ &-\frac{R_{i,1}}{3}\left[-v^R_{x,i,1}(y_{i,1}-y_{i-1,1})+v^R_{y,i,1}(x_{i,1}-x_{i-1,1})\right] \\ &-\frac{R_{i,1}}{3}\left[-v^R_{x,i,1}(y_{i+1,1}-y_{i,1})+v^R_{y,i,1}(x_{i+1,1}-x_{i,1})\right] \\ &-\frac{R_{i+1,1}}{6}\left[-v^R_{x,i+1,1}(y_{i+1,1}-y_{i,1})+v^R_{y,i+1,1}(x_{i+1,1}-x_{i,1})\right]\end{aligned} \tag{3.84}$$

For airfoils containing a stagnation point, of course, it was shown in Chapter 2 that $\mathbf{v}^R$ is zero on airfoil and wake surfaces using the Atassi modification. So this term need only be computed for airfoils that do not contain a stagnation point and the Atassi formulation is not used.

Downstream Wake Boundary Condition

As was shown in Chapter 2, there are two separate parts to the wake boundary condition that need to be considered. The first is the auxiliary pressure continuity condition, Eq. (2.86). In discretized form, the pressure continuity condition for node i may be written as

$$\begin{aligned}&j\omega R_{i-1/2}\,(s_i-s_{i-1})\left[\frac{(\phi_{i-1,1}+\phi_{i,1})}{2}-\frac{(\phi_{i-1,J}+\phi_{i,J})\,e^{-j\sigma}}{2}\right] \\ &+R_{i-1/2}V_{i-1/2}\,(s_i-s_{i-1})\left[\frac{(\phi_{i,1}-\phi_{i-1,1})}{(s_i-s_{i-1})}-\frac{(\phi_{i,J}-\phi_{i-1,J})\,e^{-j\sigma}}{(s_i-s_{i-1})}\right]=0\end{aligned} \tag{3.85}$$

where

$$s_i - s_{i-1} = \sqrt{(x_i-x_{i-1})^2+(y_i-y_{i-1})^2} \tag{3.86}$$

Equation (3.85) provides closure for the wake displacement variable r_i.

The other condition is that mass must be conserved on the wake surface. Specifically, as shown by Eq. (2.88), there is an additional upwash that must be added due to the displacement of the wake. This additional upwash is added on both wake surfaces in the computational domain. On the $(j = 1)$ surface, the equation that must be solved is

$$\begin{aligned}&[\mathrm{k}]_{i,1}\boldsymbol{\phi}_i - \mathbf{e}_{i,1} \\ &-\frac{1}{2}R_{i+1/2}\,V_{i+1/2}\,(r_{i+1}-r_i)-\frac{1}{6}j\omega R_{i+1/2}\,(s_{i+1}-s_i)\,(r_{i+1}+2r_i) \\ &-\frac{1}{2}R_{i-1/2}\,V_{i-1/2}\,(r_i-r_{i-1})-\frac{1}{6}j\omega R_{i-1/2}\,(s_i-s_{i-1})\,(2r_i+r_{i-1})\end{aligned}$$

$$-\varepsilon\left(r_{i-1}-2r_i+r_{i+1}\right)=0 \tag{3.87}$$

and

$$s_{i+1}-s_i=\sqrt{(x_{i+1}-x_i)^2+(y_{i+1}-y_i)^2} \tag{3.88}$$

The last term on the left-hand side of Eq. (3.87) represents second-difference smoothing applied to the wake displacement to prevent sawtooth modes. For most cases, the coefficient, ε, is equal to 0.1.

Similarly, on the $(j=J)$ surface,

$$\begin{aligned}
&[\mathbf{k}]_{i,1}\phi_i-\mathbf{e}_{i,1}\\
&+\left[\frac{1}{2}R_{i+1/2}\,V_{i+1/2}\left(r_{i+1}-r_i\right)+\frac{1}{6}j\omega R_{i+1/2}\left(s_{i+1}-s_i\right)\left(r_{i+1}+2r_i\right)\right]e^{j\sigma}\\
&+\left[\frac{1}{2}R_{i-1/2}\,V_{i-1/2}\left(r_i-r_{i-1}\right)+\frac{1}{6}j\omega R_{i-1/2}\left(s_i-s_{i-1}\right)\left(2r_i+r_{i-1}\right)\right]e^{j\sigma}\\
&+\varepsilon\left(r_{i-1}-2r_i+r_{i+1}\right)e^{j\sigma}=0
\end{aligned} \tag{3.89}$$

With the addition of the wake displacement variable, r_i, and the boundary conditions given above, note that there are now $J+1$ equations for $J+1$ variables at each i-station in the wake. It is useful here to define a new vector to represent the combination of the potential at each node and the wake displacement, i.e.,

$$\breve{\phi}_i=\begin{pmatrix}\phi_i\\ r_i\end{pmatrix} \tag{3.90}$$

Hence, including the auxiliary boundary condition for the wake displacement, the block stiffness matrices $[\mathbf{a}_i]$, $[\mathbf{b}_i]$, and $[\mathbf{c}_i]$ and block force vector $\mathbf{e}_i$ are replaced according to the following table

i =	...→ ITE-2	ITE-1	ITE	ITE+1 → IMAX-1	IMAX
$[\mathbf{a}_i]\rightarrow$	$[\mathbf{a}_i]$	$[\mathbf{a}_i]$	$[\mathbf{a}_i]$	$[\breve{\mathbf{a}}_i]$	$[\breve{\mathbf{a}}_i]$
$[\mathbf{b}_i]\rightarrow$	$[\mathbf{b}_i]$	$[\mathbf{b}_i]$	$[\breve{\mathbf{b}}_i]$	$[\breve{\mathbf{b}}_i]$	$[\breve{\mathbf{b}}_i]$
$[\mathbf{c}_i]\rightarrow$	$[\mathbf{c}_i]$	$[\breve{\mathbf{c}}_i]$	$[\breve{\mathbf{c}}_i]$	$[\breve{\mathbf{c}}_i]$	—
$\mathbf{e}_i\rightarrow$	$\mathbf{e}_i$	$\mathbf{e}_i$	$\breve{\mathbf{e}}_i$	$\breve{\mathbf{e}}_i$	$\breve{\mathbf{e}}_i$

So, for example, from axial grid stations $i=ITE+1$ to $i=IMAX-1$, the block equation to be solved is of the form

$$[\breve{\mathbf{a}}_i]\breve{\phi}_{i-1}+[\breve{\mathbf{b}}_i]\breve{\phi}_i+[\breve{\mathbf{c}}_i]\breve{\phi}_{i+1}=\breve{\mathbf{e}}_i \tag{3.91}$$

where $[\breve{\mathbf{a}}_i]$, $[\breve{\mathbf{b}}_i]$, $[\breve{\mathbf{c}}_i]$, and $\breve{\mathbf{e}}_i$ are the block stiffness matrices and force vector, respectively, that have been modified according to the table given above.

Finally, the computation of the rotational velocity upwash is calculated on the wake surface the same way as on the airfoil surface, using Eqs. (3.83)- (3.84).

3.2.5 Far-Field Boundary Conditions

In Chapter 2, the basic analytical description of the unsteady flow in the far field was developed. In this section, the numerical solution of these equations is considered, including the presence of unsteady vorticity. In both the upstream and downstream far-field regions, the steady flow is assumed to be uniform. If, in addition, the computational grid is regularly spaced in the axial direction, the unsteady flow at each axial grid station i satisfies the equation

$$[\mathbf{a}_i]\phi_{i-1} + [\mathbf{b}_i]\phi_i + [\mathbf{c}_i]\phi_{i+1} = \mathbf{e}_i \tag{3.92}$$

where the inhomogeneous term $\mathbf{e}_i$ results from either non-divergence-free unsteady vorticity in the flow, or a specified acoustic gust. This inhomogeneous equation may be solved by examining the combination of the homogeneous part of the potential, ϕ_i^H, and the particular part of the potential, ϕ_i^P. The goal of this analysis is to compute these two potentials so that the combination of the two results in the unsteady potential that makes the far-field boundaries nonreflective, i.e.,

$$\phi_i = \phi_i^H + \phi_i^P \tag{3.93}$$

Substituting this expression into Eq. (3.92) results in

$$[\mathbf{a}_i]\left(\phi_{i-1}^H + \phi_{i-1}^P\right) + [\mathbf{b}_i]\left(\phi_i^H + \phi_i^P\right) + [\mathbf{c}_i]\left(\phi_{i+1}^H + \phi_{i+1}^P\right) = \mathbf{e}_i \tag{3.94}$$

which may be written as two separate equations: a homogeneous equation

$$[\mathbf{a}_i]\phi_{i-1}^H + [\mathbf{b}_i]\phi_i^H + [\mathbf{c}_i]\phi_{i+1}^H = 0 \tag{3.95}$$

and an inhomogeneous equation

$$[\mathbf{a}_i]\phi_{i-1}^P + [\mathbf{b}_i]\phi_i^P + [\mathbf{c}_i]\phi_{i+1}^P = \mathbf{e}_i \tag{3.96}$$

Homogeneous Solution

The solution of the homogeneous problem may be computed by considering how pressure and vorticity waves propagate from one axial grid station to the next. For example, if ϕ_i^H represents the homogeneous potential at grid station i, how can ϕ_{i-1}^H be represented? The desired relationship between the two is of the form

$$\phi_{i-1}^H = [\mathbf{T}]\,\phi_i^H \tag{3.97}$$

where $[\mathbf{T}]$ is a matrix that acts to filter out pressure waves approaching from outside of the computational domain. This matrix may be constructed in three intermediate steps. First, the as yet unknown potential vector at the far field is Fourier transformed, so that

$$d_{i,m} = \frac{1}{G}\int_0^G \phi(x_i, y)\exp(-j\beta_m y)\,dy \tag{3.98}$$

where $d_{i,m}$ are the Fourier coefficients at axial grid station i. In the present method, the coefficients are computed using the trapezoidal rule. Typically, the coefficient vector $\mathbf{d}_i$ is much smaller in length than the number of computational nodes in the circumferential direction, since truncation error increases greatly for higher harmonics of the principal circumferential wave number. For most cases considered here, five Fourier modes ($-2 \leq m \leq 2$) are sufficient to describe the unsteady flow. In matrix notation, Eq. (3.98) may be written in the form

$$\mathbf{d}_i = [\mathbf{F}_1]\phi_i^H \tag{3.99}$$

where $[\mathbf{F}_1]$ is a (generally rectangular) matrix that represents the discretized form of the trapezoidal rule.

The next step in the analysis is to filter and propagate these Fourier modes to the next grid station. In the far field, since the steady flow is assumed to be uniform, the wave numbers of the wave propagation are known analytically. From the analysis in Chapter 2, the harmonic behavior of the potential may be written as

$$\phi(x,y) = \sum_{m=-\infty}^{\infty} d_m \exp\left[j\alpha_m(x - x_{\text{ff}}) + j\beta_m y\right] \tag{3.100}$$

where x_{ff} is the x-coordinate of the far-field boundary being examined. Therefore, if the spacing between nodes on adjacent axial grid stations is known, then the propagation of the Fourier coefficients may be expressed as

$$d_{i-1,m} = d_{i,m} \exp\left[-j\alpha_m(x_i - x_{i-1}) - j\beta_m(y_i - y_{i-1})\right] \tag{3.101}$$

where

$$\alpha_m = \frac{U(\omega + \beta_m V) \pm C\sqrt{\beta_m^2(U^2 + V^2 - C^2) + 2\beta_m\omega V + \omega^2}}{C^2 - U^2} \tag{3.102}$$

and

$$\beta_m = \frac{\sigma + 2\pi m}{G} \tag{3.103}$$

In matrix notation, the filter and propagation relationship may be written as

$$\mathbf{d}_{i-1} = [\mathbf{F}_2]\mathbf{d}_i \tag{3.104}$$

where $[\mathbf{F}_2]$ is square and diagonal, and the diagonal entries are the above exponential expression for outgoing modes; the entries corresponding to incoming modes are zero so that their contribution is not included in the final solution.

The third step in the solution process is to perform an inverse Fourier transform on the Fourier coefficients $\mathbf{d}_{i-1}$ to recover the the new values of the potential at each node. In matrix form, this may be written as

$$\phi_{i-1}^H = [\mathbf{F}_3]\ \mathbf{d}_{i-1} \tag{3.105}$$

where the (also generally rectangular) matrix $[\mathbf{F}_3]$ is the discrete matrix form of the inverse Fourier transform.

Taken together, these three steps result in

$$\boldsymbol{\phi}_{i-1}^{H} = [\mathbf{F}_3]\,[\mathbf{F}_2]\,[\mathbf{F}_1]\,\boldsymbol{\phi}_i^{H} = [\mathbf{T}]\,\boldsymbol{\phi}_i^{H} \tag{3.106}$$

so the transition matrix, $[\mathbf{T}]$, is now known. Now that the behavior of the continuous part of the potential has been described, the particular part due to incoming gusts may be calculated.

Particular Solution

The particular solution may be calculated by considering the propagation characteristics of the incoming acoustic or vortical gust. Because the waves convect with the steady flow and the steady flow is uniform in the far field, the convection relation may be expressed as

$$\boldsymbol{\phi}_{i+n}^{P} = z^n\,\boldsymbol{\phi}_i^{P} \tag{3.107}$$

where

$$z^n = \exp\left[jn\alpha_p(x_{i+1} - x_i) + jn\beta_p(y_{i+1} - y_i)\right] \tag{3.108}$$

For a pressure gust, the wave numbers α_p and β_p have the same form as those for α_m and β_m as shown above in Eqs. (3.102) and (3.103). For a vortical gust, the wave numbers α_p and β_p are defined as

$$\alpha_p = -\frac{(\omega + \beta_p V)}{U} \tag{3.109}$$

and

$$\beta_p = \frac{\sigma}{G} \tag{3.110}$$

with U and V being the x- and y-components of the steady velocity at the far field.

Consequently, the equation that describes the particular solution in the far field, Eq. (3.96), may be written as

$$\frac{1}{z}\,[\mathbf{a}_i]\boldsymbol{\phi}_i^{P} + [\mathbf{b}_i]\boldsymbol{\phi}_i^{P} + z\,[\mathbf{c}_i]\boldsymbol{\phi}_i^{P} = \mathbf{e}_i \tag{3.111}$$

So the particular solution may be computed by solving the above linear system, i.e.,

$$\boldsymbol{\phi}_i^{P} = \left[\frac{1}{z}\,[\mathbf{a}_i] + [\mathbf{b}_i] + z\,[\mathbf{c}_i]\right]^{-1}\,\mathbf{e}_i \tag{3.112}$$

Equation (3.112) gives a relatively simple result that is best applied when a vortical gust is present. For an acoustic gust, there is a simpler approach. The unsteady pressure is linearly related to the potential by the expression

$$p(x,y) = -R\left[j\omega + \nabla\Phi\cdot\nabla\right]\phi(x_{\mathrm{ff}}, y_{\mathrm{ff}})\exp\left[j\alpha_p(x - x_{\mathrm{ff}}) + j\beta_p(y - y_{\mathrm{ff}})\right] \tag{3.113}$$

where $(x_{\mathrm{ff}}, y_{\mathrm{ff}})$ refers to a coordinate at the far-field boundary. Hence, the particular solution may be specified once the magnitude and phase of the gust has been chosen, i.e.,

$$\phi^{P}(x_{\mathrm{ff}}, y_{\mathrm{ff}}) = \frac{p(x,y)}{-R\left[j\omega + j\alpha_p U + j\beta_p V\right]}\exp\left[j\alpha_p(x - x_{\mathrm{ff}}) + j\beta_p(y - y_{\mathrm{ff}})\right] \tag{3.114}$$

Now that the general procedure for calculating the homogeneous and particular parts of the unsteady potential have been described, the actual implementation for each boundary may be examined.

Upstream Far-Field Boundary

At the upstream far-field boundary, the homogeneous part of the potential satisfies Eq. (3.95) with $i = 1$.

$$[\tilde{\mathbf{a}}_1]\tilde{\boldsymbol{\phi}}_0^H + [\tilde{\mathbf{b}}_1]\tilde{\boldsymbol{\phi}}_1^H + [\tilde{\mathbf{c}}_1]\tilde{\boldsymbol{\phi}}_2^H = 0 \tag{3.115}$$

where the block matrices and potential vectors have been modified in the periodic boundary conditions using Eq. (3.76). The transition matrix from Eq. (3.106), may be modified in a similar fashion, i.e.,

$$[\mathbf{T}] \rightarrow [\bar{\tilde{\mathbf{I}}}]^T[\mathbf{T}][\tilde{\mathbf{I}}] = [\tilde{\mathbf{T}}] \tag{3.116}$$

Hence, Eq. (3.115) may be written as

$$\left([\tilde{\mathbf{a}}_1][\tilde{\mathbf{T}}] + [\tilde{\mathbf{b}}_1]\right)\tilde{\boldsymbol{\phi}}_1^H + [\tilde{\mathbf{c}}_1]\tilde{\boldsymbol{\phi}}_2^H = 0 \tag{3.117}$$

and in light of Eq. (3.93), some algebra results in

$$[\tilde{\mathbf{b}}_1^*]\tilde{\boldsymbol{\phi}}_1 + [\tilde{\mathbf{c}}_1]\tilde{\boldsymbol{\phi}}_2 = \left([\tilde{\mathbf{b}}_1^*] + z\,[\tilde{\mathbf{c}}_1]\right)\tilde{\boldsymbol{\phi}}_1^P = \tilde{\mathbf{e}}_1^* \tag{3.118}$$

where

$$[\tilde{\mathbf{b}}_1^*] = \left([\tilde{\mathbf{a}}_1][\tilde{\mathbf{T}}] + [\tilde{\mathbf{b}}_1]\right) \tag{3.119}$$

Hence, the far-field boundary conditions modify the block matrix $[\tilde{\mathbf{b}}_1]$ and the block force vector $\tilde{\mathbf{e}}_1$.

Downstream Far-Field Boundary

The downstream far-field boundary conditions are assembled in an analogous fashion at axial grid station I, with the appropriate change in the direction of propagation of the pressure modes in the homogeneous solution. The only major difference is that the wake must be accounted for. Recall from Chapter 2 that there is a continuous and discontinuous part to the unsteady potential in the downstream far field

$$\phi = \phi_c + \phi_d \tag{3.120}$$

Both the continuous and discontinuous parts of the potential must propagate correctly. The transition matrix, $[\mathbf{T}]$, derived earlier, only applies to the continuous part of the potential. The discontinuous part propagates out of the domain as a vorticity wave. Hence, a new transition matrix may be defined as

$$[\mathbf{T}^*] = [\mathbf{T}][\mathbf{I} - \mathbf{D}] + z[\mathbf{D}] \tag{3.121}$$

where $[\mathbf{D}]$ is the matrix operator that computes the discontinuous part of the potential, and $[\mathbf{I}]$ is the identity matrix. The $J + 1$ equation is the propagated form of the

mass conservation boundary condition. Since there is no grid motion in the far field, the conservation of mass boundary condition is

$$\frac{\partial \phi}{\partial n} = j\omega r + \frac{\partial \Phi}{\partial s}\frac{\partial r}{\partial s} \tag{3.122}$$

In discrete form, Eq. (3.122) may be written as

$$\frac{\partial}{\partial n}\phi_I - \frac{j\omega}{2}(r_{I+1} + r_I) - \frac{\partial \Phi}{\partial s}\frac{(r_{I+1} - r_I)}{(s_i - s_{i-1})} = 0 \tag{3.123}$$

Solving for r_{I+1} gives

$$\frac{\partial/\partial n}{j\omega/2 + (\partial\Phi/\partial s)/(s_i - s_{i-1})}\phi_I + \frac{-j\omega/2 + (\partial\Phi/\partial s)/(s_i - s_{i-1})}{j\omega/2 + (\partial\Phi/\partial s)/(s_i - s_{i-1})} r_I = r_{I+1} \tag{3.124}$$

or

$$\lfloor \mathcal{F} \rfloor \phi_I + \mathcal{G} r_I = r_{I+1} \tag{3.125}$$

So the new transition matrix, with the additional row and column for the wake displacement, has the structure

$$\left(\begin{array}{c} \phi_{I+1} \\ \hline r_{I+1} \end{array}\right) = \left[\begin{array}{c|c} [\mathbf{T}] & 0 \\ \hline \mathcal{F} & \mathcal{G} \end{array}\right] \left(\begin{array}{c} \phi_I \\ \hline r_I \end{array}\right) \tag{3.126}$$

In the wake boundary conditions, we introduced a new vector that contains the potential and wake displacement, so that

$$\breve{\phi}_i = \left(\frac{\phi_i}{r_i}\right) \tag{3.127}$$

Hence, Eq. (3.126) may be written as

$$\breve{\phi}_{i+1} = [\breve{\mathbf{T}}]\breve{\phi}_i \tag{3.128}$$

Using this new transition matrix, the matrix equation at the downstream far field may be written as

$$[\breve{\mathbf{a}}_I]\breve{\phi}_{i-1} + [\breve{\mathbf{b}}^*_I]\breve{\phi}_i = \left(\frac{1}{z}[\breve{\mathbf{a}}_I] + [\breve{\mathbf{b}}^*_I]\right)\breve{\phi}^P_i = \breve{\mathbf{e}}^*_I \tag{3.129}$$

where in this case

$$[\breve{\mathbf{b}}^*_I] = \left([\breve{\mathbf{b}}_I] + [\breve{\mathbf{c}}_I][\breve{\mathbf{T}}]\right) \tag{3.130}$$

3.2.6 Assembly and Solution

Like the steady flow equations, the unsteady flow equations may be assembled into a block-tridiagonal form. Since there is only one variable per node to be computed, however, the size of the blocks of the matrix is significantly less than the steady flow case. Schematically, the matrix structure may be written using the notation developed in this chapter as

$$\begin{bmatrix} \tilde{\mathbf{b}}_1^* & \tilde{\mathbf{c}}_1 & & & & & \\ \tilde{\mathbf{a}}_2 & \tilde{\mathbf{b}}_2 & \tilde{\mathbf{c}}_2 & & & & \\ & \ddots & \ddots & \ddots & & & \\ & & \mathbf{a}_i & \mathbf{b}_i & \mathbf{c}_i & & \\ & & & \ddots & \ddots & \ddots & \\ & & & & \breve{\mathbf{a}}_{I-1} & \breve{\mathbf{b}}_{I-1} & \breve{\mathbf{c}}_{I-1} \\ & & & & & \breve{\mathbf{a}}_I & \breve{\mathbf{b}}_I^* \end{bmatrix} \begin{Bmatrix} \tilde{\phi}_1 \\ \tilde{\phi}_2 \\ \vdots \\ \phi_i \\ \vdots \\ \breve{\phi}_{I-1} \\ \breve{\phi}_I \end{Bmatrix} = \begin{Bmatrix} \tilde{\mathbf{e}}_1^* \\ \tilde{\mathbf{e}}_2 \\ \vdots \\ \mathbf{e}_i \\ \vdots \\ \breve{\mathbf{e}}_{I-1} \\ \breve{\mathbf{e}}_I^* \end{Bmatrix} \tag{3.131}$$

or, more generally,

$$[\mathbf{W}]\{\phi\} = \{\mathbf{e}\} \tag{3.132}$$

In the periodic region, the blocks of the matrix are of size $(J-1) \times (J-1)$, since the periodic boundary condition eliminates one equation from each block equation. For i-stations on the airfoil surface [signified by equation i in Eq. (3.131)], the block matrices are of size $J \times J$, because the boundary conditions do not change the number of equations in this region. In the wake region, the block matrices are of size $(J+1) \times (J+1)$ due to the additional wake displacement variable and its corresponding equation. Recall that the asterisk indicates that the block matrix or right-hand side vector are modified due to the application of the far-field boundary conditions.

The entries in the block matrices and right-hand side vectors are taken directly from the stiffness matrix and force vector computed at each computational cell with additional boundary conditions added in the appropriate locations as described in this chapter. Once assembled, this linear system may be solved very efficiently using LU decomposition to determine the unsteady potential ϕ at each computational node.

Chapter 4

Sensitivity Analysis

Chapters 2 and 3 described a general method to calculate the steady and small disturbance unsteady flow over a two-dimensional cascade of airfoils due to blade motion and incoming gusts. The next task (and the primary goal of this report) is to determine the effect small changes in the airfoil shape or cascade geometry have on the steady and unsteady flow fields. In Section 4.1, the general procedure for this sensitivity analysis will be described. The sensitivity analysis makes use of the nominal steady and unsteady flow LU decompositions so that no additional matrices need to be factored, resulting in a very computationally efficient procedure. Section 4.2 contains a description of the steady flow sensitivity analysis procedure, including a discussion of how the perturbation of the airfoil shape is prescribed. In a similar fashion, the sensitivity of the unsteady flow is considered in Section 4.3.

4.1 General Procedure

The quantities of interest to be calculated in this report may be separated into four groups: first is the nominal steady potential and grid locations, $\mathbf{\Phi}$ and $\mathbf{x}$; second, the perturbation of the steady potential and grid due to small changes in the airfoil geometry, $\mathbf{\Phi}'$ and $\mathbf{x}'$; third, the nominal unsteady potential, $\boldsymbol{\phi}$; and fourth, the perturbation of the unsteady potential due to small changes in the airfoil geometry, $\boldsymbol{\phi}'$. Chapters 2 and 3 described how the nominal steady flow (i.e., $\mathbf{\Phi}$ and $\mathbf{x}$) and nominal unsteady flow (i.e., $\boldsymbol{\phi}$) are calculated. This section describes a general procedure for calculating the remaining quantities, which are referred to as perturbations of their associated nominal quantities. Throughout this chapter, a prime ($'$) will be used to denote these perturbations.

It should be noted that the perturbation of the steady potential, $\mathbf{\Phi}'$, and the nominal unsteady potential, $\boldsymbol{\phi}$, are not of the same order. Figure 4.1 illustrates these two *separate* perturbations. In Chapters 2 and 3, the perturbation series we examined were expanded using a small parameter on the order of the blade displacement, $\mathbf{f}$. Here we expand the equations in perturbation series using a small parameter on the order of the change in geometry, which is denoted here by ϵ. Hence, the perturbation of the unsteady potential, $\boldsymbol{\phi}'$ is not formally second order. Instead, it is first order in

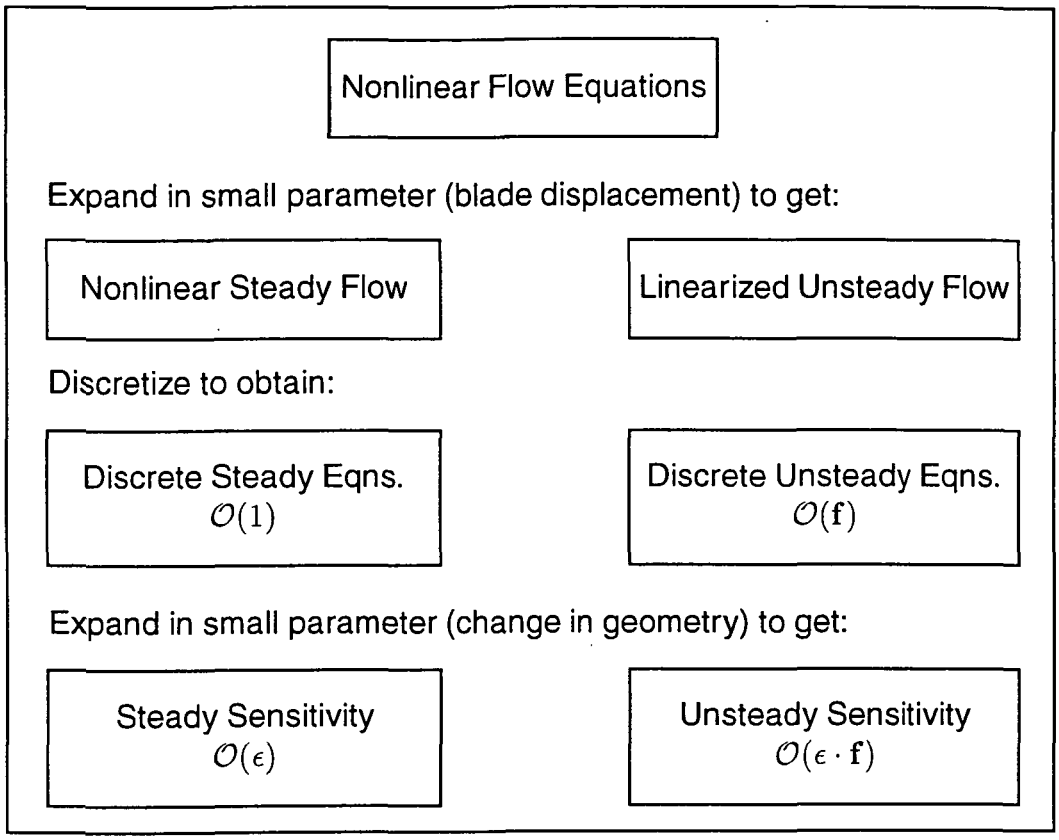

Figure 4.1: Overview of quantities in sensitivity analysis.

both ϵ and $\mathbf{f}$.

In Chapter 3, it was shown that the steady flow on a streamline grid may be computed by solving a set of nonlinear equations, Eqs. (3.8) and (3.9), for the unknown grid position and steady potential. Taken together, these equations may be written as

$$\left\{ \begin{array}{c} \mathbf{N}(\mathbf{\Phi}, \mathbf{x}; \mathbf{Z}) \\ \mathbf{M}(\mathbf{\Phi}, \mathbf{x}; \mathbf{Z}) \end{array} \right\} = \mathbf{0} \tag{4.1}$$

Because this set of equations are nonlinear, we chose to use Newton iteration to reduce the set of nonlinear equations to a series of linear equations to solve. The Newton iteration procedure [Eq. (3.47)] may be written in the form

$$\begin{pmatrix} \mathbf{\Phi} \\ \mathbf{x} \end{pmatrix}^{n+1} = \begin{pmatrix} \mathbf{\Phi} \\ \mathbf{x} \end{pmatrix}^{n} - \begin{bmatrix} \frac{\partial \mathbf{N}}{\partial \mathbf{\Phi}} & \frac{\partial \mathbf{N}}{\partial \mathbf{x}} \\ \frac{\partial \mathbf{M}}{\partial \mathbf{\Phi}} & \frac{\partial \mathbf{M}}{\partial \mathbf{x}} \end{bmatrix}_n^{-1} \begin{pmatrix} \mathbf{N} \\ \mathbf{M} \end{pmatrix}^{n} \tag{4.2}$$

When the residual of the iteration procedure has been reduced to a specified tolerance, the nominal steady potential and grid locations are obtained.

This section will consider the effect a small change in geometry has on these solutions. Consider a small perturbation $\mathbf{Z}'$ in the vector describing the airfoil shape

and cascade geometry. This will result in a perturbation of the steady potential and the grid location. The perturbed solution will satisfy the equations

$$\left\{ \begin{array}{l} \mathbf{N}(\mathbf{\Phi}+\mathbf{\Phi}', \mathbf{x}+\mathbf{x}'; \mathbf{Z}+\mathbf{Z}') \\ \mathbf{M}(\mathbf{\Phi}+\mathbf{\Phi}', \mathbf{x}+\mathbf{x}'; \mathbf{Z}+\mathbf{Z}') \end{array} \right\} = \mathbf{0} \tag{4.3}$$

where the primed quantities are small perturbation quantities arising from the prescribed perturbation in the geometry $\mathbf{Z}'$. Expanding Eq. (4.3) in a Taylor series about the nominal solution gives

$$\left[\begin{array}{cc} \frac{\partial \mathbf{N}}{\partial \mathbf{\Phi}} & \frac{\partial \mathbf{N}}{\partial \mathbf{x}} \\ \frac{\partial \mathbf{M}}{\partial \mathbf{\Phi}} & \frac{\partial \mathbf{M}}{\partial \mathbf{x}} \end{array} \right] \left(\begin{array}{c} \mathbf{\Phi}' \\ \mathbf{x}' \end{array} \right) = \left(\begin{array}{c} -\frac{\partial \mathbf{N}}{\partial \mathbf{Z}} \mathbf{Z}' \\ -\frac{\partial \mathbf{M}}{\partial \mathbf{Z}} \mathbf{Z}' \end{array} \right) \tag{4.4}$$

where we have grouped the terms so that left-hand side of Eq. (4.4) contains terms involving the perturbations of the dependent variables $\mathbf{\Phi}$ and $\mathbf{x}$, and the inhomogeneous right-hand side contains terms involving the prescribed perturbation of the independent variable $\mathbf{Z}$. To solve for the unknown perturbations $\mathbf{\Phi}'$ and $\mathbf{x}'$, Eq. (4.4) is rearranged slightly to obtain

$$\left(\begin{array}{c} \mathbf{\Phi}' \\ \mathbf{x}' \end{array} \right) = - \left[\begin{array}{cc} \frac{\partial \mathbf{N}}{\partial \mathbf{\Phi}} & \frac{\partial \mathbf{N}}{\partial \mathbf{x}} \\ \frac{\partial \mathbf{M}}{\partial \mathbf{\Phi}} & \frac{\partial \mathbf{M}}{\partial \mathbf{x}} \end{array} \right]^{-1} \left(\begin{array}{c} \frac{\partial \mathbf{N}}{\partial \mathbf{Z}} \mathbf{Z}' \\ \frac{\partial \mathbf{M}}{\partial \mathbf{Z}} \mathbf{Z}' \end{array} \right) \tag{4.5}$$

Note the similarity of Eq. (4.5) to Eq. (4.2). The same matrix must be "inverted" to obtain the perturbed steady solution that was used in the last iteration of the Newton solver. In other words, the same system of equations as in the nominal calculation must be solved, only with a different right-hand side due to the perturbation $\mathbf{Z}'$. Therefore, if Eq. (4.2) has been computed using LU decomposition, and the factored matrix has been saved, then the sensitivity analysis may be obtained for virtually no additional computational work. This is because the perturbations $\mathbf{\Phi}'$ and $\mathbf{x}'$ may be computed through a simple back-substitution, which requires significantly less computational time than a complete solution. Furthermore, the relative computational savings increases with the number of design variables examined. The perturbation of each design variable will result in a new right-hand side of Eq. (4.5), each only requiring a back-substitution, so many design variables may be examined before the cost of the sensitivity analysis approaches the cost of the single nominal calculation.

Consequently, the main task of the steady flow sensitivity analysis is to determine the prescribed perturbation $\mathbf{Z}'$ and its associated matrices $\partial \mathbf{N}/\partial \mathbf{Z}$ and $\partial \mathbf{M}/\partial \mathbf{Z}$. The details of the computation of these quantities will be examined in Section 4.2.

Having computed the perturbation of the steady potential and grid due to a change in geometry in addition to the nominal solution, we now consider the small disturbance unsteady flow. From Chapter 3, we know that the discretized unsteady flow may be represented by a linear system of equations of the form

$$[\mathbf{W}(\mathbf{\Phi}, \mathbf{x}, \omega, \sigma)]\{\phi\} = \{\mathbf{e}(\mathbf{\Phi}, \mathbf{x}, \mathbf{v}^R, \mathbf{f}, \omega, \sigma)\} \tag{4.6}$$

After solving Eq. (4.6), the perturbation of the unsteady potential due to a change in the geometry may be calculated. The governing equations of the perturbed unsteady flowfield due to small changes in geometry, frequency, rotational velocity, interblade phase angle, and mode shape will be of the form

$$[\mathbf{W}(\mathbf{\Phi}+\mathbf{\Phi}',\mathbf{x}+\mathbf{x}',\omega+\omega',\sigma+\sigma')]\{\phi+\phi'\}$$
$$=\mathbf{e}(\mathbf{\Phi}+\mathbf{\Phi}',\mathbf{x}+\mathbf{x}',\mathbf{v}^R+\mathbf{v}^{R'},\mathbf{f}+\mathbf{f}',\omega+\omega',\sigma+\sigma') \tag{4.7}$$

Expanding the discretized form of Eq. (4.7) in a perturbation series and collecting terms of first order gives the desired equation for the unknown discrete approximation to the perturbation of the unsteady potential, ϕ', i.e.,

$$[\mathbf{W}]\phi' = \left[\frac{\partial \mathbf{e}}{\partial \mathbf{\Phi}}\right]\mathbf{\Phi}' + \left[\frac{\partial \mathbf{e}}{\partial \mathbf{x}}\right]\mathbf{x}' + \left[\frac{\partial \mathbf{e}}{\partial \mathbf{v}^R}\right]\mathbf{v}^{R'} + \left[\frac{\partial \mathbf{e}}{\partial \mathbf{f}}\right]\mathbf{f}' + \left[\frac{\partial \mathbf{e}}{\partial \omega}\right]\omega' + \left[\frac{\partial \mathbf{e}}{\partial \sigma}\right]\sigma'$$
$$-\left(\left[\frac{\partial \mathbf{W}}{\partial \mathbf{\Phi}}\right]\mathbf{\Phi}' + \left[\frac{\partial \mathbf{W}}{\partial \mathbf{x}}\right]\mathbf{x}' + \left[\frac{\partial \mathbf{W}}{\partial \omega}\right]\omega' + \left[\frac{\partial \mathbf{W}}{\partial \sigma}\right]\sigma'\right)\phi \tag{4.8}$$

or, more succinctly

$$[\mathbf{W}]\phi' = \mathbf{e}' - [\mathbf{W}]'\phi \tag{4.9}$$

Note that the computation of $\mathbf{x}'$ and $\mathbf{\Phi}'$ has already been described. Section 4.3 contains a discussion of the computation of ω' and $\mathbf{f}'$ for the flutter problem, and $\mathbf{v}^{R'}$ for the forced response problem. In addition, Section 4.3 will contain a discussion of the assembly of the right-hand side of Eq. (4.8).

Note that the sensitivity analysis procedure outlined in this section is not limited to the flow model and discretization scheme chosen in the present method. Equations (4.1)–(4.9) may be applied to any linearized flow model, such as the linearized Euler or Navier-Stokes equations. Finite difference and finite volume discretizations also may be used. The only requirement to obtain the computational efficiency of the procedure described in this chapter is that the nominal flow equations must be solved using LU decomposition or some other algorithm designed to solve a linear system of equations for multiple right-hand sides.

4.2 Steady Flow Sensitivity Analysis

4.2.1 Prescribing the Perturbation

The first step in the steady flow sensitivity analysis is to prescribe the perturbation in the vector containing the airfoil shape and cascade geometry, $\mathbf{Z}'$. In general, the basis functions chosen to prescribe the geometry perturbation may be chosen arbitrarily. There is no limit on the number of functions that may be chosen, nor is there a restriction (such as orthogonality) on the choices. To provide physical insight, however, these functions should be chosen so that they are meaningful to the designer. In this work, the basis functions may be classified into two groups, cascade geometry and airfoil shape basis functions.

Recall from Chapter 3 that cascade geometry parameters refer to variables that define the cascade behavior independently of the actual airfoil shape. For example, the stagger angle, Θ, and the blade-to-blade gap, G, are both variables that are independent of the airfoil shape. Airfoil shape parameters refer to variables that define the airfoil shape, for example, the magnitude of the camber and thickness.

The details of the generation of the actual perturbation of the airfoil shape is highly dependent on the type of airfoil definition used. Although the details will not be discussed here, Appendix B contains a detailed description of how the perturbation of shapes from a common airfoil series (the NACA modified four digit series) may be generated. In the current discussion, however, it is sufficient to assume that perturbation of the airfoil shape or cascade geometry is prescribed and is contained in the vector $\mathbf{Z}'$.

Once the airfoil shape perturbation has been defined, the next task in the steady sensitivity analysis is to define the entries in the $\partial\mathbf{M}/\partial\mathbf{Z}$ and $\partial\mathbf{N}/\partial\mathbf{Z}$ matrices shown in Eq. (4.4). These matrices are extremely sparse because nearly all of the inhomogeneous terms in Eq. (4.4) arise from the boundary conditions. In practice, these matrices need not actually be formed; it is sufficiently straightforward to compute the matrix-vector product [the right-hand side of Eq. (4.4)] directly.

There are three main sources of inhomogeneous terms in Eq. (4.4). First, the near-field boundary conditions contribute terms because these conditions require the grid to remain on the airfoil surface. Any change in the airfoil shape, then, will influence the location of the grid points. Second, there is a contribution from the far-field boundary conditions primarily due to changes in the blade-to-blade gap. Finally, there are inhomogeneous terms due to the the grid equations, Eq. (3.8), because of the requirement that the grid follow the flow streamlines.

4.2.2 Near-Field Boundary Conditions

Periodic Boundary Condition

Consider the steady periodic boundary conditions, Eqs. (3.23)–(3.25). Taking the derivative of the boundary condition equations with respect to the shape variables described earlier and multiplying by the perturbation of the vector containing the airfoil shape results in terms that contribute to the right-hand side of Eq. (4.4). Assuming that the fractional arc length array F_i is not a design variable, the boundary conditions on the $j = 1$ periodic boundary of the computational domain do not result in inhomogeneous terms in Eq. (4.4), i.e,

$$\frac{\partial M^x_{i,1}}{\partial \mathbf{Z}}\,\mathbf{Z}' = \frac{\partial M^y_{i,1}}{\partial \mathbf{Z}}\,\mathbf{Z}' = 0 \tag{4.10}$$

On the $j = J$ surface, although the boundary condition governing the x-location is only dependent on the grid, the y-location is also dependent on the blade-to-blade gap, so there is an inhomogeneous term associated with the boundary condition on the y-grid equation, i.e.,

$$\frac{\partial M^x_{i,J}}{\partial \mathbf{Z}}\,\mathbf{Z}' = 0 \tag{4.11}$$

and

$$\frac{\partial M^y_{i,J}}{\partial \mathbf{Z}} \mathbf{Z}' = -G' \tag{4.12}$$

where G' is the perturbation in the blade-to-blade gap. Hence, the periodic boundary conditions are not directly dependent on the airfoil shape.

Airfoil Surface Boundary Conditions

The next set of boundary conditions to consider are those that constrain the grid points to lie on the airfoil surface, Eqs. (3.27)–(3.30). On the $j = 1$ surface, there are inhomogeneous terms that result from the spline evaluation, i.e.,

$$\frac{\partial M^x_{i,1}}{\partial \mathbf{Z}} \mathbf{Z}' = -X'_S(s_{i,1}) \tag{4.13}$$

and

$$\frac{\partial M^y_{i,1}}{\partial \mathbf{Z}} \mathbf{Z}' = -Y'_S(s_{i,1}) \tag{4.14}$$

where X'_S and Y'_S are the perturbations in the cubic spline evaluation of the airfoil surface coordinates corresponding to the arc length $s_{i,1}$. Similarly, on the $j = J$ surface,

$$\frac{\partial M^x_{i,J}}{\partial \mathbf{Z}} \mathbf{Z}' = -X'_S(s_{i,J}) \tag{4.15}$$

and

$$\frac{\partial M^y_{i,J}}{\partial \mathbf{Z}} \mathbf{Z}' = -Y'_S(s_{i,J}) - G' \tag{4.16}$$

where the latter equation also includes perturbations of the blade-to-blade gap, G'.

The next two boundary conditions are those that require the grid to move proportionally to the movement of the stagnation point, Eqs. (3.33)–(3.34). These conditions are applied at every airfoil surface grid location except the stagnation point. On the $j = 1$ surface,

$$\frac{\partial M^x_{i,J+1}}{\partial \mathbf{Z}} \mathbf{Z}' = -\frac{F_i - F_{i-1}}{1 - F_{i-1}} S'_1 \tag{4.17}$$

while on the $j = J$ surface,

$$\frac{\partial M^y_{i,J+1}}{\partial \mathbf{Z}} \mathbf{Z}' = -\frac{F_i - F_{i-1}}{1 - F_{i-1}} S'_N \tag{4.18}$$

Recall that S_1 and S_N are the arc length of the first and last points, respectively, of the set of points defining the surface of the airfoil, as shown in Fig. 3.4.

The final surface boundary condition to consider is the condition at the stagnation point, Eq. (3.35). This boundary condition requires that the grid node at the leading edge of the airfoil be located at the stagnation point. The right-hand side term is found to be

$$\frac{\partial M^x_{ILE,J+1}}{\partial \mathbf{Z}} \mathbf{Z}' = -\frac{1}{s_{ILE+1,1} - s_{ILE+1,J}} \left[\frac{s_{ILE} - s_{ILE+1,J}}{s_{ILE+1,1} - s_{ILE}} V_{-\infty} G' \right] \tag{4.19}$$

The term shown here arises from the steady periodicity condition. The potential on the upper surface must be evaluated on the reference airfoil. From the steady upstream far-field boundary conditions it can be shown that the steady potential on the upper periodic surface and the steady potential on the lower periodic surface are related through the parameters G and $V_{-\infty}$. Specifically,

$$\Phi_{i,1} = \Phi_{i,J} - G\,V_{-\infty} \tag{4.20}$$

so clearly there is an inhomogeneous term arising from perturbations in the blade-to-blade gap.

Downstream Wake Boundary Conditions

The final set of near-field boundary conditions to consider are those on the downstream wake boundary, Eqs. (3.36)–(3.38). Recall from Chapter 3 that the steady wake boundary conditions are nearly identical to the boundary conditions applied on the periodic surfaces. Hence, like the periodic boundary, there are no inhomogeneous terms in the perturbation of the boundary conditions on the $j = 1$ surface, i.e.,

$$\frac{\partial M^x_{i,1}}{\partial \mathbf{Z}}\,\mathbf{Z}' = \frac{\partial M^y_{i,1}}{\partial \mathbf{Z}}\,\mathbf{Z}' = 0 \tag{4.21}$$

On the $j = J$ surface, the inhomogeneous terms account for perturbations in the blade-to-blade gap as well as the possibility of a blunt trailing edge, so that

$$\frac{\partial M^x_{i,J}}{\partial \mathbf{Z}}\,\mathbf{Z}' = 0 \tag{4.22}$$

$$\frac{\partial M^y_{i,J}}{\partial \mathbf{Z}}\,\mathbf{Z}' = -\left[G' - (Y_1' - Y_N')\right] \tag{4.23}$$

4.2.3 Far-Field Boundary Conditions

Upstream Far-Field Boundary Conditions

On the inflow boundary, only the equations governing the computational grid location, Eqs. (3.41)–(3.42), may result in inhomogeneous terms. Since the x-coordinate of the upstream boundary is fixed in this analysis, however, it is not considered to be a design variable, and therefore only the boundary condition on the y-coordinate actually has an inhomogeneous part to consider. Linearization of the boundary conditions results in the expressions

$$\frac{\partial M^x_{1,j}}{\partial \mathbf{Z}}\,\mathbf{Z}' = 0 \tag{4.24}$$

and

$$\frac{\partial M^y_{1,j}}{\partial \mathbf{Z}}\,\mathbf{Z}' = -F_j G' \tag{4.25}$$

where it is assumed that the fractional arc length array in the far field, F_j, is not a design variable, i.e., it is not subject to change in the design process.

Downstream Far-Field Boundary Conditions

The boundary conditions at the exit boundary are more complicated, mainly due to the possibility of a blunt trailing edge. It is assumed here that any perturbation in blade-to-blade gap G' is constant throughout the computational domain. Hence, if the airfoil being analyzed has a blunt trailing edge, the space in the grid representing the viscous wake from the trailing edge of the airfoil to the far-field boundary (see Fig. 3.5) is constant regardless of the perturbation of the gap. The size of the space representing the wake is only affected by perturbations in the first and last points of the airfoil definition. Consequently, the inhomogeneous terms arising from the flow boundary conditions, Eqs. (3.43)-(3.44), may be written as

$$\frac{\partial N_{I,j}}{\partial \mathbf{Z}}\mathbf{Z}' = \frac{\partial N_{I,j+1}}{\partial \mathbf{Z}}\mathbf{Z}' = -\frac{1}{2}Q_\infty \frac{G'(y_{I,j+1}-y_{I,j})}{G-(Y_1-Y_N)}$$

$$+\frac{1}{2}Q_\infty \frac{G(y_{I,j+1}-y_{I,j})}{[G-(Y_1-Y_N)]^2}[G'-(Y_1'-Y_N')] \tag{4.26}$$

The terms arising from the grid boundary conditions, Eqs. (3.45)-(3.46), are similar to those for the inflow boundary, modified for the possibility of airfoil shapes with a blunt trailing edge, i.e.,

$$\frac{\partial M^x_{I,j}}{\partial \mathbf{Z}}\mathbf{Z}' = 0 \tag{4.27}$$

$$\frac{\partial M^y_{I,j}}{\partial \mathbf{Z}}\mathbf{Z}' = -F_j[G'-(Y_1'-Y_N')] \tag{4.28}$$

4.2.4 Sensitivity of the Stream Function

The final step in the steady sensitivity analysis is to consider the inhomogeneous terms due to a perturbation in the stream function, Ψ'. Inhomogeneous terms arise because in this analysis the stream function at any node j is linearly related to the blade-to-blade gap, i.e.,

$$\Psi_j = Q_\infty F_j G \tag{4.29}$$

where Q_∞ is the prescribed mass flux at the exit of the computational domain and F_j is the fractional arc length array value at node j. Consequently, a perturbation in the gap results in a perturbation of the stream function, so that

$$\Psi_j' = Q_\infty F_j G' \tag{4.30}$$

Hence, any perturbation in the gap results in inhomogeneous terms in Eq. (4.4) arising from the field grid generation equations, Eqs. (3.3)-(3.4). These inhomogeneous terms may be written as

$$\frac{\partial M^x_{i,j}}{\partial \mathbf{Z}}\mathbf{Z}' = \overline{\alpha}'\frac{\partial^2 x}{\partial \Xi^2} - 2\overline{\beta}'\frac{\partial^2 x}{\partial \Xi \partial \Psi} - 2\overline{\beta}\frac{\partial^2 x}{\partial \Xi \partial \Psi'} + \overline{\gamma}\frac{\partial^2 x}{(\partial \Psi^2)'}$$

$$+\left(\overline{\delta}^2\right)'\mathcal{Q}\frac{\partial x}{\partial \Psi} + \overline{\delta}^2\mathcal{Q}'\frac{\partial x}{\partial \Psi} + \overline{\delta}^2\mathcal{Q}\frac{\partial x}{\partial \Psi'} \tag{4.31}$$

and

$$\frac{\partial M^y_{i,j}}{\partial \mathbf{Z}}\mathbf{Z}' = \overline{\alpha}'\frac{\partial^2 y}{\partial \Xi^2} - 2\overline{\beta}'\frac{\partial^2 y}{\partial \Xi \partial \Psi} - 2\overline{\beta}\frac{\partial^2 y}{\partial \Xi \partial \Psi'} + \overline{\gamma}\frac{\partial^2 y}{(\partial \Psi^2)'}$$
$$+ \left(\overline{\delta}^2\right)' \mathcal{Q}\frac{\partial y}{\partial \Psi} + \overline{\delta}^2 \mathcal{Q}'\frac{\partial y}{\partial \Psi} + \overline{\delta}^2 \mathcal{Q}\frac{\partial y}{\partial \Psi'} \tag{4.32}$$

where the primes in the denominator of some of the terms refer to the perturbation of the finite difference representation of the $\partial/\partial\Psi$ operator. Note that the terms in Eqs. (4.31) and (4.32) only appear if there is a perturbation in the gap.

4.3 Unsteady Flow Sensitivity Analysis

4.3.1 Sensitivity of the Drift Function

For forced response problems, the first unsteady quantity that must be examined is the rotational velocity, $\mathbf{v}^R$. In Chapter 2 it was shown that the rotational velocity is a function of the drift function, Δ, the stream function, Ψ, in addition to the cascade geometry and prescribed flow conditions. Since the method for computing the sensitivity of the cascade geometry and stream function were presented earlier in this chapter, only the sensitivity of the drift function needs to be determined to calculate the sensitivity of the rotational velocity.

Since the perturbed grid will still follow the flow streamlines, the sensitivity of the drift function may be calculated by linearizing Eq. (3.55), i.e.,

$$\Delta'_{i,j} = \Delta'_{i-1,j} + 2\frac{(x_{i,j} - x_{i-1,j})(x'_{i,j} - x'_{i-1,j}) + (y_{i,j} - y_{i-1,j})(y'_{i,j} - y'_{i-1,j})}{\Phi_{i,j} - \Phi_{i-1,j}}$$
$$- \frac{(x_{i,j} - x_{i-1,j})^2 + (y_{i,j} - y_{i-1,j})^2}{(\Phi_{i,j} - \Phi_{i-1,j})^2}(\Phi'_{i,j} - \Phi'_{i-1,j}) \tag{4.33}$$

Note that the drift function at the inlet boundary remains prescribed to be zero, as shown in Eq. (3.55). Earlier in this chapter, the steady flow sensitivity analysis procedure was described, which resulted in expressions for the grid perturbations x' and y' and the steady potential perturbation Φ'. Hence, the summation in Eq. (4.33) may be computed in a straightforward manner.

4.3.2 Sensitivity of the Rotational Velocity

The sensitivity of the rotational velocity, $\mathbf{v}^R$, may be computed through careful application of the chain rule to the definition of the rotational velocity, Eq. (2.37). Considering that the coefficients c_1 and c_2 as well as the wave numbers K_1 and K_2 may have perturbations associated with them in addition to the perturbations already discussed in this chapter, the sensitivity of the rotational velocity, $\mathbf{v}^{R'}$, may be written as

$$\mathbf{v}^{R'} = \left\{\left[\left(c'_1 + jK'_1\tilde{\Phi} + jK_1\tilde{\Phi}'\right)\nabla\Delta + \left(c_1 + jK_1\tilde{\Phi}\right)(\nabla'\Delta + \nabla\Delta')\right.\right.$$

$$+\left(c_2' + jK_2'\tilde{\Phi} + jK_2\tilde{\Phi}' + \frac{\partial\tilde{\Phi}}{\partial\Psi'} + \frac{\partial\tilde{\Phi}'}{\partial\Psi}\right)\nabla\Psi$$

$$+\left(c_2 + jK_2\tilde{\Phi} + \frac{\partial\tilde{\Phi}}{\partial\Psi}\right)(\nabla'\Psi + \nabla\Psi')\Big] + j\left(K_1'\Delta + K_1\Delta' + K_2'\Psi + K_2\Psi'\right)$$

$$\times\left[\left(c_1 + jK_1\tilde{\Phi}\right)\nabla\Delta + \left(c_2 + jK_2\tilde{\Phi} + \frac{\partial\tilde{\Phi}}{\partial\Psi}\right)\nabla\Psi\right]\Big\}\exp[j(K_1\Delta + K_2\Psi)] \qquad (4.34)$$

where ∇' refers to the perturbation of the finite difference representation of the gradient operator due to the grid perturbation. Recall from Chapter 3 that the gradient operator used in this report is evaluated using a generalized coordinate transformation to the (Ξ, H) grid generation coordinate system [see Eqs. (3.67) and (3.68)]. Hence, perturbations in the grid locations result in a perturbation of the discretized gradient operator.

4.3.3 Sensitivity of the Blade Structural Dynamics

For flutter problems, the first task in the unsteady sensitivity analysis is to determine the perturbation of the blade motion. Once the perturbation in the vibratory mode shape of the blade is known, the perturbation of the grid motion may be calculated, so the complete unsteady sensitivity analysis may be computed.

Thus far, very little has been said about the structure of the blade. In Chapters 2 and 3, it was assumed that the vibratory frequency and mode shape are specified as part of the flutter problem description. The question then becomes, how do small changes in the blade shape affect the frequency and mode shape of the vibration?

It is beyond the scope of the present analysis to discuss a complete structural model of a turbomachine blade. In this analysis it is assumed that there is some independent structural model of the blades (e.g., a finite element model) that is used to calculate the frequency and mode shape of vibration. For turbomachinery blades, unlike aircraft wings, it is reasonable to assume that the ratio of the mass of the structure to the mass of the fluid is sufficiently high that the effect of steady aerodynamic loading on the calculation of the structural modes may be neglected. Hence, the sensitivity of the blade vibration may be calculated independently from the present analysis.

The sensitivity of the equations describing the blade structure may be calculated using some of the techniques described earlier or by using similar methods developed for analysis of structures [41, 42]. In any event, it is clear that the frequency and mode shape of vibration are functions of the design variables. For example, if the airfoil is described using the modified NACA four digit definition (see Appendix B), the sensitivity of the frequency can be written as

$$\omega' = \frac{\partial\omega}{\partial m_t}m_t' + \frac{\partial\omega}{\partial m_c}m_c' + \frac{\partial\omega}{\partial \ell_t}\ell_t' + \frac{\partial\omega}{\partial \ell_c}\ell_c' + \frac{\partial\omega}{\partial r_t}r_t' \qquad (4.35)$$

where m_t, m_c, ℓ_t, ℓ_c, and r_t are the shape definition variables of the NACA airfoil description, as discussed in Appendix B. Similarly, the sensitivity of the mode shape

is

$$\mathbf{f}' = \frac{\partial \mathbf{f}}{\partial m_t} m_t' + \frac{\partial \mathbf{f}}{\partial m_c} m_c' + \frac{\partial \mathbf{f}}{\partial \ell_t} \ell_t' + \frac{\partial \mathbf{f}}{\partial \ell_c} \ell_c' + \frac{\partial \mathbf{f}}{\partial r_t} r_t' \tag{4.36}$$

To calculate the derivatives in Eqs. (4.35)–(4.36), a sensitivity analysis must be performed on the structural model used to compute the nominal natural frequency and mode shape of vibration. Once the derivatives of the frequency and mode shape have been computed, Eqs. (4.35)–(4.36) may then be substituted into the overall unsteady sensitivity analysis expression, Eq. (4.8).

4.3.4 Sensitivity of the Grid Motion

Now that the sensitivity of the blade motion has been determined, the next task is to compute the perturbation of the grid motion in the computational domain. In Chapter 3, the field grid motion was shown to be a linear interpolation of the motion on the airfoil surface [Eq. (3.69)]. Hence, the sensitivity analysis is quite simple, since the distribution fractions L_i and L_j do not change, (i.e., they are not design variables). The perturbation of the grid motion, then, may be written as

$$\mathrm{f}'_{i,j} = L_i \, L_j \, \mathrm{f}'_{\mathrm{AIR}} \tag{4.37}$$

where $\mathrm{f}'_{\mathrm{AIR}}$ is the sensitivity of the blade mode shape calculated earlier.

4.3.5 Sensitivity of the Finite Element Assembly

Now that all of the perturbation terms have been computed, the right-hand side of Eq. (4.8) may be formed. The matrices on the right-hand side of this equation are large sparse matrices that may be obtained by linearizing the computer code which assembles the global matrix [**W**] and vector **e**. The elemental stiffness matrix and force vector, along with all of the unsteady boundary conditions, all have a first-order sensitivity that may be computed using the methods shown in this chapter.

For example, the sensitivity of the elemental stiffness matrix, [k] [defined in Eq. (3.74)] may be computed by linearizing the matrix with respect to all of the variables it is a function of, and multiplying by the actual perturbation, i.e.,

$$[\mathrm{k}]' = \frac{\partial [\mathrm{k}]}{\partial \mathbf{\Phi}} \mathbf{\Phi}' + \frac{\partial [\mathrm{k}]}{\partial \mathbf{x}} \mathbf{x}' + \frac{\partial [\mathrm{k}]}{\partial \omega} \omega' \tag{4.38}$$

Since $\mathbf{\Phi}'$ and $\mathbf{x}'$ may be determined from the steady flow sensitivity analysis, and ω' may be computed from the structural sensitivity analysis, the sensitivity of the stiffness matrix may be computed. To increase the efficiency of the right-hand side calculation, the perturbation of the stiffness matrix is multiplied by the appropriate entries in the ϕ vector at the element level. The details of this procedure do not substantially increase the understanding of the sensitivity analysis procedure, and are best understood by examining the actual computer code.

The sensitivity of the force vector, **e**, [see Eq. (3.75)] may be computed in a similar fashion, i.e.,

$$\mathbf{e}' = \frac{\partial \mathbf{e}}{\partial \mathbf{\Phi}} \mathbf{\Phi}' + \frac{\partial \mathbf{e}}{\partial \mathbf{x}} \mathbf{x}' + \frac{\partial \mathbf{e}}{\partial \omega} \omega' + \frac{\partial \mathbf{e}}{\partial \mathbf{v}^R} \mathbf{v}^{R\prime} + \frac{\partial \mathbf{e}}{\partial \mathbf{f}} \mathbf{f}' \tag{4.39}$$

Like the sensitivity of the stiffness matrix, the sensitivity of the force vector [i.e., the right-hand side of Eq. (4.39)] is best computed at the element level.

4.3.6 Near-Field Boundary Conditions

Periodic Boundary Condition

The periodic boundary condition may contribute inhomogeneous terms to the unsteady sensitivity equation because the transformation matrix $[\tilde{\mathbf{I}}]$ [see Eq. (3.77)] is a function of the interblade phase angle, σ. As a result, for example, the linearized form of the block equation to be solved at i-stations from $i = 2$ to $i = ILE - 1$ [see Eq. (3.81)] may be written as

$$[\bar{\tilde{\mathbf{I}}}]^T[\mathbf{a}_i][\tilde{\mathbf{I}}]\tilde{\boldsymbol{\phi}}'_{i-1} + [\bar{\tilde{\mathbf{I}}}]^T[\mathbf{b}_i][\tilde{\mathbf{I}}]\tilde{\boldsymbol{\phi}}'_{i} + [\bar{\tilde{\mathbf{I}}}]^T[\mathbf{c}_i][\tilde{\mathbf{I}}]\tilde{\boldsymbol{\phi}}'_{i+1} = [\bar{\tilde{\mathbf{I}}}]^{T'}\mathbf{e}_i + [\bar{\tilde{\mathbf{I}}}]^T\mathbf{e}'_i$$
$$- \left([\bar{\tilde{\mathbf{I}}}]^T[\mathbf{a}_i][\tilde{\mathbf{I}}]\right)'\tilde{\boldsymbol{\phi}}_{i-1} - \left([\bar{\tilde{\mathbf{I}}}]^T[\mathbf{b}_i][\tilde{\mathbf{I}}]\right)'\tilde{\boldsymbol{\phi}}_{i} - \left([\bar{\tilde{\mathbf{I}}}]^T[\mathbf{c}_i][\tilde{\mathbf{I}}]\right)'\tilde{\boldsymbol{\phi}}_{i+1} \qquad (4.40)$$

Although this appears to be a formidable equation to solve, the sparseness of the $[\tilde{\mathbf{I}}]$ matrix requires very few entries to be perturbed. Hence, the nominal $[\mathbf{a}_i]$, $[\mathbf{b}_i]$, and $[\mathbf{c}_i]$ matrices need not be stored in their entirety to perform the sensitivity analysis.

Airfoil Surface Boundary Condition

The sensitivity of the unsteady airfoil surface boundary condition need only be considered when $\mathbf{v}^R$ is not zero on the surface. As described in Chapter 3, $\mathbf{v}^R$ is zero on the airfoil surface and wake for airfoils using the Atassi modification of the rotational velocity. For geometries where this is not the case (e.g., flat plate airfoils using the Goldstein formulation), the equation to be solved on the airfoil surfaces may be derived by linearizing Eqs. (3.83) and (3.84) about the nominal solution.

Downstream Wake Boundary Conditions

Now consider the perturbation of the downstream wake boundary conditions, given by Eqs. (3.85)–(3.89). The wake displacement has a perturbation that must be computed along with the perturbation to the unsteady potential. The first boundary condition, Eq. (3.85) enforces the pressure continuity across the wake. The appropriate form of the perturbation of the pressure continuity equation may be obtained by linearizing Eq. (3.85) about the nominal solution.

The other condition is the conservation of mass on the wake surface, given by Eqs. (3.87)–(3.89). In matrix form, the linearized form of the block equation to be solved at i-stations from $i = ITE + 1$ to $i = IMAX - 1$ [see Eq. (3.91)] may be written as

$$[\breve{\mathbf{a}}_i]\breve{\boldsymbol{\phi}}'_{i-1} + [\breve{\mathbf{b}}_i]\breve{\boldsymbol{\phi}}'_{i} + [\breve{\mathbf{c}}_i]\breve{\boldsymbol{\phi}}'_{i+1} = \breve{\mathbf{e}}'_i - [\breve{\mathbf{a}}_i]'\breve{\boldsymbol{\phi}}_{i-1} - [\breve{\mathbf{b}}_i]'\breve{\boldsymbol{\phi}}_{i} - [\breve{\mathbf{c}}_i]'\breve{\boldsymbol{\phi}}_{i+1} \qquad (4.41)$$

Finally, the perturbation of the rotational velocity may be computed in the same way as on the airfoil surface, if it is required.

4.3.7 Far-Field Boundary Conditions

Upstream Far-Field Boundary Conditions

There are new inhomogeneous terms at the far-field boundaries as well. At the upstream far field, the equation to be solved is

$$[\tilde{b}_1^*]\tilde{\phi}'_1 + [\tilde{c}_1]\tilde{\phi}'_2 = \tilde{e}_1^{*'} - [\tilde{b}_1^*]'\tilde{\phi}_1 - [\tilde{c}_1]'\tilde{\phi}_2 \tag{4.42}$$

where the inhomogeneous term $\tilde{e}_1^{*'}$ is

$$\tilde{e}_1^{*'} = \left([\tilde{b}_1^*]' + z'[\tilde{c}_1] + z[\tilde{c}_1]'\right)\tilde{\phi}_1^P + \left([\tilde{b}_1^*] + z[\tilde{c}_1]\right)\tilde{\phi}'^P_1 \tag{4.43}$$

and

$$[\tilde{b}_1^*]' = [\tilde{b}_1]' + [\tilde{a}_1]'[\tilde{T}] + [\tilde{a}_1][\tilde{T}]' \tag{4.44}$$

The perturbation of the transition matrix, $[\tilde{T}]$, using the notation of Chapter 3, is

$$[\tilde{T}]' = [\mathbf{F}_3]'[\mathbf{F}_2][\mathbf{F}_1] + [\mathbf{F}_3][\mathbf{F}_2]'[\mathbf{F}_1] + [\mathbf{F}_3][\mathbf{F}_2][\mathbf{F}_1]' \tag{4.45}$$

and the perturbation of the particular part of the potential, $\tilde{\phi}^P$, is

$$\begin{aligned}\left(-\frac{1}{z}[\tilde{a}_1] + [\tilde{b}_1] + z[\tilde{c}_1]\right)\tilde{\phi}'^P_1 &= \tilde{e}'_1 \\ -\left(-\frac{z'}{z^2}[\tilde{a}_1] + \frac{1}{z}[\tilde{a}_1]' + [\tilde{b}_1]' + z'[\tilde{c}_1] + z[\tilde{c}_1]'\right)\tilde{\phi}_1^P &\end{aligned} \tag{4.46}$$

Hence, it is useful to retain the nominal $[\tilde{a}_1]$, $[\tilde{b}_1]$, and $[\tilde{c}_1]$ matrices for the sensitivity analysis.

Downstream Far-Field Boundary Conditions

Downstream, the equations are somewhat more complicated, since the wake has a perturbation associated with it. The equation to be solved at the downstream far-field boundary, is

$$[\breve{a}_I]\breve{\phi}_{I-1} + [\breve{b}_I^*]\breve{\phi}_I = \breve{e}_I^{*'} - [\breve{a}_I]'\breve{\phi}_{I-1} - [\breve{b}_I]'\breve{\phi}_I \tag{4.47}$$

where

$$\breve{e}_I^{*'} = \left(-\frac{z'}{z^2}[\breve{a}_I] + \frac{1}{z}[\breve{a}_I]' + [\breve{b}_I^*]'\right)\breve{\phi}_I + \left(\frac{1}{z}[\breve{a}_I] + [\breve{b}_I^*]\right)\breve{\phi}'_I \tag{4.48}$$

The perturbation of the downstream transition matrix, $[\mathbf{T}^*]'$, is

$$[\mathbf{T}^*]' = [\mathbf{T}]'[\mathbf{I} - \mathbf{D}] + [\mathbf{T}][\mathbf{I} - \mathbf{D}]' + z'[\mathbf{D}] + z[\mathbf{D}]' \tag{4.49}$$

and the perturbation of the particular part of the potential is

$$\begin{aligned}\left(-\frac{1}{z}[\tilde{a}_I] + [\tilde{b}_I] + z[\tilde{c}_I]\right)\breve{\phi}'_I &= \breve{e}'_I \\ -\left(-\frac{z'}{z^2}[\breve{a}_I] + \frac{1}{z}[\breve{a}_I]' + [\breve{b}_I]' + z'[\breve{c}_I] + z[\breve{c}_I]'\right)\breve{\phi}_I &\end{aligned} \tag{4.50}$$

The nominal $[\breve{a}_I]$, $[\breve{b}_I]$, and $[\breve{c}_I]$ matrices are also stored for use in the sensitivity analysis.

Chapter 5

Results

This chapter will illustrate how the present method may be used to analyze typical aeroelastic and aeroacoustic problems encountered in turbomachines. The results of the sensitivity analysis will be used to suggest design changes to improve the unsteady aerodynamic behavior. The newly redesigned airfoils will then be analyzed and compared to the initial design to assess the effectiveness of the procedure. The computational cost of the procedure will also be examined. In Section 5.1, the flutter stability of a compressor rotor will be analyzed as an example of a typical aeroelastic problem. The aeroacoustic capabilities of the present method will be demonstrated in Sections 5.2 and 5.3, where the acoustic response of two fan exit guide vanes (EGV) due to an upstream vortical rotor wake will be examined. Finally, Section 5.4 will summarize the conclusions from the results of the analysis.

In the computational results presented here, lengths are nondimensionalized by the airfoil chord, c, steady and unsteady velocities by the upstream steady velocity $|\mathbf{V}_{-\infty}|$, frequencies by $|\mathbf{V}_{-\infty}|/c$, pressures by $R_{-\infty}|\mathbf{V}^2_{-\infty}|$, lifts per unit span by $R_{-\infty}|\mathbf{V}^2_{-\infty}|c$, and moments per unit span by $R_{-\infty}|\mathbf{V}^2_{-\infty}|c^2$.

5.1 Aeroelastic Analysis and Design of a Compressor

5.1.1 Steady Flow Through a Compressor

To demonstrate the aeroelastic capabilities of the present sensitivity analysis, a linear cascade of NACA four digit series airfoils will be analyzed. The nominal cascade considered here is similar to modern compressor cascades, and is composed of NACA 5506 airfoils. The inflow Mach number $M_{-\infty}$ is 0.5, the inflow angle $\Omega_{-\infty}$ (measured from the axial direction) is 55°, the stagger angle Θ is 45°, and the blade-to-blade gap G is 0.9.

The steady flow through the cascade was computed using two different computational grids — a 65×17 node H-grid and a 129×33 node grid. Figure 5.1 shows the nominal steady surface pressure, P, for these two different grid resolutions. Note the good agreement between the coarse grid and fine grid solutions, indicating that the

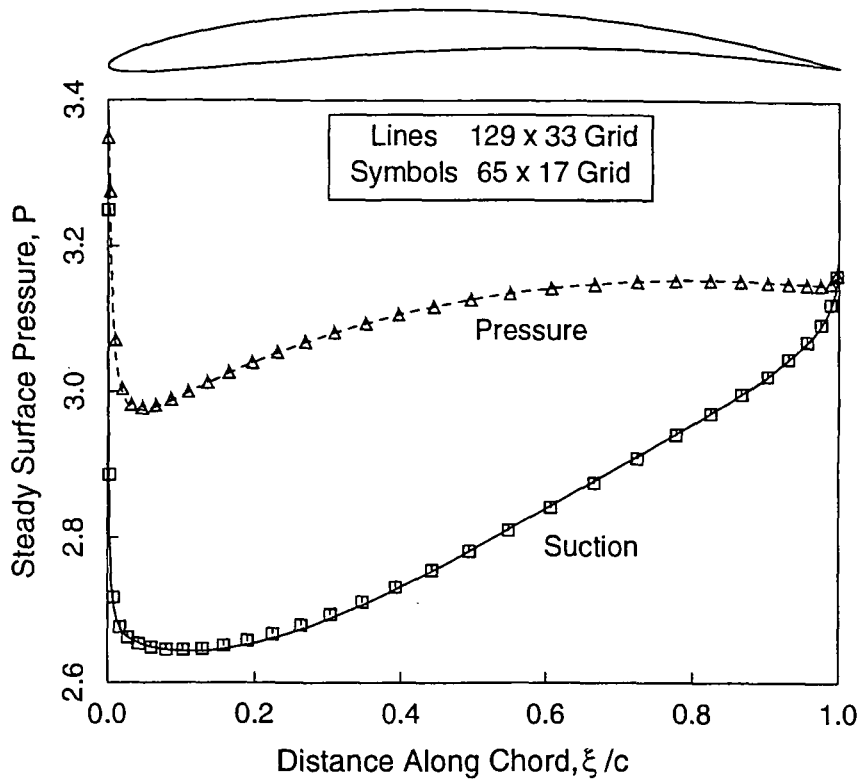

Figure 5.1: Steady surface pressure of cascade of NACA 5506 airfoils. $M_{-\infty} = 0.5$, $\Omega_{-\infty} = 55°$, $\Theta = 45°$.

solution is "grid converged." The steady surface pressure may be integrated along the chord to determine the steady forces acting on the airfoil. In this case, the steady lift, L (measured normal to the airfoil chord), is 0.2907, and the steady drag, D (measured tangent to the airfoil chord), is -0.0177. The steady moment may be calculated by integrating the product of the pressure and the distance to the point about which the moment is being taken. For this case, the moment measured about the leading edge, M_{LE}, is -0.1215. It should also be noted that the flow is entirely subsonic with a maximum Mach number on the suction surface of about 0.61.

5.1.2 Unsteady Flow Through a Compressor

Now that the steady flow through the cascade has been computed, we consider the unsteady flow due to plunging and torsional vibration of the airfoils. On the surface of the reference (i.e., unrotated) airfoil, the grid motion vector $\mathbf{f}$ for this rigid body motion may be written as

$$\mathbf{f}(x,y) = [-(y - y_p)\alpha]\,\mathbf{i} + [(x - x_p)\alpha + h]\,\mathbf{j} \tag{5.1}$$

where h is the amplitude of the bending vibration normal to the blade chord, α is the amplitude of the pitching motion (positive nose down), and the airfoil is pitching

about the point (x_p, y_p). The vectors i and j are unit vectors in the x- and y-directions, respectively.

As described in Chapter 1, the unsteady aerodynamic portion of a flutter analysis is to determine the unsteady work done on the blade due to self-induced oscillations. The blade work is the product of the aerodynamic force and the unsteady blade motion. A particularly useful quantity is the unsteady work done on the blade over one period of the oscillation, denoted $\hat{W}_{\text{CYCLE}}$. The complete work per cycle is defined as [55]

$$\hat{W}_{\text{CYCLE}} = -\int_0^{\Lambda} \oint_{\Gamma} \hat{P} \frac{\partial \mathbf{f}}{\partial t} \cdot \hat{\mathbf{n}} \, ds \, dt \tag{5.2}$$

where Λ is the period of the oscillation, $\hat{P}$ is the complete time-varying pressure, and $\hat{\mathbf{n}}$ is the unsteady unit normal to the blade surface. A positive value of the work per cycle indicates that the fluid is adding work to the motion, which continues to increase the amplitude of the motion, and is therefore considered to be destabilizing. After some algebra [56], it may be shown that

$$w_{\text{CYCLE}} = \pi \oint_{\Gamma} \left[(p_R \mathbf{f}_I - p_I \mathbf{f}_R) \cdot \mathbf{n} - P \left(\mathbf{f}_R \cdot \mathbf{n}'_I - \mathbf{f}_I \cdot \mathbf{n}'_R \right) \right] ds \tag{5.3}$$

where the subscripts R and I refer to the real and imaginary parts of the quantity, respectively. The vector $\mathbf{n}'$ arises from the tilting of the unit normal due to the pitching of the blade. On the reference airfoil, note that the grid motion is defined to be purely real. We will define the unsteady lift, ℓ, to be defined as

$$\ell = -\pi h \oint_{\Gamma} p \, dx - \alpha \oint_{\Gamma} P \, dx \tag{5.4}$$

In a similar fashion, the unsteady moment, m_T, will be defined as

$$m_T = -\pi \alpha \oint_{\Gamma} p \left[(x - x_p) dy + (y - y_p) dx \right] \tag{5.5}$$

We wish to express the work per cycle in terms of the unsteady lift and moment. To accomplish this, consider a single-degree-of-freedom bending or torsional vibration (i.e., the blade is either pitching or plunging, but not both). In this case, from Eq. (5.3) it may be shown that for a purely bending vibration,

$$w_{\text{CYCLE}} = \pi h \, \text{Im}[\ell] \tag{5.6}$$

Similarly, for a purely torsional vibration,

$$w_{\text{CYCLE}} = \pi \alpha \, \text{Im}[m_T] \tag{5.7}$$

So for a single degree of freedom motion, it is the out-of-phase (with blade displacement) component of the lift for plunging motion, or moment for a pitching motion that determines whether the motion is stable or unstable. In structural dynamic terms, Carta [57] has shown that for single-degree-of-freedom motions the work per cycle may be expressed as the aerodynamic damping of the system. Since the structural damping of the aeroelastic system is usually small, the aerodynamic damping

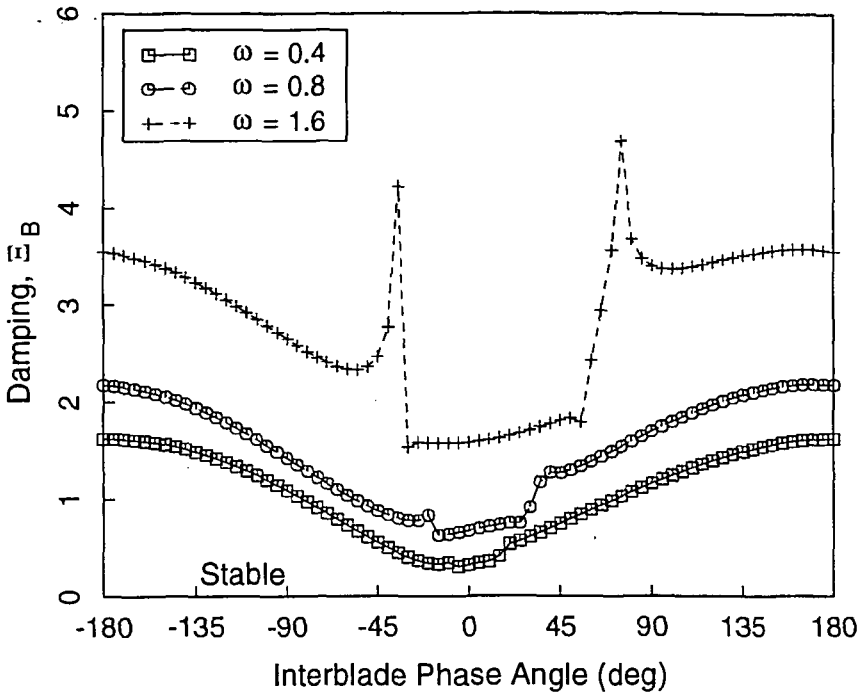

Figure 5.2: Aerodynamic damping of cascade of NACA 5506 airfoils vibrating in plunge at frequencies of 0.4, 0.8, and 1.6 for a range of interblade phase angles.

essentially determines the aeroelastic stability of the system. For a purely bending vibration, the aerodynamic damping Ξ_B may be written as

$$\Xi_B = -\frac{1}{\pi h} w_{\text{CYCLE}} = -\text{Im}[\ell] \tag{5.8}$$

and for a purely torsional vibration, Ξ_T is

$$\Xi_T = -\frac{1}{\pi \alpha} w_{\text{CYCLE}} = -\text{Im}[m_T] \tag{5.9}$$

These expressions clearly show that positive aerodynamic damping indicates that the motion is stable.

To evaluate the stability of the cascade under consideration, we will calculate the aerodynamic damping for both plunging and pitching for three different "reduced" frequencies. The term "reduced frequency" indicates that the frequency of vibration has been nondimensionalized by the airfoil chord, c, and the upstream freestream velocity, $|\mathbf{V}_{-\infty}|$. Figure 5.2 shows the aerodynamic damping Ξ_B of the cascade vibrating in plunge at three reduced frequencies and for a range of interblade phase angles. Note that for plunging motion, the system is stable, that is, the aerodynamic damping is positive for all interblade phase angles. However, the aerodynamic damping is generally less for low reduced frequencies. The pronounced peaks in the damping curves correspond to acoustic resonances of the duct containing the blade row. At interblade phase angles between these acoustic resonance points, at least

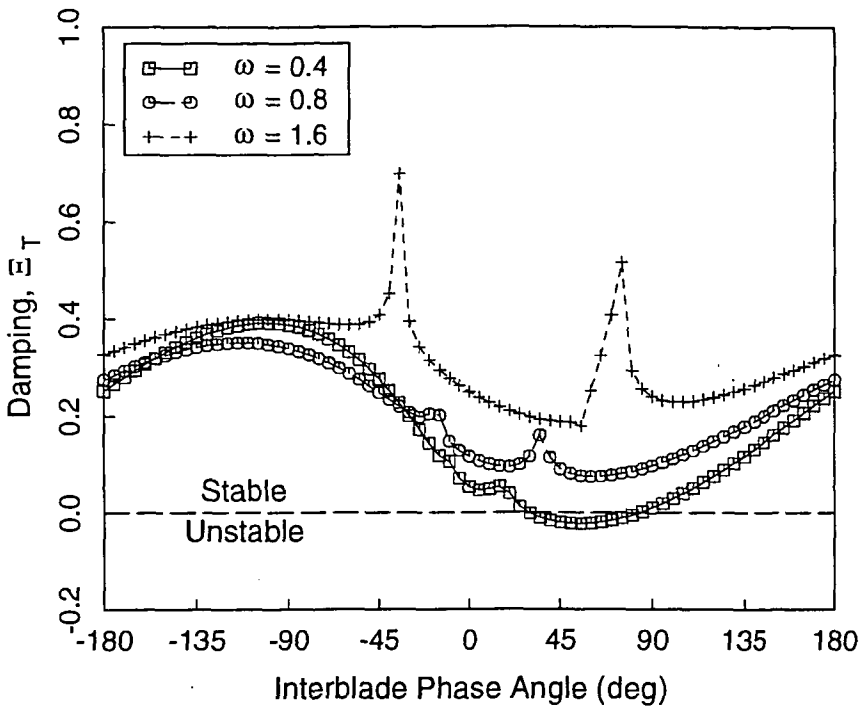

Figure 5.3: Aerodynamic damping of cascade of NACA 5506 airfoils pitching about their midchords at frequencies of 0.4, 0.8, and 1.6 for a range of interblade phase angles.

one of the pressure modes propagates unattenuated, i.e., it is "cut-on." At interblade phase angles outside of this region, all the pressure modes decay as the propagate, or are "cut-off."

Figure 5.3 shows the aerodynamic damping Ξ_T for the case where the airfoils vibrate in pitch about their midchords. Again, the cascade is least stable at the low reduced frequencies. In particular, note that the system is unstable ($\Xi_T < 0$) for several interblade phase angles at the lowest reduced frequency ω of 0.4. In other words, we have discovered an instability in the aeroelastic system.

We wish to use the sensitivity analysis developed in this report to suggest changes in the shape of the airfoil so that the instability may be eliminated. Hence, it is useful to examine in detail the case where the motion is least stable. As shown in Fig. 5.3, the least stable case occurs when the airfoils pitch about their midchords with a reduced frequency ω of 0.4 and an interblade phase angle σ of 60° (this is the least stable interblade phase angle for the reduced frequency ω of 0.4).

Figure 5.4 shows the real and imaginary parts of the complex amplitude of the nominal unsteady pressure, p, on the surface of the reference airfoil computed using two different grid resolutions, a 65 × 17 node grid and a 129 × 33 node grid. Note that the imaginary part of the pressure distribution is the part that does work on the vibrating airfoil. For this case, it is apparent that the imaginary part of the pressure difference across the airfoil is generally negative over the front half of the airfoil and

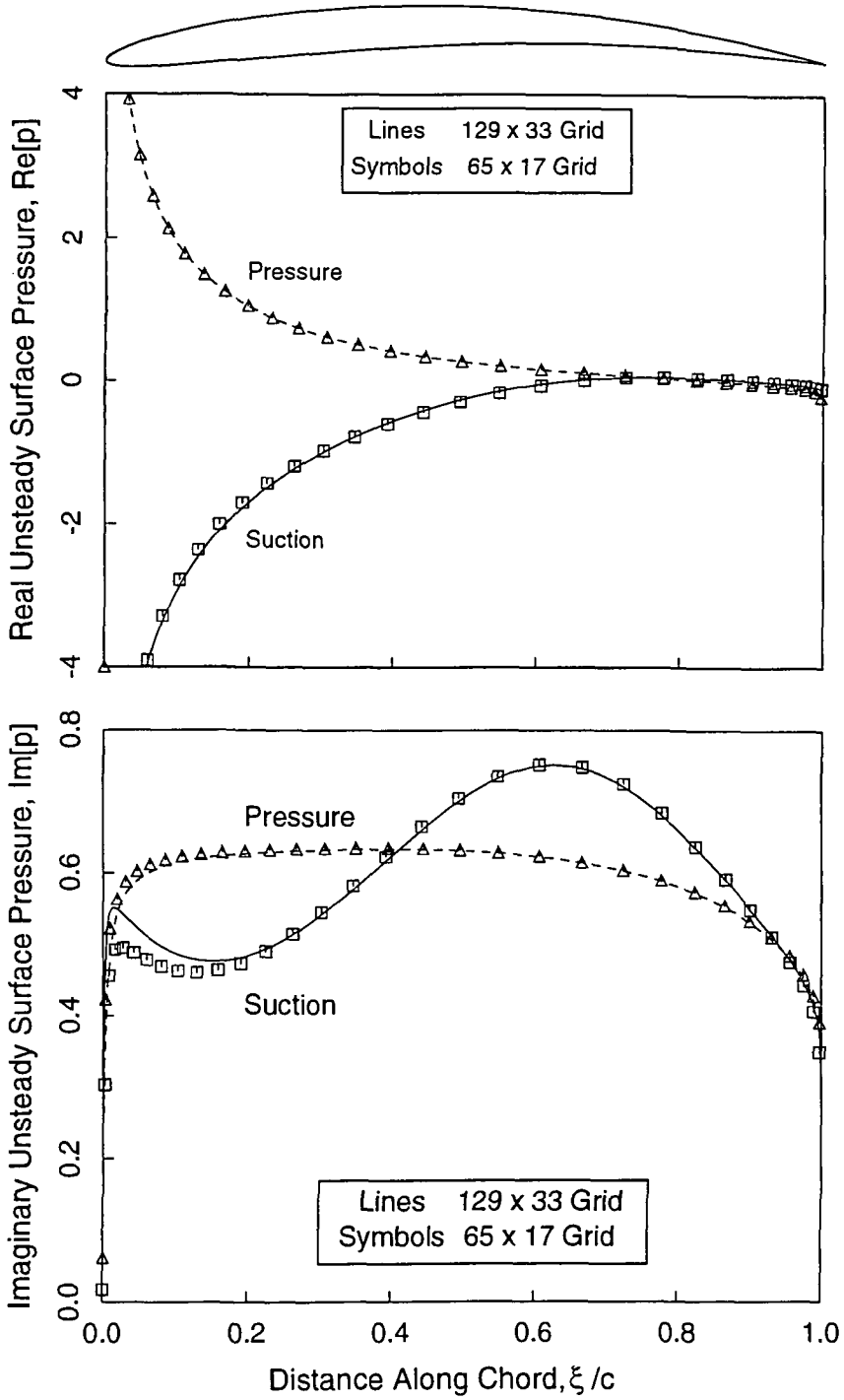

Figure 5.4: Imaginary part of unsteady surface pressure of NACA 5506 airfoils pitching about their midchords. $\omega = 0.4$, $\sigma = 60°$.

positive over the aft half. Thus, since the airfoil pitches about its midchord (positive nose up), the unsteady pressure does positive aerodynamic work (corresponding to negative aerodynamic damping) on the airfoil over most of the airfoil, making the cascade unstable in pitch for these conditions.

5.1.3 Sensitivity Analysis

Having computed the nominal flow through the cascade, the effect of five different design parameters on the steady flowfield will now be studied. Two of these parameters are from the NACA four digit airfoil definition, i.e., the magnitudes of the airfoil thickness and camber. (See Appendix B for a discussion of the NACA airfoil definition.) Each of these quantities are measured in fractions of the airfoil chord c. Also considered are the effect of changes in the cascade stagger angle Θ, and blade-to-blade gap G. Finally, an additional design variable, the reflex, is introduced here. The reflex parameter modifies the height of the mean line

$$h_m = h_c + rc\sin(2\pi\xi/c) \tag{5.10}$$

where h_m is the height of the mean line, h_c is the height of the mean line due to camber, r is the magnitude of the reflex in fractions of chord, c is the chord, and ξ is the distance along the airfoil chord. Reflex has been added to provide an "S shape" parameter to the design, to allow more flexibility in the airfoil shape than the strict NACA definition.

Figure 5.5 shows the sensitivity of the steady surface pressure to changes in these five geometry variables. The sensitivities are computed using the present sensitivity analysis; all results were computed on a 65×17 node grid. To check these results, the sensitivities using a finite difference approach are also computed. The finite-difference result is computed by solving for the steady flow about two slightly different airfoils, differencing the two solutions, and dividing the result by the difference in the airfoil parameter. Note the excellent agreement between the two solutions indicating that the effect of small changes in the design variables is linear, and that the present sensitivity analysis correctly predicts the sensitivities. Also, not surprisingly, the largest sensitivity in pressure occurs near the leading edge of the airfoil.

Next, the surface pressure sensitivities were integrated to obtain the sensitivity of the steady lift and drag (measured normal to and along the chord) and the moment about the leading edge. These results are given in Table 5.1. The sensitivity to changes in maximum camber location is also shown. In addition, the sensitivity of the lift in the y-direction (the cascade direction) is tabulated. The steady lift in the y-direction is a measure of the turning done by the cascade and hence is related to the steady work done by the cascade. Table 5.1 shows that the lift in the y-direction is most sensitive to changes in camber, stagger angle, and reflex. Since these parameters control the metal angle of the trailing edge, and the deviation between the exit flow angle and the metal angle is small for cascades, one would expect them to have a strong influence on the steady lift.

Next, the sensitivities of the unsteady surface pressure to changes in geometry are computed. Figures 5.6 and 5.7 show the real and imaginary parts, respectively, of

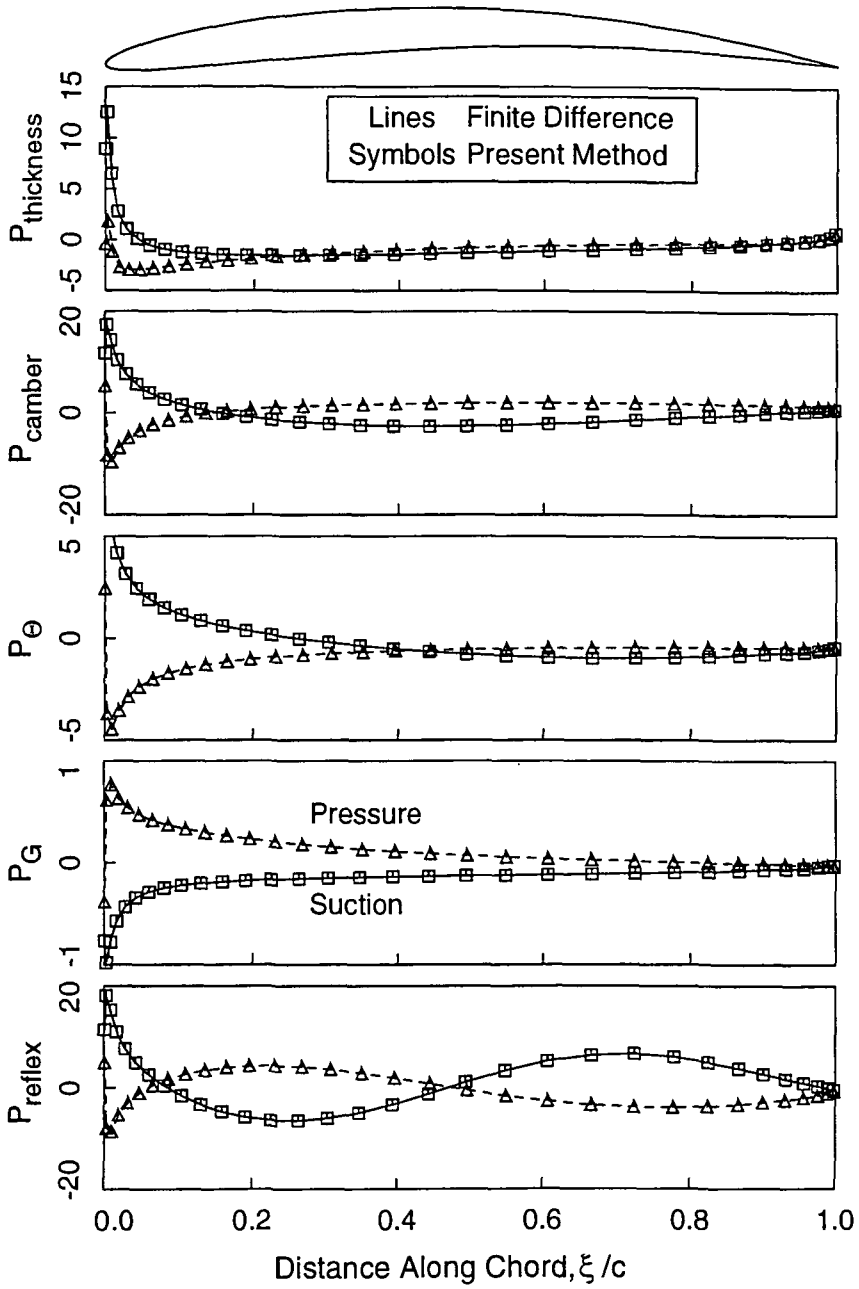

Figure 5.5: Sensitivity of steady surface pressure of cascade of NACA 5506 airfoils to perturbations in thickness, camber, stagger, gap, and reflex. $M_{-\infty} = 0.5$, $\Omega_{-\infty} = 55°$, $\Theta = 45°$.

Table 5.1: Sensitivity of steady forces and moment. The nominal steady lift, L, is 0.2907, the nominal drag, D, is -0.0177, the nominal moment about the leading edge, M_{LE}, is -0.1215, and the nominal lift in the y-direction, L_Y, is 0.1931.

Design Variable	L'	D'	M'_{LE}	L'_Y
Thickness	-0.1935	-0.0135	-0.1234	-0.1464
Camber	1.5637	0.1446	-1.4003	1.2080
Stagger	-0.6632	-0.0642	-0.0548	-0.5144
Gap	0.2743	-0.0244	-0.0764	0.1767
Max Camber Location	0.0873	0.0083	-0.1060	0.0676
Reflex	-1.5506	-0.1476	1.9235	-1.2008

the sensitivity of the unsteady pressure to small changes in six design variables (the reduced frequency ω is included as a design variable for unsteady flow calculations). All results were computed on a 65×17 node grid. The sensitivities are also compared to a finite difference calculation. Note the excellent agreement between the two solutions indicating that the present method correctly predicts the sensitivities. Also, the imaginary parts of the sensitivities to changes in stagger and reflex have pressure distributions that are fairly large in magnitude and have shapes that would tend to do work on pitching airfoils. That is, the sign of the pressure difference across the airfoil changes at roughly the midchord of the airfoil.

The sensitivities of the surface pressure to design variables may now be integrated to obtain the sensitivities of the aerodynamic damping. Table 5.2 shows the sensitivity of the aerodynamic damping to small changes in the design variables, including maximum camber location. The column labeled "Unconstrained" gives the sensitivity of the aerodynamic damping to changes in a single parameter. Here Ξ'_T is the sensitivity of the aerodynamic damping due to pitching motions, and Ξ'_B is the sensitivity of the aerodynamic damping due to plunging motion. In both cases, the nominal reduced frequency ω is 0.4. Note that as expected, stagger and reflex have a strong influence on the aerodynamic damping in pitch. Also note that for both pitching and plunging, the sensitivity of the damping to changes in frequency is positive. This is consistent with the results shown in Figures 5.2 and 5.3.

The results in the "Unconstrained" column of Table 5.2, however, can be somewhat misleading since changing each design variable independently also changes the steady work done by the blade row and changes the steady incidence at the leading edge of the airfoils. Generally, one would want to leave these quantities unchanged. To avoid this difficulty, it is useful to let two of the design variables "float" so that the steady turning done by the blade row, L_y/G, and the leading edge incidence angle, α, remain constant. In this study, the stagger angle Θ and the reflex r are allowed to

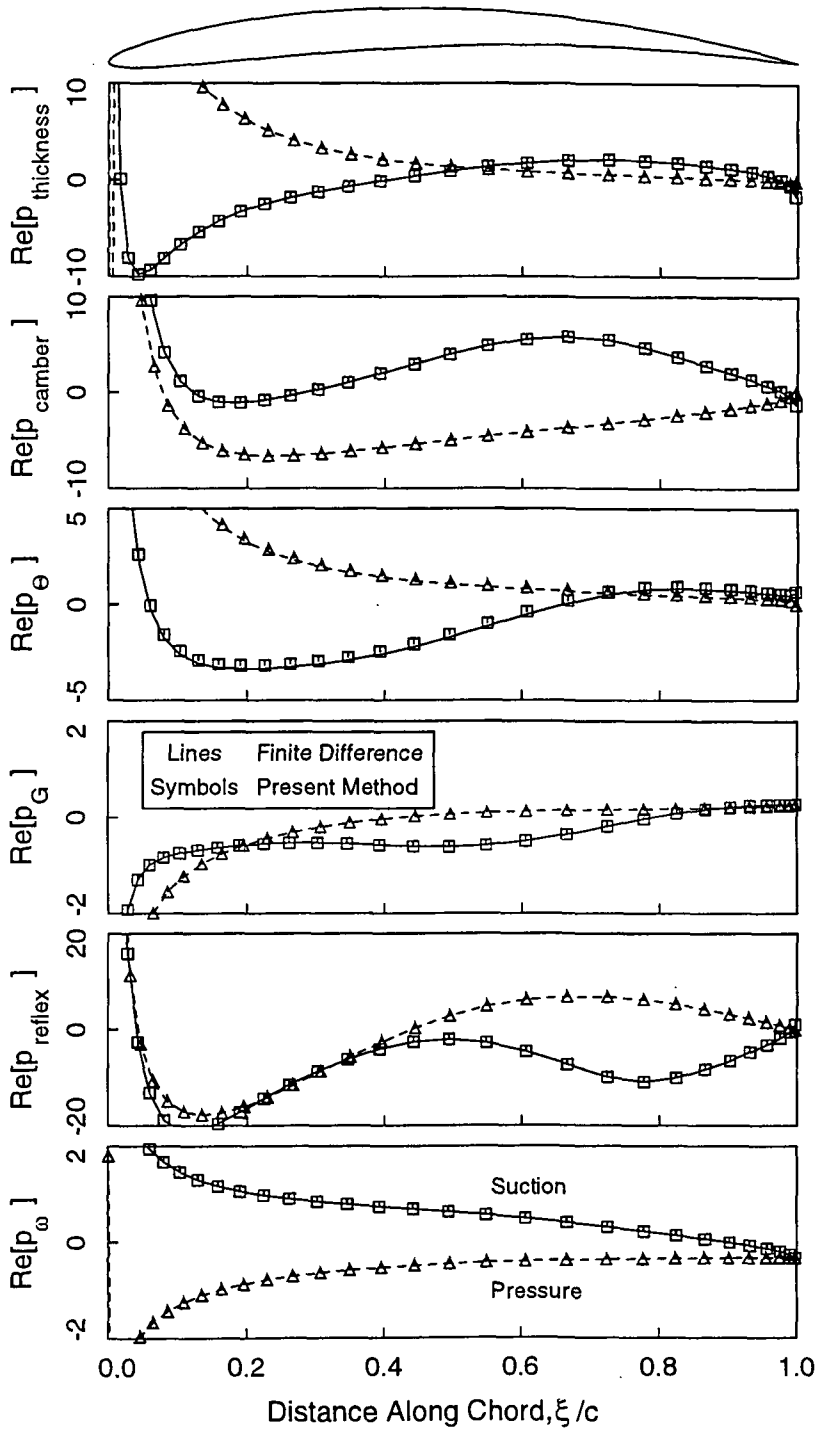

Figure 5.6: Real part of sensitivity of unsteady surface pressure of NACA 5506 airfoils pitching about their midchords due to perturbations in thickness, camber, stagger, gap, reflex, and frequency. $\omega = 0.4$, $\sigma = 60°$.

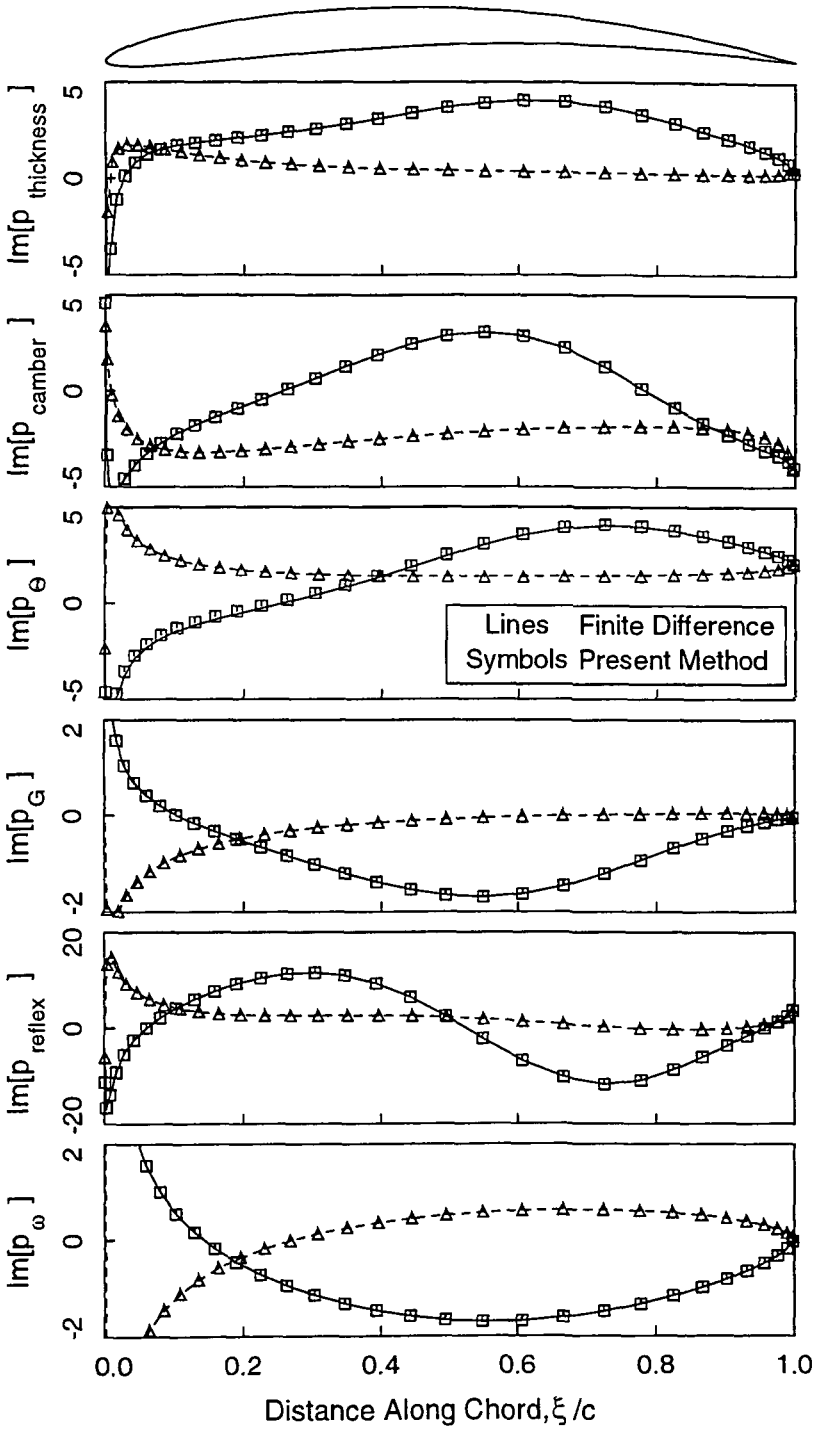

Figure 5.7: Imaginary part of sensitivity of unsteady surface pressure of NACA 5506 airfoils pitching about their midchords due to perturbations in thickness, camber, stagger, gap, reflex, and frequency. $\omega = 0.4$, $\sigma = 60°$.

Table 5.2: Sensitivity of aerodynamic damping. The nominal aerodynamic damping in torsion, Ξ_T, is -0.0214, and the damping in plunging, Ξ_B, is 0.8882.

	Unconstrained		Constrained	
Design Variable	Ξ'_T	Ξ'_B	Ξ'_T	Ξ'_B
Thickness	−0.2208	0.3046	0.1344	−0.1879
Camber	−0.0018	−1.9868	−5.2561	3.3668
Stagger	−0.6672	1.4079	—	—
Gap	0.1723	−0.0237	0.2643	−0.1511
Max Camber Location	−0.0383	−0.1143	0.0300	−0.0159
Reflex	0.7362	2.0131	—	—
Frequency	0.4030	1.3337	0.4030	1.3337

float. For example, then, if the gap G varies, the stagger angle and reflex must vary such that

$$\frac{\partial L_y}{\partial \Theta}\Theta' + \frac{\partial L_y}{\partial r}r' + \frac{\partial L_y}{\partial G}G' - \frac{L_y}{G}G' = 0 \tag{5.11}$$

and

$$\frac{\partial \alpha}{\partial \Theta}\Theta' + \frac{\partial \alpha}{\partial r}r' + \frac{\partial \alpha}{\partial G}G' = 0 \tag{5.12}$$

Equations (5.11) and (5.12) give two equations for the two unknowns Θ' and r' in terms of the gap perturbation G' and the sensitivities. The sensitivity of the incidence angle, α, and the resulting perturbations in Θ and r for each design variable are shown in Table 5.3. In Table 5.2, the column labeled "Constrained" refers to the sensitivities to each variable using this procedure. For both the pitching and plunging cases, it is clear that changing the camber has a very strong effect on the aerodynamic damping. In the pitching case, an increase in camber is destabilizing; in the plunging case, an increase in camber is stabilizing.

5.1.4 Redesign of a Compressor for Aeroelastic Stability

Next, the constrained sensitivity analysis is used to redesign an unstable cascade to make it stable. The nominal cascade has a reduced frequency ω of 0.4 and an interblade phase angle σ of 60°. Note from Table 5.2 that decreasing the camber has a stabilizing influence on torsional flutter. Thus, for the first redesign (Redesign A), the camber is reduced by 0.004 units. Using the constraint relations shown earlier, this requires that the stagger angle must be reduced by approximately 1.4° and the reflex must be increased by 0.0064 units (see Table 5.3). Although the sensitivity

Table 5.3: Sensitivity of incidence angle to design variables, and resulting perturbations in stagger angle and reflex for a unit change in design variables.

Design Variable	$\partial\alpha/\partial(\text{var})$	Θ'	r'
Thickness	0	−0.4533	0.0721
Camber	$2/\ell_c$	6.1033	−1.6080
Stagger	1	——	——
Gap	0	0.5465	−0.0870
Max Camber Location	$-2m_c/(\ell_c)^2$	−0.0274	0.0680
Reflex	2π	——	——
Frequency	0	0.0000	0.0000

analysis predicts that these changes alone will make the airfoil stable, the sensitivity analysis also predicts a large steady pressure gradient on the suction surface near the leading edge which would very likely cause the flow to separate, an undesirable result. To reduce the adverse pressure gradient in the pressure distribution, the thickness is increased by 0.02 units, which in turn requires the stagger be reduced by approximately 0.52° and 0.0014 units of reflex be added.

For the second redesign (Redesign B), the gap G is increased by 0.1. Again Table 5.2 predicts that this change will make the cascade stable, and requires that the stagger angle be reduced by approximately 0.61° and 0.0017 units of reflex be added.

Figure 5.8 shows the computed steady surface pressure on the nominal and redesigned airfoils. Also shown is the pressure predicted by the linear sensitivity analysis. The good agreement between the two indicates that steady nonlinear geometrical effects are small, at least for the subsonic flow conditions considered here. For Redesign A, although the steady lift on the airfoil in the y-direction has only slightly changed, the pressure distribution has changed significantly. For Redesign B, the net lift in the y-direction has increased, since the increase in gap means that the steady work per airfoil must increase. Note that the pressure gradient on the suction surface is larger for both redesigned airfoils. Both redesigns are therefore likely to increase somewhat the aerodynamic losses of the cascade.

Figures 5.9 and 5.10 show the real and imaginary parts of the unsteady pressure on the surface of the redesigned airfoils for Redesign A and Redesign B, respectively. Although in both cases the real part shows very little change, the imaginary part shows significant changes, particularly on the suction surface. Although there is a larger difference between the sensitivity analysis prediction and the actual pressure distribution than in the steady case, the sensitivity analysis still provides an excellent

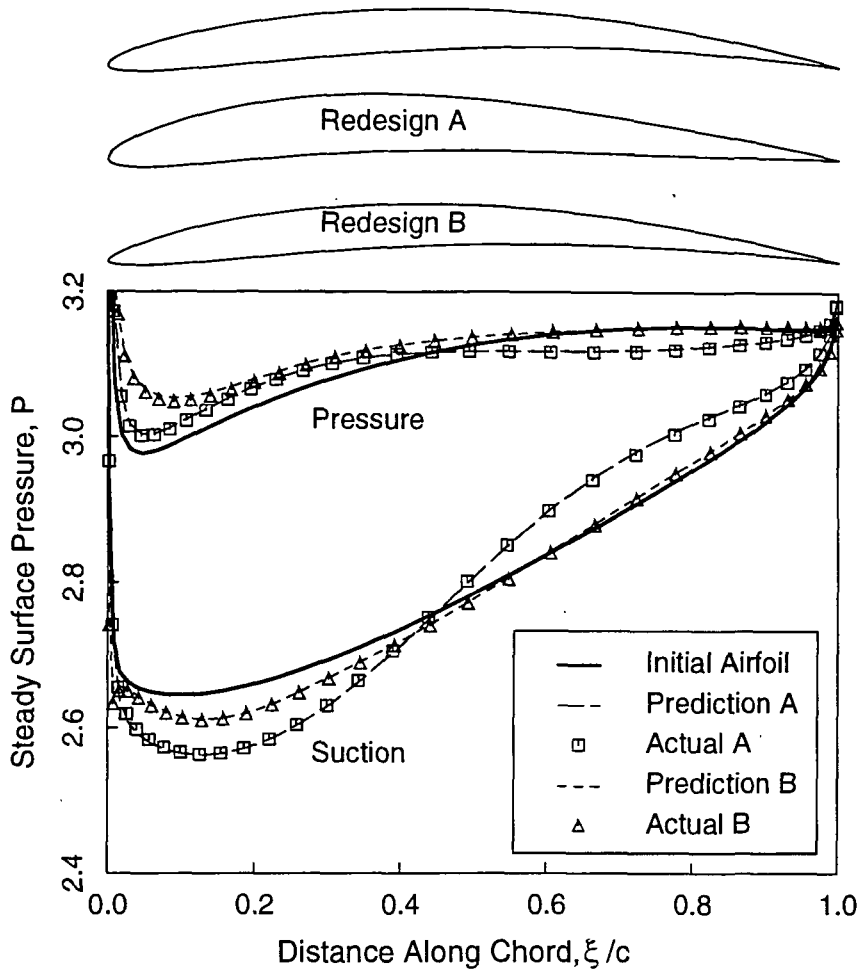

Figure 5.8: Steady surface pressure of cascade of redesigned airfoils. $M_{-\infty} = 0.5$, $\Omega_{-\infty} = 55^{\circ}$.

qualitative estimate of the actual unsteady flow behavior. The actual computed damping of the Redesign A cascade is 0.0086, indicating that the new cascade is stable. The damping of the Redesign B cascade is 0.0015, so this cascade is also stable.

At this point, it is useful to consider the accuracy of the sensitivity analysis prediction for relatively large changes in the airfoil shape. If the change in the design variables in Redesign A is considered to be one unit, Fig. 5.11 shows the change in the aerodynamic damping predicted by the sensitivity analysis and the actual change for various magnitudes of the design change. Figure 5.11 shows that the behavior of the aerodynamic damping is remarkably linear, i.e., the airfoils become physically unrealistic before substantial differences occur between the sensitivity analysis prediction and the actual airfoil behavior.

Figures 5.12 and 5.13 show the aerodynamic damping of the redesigned airfoils for a reduced frequency ω of 0.4 for a range of interblade phase angles σ. In each

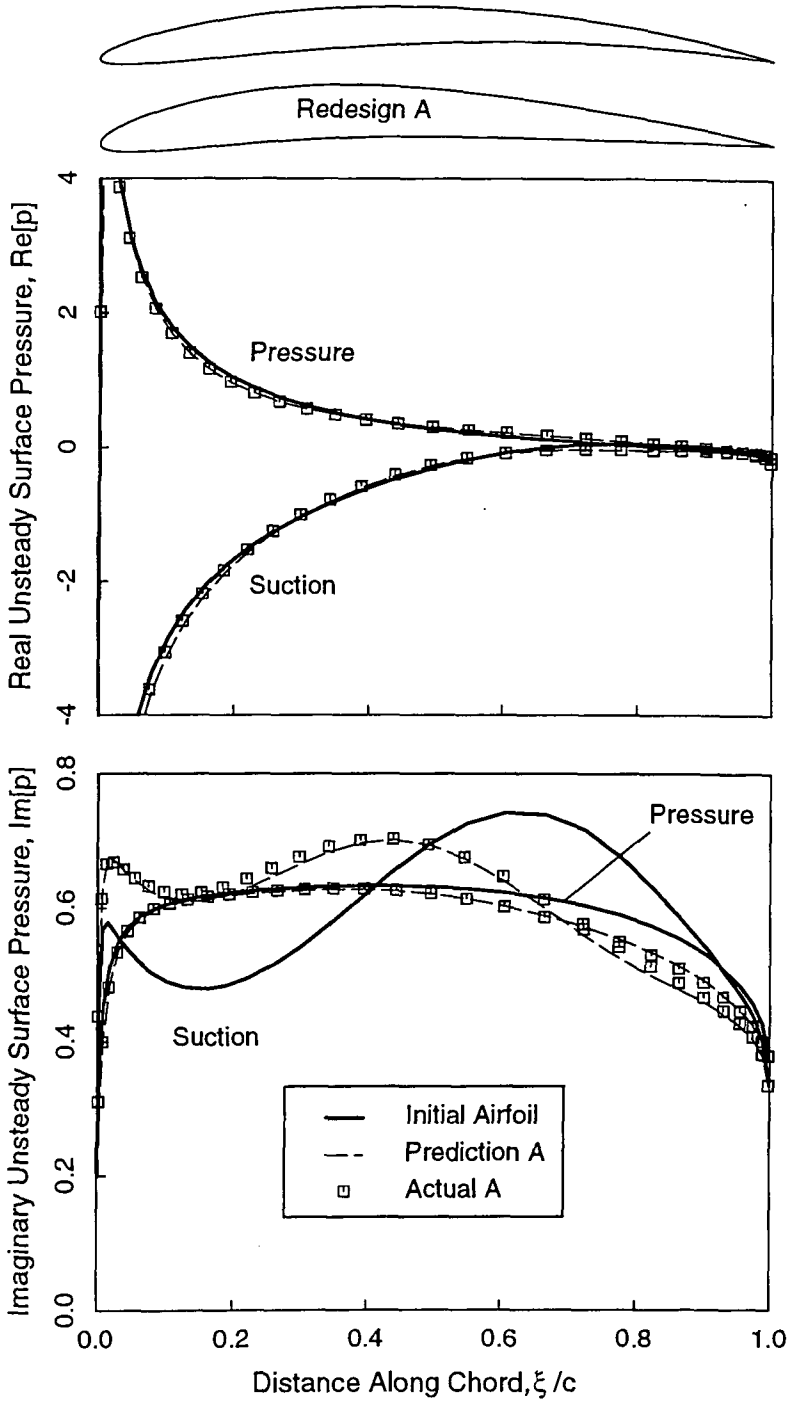

Figure 5.9: Real and imaginary parts of unsteady surface pressure of redesigned airfoils (Redesign A) pitching about their midchords. $\omega = 0.4$, $\sigma = 60°$.

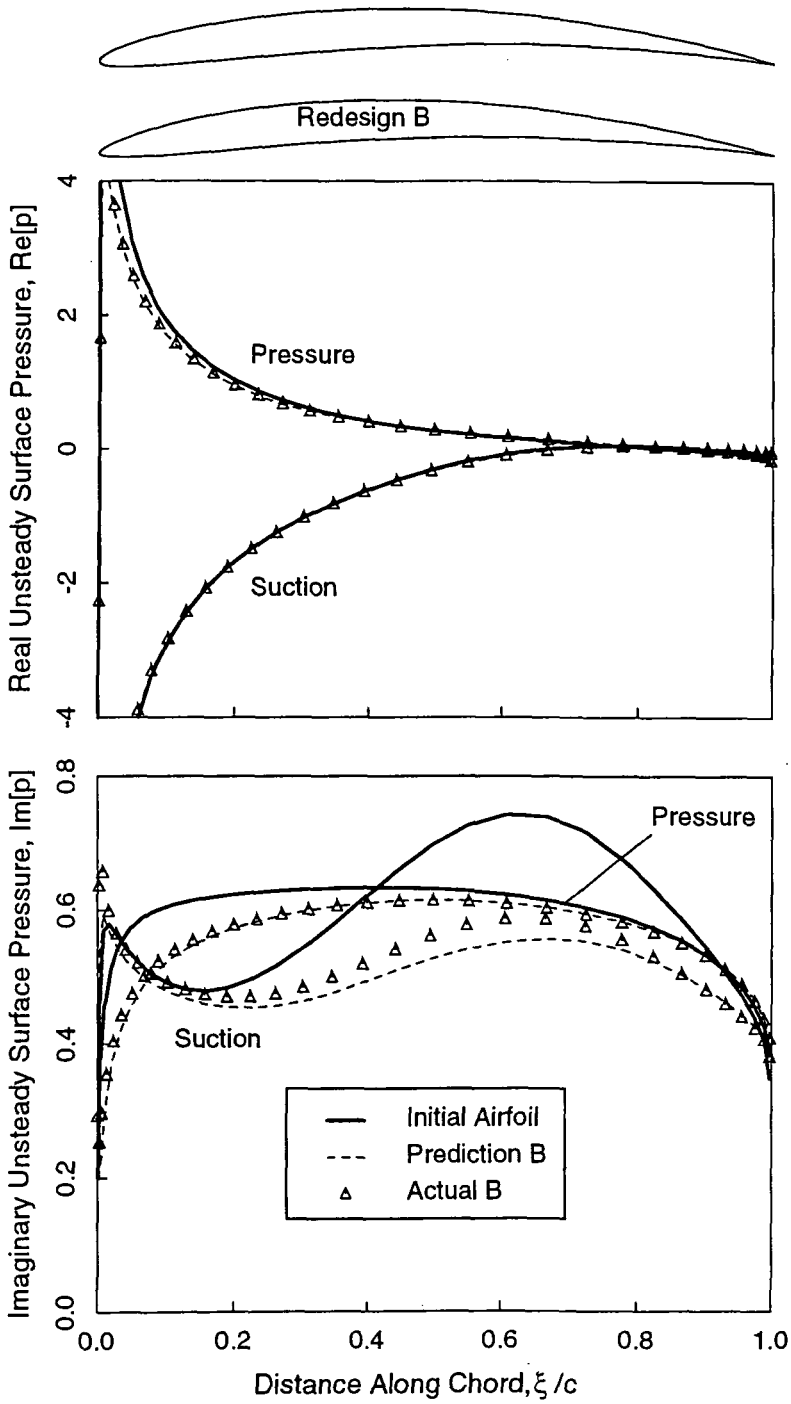

Figure 5.10: Real and imaginary parts of unsteady surface pressure of redesigned airfoils (Redesign B) pitching about their midchords. $\omega = 0.4$, $\sigma = 60°$.

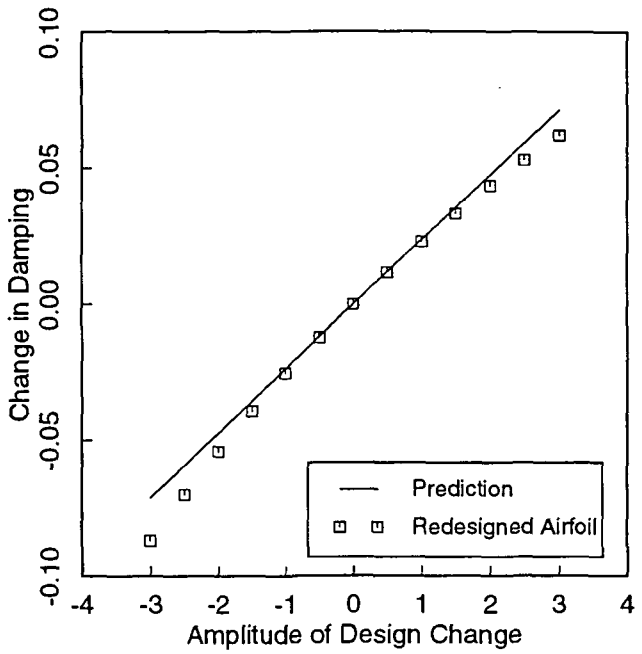

Figure 5.11: Accuracy of sensitivity analysis for various perturbation amplitudes.

figure, the original nominal damping, the damping of the redesigned airfoils predicted by the sensitivity analysis, and the actual damping of the redesigned airfoils are presented. Note that both redesigned airfoils are stable for all interblade phase angles. In addition, the sensitivity analysis prediction gives excellent estimates of the actual damping of the redesigned airfoils.

5.1.5 Computational Efficiency

Finally, a note about computational times. Table 5.4 shows the CPU time required to perform various calculations using the present method on a Silicon Graphics Indigo R4400 workstation. All time calculations were performed using a 129×49 node computational grid. The steady sensitivity analysis requires only a fraction of the CPU time necessary to perform a single nominal steady calculation. For the six design variables considered here, the unsteady sensitivity analysis required about three times the CPU time as a single nominal unsteady calculation, but only about one-fifth of what was required for a finite difference sensitivity analysis. Furthermore, the present sensitivity analysis, unlike the finite difference analysis, is not susceptible to truncation and round-off errors.

It should be noted, however, that for this aeroelastic example, the computational grid was computed independently from the steady potential, since a streamline grid is not necessary for this case. Decoupling the grid and steady flow equations significantly reduces the computational expense of the present method, as will be shown in the next section.

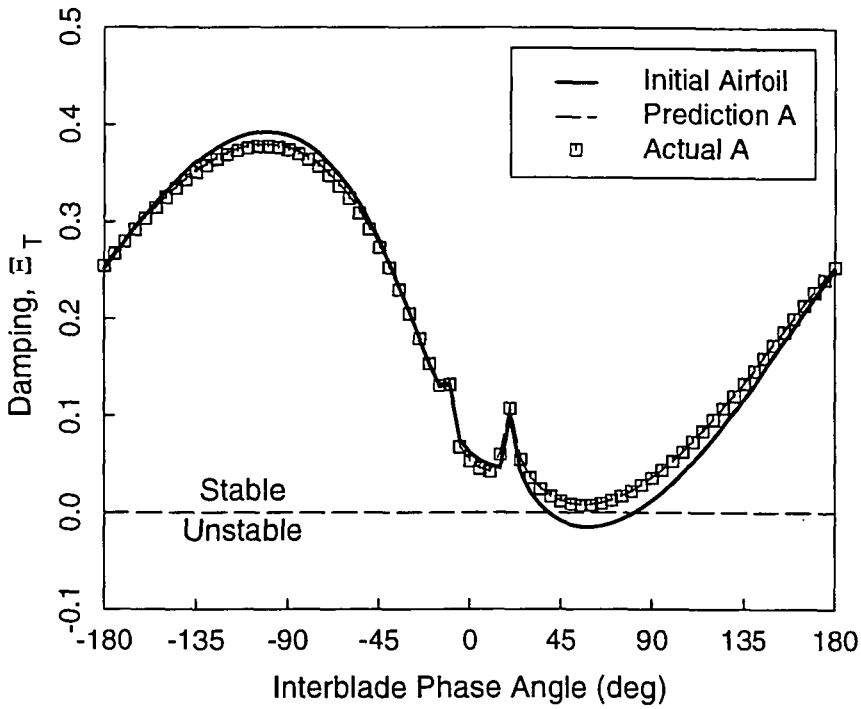

Figure 5.12: Aerodynamic damping of cascade of redesigned airfoils (Redesign A) pitching about their midchords at a frequency of 0.4 for a range of interblade phase angles.

Table 5.4: Computational times for present method using 129×49 node grid.

Procedure	CPU Time (sec)
Nominal Steady	85.3
Nominal Unsteady	12.1
Steady Sensitivity Analysis (5 var)	10.2
Unsteady Sensitivity Analysis (6 var)	30.6
Finite Difference Steady Sensitivity Analysis (5 var)	853.0
Finite Difference Unsteady Sensitivity Analysis (6 var)	145.2

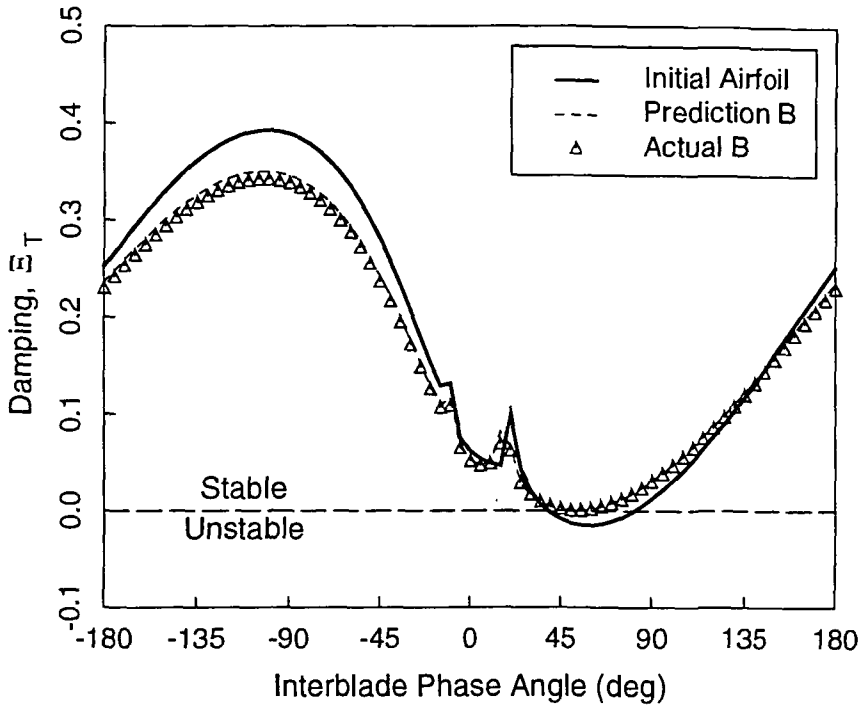

Figure 5.13: Aerodynamic damping of cascade of redesigned airfoils (Redesign B) pitching about their midchords at a frequency of 0.4 for a range of interblade phase angles.

5.2 Aeroacoustic Analysis and Design of a Fan Exit Guide Vane

To demonstrate the aeroacoustic capability of the present method, in this section a cascade of exit guide vanes (EGV) typical of those found in modern high-bypass ratio fans is analyzed. The nominal airfoil shape is a NACA 8508–65 profile. The ratio of the number of fan rotor blades to EGVs, N_R/N_V, is 0.4. The blade-to-blade gap G is 1.0, the inlet Mach number $M_{-\infty}$ is 0.5, the inlet flow angle $\Omega_{-\infty}$ is 30°, and the stagger angle Θ is 16°. The wheel speed of the upstream rotor V_{Rotor} is 1.5.

The physical system being modeled here is shown schematically in Fig. 5.14. A row of exit guide vanes (EGVs) is subjected to unsteady aerodynamic excitation arising from interaction with the viscous wakes from the upstream rotor. In the rotor (relative) frame of reference, these wakes are steady, and the steady freestream velocity is V_{Rel}. However, in the EGV (absolute) frame of reference, the wakes appear to be unsteady, and the steady freestream velocity is V_{Abs}. The two reference frames are related by the wheel speed, V_{Rotor}, due to the relative motion of the rotor.

The unsteadiness of the rotor wakes may be decomposed into harmonics with frequencies that are multiples of blade passing frequency (BPF). The BPF is referred

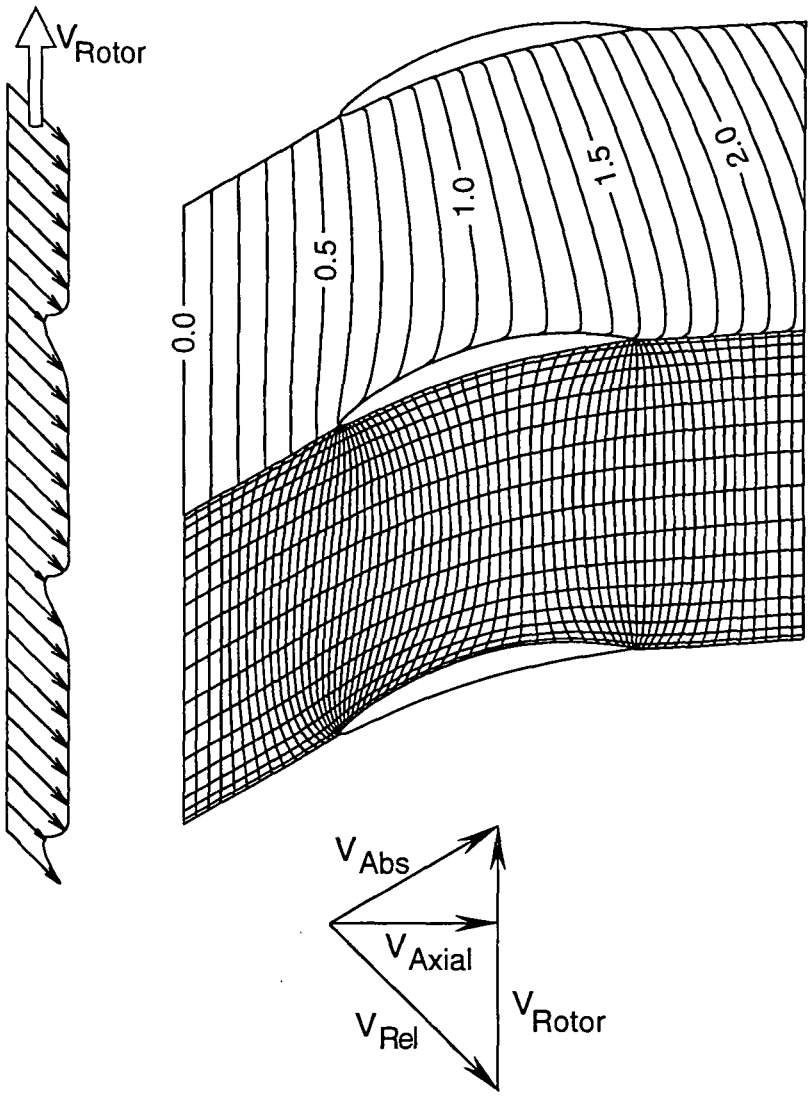

Figure 5.14: Schematic showing wake/EGV interaction. Inserts in blade passage show contours of "drift" (top) and a streamline computational grid (bottom).

to as the fundamental (i.e., 0th harmonic) frequency that the rotor wakes impinge on the stator. Typically, the number of rotor blades and stator vanes are chosen so that no pressure waves propagate ("cut-on") at this frequency. Unfortunately, it is not possible to choose the blade counts so that pressure waves do not propagate at harmonics of the BPF. Hence, the goal for this investigation is to use the sensitivity analysis to suggest design changes in the airfoil shape to reduce the magnitude of the propagating pressure waves at multiples of BPF.

5.2.1 Steady Flow Through a Fan Exit Guide Vane

First, consider the steady flow through the EGVs. The steady flow was computed using an H-grid containing 129 nodes in the streamwise direction and 49 nodes in the normal direction (a 129×49 grid). Figure 5.15 shows the nominal steady surface

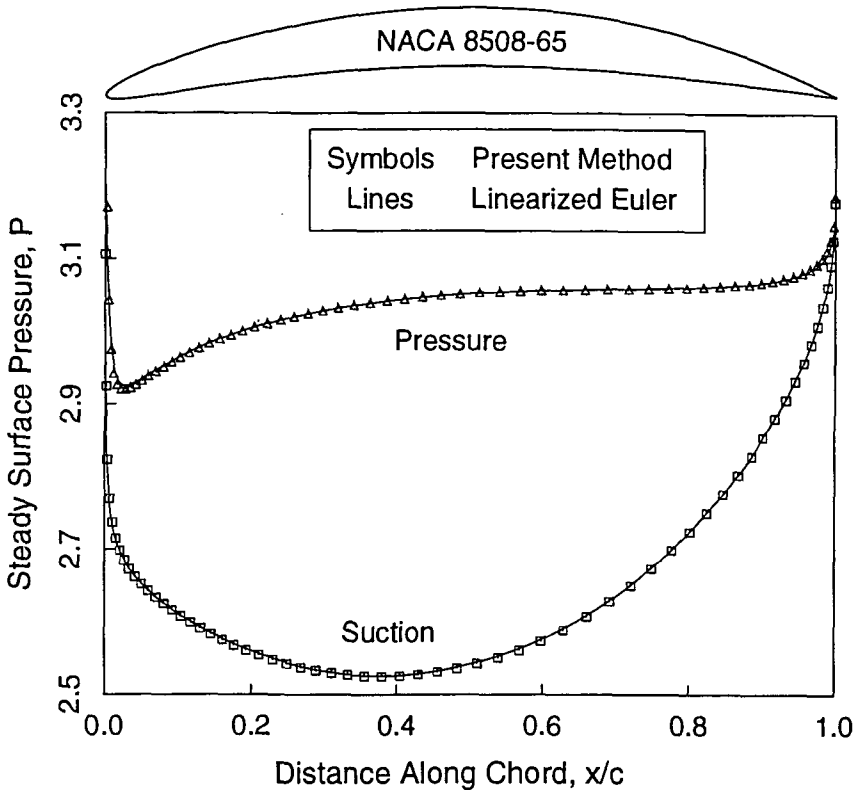

Figure 5.15: Steady surface pressure for cascade of NACA 8508–65 airfoils. $\Theta = 16°$, $\Omega_{-\infty} = 30°$, $M_{-\infty} = 0.5$, G = 1.0.

pressure P for this case. The steady lift, L, is 0.3942, and the steady drag, D, is -0.0168. The moment measured about the leading edge, M_{LE}, is -0.1837. For comparison, Fig. 5.15 also shows the grid-converged solution computed using an Euler code [30]. The excellent agreement between the two solutions, while reassuring, is to be expected since the steady flow is subsonic, irrotational, and homentropic.

5.2.2 Unsteady Flow Through a Fan Exit Guide Vane

Next, consider the acoustic response due to viscous wakes from the upstream fan impinging on the EGV. When viewed in the EGV frame of reference, the wake excitation has temporal frequencies $\omega_n = 2\pi n V_{\text{Rotor}}/G_R$, where V_{Rotor} is the wheel speed of the fan, G_R is the blade-to-blade gap of the rotor, and n takes on all integer values. Blade passing frequency (BPF) corresponds to $n = 1$. The corresponding interblade phase angles are $\sigma_n = -2\pi n G/G_R$. The acoustic response of this cascade to excitations at 1×BPF is cut-off, i.e. the unsteady pressure decays exponentially away from the EGVs. For excitations at 2×BPF, however, a single acoustic mode with interblade phase angle $\sigma = 72°$ is cut-on in the upstream and downstream regions.

In the following, the acoustic response of the EGV to 1×BPF and 2×BPF vortical gusts with "unit amplitude" are considered. A unit amplitude gust is one in which the

magnitude of the perturbation velocity normal to the steady flow direction would be unity at the leading edge of the airfoil if the steady flow were uniform and undeflected by the EGV. The real and imaginary parts of the unsteady surface pressure computed using the present analysis are shown in Figs. 5.16 and 5.17. Also shown for comparison is the pressure distribution computed using the linearized Euler analysis of Hall and Clark [30]. The agreement between these two theories is quite good, especially considering the high reduced frequency ($\omega = 7.54$) of the 2×BPF case. These results indicate that the 129×49 grid is sufficiently fine to resolve the acoustic behavior of the EGV — at least up to 2×BPF. They also indicate that the rotational velocity has been formulated and computed correctly.

Figures 5.18 and 5.19 show contours of the magnitude of the unsteady pressure for the 1×BPF and 2×BPF cases, respectively. In both cases, note that the unsteady pressure is somewhat larger in the downstream region than in the upstream region. The unsteady pressure in the far field of the 2×BPF case was Fourier transformed in the circumferential direction to determine the magnitude of the single cut-on pressure wave upstream and downstream ($\sigma = 72°$). For this case, the magnitude of the cut-on unsteady pressure wave (for a unit strength gust) is 0.102 upstream and 0.249 downstream.

5.2.3 Sensitivity Analysis

Next, the change in the steady and unsteady aerodynamic response due to small changes in the EGV geometry is considered. The steady sensitivity analysis was performed using eight different design variables. Five of these variables correspond to the modified NACA definition parameters: magnitude of thickness, maximum thickness location, magnitude of camber, maximum camber location, and leading edge radius. Two design variables define the placement of the airfoils in the cascade: the blade-to-blade gap G and stagger angle Θ. The final design variable is the reflex, which was defined earlier.

Using the steady sensitivity analysis outlined in the previous section, the sensitivity of the lift, drag, and moment to changes in the design variables were computed. These results are given in Table 5.5. Like the previous example, Table 5.5 shows that the steady work is very sensitive to changes in camber, reflex, and stagger angle. This is not too surprising since these parameters affect the trailing edge metal angle of the airfoil and hence the turning (work). On the other hand, the steady work is insensitive to changes in the maximum thickness location and the size of the leading edge radius.

Next, the sensitivities of the unsteady pressure to small changes in the design variables for the 2×BPF case were computed. In addition to the eight design variables described above, the frequency ω and interblade phase angle σ of the excitation have been added. Figures 5.20 and 5.21 show the real and imaginary parts, respectively, of the sensitivity of the unsteady surface pressure to changes in five of these design variables. Also shown are the sensitivities calculated using a finite-difference approach, i.e. the difference of the pressures calculated using the nominal analysis on two slightly different airfoils normalized by the difference in geometry. The nearly

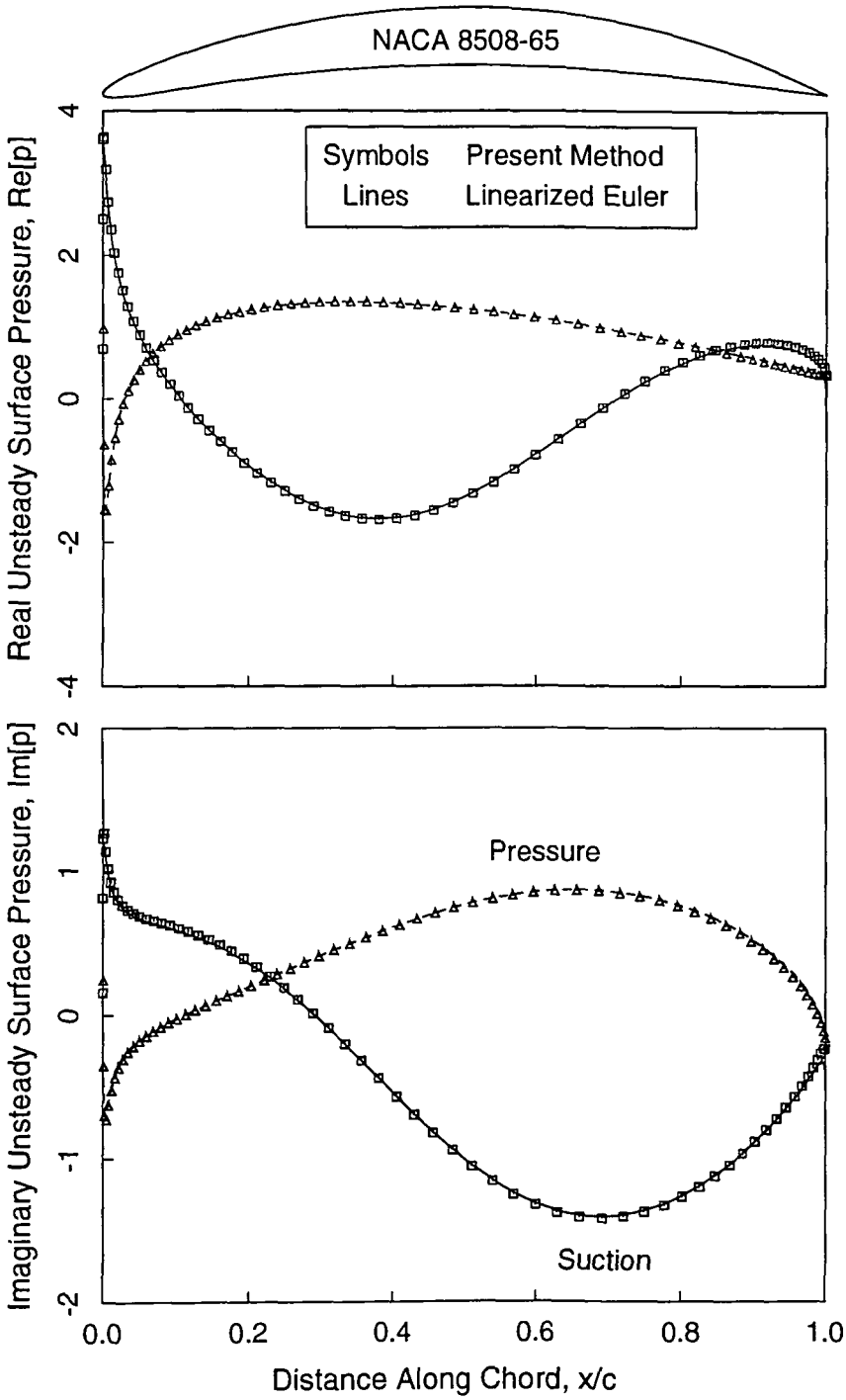

Figure 5.16: Unsteady surface pressure of cascade of NACA 8508–65 airfoils due to incoming vortical gust at $1\times$BPF. $\omega = 3.7687$, $\sigma = -144°$.

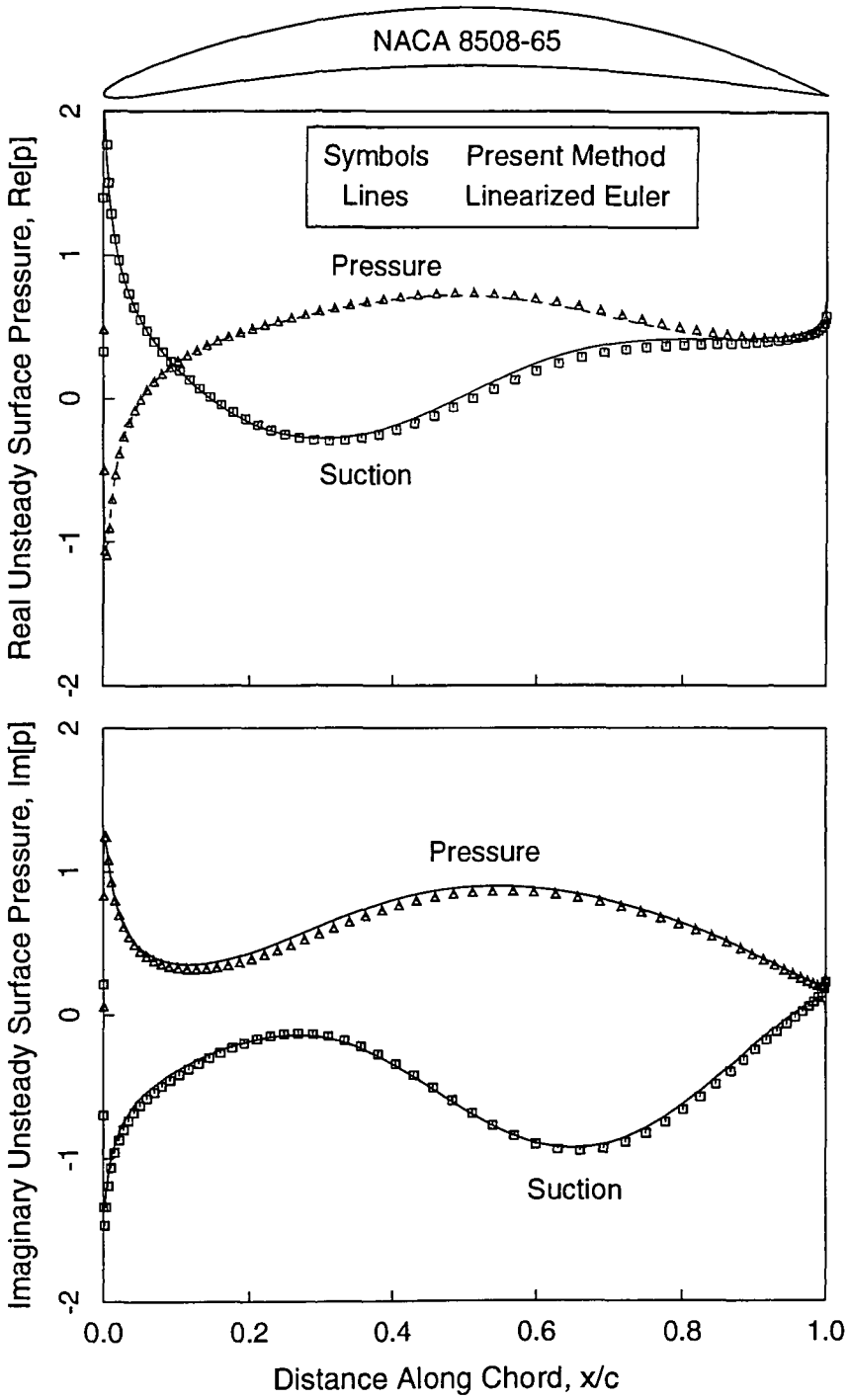

Figure 5.17: Unsteady surface pressure for cascade of NACA 8508–65 airfoils due to incoming vortical gust at 2×BPF. $\omega = 7.54$, $\sigma = -288°$.

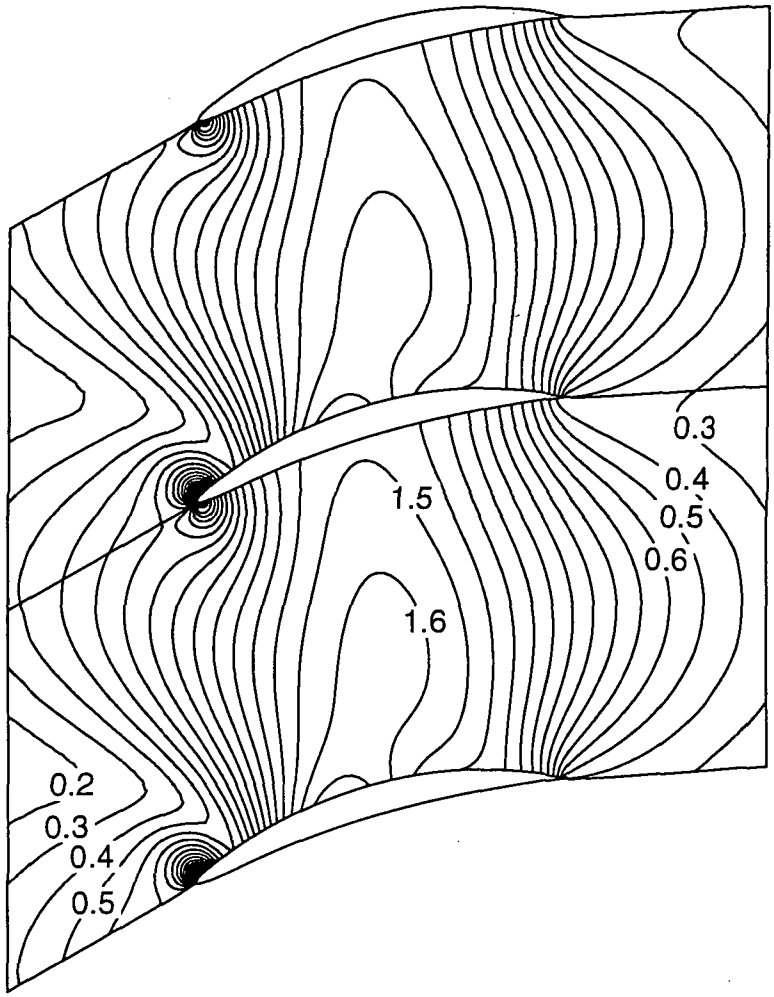

Figure 5.18: Contours of magnitude of unsteady pressure for cascade of NACA 8508–65 airfoils due to incoming vortical gust at 1×BPF. $\omega = 3.77$, $\sigma = -144°$.

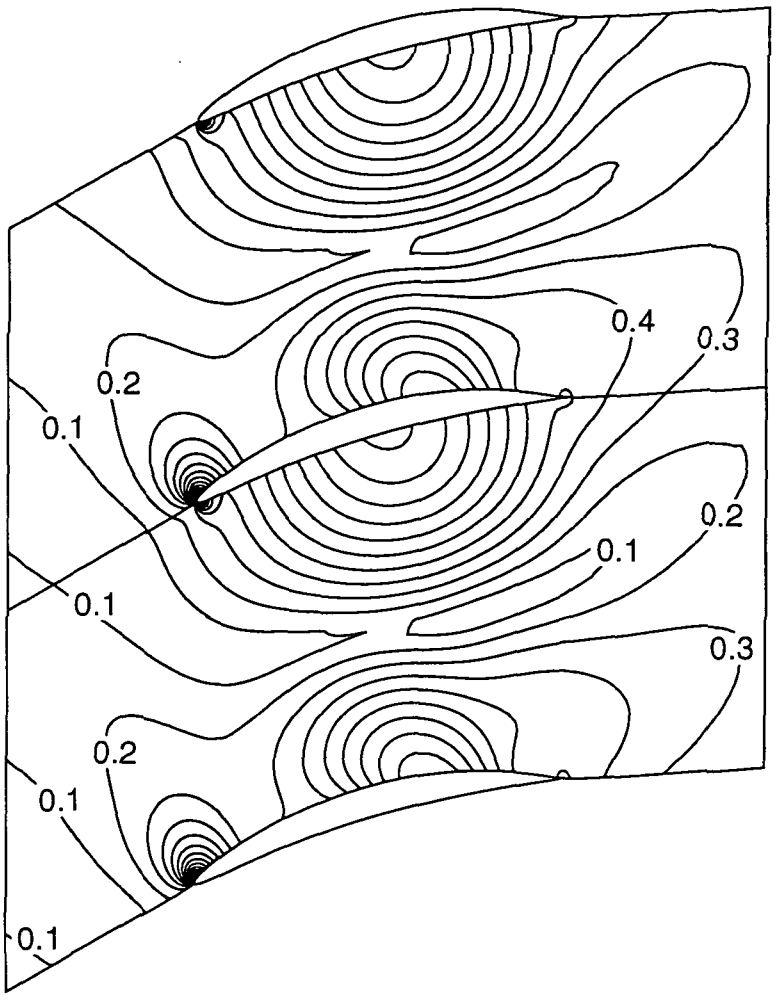

Figure 5.19: Contours of magnitude of unsteady pressure for cascade of NACA 8508–65 airfoils due to incoming vortical gust at 2×BPF. $\omega = 7.54$, $\sigma = -288°$.

Table 5.5: Change in steady flow quantities due to unit perturbations in ten design variables. The nominal steady lift, L, is 0.3942, the nominal drag, D, is -0.0168, the nominal moment about the leading edge, M_{LE}, is -0.1837, and the nominal lift in the y-direction, L_Y, is 0.3743.

Design Variable	L'_y	L'	D'	M'_{LE}
Thickness	0.0289	0.0284	0.0059	0.1751
Max Thickness Location	0.0084	0.0082	0.0017	−0.0164
Camber	1.9254	1.8941	0.3799	−1.6300
Max Camber Location	0.1991	0.1959	0.0394	−0.2154
Leading Edge Radius	0.0000	0.0000	0.0000	−0.0001
Stagger	−0.7558	−0.7266	0.2448	0.0392
Gap	0.3008	0.3220	−0.0313	−0.1123
Reflex	−2.2190	−2.1827	−0.4387	2.4383

exact agreement between the two methods demonstrates that the present sensitivity analysis has been formulated correctly.

Of particular interest in aeroacoustic applications is the influence of the blade shape on the sound radiated upstream and downstream of the EGV. The sensitivity of the magnitude of the cut-on propagating pressure waves to changes in the design variables is given in Table 5.6. The label "Unconstrained" indicates that each of the design variables is perturbed independently. Like the previous example, to compute the "Constrained" sensitivity, each of the design variables is perturbed as before, but the stagger angle and reflex are allowed to float to satisfy the constraints that the steady work and incidence angles remain fixed. Examining the "Constrained" columns in Table 5.6, it is clear for example that moving the position of the maximum camber location aft now *increases* the magnitude of the upstream pressure wave and *decreases* the magnitude of the downstream pressure wave. Note further that both the gap G and camber have a strong influence on the strength of the acoustic waves (although large changes in the gap are more realistic than large changes in camber).

5.2.4 Redesign of an EGV for Reduced Acoustic Response

Next, the constrained sensitivities were used to guide the redesign of the EGV to reduce the sound pressure levels in the downstream region. As previously noted, the camber and gap strongly influence the outgoing pressure waves. Therefore, to reduce the downstream pressure wave, the blade-to-blade gap is increased by 0.1 and the

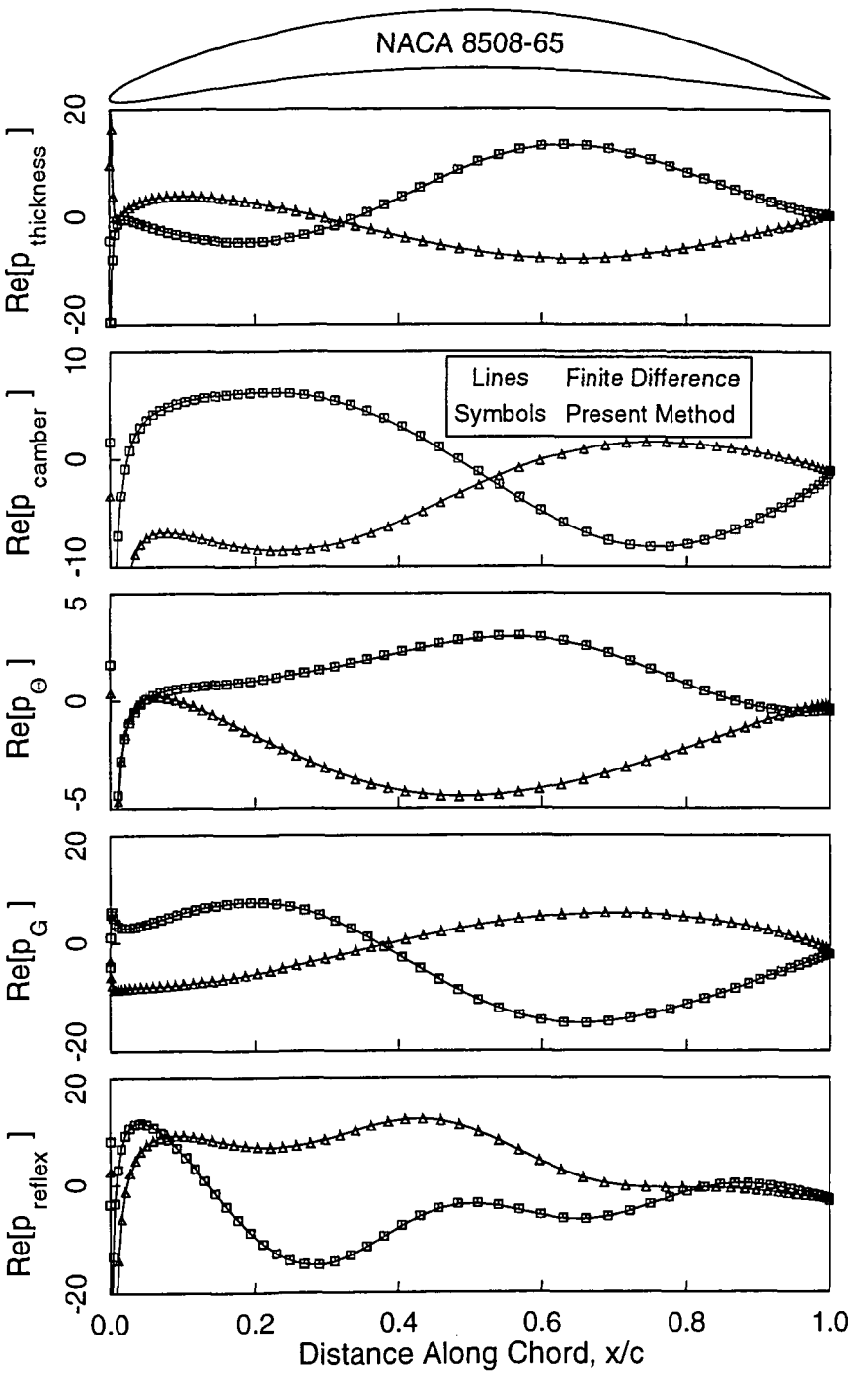

Figure 5.20: Sensitivity of unsteady surface pressure on NACA 8508–65 airfoils due to perturbations in thickness, camber, stagger, gap, and reflex. $\omega = 7.54$, $\sigma = -288°$. □, suction surface; △, pressure surface.

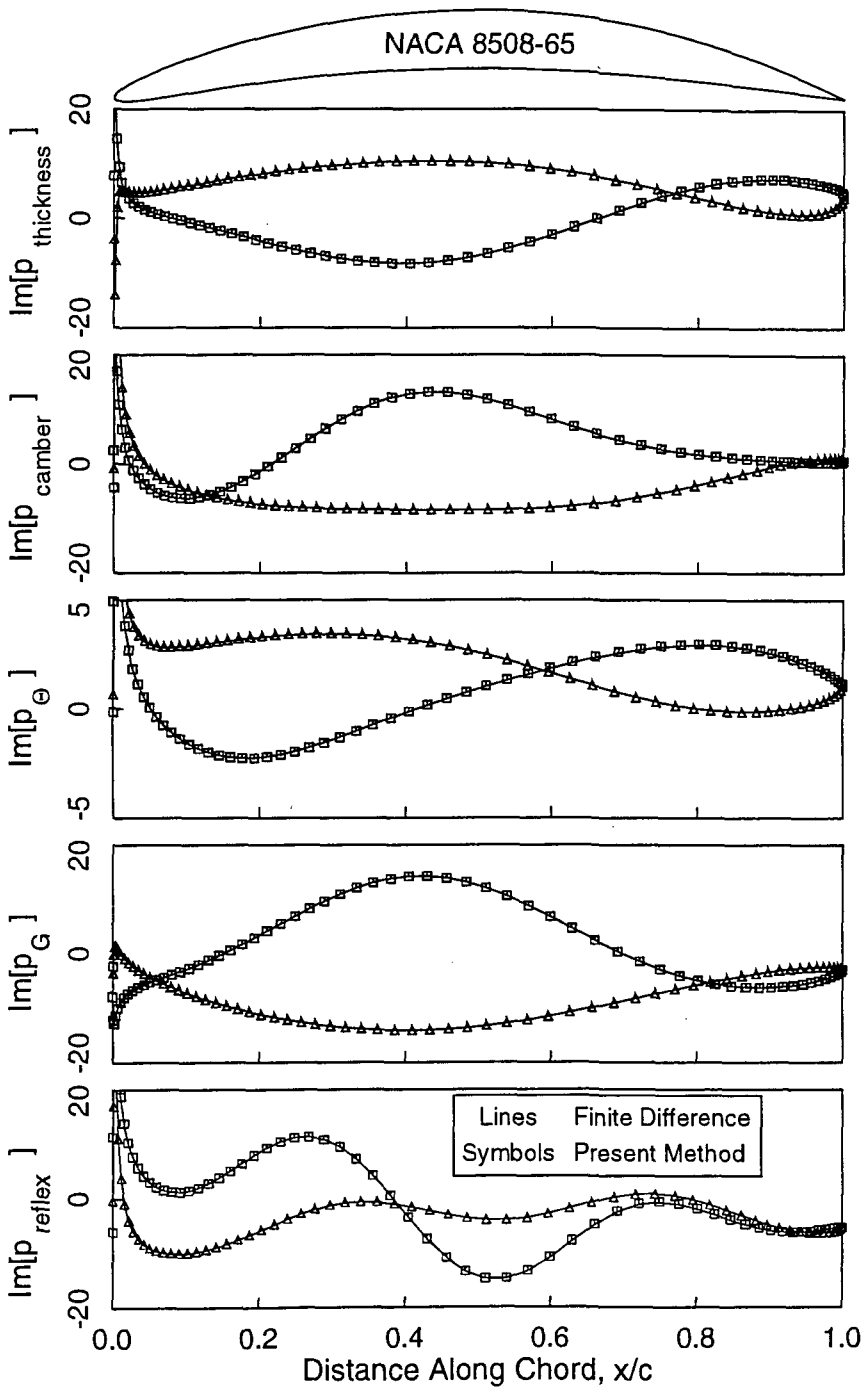

Figure 5.21: Sensitivity of unsteady surface pressure on NACA 8508–65 airfoils due to perturbations in thickness, camber, stagger, gap, and reflex. $\omega = 7.54$, $\sigma = -288°$. □, suction surface; △, pressure surface.

Table 5.6: Change in unsteady flow quantities due to unit perturbations in ten design variables. The nominal magnitude of the upstream pressure wave, $|p_{up}|$, is 0.102, and the magnitude of the downstream pressure wave, $|p_{down}|$, is 0.249.

	Unconstrained		Constrained	
Design Variable	$\|p_{up}\|'$	$\|p_{down}\|'$	$\|p_{up}\|'$	$\|p_{down}\|'$
Thickness	−0.8985	0.2494	−0.9447	0.3099
Max Thickness Location	0.0084	0.0082	−0.0810	0.1161
Camber	0.4441	−1.4103	−6.0899	6.5867
Max Camber Location	−0.1312	0.1224	0.1023	−0.0953
Leading Edge Radius	0.0023	0.0023	0.0023	0.0023
Stagger	−0.3471	0.5910	—	—
Gap	1.3244	−1.6624	1.4421	−1.8163
Reflex	1.8692	−1.5834	—	—
Frequency	0.1696	−0.2830	0.1696	−0.2830
Interblade Phase Angle	−0.0822	0.0222	−0.0822	0.0222

camber is decreased by 0.0025. To satisfy the constraints, the stagger angle, Θ, must be reduced by 2.23°, and 0.0078 units of reflex must be added. Also note that the interblade phase angle, σ, is decreased by 0.5027 radians since the interblade phase angle is proportional to the gap. For the 2×BPF case, this means that the interblade phase angle is decreased from −288° to −317°.

Figure 5.22 shows the nominal and redesigned airfoils and their respective steady surface pressure distributions. The redesigned pressure distribution was computed in two ways: first by linear extrapolation using the sensitivities, and second using the nonlinear steady flow analysis with the actual redesigned airfoil geometry. The good agreement between the two techniques shows that the present sensitivity analysis is valid for moderate changes in geometry. Also, one can see in Fig. 5.22 that the net lift has increased to account for the additional steady work done by each blade due to the increase in blade-to-blade gap.

Figure 5.23 shows the real and imaginary parts of the unsteady surface pressure for the nominal and redesigned cascade. Note that although the sensitivity analysis predicts the trends of the actual new unsteady pressure distribution, there is a significant difference in magnitude between the two curves. The reason for this difference can be explained by examining the size of the design change. Figure 5.24 shows the

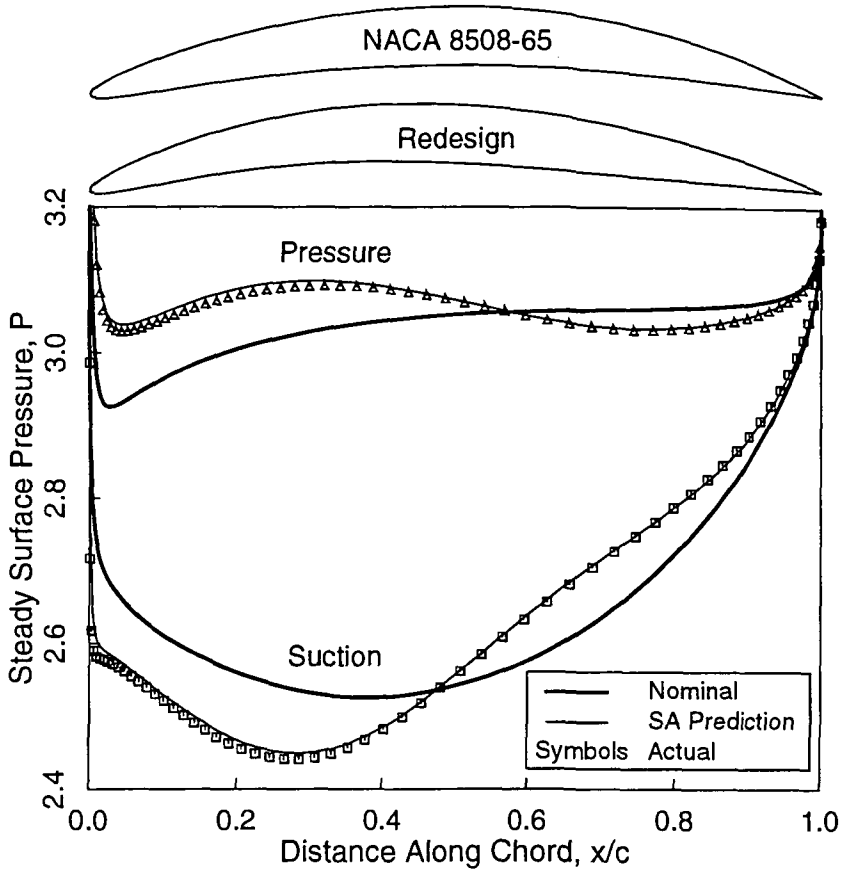

Figure 5.22: Steady surface pressure for cascade of redesigned airfoils. $M_{-\infty} = 0.5$, $\Omega_{-\infty} = 30°$.

sensitivity analysis prediction of the change in the upstream and downstream pressure waves versus the actual change for several different design change amplitudes. The design change amplitudes are normalized by the amplitude described above, i.e., the above design change is considered to have an amplitude of unity. Figure 5.24 shows that the differences between the predicted pressure distribution and the actual distribution are due to nonlinear effects that are not predicted using the present analysis. If a smaller change in the geometry had been made, the prediction would have been more accurate. Even for this large a design change, however, the sensitivity analysis still gives an excellent qualitative prediction of the change in the magnitude of propagating pressure waves.

Figures 5.25 and 5.26 show the unsteady pressure contours for the redesigned cascade for both cases. Comparing with Figs. 5.18 and 5.19, note that the downstream pressure levels have been substantially reduced, although the upstream pressure levels have been increased. For the 2×BPF case, the magnitude of the downstream pressure wave was reduced about 60%, from 0.249 to 0.099. In acoustic terms, the sound

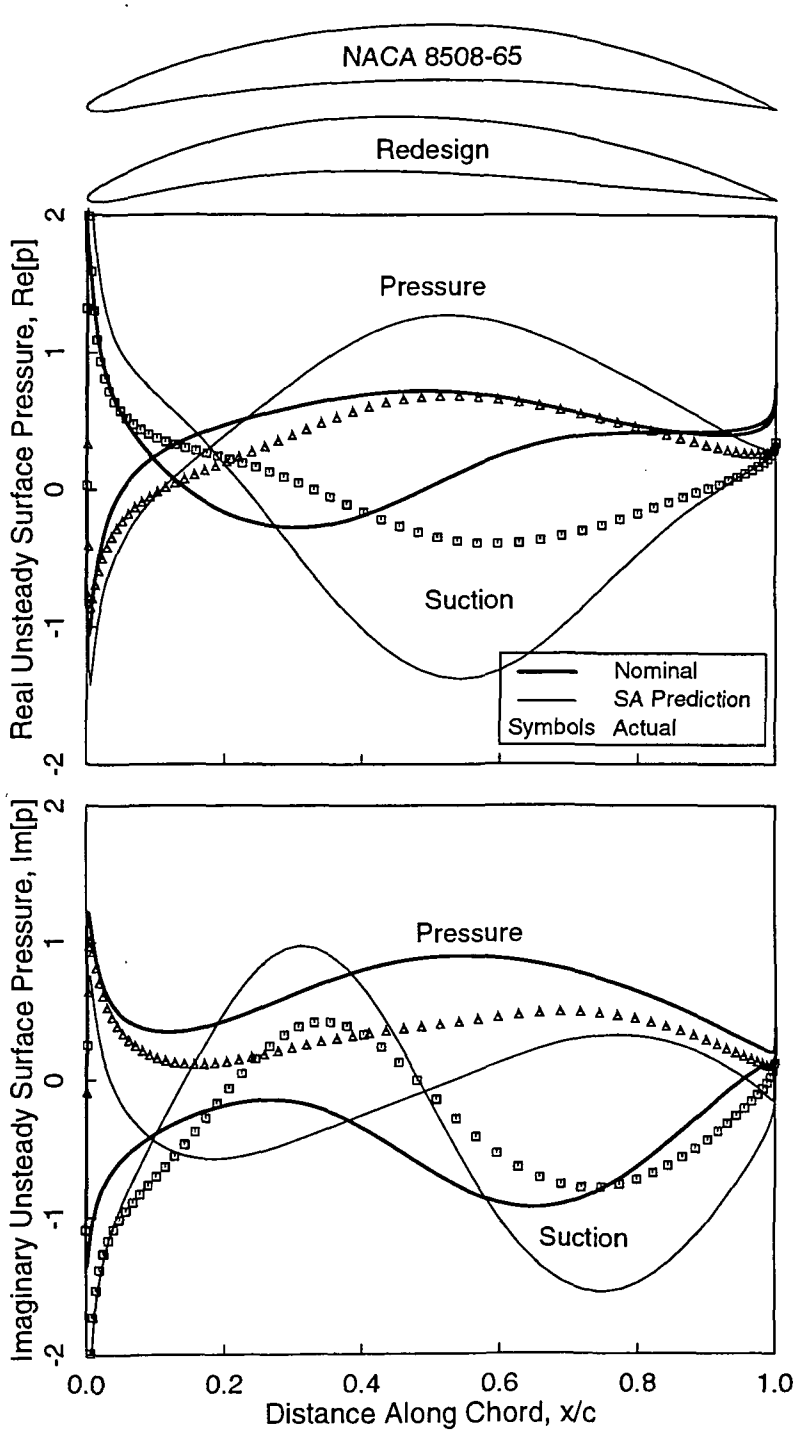

Figure 5.23: Real and imaginary parts of unsteady surface pressure for redesigned airfoils due to incident vortical gust at 2×BPF. $\omega = 7.54$, $\sigma = -317°$.

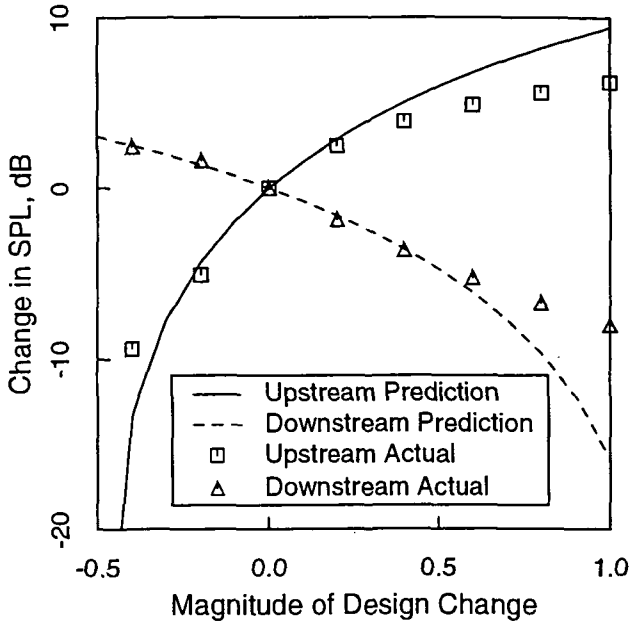

Figure 5.24: Accuracy of sensitivity analysis for various perturbation amplitudes.

pressure level (SPL) is reduced by 8.0 dB, since the change in SPL may be defined as

$$\text{Change in SPL} = 20 \log_{10} \frac{|p_{\text{redesign}}|}{|p_{\text{nominal}}|} \tag{5.13}$$

Upstream, the SPL increased from 0.102 to 0.209, an increase of 6.2 dB. Referring to Table 5.6, it is clear that in all cases perturbing one of the design variables so as to decrease to sound level downstream produces an increase in sound upstream. Thus, it is difficult in this case to simultaneously reduce the radiated noise both upstream and downstream. Some physical insight may help to explain this behavior.

At this point, it may be unclear why changing the blade shape has any effect on the radiated noise. Consider subsonic flow over an unloaded flat plate. Smith [10] showed that the magnitude of the outgoing pressure waves may be expressed by an equation of the form

$$|p| = \int_0^c [\![p(x)]\!] K(M_{-\infty}, G, \Theta, \omega, \sigma, x) dx \tag{5.14}$$

where $[\![p(x)]\!]$ is the jump in pressure at some location x on the blade surface, and K is a kernel function relating the blade load at x to the outgoing pressure. A similar expression may be used to describe the unsteady lift on the blade. Note that the kernel function is essentially only dependent on the form of the incoming gust and the steady flow conditions upstream of the airfoil. Hence, the kernel function is essentially independent of the blade shape.

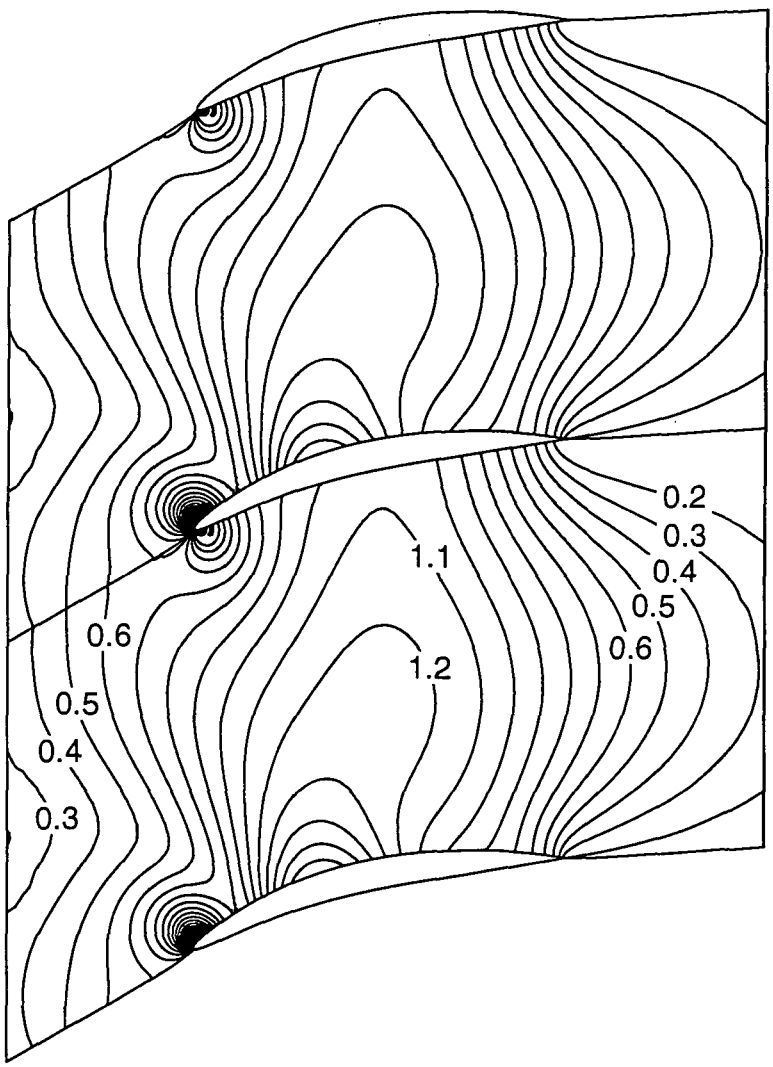

Figure 5.25: Contours of unsteady pressure for cascade of redesigned airfoils due to incoming vortical gust at 1×BPF. $\omega = 3.77$, $\sigma = -158.4°$.

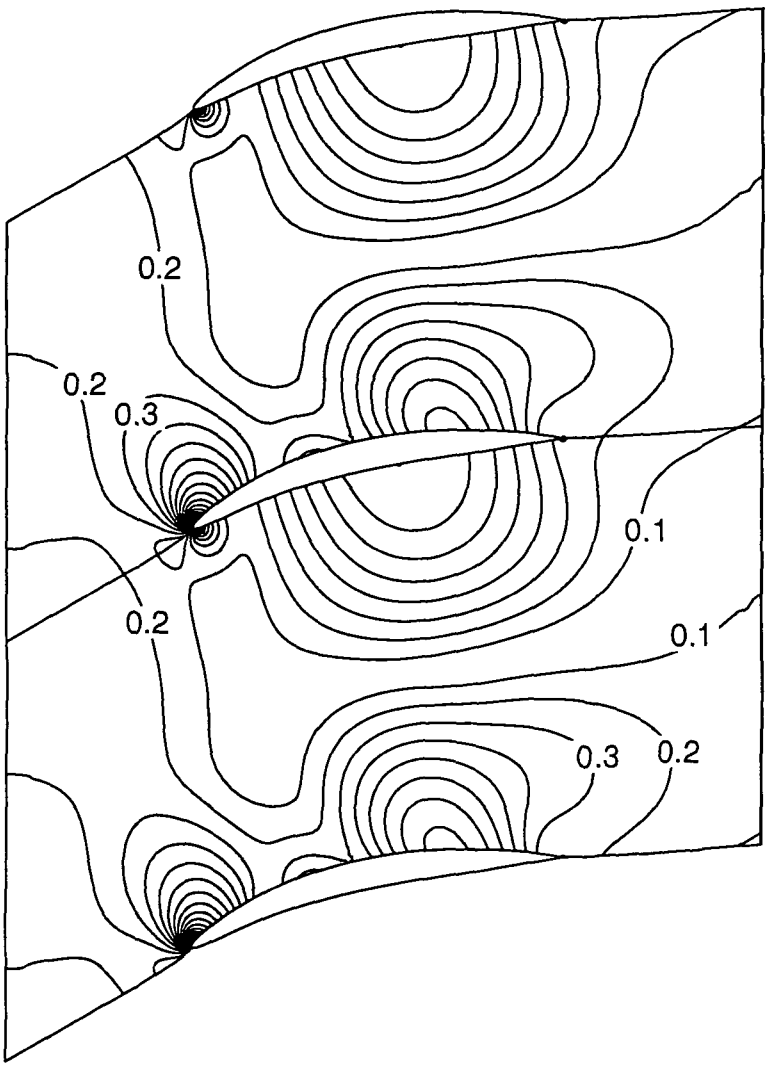

Figure 5.26: Contours of unsteady pressure for cascade of redesigned airfoils due to incoming vortical gust at 2×BPF. $\omega = 7.54$, $\sigma = -317°$.

Next, consider the discretized vector form of Eq. (5.14), i.e.,

$$\left\{ \begin{array}{c} |p_{\text{up}}| \\ |p_{\text{down}}| \\ \ell \end{array} \right\} = \left[\quad \mathbf{X} \quad \right] \left\{ \mathbf{\Gamma} \right\} \tag{5.15}$$

Here the left-hand side of Eq. (5.15) represents the blade row response to the gust, consisting of the upstream and downstream going pressure waves and the unsteady lift. The matrix [**X**] is the discretized form of the kernel function K. The vector $\mathbf{\Gamma}$ represents the discretized values of the pressure jumps along the blade surface. Assuming that the duct geometry, upstream flow conditions, and the form of the gust are fixed in the design process, the matrix [**X**], like the kernel function, is essentially independent of the blade shape. Therefore, the magnitude of the outgoing pressure waves (and the unsteady lift) is only a function of the distribution of the pressure jumps on the blade surface. Because changing the blade shape will change the distribution of the pressure jumps, the magnitudes of the pressure waves will change as a function of the airfoil shape.

The relationship between the outgoing pressure waves and blade loading may also help explain why it appears to be difficult to simultaneously reduce the magnitude of the upstream and downstream going pressure waves. The response of a cascade to an incoming gust generates acoustic radiation in the flow in the form of pressure waves. Examination of Figs. 5.17 and 5.23 shows that the magnitude of the unsteady lift is nearly the same for the nominal and redesigned airfoil. The acoustic radiation in the flow, therefore, should be nearly the same in both cases. Clearly, some of the radiation contained in the nominal propagating pressure waves has been transferred from the downstream going wave to the upstream going wave. For net noise reduction to be achieved, however, some of the radiation must be transferred into acoustic modes that do not propagate. In the present two-dimensional analysis, the energy would have to be transferred to higher Fourier modes in the circumferential direction, since the radial mode shapes are assumed to be uniform. Examination of the magnitudes of the pressure waves before and after the redesign shows that some net noise reduction has been accomplished.

The above discussion does not tell the complete acoustic story, however. First, the analysis is based an unloaded flat plate theory, while the case in question has steady loading and flow turning. Still, the analysis should be applicable in a qualitative sense. Second, and perhaps more importantly, all radial effects have been neglected. Chapter 6 contains a discussion of the three-dimensional acoustic behavior of annular ducts. The radial behavior of the pressure modes may be described by a series of orthogonal mode shapes, each of which has an associated axial wavenumber that increases with the order of the radial mode. Typically, if the pressure waves associated with a given Fourier mode propagate, the energy is contained in a small number of these radial modes. The higher order radial modes are cut-off. Hence, net noise reduction may be achieved by transferring energy from the lower, propagating radial modes to the higher, nonpropagating modes. Therefore, a three-dimensional analysis of the

Table 5.7: Computational times for present method using 129 × 49 node grid.

Procedure	CPU Time (sec)
Nominal Steady	837.0
Nominal Unsteady	12.8
Steady Sensitivity Analysis (8 var)	28.8
Unsteady Sensitivity Analysis (10 var)	61.0
Finite Difference Steady Sensitivity Analysis (8 var)	13394
Finite Difference Unsteady Sensitivity Analysis (10 var)	256

duct acoustics appears to be important to correctly predicting the radiated noise. Furthermore, shape changes along the span of the blade may have a dramatic effect on the outgoing pressure.

5.2.5 Computational Efficiency

Finally, a note about the computational times for this case. Table 5.7 shows the required computational times for the present method and for a finite difference calculation. Note that the steady flow calculation times are substantially higher than those shown in Table 5.4. In this case, the grid and steady flow equations are solved simultaneously, which increases the cost of the steady flow calculation. The time required for the unsteady flow calculation is somewhat higher due to the cost of calculating the rotational velocity, $\mathbf{v}^R$. Still, the nominal computational time is significantly less than a comparable Euler calculation, while retaining all the dominant physics of the problem. Comparing the computational times for the sensitivity analysis to the finite difference calculation, there is an even more dramatic difference in computational cost than the difference shown in Table 5.4. This indicates that the computational savings of the present sensitivity analysis greatly increases as the flow model becomes more complicated (e.g., the Euler or Navier-Stokes equations).

5.3 Modern Fan Exit Guide Vane

The final test case is a three-dimensional fan exit guide vane from a modern high-bypass ratio engine. In the previous example, we examined the acoustic response of the blade row at a single representative radius of the machine. Furthermore, in the previous example we attempted to reduce the downstream acoustic response using all of the available design variables. In this example, the objective will be to reduce the

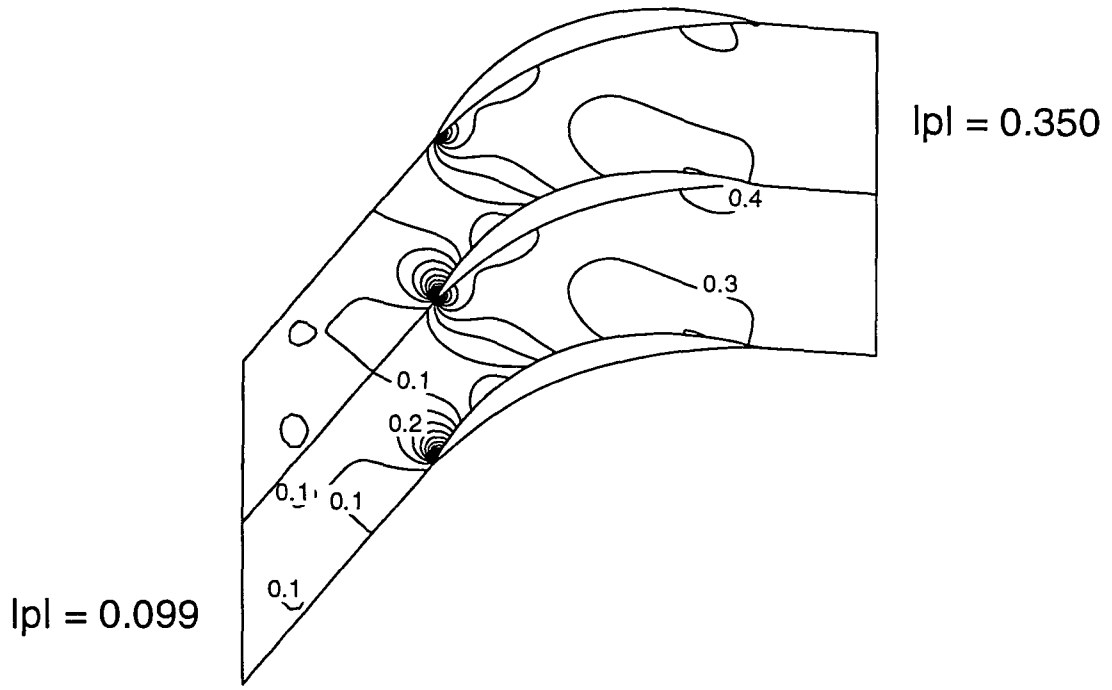

Figure 5.27: Contours of magnitude of unsteady pressure for radial station near the hub of a modern fan exit guide vane due to incoming vortical gust at 2×BPF. $M_{-\infty} = 0.32$, $G = 0.46$, $\omega = 12.5$, $\sigma = -288°$.

overall acoustic response using only variables that affect the airfoil shape (i.e., the blade-to-blade gap does not change).

5.3.1 Nominal Analysis

We will examine the acoustic response and redesign the blade shape at three representative radial locations near the hub, midspan, and tip of the vane. Because of the solid body rotation in the steady flow due to the upstream row of rotor blades, the steady and unsteady flow conditions vary along the span. For brevity, we will not examine the steady flow in detail.

Consider the unsteady flow due to rotor wakes impinging on the EGVs as in the previous section. At all radial stations, the 1×BPF pressure waves are cutoff. Figures 5.27–5.29 show contours of the magnitude of the unsteady pressure due to the vortical wakes at 2×BPF. At the radial location near the hub, the inflow Mach number, $M_{-\infty}$, is approximately 0.32, the blade-to-blade gap G is about 0.46, the reduced frequency, ω, is 12.5, and the interblade phase angle, σ, is $-288°$. Because the angular gap between the blades is constant along the span, the blade-to-blade gap increases along the span of the EGV, and the lowest value is at the hub. The Mach number in the stator frame varies, due to the relative motion of the rotor blades, from approximately 0.32 at the hub to a maximum of about 0.56 near the midspan and 0.40 near the tip. In a similar fashion, the reduced frequency has a maximum value

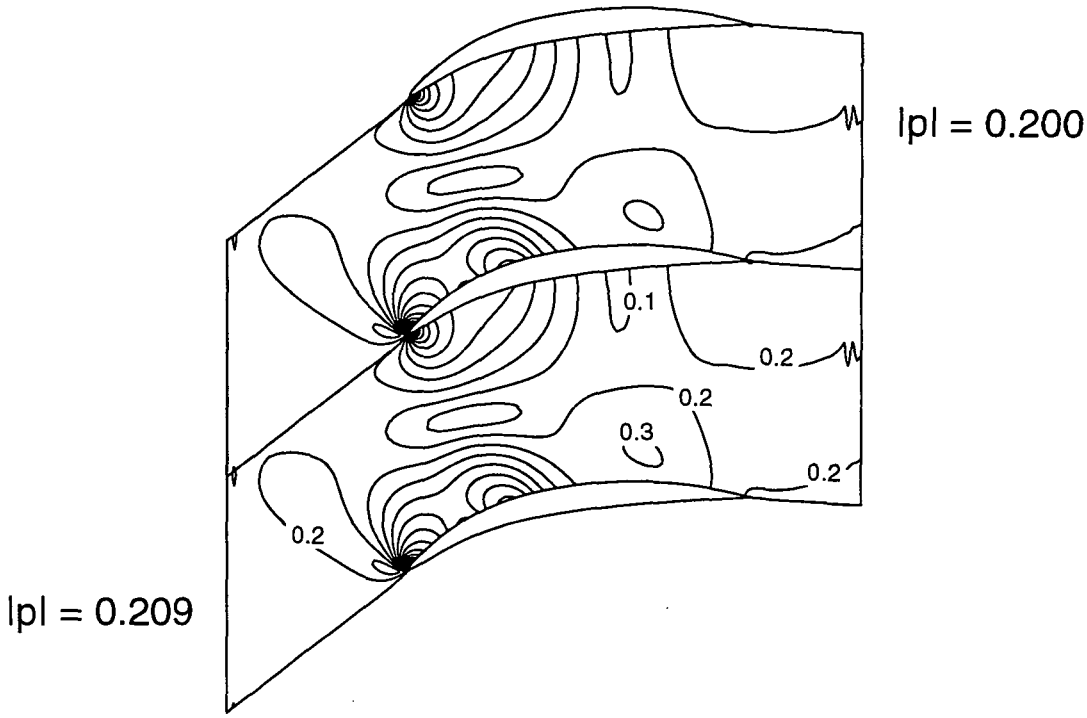

Figure 5.28: Contours of magnitude of unsteady pressure for radial station near the midspan of a modern fan exit guide vane due to incoming vortical gust at 2×BPF. $M_{-\infty} = 0.56$, $G = 0.71$, $\omega = 7.7$, $\sigma = -288°$.

near the hub of about 12.5, a minimum value near the midspan of about 7.7, and a value of about 10.4 near the tip.

Note that near the hub the magnitude of the downstream pressure wave is significantly higher than the upstream wave. At the midspan, the two waves are nearly equal in magnitude, while at the tip the downstream wave again has a larger magnitude than the upstream wave. Hence, we will primarily attempt to reduce the magnitude of the downstream pressure wave.

5.3.2 Sensitivity Analysis

Tables 5.8–5.10 show the sensitivity of the steady lift in the cascade direction and the outgoing pressure waves to perturbations in ten design variables. Note that the steady turning increases along the span so that the steady flow is nearly aligned with the axial direction after it passes through the EGVs. For the most part, the steady lift sensitivities are very similar from hub to tip, although the actual magnitudes differ. In particular, as was the case in the previous exit guide vane analysis, the steady loading is strongly influenced by changes in camber, reflex, blade-to-blade gap, and stagger.

The unsteady sensitivities are not as easily characterized. From the "constrained" sensitivities, it is clear that thickness and camber play a significant role in the acoustic

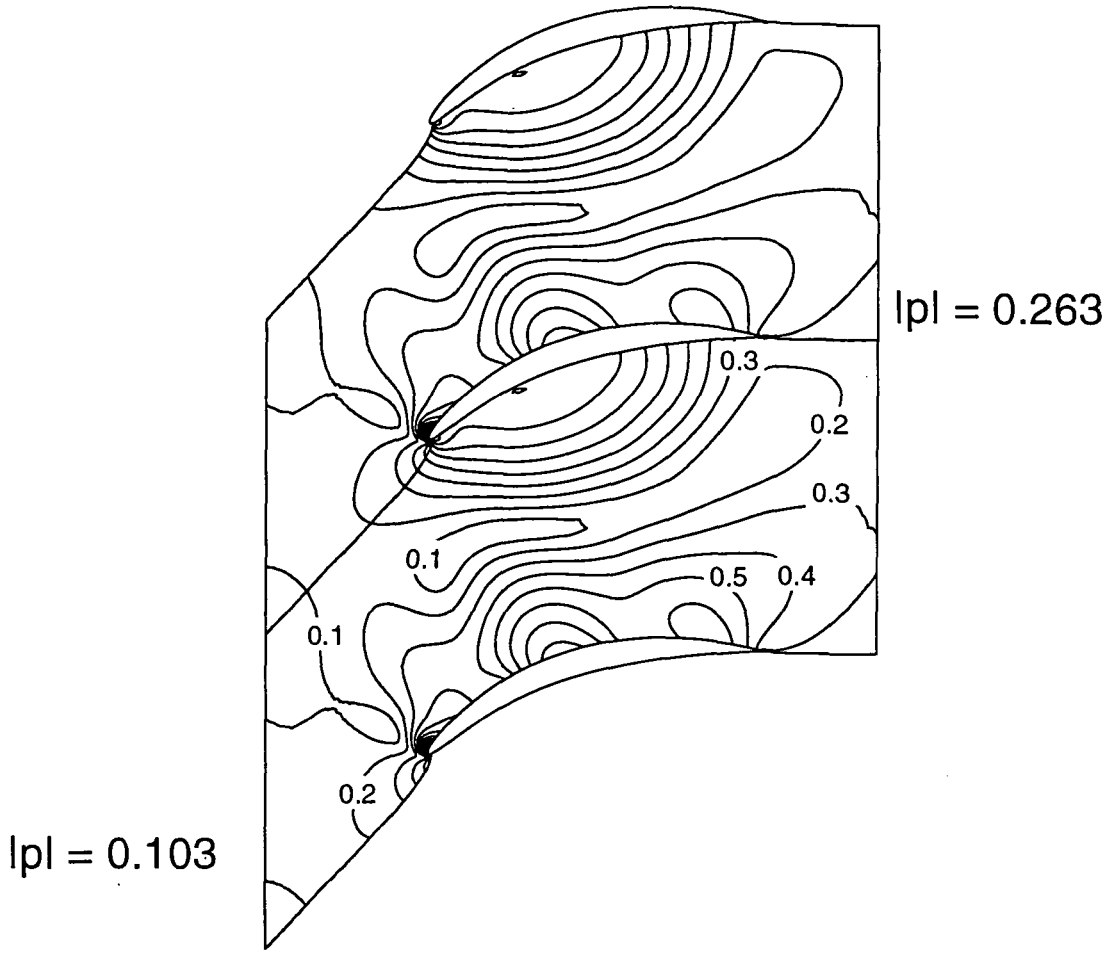

Figure 5.29: Contours of magnitude of unsteady pressure for radial station near the tip of a modern fan exit guide vane due to incoming vortical gust at 2×BPF. $M_{-\infty} = 0.40$, $G = 0.90$, $\omega = 10.4$, $\sigma = -288°$.

response of the EGV at all three radial locations. Also, changing the leading edge radius and maximum thickness location of the blade results in a moderate change in the acoustic response, considering that the leading edge radius has virtually no effect on the steady loading. As a result, the "unconstrained" and "constrained" sensitivities due to changes in maximum thickness location and leading edge radius are nearly the same.

Note that there does not appear to be a clear pattern to indicate the reason for the "trade-off" phenomena between the upstream and downstream pressure waves encountered here and in the previous section. For example, changes in camber at the hub and midspan require some trade-off between the two pressure waves, while at the tip, the magnitude of both pressure waves may be reduced. The lack of consistent behavior along the span may further indicate that three-dimensional effects play an important role in the overall acoustic response of a blade row, as discussed in the previous section.

Table 5.8: Change in steady and unsteady flow quantities due to unit perturbations in ten design variables near the hub of a modern fan exit guide vane. The nominal lift in the cascade direction, L_y, is 0.4425, the nominal magnitude of the upstream pressure wave, $|p_{\text{up}}|$, is 0.099, and the magnitude of the downstream pressure wave, $|p_{\text{down}}|$, is 0.350.

		Unconstrained		Constrained	
Design Variable	L'_y	$\|p_{\text{up}}\|'$	$\|p_{\text{down}}\|'$	$\|p_{\text{up}}\|'$	$\|p_{\text{down}}\|'$
Thickness	0.0253	0.4339	0.3562	0.4292	0.3937
Max Thick. Location	0.0009	0.0353	0.0133	0.0351	0.0147
Camber	1.1135	0.1606	1.0434	−0.6320	3.9260
Max Camber Location	0.2333	−0.1498	−0.0747	−0.0115	−0.1116
Leading Edge Radius	0.0000	0.0010	−0.0018	0.0010	−0.0018
Stagger	−0.3880	0.0591	0.2987	—	—
Gap	0.5000	−0.0607	0.3196	−0.0526	0.2553
Reflex	−1.7127	0.5068	0.8007	—	—
Frequency	—	0.0341	−0.0503	0.0341	−0.0503
Interblade Phase Ang.	—	0.0609	−0.5775	0.0609	−0.5775

5.3.3 Redesign of EGV for Reduced Acoustic Response

Using the sensitivities contained in Tables 5.8–5.10, we now attempt to reduce the acoustic response using changes in the airfoil shape. As noted earlier, in this example we will only change the airfoil shape — changes in the blade-to-blade gap will not be considered.

At the station near the hub, the leading edge radius was substantially increased, along with a small increase in the maximum camber location. The thickness, camber, and maximum thickness location were all decreased slightly. Figure 5.30 shows contours of unsteady pressure for the redesigned airfoil near the hub. In this case, the downstream SPL was reduced by 1.0 dB at the expense of a 2.0 dB increase in the upstream SPL. Because the magnitude of the downstream pressure wave is significantly larger than the upstream wave, we consider this to be a reasonable trade-off.

At the station near the midspan, the leading edge radius and maximum camber location were also increased, as well as the thickness. The camber and maximum thickness location were decreased. Figure 5.31 shows contours of unsteady pressure for the redesigned airfoil near the midspan. In this case, net noise reduction was

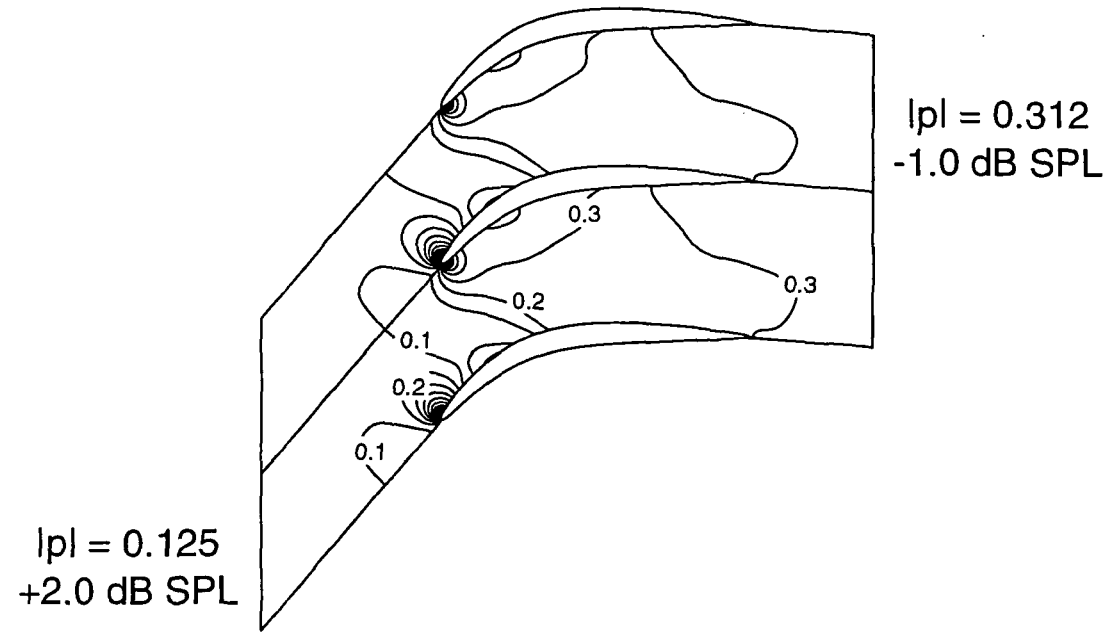

Figure 5.30: Contours of magnitude of unsteady pressure for radial station near the hub of a redesigned modern fan exit guide vane due to incoming vortical gust at 2×BPF. $M_{-\infty} = 0.32$, $G = 0.46$, $\omega = 12.5$, $\sigma = -288°$.

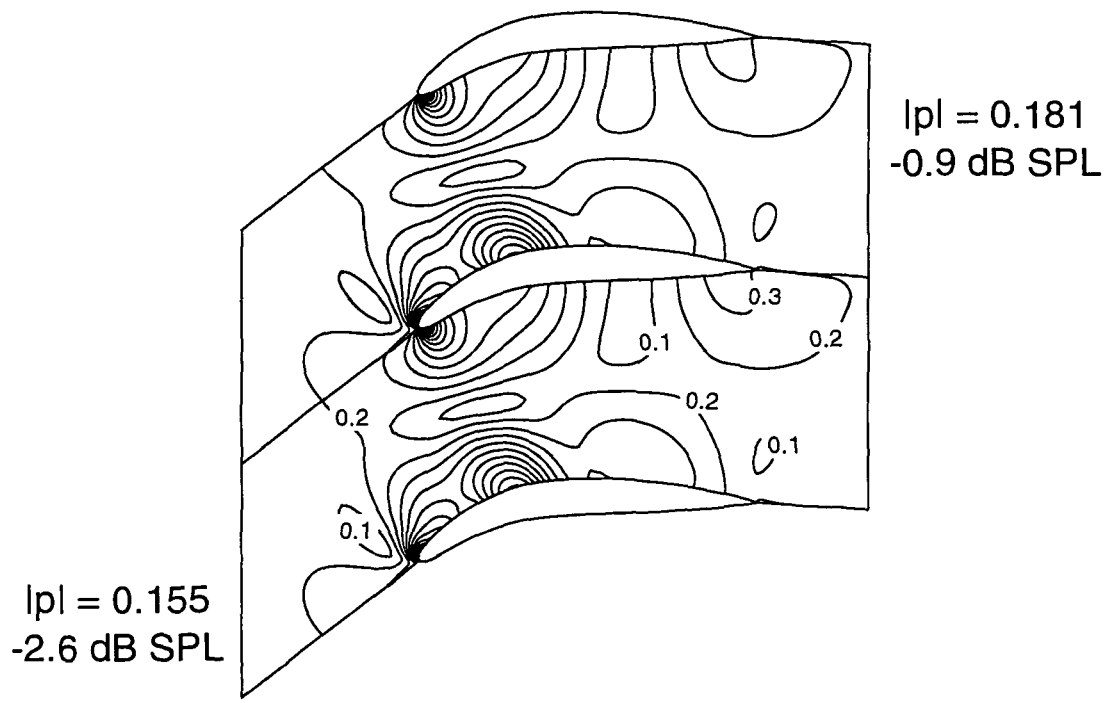

Figure 5.31: Contours of magnitude of unsteady pressure for radial station near the midspan of a redesigned modern fan exit guide vane due to incoming vortical gust at 2×BPF. $M_{-\infty} = 0.56$, $G = 0.71$, $\omega = 7.7$, $\sigma = -288°$.

Table 5.9: Change in steady and unsteady flow quantities due to unit perturbations in ten design variables near the midspan of a modern fan exit guide vane. The nominal lift in the cascade direction, L_y, is 0.6579, the nominal magnitude of the upstream pressure wave, $|p_{\text{up}}|$, is 0.209, and the magnitude of the downstream pressure wave, $|p_{\text{down}}|$, is 0.200.

		Unconstrained		Constrained	
Design Variable	L'_y	$\|p_{\text{up}}\|'$	$\|p_{\text{down}}\|'$	$\|p_{\text{up}}\|'$	$\|p_{\text{down}}\|'$
Thickness	0.0843	−0.2852	−0.1564	−0.3208	−0.0647
Max Thick. Location	0.0077	−0.0262	0.0106	−0.0294	0.0190
Camber	2.2503	−0.3106	0.9183	−2.3070	6.5816
Max Camber Location	0.3090	−0.2830	0.0384	−0.1242	−0.5140
Leading Edge Radius	0.0000	−0.0023	−0.0004	−0.0023	−0.0004
Stagger	−0.8514	−0.1605	0.3151	—	—
Gap	0.4932	−0.2381	0.2108	−0.2155	0.1526
Reflex	−3.5867	−0.2646	0.0623	—	—
Frequency	—	−0.1082	−0.0319	−0.1082	−0.0319
Interblade Phase Ang.	—	−0.7778	−0.0655	−0.7778	−0.0655

achieved, by 0.9 dB downstream and 2.6 dB upstream.

At the station near the tip, again the leading edge radius and maximum camber location were increased. Also, the thickness and camber were slightly increased, and the maximum thickness location was decreased. Figure 5.32 shows contours of unsteady pressure for the redesigned airfoil near the tip. A small trade-off was made here, decreasing the downstream SPL by 1.4 dB while increasing the upstream SPL by 0.6 dB.

Finally, it is clear that the reduction in acoustic response is not as dramatic as the reduction achieved in the previous example. One reason for the small reduction is that the blade-to-blade gap was held fixed in this example. Although the sensitivities shown in Tables 5.8–5.10 indicate that the gap only plays a moderate role in the acoustic response, the sensitivities alone do not completely illustrate the role the gap plays in the redesign process. Changing the gap also moderates the constraint relationship between the camber and reflex so that larger changes in camber may be employed, thereby achieving greater noise reduction. Changing the airfoil shape alone appears to have only a moderate effect on the radiated noise, at least in the

Table 5.10: Change in steady and unsteady flow quantities due to unit perturbations in ten design variables near the tip of a modern fan exit guide vane. The nominal lift in the cascade direction, L_y, is 0.8140, the nominal magnitude of the upstream pressure wave, $|p_{\text{up}}|$, is 0.103, and the magnitude of the downstream pressure wave, $|p_{\text{down}}|$, is 0.263.

		Unconstrained		Constrained	
Design Variable	L'_y	$\|p_{\text{up}}\|'$	$\|p_{\text{down}}\|'$	$\|p_{\text{up}}\|'$	$\|p_{\text{down}}\|'$
Thickness	0.0921	1.2871	−1.6826	1.2239	−1.8322
Max Thick. Location	0.0122	0.0782	0.0534	0.0698	0.0335
Camber	1.9340	−0.5630	−0.2809	−3.2040	−6.6747
Max Camber Location	0.2967	−0.0227	−0.0706	0.1325	0.3363
Leading Edge Radius	−0.0002	0.0008	−0.0025	0.0009	−0.0021
Stagger	−0.7708	−0.2338	−0.5205	—	—
Gap	0.4326	−0.8044	1.4336	−0.7506	1.5608
Reflex	−2.4583	0.1682	0.6038	—	—
Frequency	—	−0.2758	0.2425	−0.2758	0.2425
Interblade Phase Ang.	—	−0.8420	0.5372	−0.8420	0.5372

present two-dimensional analysis.

5.4 Summary

Although extensive parametric studies have not been performed, the results presented in this chapter point to some possible general trends. It appears that the effectiveness of the sensitivity analysis increases with reduced frequency. The redesign of the aeroacoustic examples resulted in a much larger change in the unsteady aerodynamic behavior than the aeroelastic example. This may be due to the difference in frequency (an order of magnitude) between the two cases. At high frequencies, the wavelengths of the unsteady waves are shorter, and therefore are more dependent on the airfoil shape.

An interesting result from the first aeroacoustic example was that there appears to be a trade-off between noise reduction upstream and downstream. In other words, it may be difficult to achieve global noise reduction for a particular operating condition. The analysis appears to be better suited to cases where there is a noise problem either

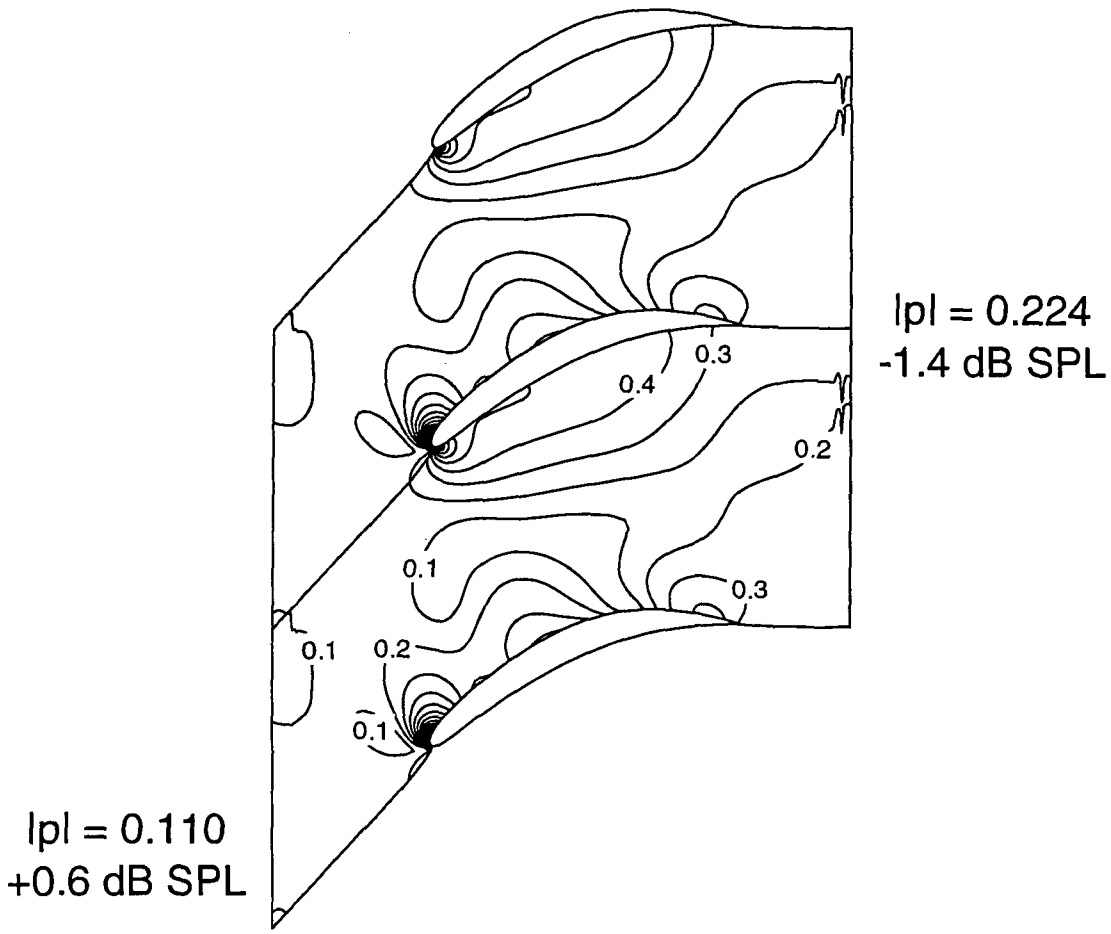

Figure 5.32: Contours of magnitude of unsteady pressure for radial station near the tip of a redesigned modern fan exit guide vane due to incoming vortical gust at 2×BPF. $M_{-\infty} = 0.40$, $G = 0.90$, $\omega = 10.4$, $\sigma = -288°$.

upstream or downstream of the blade row, but not both. An analysis using subsonic flat plate theory described a possible reason for this trade-off between the upstream and downstream radiated noise, and concluded that three-dimensional effects may play a large role in the accurate prediction of the outgoing pressure.

In all three cases, the steady loading on the redesigned airfoil was moved forward, with an increase in the steady pressure gradient on the surface. This points to the need for a viscous version of this analysis, so that the increase in steady aerodynamic losses can be quantified.

Finally, the computational efficiency of the analysis indicates that the computational savings greatly increases with the complexity of the flow model. Consequently, the results presented here would be even more impressive if a Euler or Navier-Stokes analysis had been used.

Chapter 6

Application to Three-Dimensional Problems

Although the preceding development is well-suited to the design and analysis of two-dimensional cascades, it is not entirely obvious how to analyze an actual three-dimensional blade row using this method. This chapter provides a framework for analyzing three-dimensional aeroacoustic problems using the present two-dimensional procedure. Section 6.1 contains a discussion of the general three-dimensional problem and the importance of the annular nature of the geometry. In addition, an analytical procedure for calculating the natural acoustic modes of an annular duct will be developed. Next, Section 6.2 contains a discussion of how the unsteady pressure at the far field of a three-dimensional blade row may be calculated. Finally, in Section 6.3, a general method for calculating the magnitude of the outgoing three-dimensional pressure waves in the far field from the computed two-dimensional unsteady potential will be described. Also, the application of the sensitivity analysis to the calculation procedure described in this chapter will be discussed.

6.1 Acoustic Modes in an Annular Duct

The fluid in an axial flow turbomachine is typically modeled as flow through an annular duct. A schematic of such a duct is shown in Figure 6.1. The duct has an inner (or hub) radius, r_H, and an outer (or tip) radius, r_T. A key parameter defining the duct geometry is the so-called hub-to-tip ratio, r_H/r_T. As this ratio approaches unity, the flow becomes nearly two-dimensional. For lower hub-to-tip ratios, however, annular effects become more significant.

The first step in analyzing the three-dimensional acoustic behavior of a blade row is to examine the natural acoustic modes in an annular duct such as the one shown in Figure 6.1. For a completely general steady flow, this would be a formidable problem to solve analytically. Fortunately, the steady flow field is relatively uniform away from the blade row (i.e., the far field). Furthermore, in this analysis, all streamtube contraction effects are neglected, i.e., the hub and tip radii are constants along the axis of the turbomachine. It is also assumed that there is no radial component of the

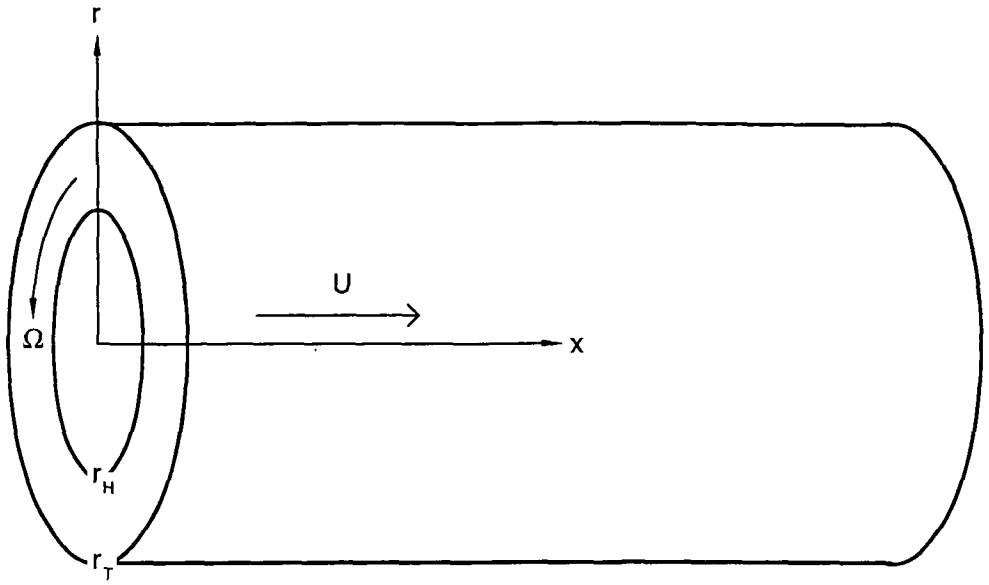

Figure 6.1: Annular duct geometry.

steady flow.

For steady flows without swirl, a classic analysis of acoustic modes in annular ducts applied to axial flow turbomachines was performed by Tyler and Sofrin [62]. The following analysis, to a large extent, will follow their approach. It is assumed that the steady flow is entirely axial, with velocity U. Instead of using a reference frame fixed in space, however, it will be convenient to solve for the acoustic modes in a reference frame attached to the steady flow field, i.e., the relative steady fluid motion is zero. In this case, the unsteady pressure field is governed by the three-dimensional wave equation in cylindrical coordinates, i.e.,

$$\nabla^2 p - \frac{1}{C^2}\frac{\partial^2 p}{\partial t^2} = 0 \tag{6.1}$$

where

$$\nabla^2 = \frac{\partial^2}{\partial \hat{r}^2} + \frac{1}{\hat{r}}\frac{\partial}{\partial \hat{r}} + \frac{1}{\hat{r}^2}\frac{\partial^2}{\partial \hat{\theta}^2} + \frac{\partial^2}{\partial \hat{x}^2}$$

Here $\hat{x}$ is the axial coordinate, $\hat{\theta}$ is the circumferential coordinate, and $\hat{r}$ is the radial coordinate in the reference frame attached to the fluid. Substituting this expression into Eq. (6.1) results in

$$\frac{\partial^2 p}{\partial \hat{r}^2} + \frac{1}{\hat{r}}\frac{\partial p}{\partial \hat{r}} + \frac{1}{\hat{r}^2}\frac{\partial^2 p}{\partial \hat{\theta}^2} + \frac{\partial^2 p}{\partial \hat{x}^2} - \frac{1}{C^2}\frac{\partial^2 p}{\partial t^2} = 0 \tag{6.2}$$

As was assumed earlier, the small disturbance unsteady flow is harmonic with known temporal frequency ω, as yet unknown axial wave number α, and known circumferential wave number β_m. In this analysis, the circumferential wave number

will be referred to by an integer m that denotes the circumferential mode number, i.e.,

$$\beta_m = \frac{(\sigma + 2\pi m)\theta}{\Theta_G} \tag{6.3}$$

where Θ_G is the angular gap between the blades. For now, the radial behavior of the unsteady pressure is still unknown. Hence, the behavior of the unsteady pressure may be written in the form

$$p(\hat{r}, \hat{\theta}, \hat{x}, t) = \mu(\hat{r}) \exp[jm\hat{\theta} + j\alpha\hat{x} + j\omega t] \tag{6.4}$$

where $\mu(\hat{r})$ is some as yet undetermined function. Substituting this functional form into Eq. (6.2) results in

$$\frac{d^2\mu}{d\hat{r}^2} + \frac{1}{\hat{r}}\frac{d\mu}{d\hat{r}} - \frac{m^2}{\hat{r}^2}\mu - \alpha^2\mu + \frac{\omega^2}{C^2}\mu = 0 \tag{6.5}$$

If a new variable α^* is defined such that

$$\alpha^{*2} = \frac{\omega^2}{C^2} - \alpha^2 \tag{6.6}$$

then Eq. (6.5) may be written as

$$\hat{r}^2\frac{d^2\mu}{d\hat{r}^2} + \hat{r}\frac{d\mu}{d\hat{r}} + \left(\alpha^{*2}\hat{r}^2 - m^2\right)\mu = 0 \tag{6.7}$$

Equation (6.7) is simply Bessel's Equation. The solution, therefore, is composed of Bessel functions of order m, i.e.,

$$\mu(\hat{r}) = \mathcal{A}J_m(\alpha^*\hat{r}) + \mathcal{B}Y_m(\alpha^*\hat{r}) \tag{6.8}$$

The constants $\mathcal{A}$ and $\mathcal{B}$ are determined by the boundary conditions on the radial behavior of the unsteady pressure. Because the hub and tip are solid surfaces, the flow tangency boundary condition requires that radial component of velocity on these surfaces must be zero. From the radial momentum equation, then, the radial (or normal) component of the pressure gradient at the hub and tip surfaces must be zero, i.e.,

$$\left.\frac{\partial p}{\partial \hat{r}}\right|_{r_H} = 0 \tag{6.9}$$

and

$$\left.\frac{\partial p}{\partial \hat{r}}\right|_{r_T} = 0 \tag{6.10}$$

Application of the boundary conditions results in a homogeneous system of equations for the constants $\mathcal{A}$ and $\mathcal{B}$. Cramer's rule implies that if the constants $\mathcal{A}$ and $\mathcal{B}$ are not both zero, then

$$\begin{vmatrix} \frac{dJ_m}{d\hat{r}}(\alpha^* r_H) & \frac{dY_m}{d\hat{r}}(\alpha^* r_H) \\ \frac{dJ_m}{d\hat{r}}(\alpha^* r_T) & \frac{dY_m}{d\hat{r}}(\alpha^* r_T) \end{vmatrix} = 0 \tag{6.11}$$

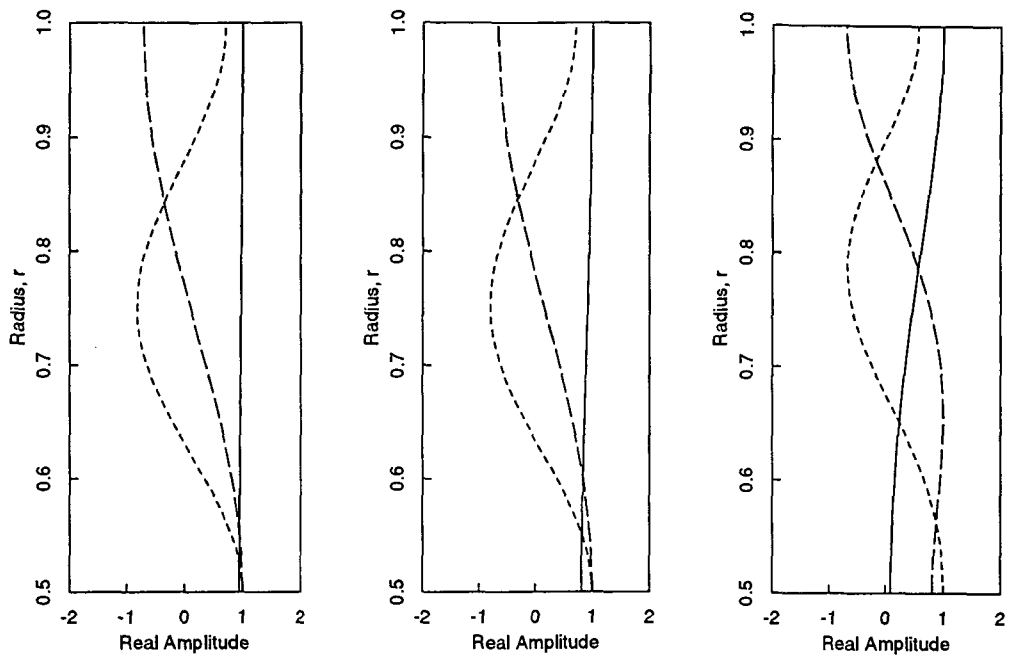

Figure 6.2: Typical radial mode shapes μ_{mn} for annular duct. Hub-to-tip ratio, $r_H/r_T = 0.5$; solid line, $n = 0$; dashed line, $n = 1$; dotted line, $n = 2$. Left, Fourier mode $m = 1$; center, Fourier mode $m = 2$; right, Fourier mode $m = 8$.

This transcendental equation has an infinite number of roots α^* for every integer m. For simplicity, the roots will be ordered by magnitude and denoted by the index n. Hence, the radial mode shape $\mu_{mn}(\hat{r})$ has n zeros in the interval $r_H \leq \hat{r} \leq r_T$. The mode shapes are also orthogonal with respect to the weighting function $\hat{r}$. In addition, since Eq. (6.11) only determines the constants $\mathcal{A}$ and $\mathcal{B}$ to within an arbitrary multiplicative factor, the constants may be chosen so that the radial mode shapes are orthonormal with respect to the weighting function $\hat{r}$, i.e.,

$$\int_{r_H}^{r_T} \mu_{mn}(\hat{r})\mu_{m\ell}(\hat{r})\ \hat{r}\ d\hat{r} = 0 \tag{6.12}$$

for all $\ell \neq n$, and

$$\int_{r_H}^{r_T} \mu_{mn}(\hat{r})\mu_{m\ell}(\hat{r})\ \hat{r}\ d\hat{r} = 1 \tag{6.13}$$

for all $\ell = n$.

Figure 6.2 shows some typical radial mode shapes μ_{mn} computed using this analysis. As noted above, each mode shape has n zeros between the hub and tip radii. Now that the radial mode shape is known, the only remaining variable is the axial wavenumber α_{mn}.

The axial wave number α_{mn} corresponding to the radial mode specified by α^*_{mn}

may be determined from the roots of Eq. (6.11), and Eq. (6.6), so that

$$\alpha_{mn}^2 = \frac{\omega^2}{C^2} - \alpha^{*2}_{mn} \tag{6.14}$$

In summary, if the steady flow relative to the frame of reference is zero, the behavior of unsteady pressure waves in an annular duct may be determined by the temporal frequency ω, the circumferential mode number m, and the hub and tip radii, r_H and r_T.

6.2 Calculation of Far-Field Unsteady Pressure

We wish to apply the sensitivity analysis procedure developed in this report to the complete three-dimensional flowfield. At first glance, it would appear that one possible approach would be to simply solve the three-dimensional governing equations of the fluid instead of the two-dimensional versions developed here. To obtain the computational efficiency of the present method, however, the nominal steady and unsteady flow equations must be solved using LU decomposition, i.e., the discretized flow equations must be solved directly. Unfortunately, a direct solution of the three-dimensional flow equations is not feasible on current computers. Hence, an alternative approach to calculating the three-dimensional flowfield needs to be developed.

Because even iterative fully three-dimensional unsteady aerodynamic analyses of cascades have only recently become available for use on modern workstation computers, most cascade analyses have used a two-dimensional aerodynamic model. The blades are analyzed in what is referred to as "strip-theory." In this approach, the unsteady aerodynamic loads at a number of radial locations along the blade surface are computed using a two-dimensional aerodynamic model. In the aeroelastic problem, these aerodynamic loads are then integrated along the span to obtain modal forces. In the aeroacoustic problem, the unsteady pressure at the far field $p(r, x)$ may be computed from these aerodynamic loads using a Green's function approach, i.e.,

$$p(r, x) = \int_\Gamma [\![p(r_0, x_0)]\!] G(r, x; r_0, x_0) d\Gamma \tag{6.15}$$

where $[\![p(r_0, x_0)]\!]$ is the jump in pressure at the point (r_0, x_0) on the blade surface, and G is the Green's function derived for a specific annular geometry and steady flow condition [1, 58]. The Green's function may be considered an "influence coefficient" relating the loads on the surface to the pressure in the far field. The Green's function approach relies on a relatively idealized model, however. Typically, the model does not include blade thickness or camber, and may only approximate the actual steady loading on the blade.

The linearized potential analysis described in this report improves on the Green's function approach by solving the governing equations of the steady and unsteady flow using modern computational fluid dynamic techniques. Arbitrary blade shapes may be analyzed, the actual steady blade loading is accounted for, and the far-field pressure is computed with the rest of the unsteady flow solution.

Although the strip theory approach for modeling quasi-three-dimensional effects is a simple and straightforward method, it should be noted that in some cases the results computed in this way may be misleading. In particular, Hall and Lorence [35] found that real three-dimensional effects may be extremely important in the aeroelastic behavior of fans and compressors with low hub-to-tip ratios.

With this in mind, the next step is to calculate the magnitudes of the actual three-dimensional outgoing pressure waves in the duct using the two-dimensional analysis developed in this report. Specifically, the two-dimensional unsteady potential calculated at the far field will be matched with a three-dimensional analysis of the surrounding duct.

6.3 Calculation of the Outgoing Pressure

As described earlier in this chapter, Tyler and Sofrin developed an analytical description of the small disturbance behavior of acoustic modes in annular ducts. However, their analysis is limited to flows without mean flow swirl. For more general steady flows, a more complicated model is required. For example, Kerrebrock [59] has developed an analytical model for certain cases of swirling flows. General analytical solutions for flows in annular ducts, however, are not available. If the mean flow field is axisymmetric, however, the shape of the eigenmodes in the circumferential direction will be Fourier modes. Hall, Lorence, and Clark [51] developed a procedure to take advantage of this behavior in their formulation of fully three-dimensional nonreflecting boundary conditions for the linearized Euler equations. Their method will be adapted here to compute the magnitude of the actual three-dimensional outgoing pressure waves using the unsteady potential computed from the analysis developed in this report.

The modeling of the three-dimensional flowfield begins with the full unsteady Euler equations in cylindrical coordinates expressed in the rotating frame of reference, which may be written as

$$\frac{\partial \hat{\mathbf{U}}}{\partial t} + \frac{\partial \hat{\mathbf{F}}}{\partial x} + \frac{1}{r}\frac{\partial \hat{\mathbf{G}}}{\partial \theta} + \frac{1}{r}\frac{\partial r\hat{\mathbf{H}}}{\partial r} - \hat{\mathbf{S}} = 0 \tag{6.16}$$

Here x, θ, and r are the coordinates in the axial, circumferential, and radial directions. Also, $\hat{\mathbf{U}}$ is the vector of conservation flow variables, and $\hat{\mathbf{F}}$, $\hat{\mathbf{G}}$, and $\hat{\mathbf{H}}$ are the flux vectors, and $\hat{\mathbf{S}}$ is a source term due to rotation. These terms are given by

$$\hat{\mathbf{U}} = \begin{bmatrix} \hat{\rho} \\ \hat{\rho}\hat{u} \\ \hat{\rho}\hat{v} \\ \hat{\rho}\hat{w} \\ \hat{e} \end{bmatrix} \qquad \hat{\mathbf{F}} = \begin{bmatrix} \hat{\rho}\hat{u} \\ \hat{\rho}\hat{u}^2 + \hat{p} \\ \hat{\rho}\hat{u}\hat{v} \\ \hat{\rho}\hat{u}\hat{w} \\ \hat{\rho}\hat{u}\hat{I} \end{bmatrix} \qquad \hat{\mathbf{G}} = \begin{bmatrix} \hat{\rho}\hat{v} \\ \hat{\rho}\hat{v}\hat{u} \\ \hat{\rho}\hat{v}^2 + \hat{p} \\ \hat{\rho}\hat{v}\hat{w} \\ \hat{\rho}\hat{v}\hat{I} \end{bmatrix}$$

$$\hat{\mathbf{H}} = \begin{bmatrix} \hat{\rho}\hat{w} \\ \hat{\rho}\hat{u}\hat{w} \\ \hat{\rho}\hat{v}\hat{w} \\ \hat{\rho}\hat{w}^2 + \hat{p} \\ \hat{\rho}\hat{w}\hat{I} \end{bmatrix} \qquad \hat{\mathbf{S}} = \begin{bmatrix} 0 \\ 0 \\ -\hat{\rho}\hat{w}(\hat{v}/r - 2\Omega) \\ \hat{\rho}(\hat{v} - \Omega r)^2/r + \hat{p}/r \\ 0 \end{bmatrix}$$

where $\hat{\rho}$ is the density, $\hat{p}$ is the pressure, $\hat{e}$ is the internal energy, and $\hat{I}$ is the rothalpy. Here we have assumed that the coordinate system is rotating about the x-axis with rotational speed Ω. The pressure, $\hat{p}$, and the rothalpy, $\hat{I}$ are given by

$$\hat{p} = (\gamma - 1)\left[\hat{e} - \frac{1}{2}\hat{\rho}(\hat{u}^2 + \hat{v}^2 + \hat{w}^2) + \frac{1}{2}\hat{\rho}\Omega^2 r^2\right]$$

and

$$\hat{I} = \frac{\hat{e} + \hat{p}}{\hat{\rho}} = \frac{\gamma}{\gamma - 1}\frac{\hat{p}}{\hat{\rho}} + \frac{1}{2}(\hat{u}^2 + \hat{v}^2 + \hat{w}^2) - \frac{1}{2}\Omega^2 r^2$$

where r is the distance from the x-axis ($r = \sqrt{y^2 + z^2}$). Note that $\hat{u}$, $\hat{v}$, and $\hat{w}$ are now the flow velocities in the axial, circumferential, and radial directions, respectively.

It is assumed that the mean flow, $\mathbf{U}$, is axisymmetric and uniform in the axial direction. The small disturbance behavior in the far field is then governed by

$$\frac{\partial \mathbf{u}}{\partial t} + \frac{\partial \mathbf{F}}{\partial \mathbf{U}}\frac{\partial \mathbf{u}}{\partial x} + \frac{1}{r}\frac{\partial \mathbf{G}}{\partial \mathbf{U}}\frac{\partial \mathbf{u}}{\partial \theta} + \frac{1}{r}\frac{\partial}{\partial r}\left(\frac{r\partial \mathbf{H}}{\partial \mathbf{U}}\mathbf{u}\right) - \frac{\partial \mathbf{S}}{\partial \mathbf{U}}\mathbf{u} = 0 \tag{6.17}$$

where $\mathbf{u}$ is the perturbation flow and $\partial\mathbf{F}/\partial\mathbf{U}$, $\partial\mathbf{G}/\partial\mathbf{U}$, $\partial\mathbf{H}/\partial\mathbf{U}$, and $\partial\mathbf{S}/\partial\mathbf{U}$ are Jacobians based on the mean flowfield, $\mathbf{U}$.

As discussed in Chapter 2, it is assumed that the shape of the eigenmodes in the circumferential direction are Fourier modes. In addition, it is assumed that the frequency of the unsteady excitation is ω and the interblade phase angle is σ. Using these assumptions, the unsteady conservation variables may be expressed as the series

$$\mathbf{u}(x, \theta, r, t) = \sum_{m=-\infty}^{\infty}\sum_{n=-\infty}^{\infty} w_{mn}\mathbf{u}_{mn}(r)\, e^{j\omega t}\, e^{j\alpha_{mn}x}\, e^{j\beta_m\theta/\Theta_G} \tag{6.18}$$

where $\beta_m = (\sigma + 2\pi m)$ is the circumferential wave number of the mth Fourier mode, Θ_G is the angular gap between any two adjacent airfoils, w_{mn} is a coefficient which indicates how much of a given mode $\mathbf{u}_{mn}$ is contained in the solution $\mathbf{u}$.

Substituting Eq. (6.18) into Eq. (6.17), and noting that each term in the series must vanish gives

$$j\omega\,[\mathbf{I}]\,\mathbf{u}_{mn} + j\alpha_{mn}\left[\frac{\partial \mathbf{F}}{\partial \mathbf{U}}\right]\mathbf{u}_{mn} + \frac{j\beta_m}{r\Theta_G}\left[\frac{\partial \mathbf{G}}{\partial \mathbf{U}}\right]\mathbf{u}_{mn}$$

$$+ \frac{1}{r}\frac{\partial}{\partial r}\left(r\left[\frac{\partial \mathbf{H}}{\partial \mathbf{U}}\right]\mathbf{u}_{mn}\right) - \left[\frac{\partial \mathbf{S}}{\partial \mathbf{U}}\right]\mathbf{u}_{mn} = 0 \tag{6.19}$$

Equation (6.19) is an eigenvalue problem for the mnth eigenvalue α_{mn} and associated radial eigenvector $\mathbf{u}_{mn}(r)$. Because the hub and tip casings are solid surfaces, this eigenvalue problem is solved subject to the condition that there be no radial flow on these surfaces. Since no closed form solution exists for Eq. (6.19) (except for a few special cases), the eigenmodes and eigenvalues must be found numerically. This may be accomplished by discretizing Eq. (6.19) on a one-dimensional computational grid which extends from the hub to the tip of the duct at the far-field boundary. The derivatives in Eq. (6.19) may be approximated using finite difference operators. For each Fourier mode m, the resulting eigenvalue problem will be of the form

$$[\mathbf{M}_m]\mathbf{u}_{mn} = \alpha_{mn}[\mathbf{N}_m]\mathbf{u}_{mn} \tag{6.20}$$

where $[\mathbf{M}_m]$ and $[\mathbf{N}_m]$ are sparse, complex, non-Hermitian matrices of size $5K \times 5K$ where K is the number of grid points in the radial direction.

To determine the direction the eigenmodes travel, we examine the wave numbers of the eigenmodes. As described in the far-field boundary condition section of Chapter 2, waves that have complex wave numbers decay as they propagate and hence do not contribute to the radiated noise. We only wish to examine the waves which propagate unattenuated (i.e., the wave number is purely real). Recall from Chapter 2 that the direction of propagation is determined by the group velocity, given by Eq. (2.96). Because the propagating pressure waves have distinct eigenvalues, we may calculate $\partial\alpha/\partial\omega$ using the expression [60]

$$\frac{\partial\alpha_{mn}}{\partial\omega} = \frac{\mathbf{v}_{mn}^T\left[\frac{\partial[\mathbf{M}_m]}{\partial\omega} - \alpha_{mn}\frac{\partial[\mathbf{N}_m]}{\partial\omega}\right]\mathbf{u}_{mn}}{\mathbf{v}_{mn}^T[\mathbf{N}_m]\mathbf{u}_{mn}} \tag{6.21}$$

where $\mathbf{v}_{mn}^T$ and $\mathbf{u}_{mn}$ are the left and right eigenvectors of the mode. Hence, once the eigenvalues and left and right eigenvectors of the individual modes are known, the group velocity may be determined, which specifies the direction of propagation.

The next step is to determine the far-field values of the conservation variables from the two-dimensional analysis. Because the steady flow is subsonic, there is a simple linear relationship between the primitive and conservation variables, i.e., $\mathbf{u} = \mathcal{L}[\mathbf{u}_p]$, where $\mathbf{u}_p$ is the vector of primitive variables and $\mathcal{L}$ is a linear operator. Hence, for simplicity, we write the primitive variables in terms of the unsteady potential, ϕ, so that

$$\mathbf{u}_p = \left\{ \begin{array}{rcl} \rho & = & -\frac{R}{C^2}\left(j\omega\phi + \nabla\Phi\cdot\nabla\phi\right) \\ u & = & \partial\phi/\partial x \\ v & = & \partial\phi/\partial y \\ w & = & 0 \\ p & = & -R\left(j\omega\phi + \nabla\Phi\cdot\nabla\phi\right) \end{array} \right\} \tag{6.22}$$

Note that the radial component of the velocity, w, is zero because the potential has been calculated using a two-dimensional aerodynamic model.

Next, the unsteady conservation variables are Fourier transformed at each radial station at the far field. The mth Fourier coefficient is given by

$$\mathbf{u}_m = \frac{1}{\Theta_G} \int_0^{\Theta_G} \mathbf{u} \exp\left[-j\beta_m \theta / \Theta_G\right] \, d\theta \tag{6.23}$$

Equation (6.23) may be approximated numerically using the trapezoidal rule.

For each Fourier mode, in general the vector $\mathbf{u}_m$ is composed of both incoming and outgoing eigenvectors, $\mathbf{u}_{mn}$. We wish to modify the solution (now denoted $\mathbf{u}_m^{\text{old}}$) so that only the contribution due to the outgoing propagating modes are retained. To accomplish this, we discretize Eq. (6.19) to obtain the eigenmode description of the mth Fourier mode. Having computed these mode shapes, we expand $\mathbf{u}_m^{\text{old}}$ as a sum of eigenvectors as in Eq. (6.18) Using the biorthogonality condition, the coefficient w_{mn} may be expressed as

$$w_{mn} = \frac{\mathbf{v}_{mn}^T [\mathbf{N}_m] \mathbf{u}_m^{\text{old}}}{\mathbf{v}_{mn}^T [\mathbf{N}_m] \mathbf{u}_{mn}} \tag{6.24}$$

Hence, to eliminate all but the outgoing propagating modes from the solution, we let

$$\mathbf{u}_m^{\text{new}} = \sum_{n_{\text{prop}}} \mathbf{u}_{mn} \frac{\mathbf{v}_{mn}^T [\mathbf{N}_m] \mathbf{u}_m^{\text{old}}}{\mathbf{v}_{mn}^T [\mathbf{N}_m] \mathbf{u}_{mn}} = [\mathbf{Z}_m] \mathbf{u}_m^{\text{old}} \tag{6.25}$$

In this form, Eq. (6.25) acts like a linear filter, removing all but the propagating outgoing modes. This process is repeated for each Fourier mode. The modified Fourier coefficients $\mathbf{u}_m^{\text{new}}$ are then summed using Eq. (6.18) to form the new solution $\mathbf{u}$ at the far-field boundary. The new solution may then be used to calculate the sound pressure level (SPL), sound power level (PWL), or other measure of the sound output from the blade row. The process may then be repeated for other multiples of the blade passing frequency (BPF) to determine the complete tonal noise signature of the blade row.

Equation (6.25) is an important result. Recall that the computation of the eigenanalysis required only the duct geometry and the steady flow at the far field. Hence, the matrix $[\mathbf{Z}_m]$ is not dependent on the airfoil shape if the steady flow angle at the far field does not change.

The calculation of the perturbation of the radiated tonal noise, then, is actually quite straightforward. From Eq. (6.25), the perturbed solution at the far field may be written as

$$\mathbf{u}_m'^{\text{new}} = [\mathbf{Z}_m] \mathbf{u}_m'^{\text{old}} - [\mathbf{Z}_m]' \mathbf{u}_m^{\text{old}} \tag{6.26}$$

where the primes refer to the perturbed quantities. If the duct geometry and steady flow at the far field do not change (a very reasonable assumption), then $[\mathbf{Z}_m]'$ is zero, and there is simply a linear relationship between the perturbation of the solution calculated by the two-dimensional analysis and the perturbed three-dimensional radiated noise.

In summary, because of the simplicity of the model, this method is an efficient approach to more realistic three-dimensional modeling of the aeroacoustic behavior of a blade row. Furthermore, the method is well-suited to the sensitivity analysis developed in this report, and is consistent with three-dimensional analysis techniques currently in use.

Chapter 7

Conclusions and Future Work

This chapter summarizes the important features of the present method, and includes the important conclusions from the computed results. In addition, some suggestions for future work in this area are offered.

7.1 Conclusions

This report has presented a new method for calculating the aeroacoustic and aeroelastic response of a cascade to small changes in the airfoil or cascade geometry. Previous methods have calculated the steady and unsteady aerodynamic behavior of a cascade based on the airfoil shape and flow conditions. The present method addresses how the steady and unsteady flowfields are dependent on the airfoil shape and cascade geometry. The information from this sensitivity analysis can be used to suggest design changes for improved aeroacoustic and/or aeroelastic performance. In this report, the procedure has been applied to the linearized potential equation. The method is general in nature, however, and may be applied to other flow models.

The present method begins with the assumption that the nonlinear unsteady flow may be split into a nonlinear steady (or mean) flow, and a small disturbance unsteady flow that is harmonic in time. The steady flow is modeled by the steady form of the full potential equation, which is discretized using a variational finite element technique. The discretized steady equations are solved using Newton iteration with LU decomposition at each iteration. Once the steady flow has been computed, the unsteady flow is governed by a set of variable coefficient differential equations (the discretized form of the linearized potential equation), where the coefficients are dependent on the steady flow. The linearized potential equation is also discretized by a variational finite element procedure. For flutter problems, the variational principle incorporates a deforming grid to improve the accuracy of the unsteady solution. For forced response problems, the variational principle includes the effect of incident vortical gusts using rapid distortion theory. The discretized small disturbance equations are solved using a single LU decomposition.

The sensitivities of the steady and unsteady flow to changes in design variables are computed in a straightforward fashion by expanding the steady and unsteady flow

equations in perturbation series and collecting terms of equal order. The resulting equations for the sensitivities may be solved very efficiently by performing one forward and one back substitution for each design variable using the LU factors obtained from the nominal solutions.

To demonstrate the effectiveness of the procedure, representative examples of aeroelastic and aeroacoustic problems in turbomachinery were presented. In the first example, a cascade of compressor blades that was aeroelastically unstable in torsion was redesigned to be aeroelastically stable. In the second example, a fan exit guide vane was redesigned to significantly reduce the downstream acoustic response. In the final example, a fan exit guide vane was redesigned to reduce the overall acoustic response using only changes in the blade shape. In all three cases, the redesign was accomplished while keeping the steady work done by the cascade and the airfoil incidence angle unchanged.

Analysis of the computed results indicates that the sensitivity analysis gives excellent predictions of the the actual redesigned airfoil response. In addition, it appears that the effectiveness of the modifying the blade shape to improve unsteady aerodynamic performance increases with frequency, i.e., high frequency problems appear to be more heavily dependent on the details of the airfoil shape. For aeroacoustic problems, there appears to be a trade-off between upstream and downstream acoustic radiation, indicating that it may be difficult to simultaneously reduce the upstream and downstream radiated noise, at least in the present two-dimensional analysis. Finally, the sensitivity analysis was found to be computationally very efficient, with the sensitivity analysis requiring a fraction of the time necessary for the nominal calculation, and orders of magnitude less time than a finite difference calculation would require. Furthermore, the computational efficiency dramatically increases with the size of the problem, so the savings will be even more dramatic for flow models with increased sophistication.

7.2 Future Work

Although the results presented here are extremely encouraging, more work needs to be done to fully realize the potential of this method as a design tool. This section will discuss some possible avenues for future research.

7.2.1 Other Flow Models

Throughout this report, it was emphasized that the sensitivity analysis procedure presented here is general in nature and may be applied to a wide variety of flow models and discretization schemes. Hence, the first logical extension of the present method is to apply it to a more sophisticated flow model.

Linearized Euler analyses of unsteady flow problems have become more common in recent years [30, 31, 35]. Unlike the linearized potential formulation, the Euler equations allow transonic problems including shocks to be modeled accurately by including the effect of vorticity and entropy generation. One advantage of this ap-

proach is that a sensitivity analysis using the linearized Euler equations could be used to predict the movement of the shock location due to changes in the airfoil shape.

A more powerful application would be to apply the sensitivity analysis procedure to the linearized Navier-Stokes equations. Recently, Clark and Hall [34] used the linearized Navier-Stokes equations to examine stall flutter in cascades. Although they used an iterative approach to calculate the steady and unsteady solutions, their procedure could be used to generate the matrix entries for a direct solution method. There are several advantages in using a Navier-Stokes-based approach. For example, the steady losses due to blade shape changes can be quantified. This would allow the designer to examine the actual trade-off between steady efficiency and unsteady performance. Another example is that the sensitivity analysis could be used to examine stall flutter problems. Specifically, the analysis could suggest design changes to help prevent flow separation, or at least blade design changes which suppress stall flutter. Although Navier-Stokes-based analyses are relatively immature, a sensitivity analysis based on the Navier-Stokes equations would be a powerful design tool.

7.2.2 Multidisciplinary Optimization

As was demonstrated in Chapter 5, the aeroacoustic and aeroelastic design strategy currently implemented involves simply using the results of the sensitivity analysis directly. A more sophisticated design strategy would be to consider finding the *optimal* design of an airfoil for an operating condition. For example, a designer may wish to minimize the radiated noise subject to the constraint that the desired turning is achieved. Additional constraints may be necessary. For example, a constraint on the surface pressure gradient may be imposed so that the flow does not separate. The resulting optimal solution may be determined through the use of a nonlinear constrained minimization procedure [63]. The problem is nonlinear because the acoustic behavior of the cascade is a nonlinear function of the blade shape. Efficient optimization procedures require accurate estimates of the sensitivity of the cost function being optimized to changes in the design variables. The previously described sensitivity analysis is well-suited to such a procedure because the sensitivities are calculated accurately and efficiently.

Another advantage of an optimal design procedure is that it may be *multidisciplinary.* The sensitivity analysis procedure developed in this report only addresses the aerodynamic behavior of the aeroelastic or aeroacoustic problem under consideration. Similar analyses could be performed, for example, on the equations governing the blade structure. In the optimization procedure, both the structural and aerodynamic sensitivities could be combined to create a multidisciplinary optimal design procedure.

7.2.3 Multiple Blade Rows

In this report, the blade row being analyzed is assumed to be isolated in an infinitely long duct. In reality, of course, these blade rows are not isolated, and in fact the blade rows in a turbomachine are spaced together quite closely. As a result, it is necessary

to model the blade row interaction to obtain a more complete model of the flowfield within a turbomachine. Unfortunately, blade row interaction is a very complicated problem to model because of the relative motion between blade rows. This relative motion produces a shifting of the frequencies of the acoustic, vortical, and entropic waves as they propagate from one blade row to the next. Furthermore, the blade rows reflect these waves at a number of shifted frequencies and scattered interblade phase angles, violating the assumption that the solution is harmonic in time with a fixed interblade phase angle.

Recently, Hall and Silkowski [64] and Hanson [65] have developed a technique to analyze blade row interaction by analyzing each blade row independently, and computing the reflection and transmission coefficients for each pressure and vorticity mode in the duct. A set of linear equations may then be constructed that couples together these coefficients to determine the interaction. Although these methods so far have used only flat-plate unsteady aerodynamics, in principle any linearized solution procedure could be used to model the unsteady flowfield. Hence, the present sensitivity analysis could be applied to this procedure. Changes to the airfoil shape or cascade geometry will result in perturbations in the reflection and transmission coefficients associated with the blade row. Also, perturbations in the incoming pressure and vorticity waves to a blade row will also affect its unsteady response. Once these sensitivities are calculated, the coupling equations may be expanded in a perturbation series. The first-order terms will determine the change in the blade row interaction due to a change in the blade shape.

7.2.4 Three-Dimensional Problems

In Chapter 6, some aspects of the three-dimensionality of unsteady flows in turbomachines were examined. A framework was then presented of how the present two-dimensional analysis could be used to analyze three-dimensional problems. Although the approach described in Chapter 6 is clearly better than simply ignoring three-dimensional effects, it does not model fully the annular nature of the blade row. To do this, a fully three-dimensional model is required. Unfortunately, most three-dimensional unsteady aerodynamic models are extremely computationally expensive, due to the large number of computational nodes required. Potential methods are generally not suitable for three-dimensional analyses because they are unable to model the mean flow swirl produced by the rotating blades. As a result, the Euler equations model the minimum amount of physics necessary to realistically examine the three-dimensional unsteady aerodynamic problem. Three-dimensional linearized analyses are relatively new, the first implementation being the Euler method of Hall and Lorence [35].

Unfortunately, even if a linearized solver has been obtained, extending the previous two-dimensional approach to three dimensions is not a straightforward task. In particular, LU factorization requires far too much computer time and computer storage to be feasible. To overcome this problem, Hall and Lorence used an iterative method to compute the steady and unsteady flowfields. This approach, however, is not useful for the sensitivity analysis because the computation of the sensitivities

would take as much time as the nominal calculation.

One possible approach to the three-dimensional sensitivity analysis would be to use a preconditioned conjugate gradient (CG) method, such as GMRES [66]. Burgreen and Baysal [67] have used such an approach for steady aerodynamic optimization problems. In addition, to reduce the computational expense, they used the domain decomposition scheme developed by Eleshaky and Baysal [68], where the computational domain is divided into subdomains, each of which contains internal cells and boundary/interface cells. In this method, the subdomains are solved independently after the influences of the boundary cells is calculated. Unfortunately, the GMRES algorithm would still have to be applied for each right-hand side, which significantly reduces the efficiency of the sensitivity analysis.

A solution method developed for solution of a system of linear equations with multiple right-hand sides is required. Consider the following approach. Instead of insisting on *exactly* factoring the large sparse matrices in the steady and unsteady solution procedure, an *approximate* but accurate factorization based on the Lanczos algorithm may be sufficient. The Lanczos algorithm is a recursive algorithm which factors a matrix into a symmetric tridiagonal matrix and an orthonormal matrix containing the so-called Lanczos vectors at each iteration [69]. In principle, the recursive algorithm *exactly* factors the matrix after n iterations where n is the number of unknowns. However, unlike LU decomposition, the recursion may be stopped after only m iterations where $m \ll n$ to obtain an *approximate* factorization of the matrix. In this case, only m Lanczos vectors are retained, and the solution to the system of equations may be obtained for considerably less computational effort than solving the system exactly. Furthermore, the Lanczos vectors only depend on the matrix, not the right-hand side, so once the Lanczos vectors have been computed, the solution for multiple right-hand sides may be obtained for little additional computational effort.

The proposed algorithm is similar in many respects to the popular GMRES algorithm. In fact, the conjugate gradient algorithm may be derived from the Lanczos algorithm. One of the disadvantages of the conjugate gradient method, as noted earlier, is that it is a "one-shot" method. For each right hand side, the GMRES algorithm must be restarted. The Lanczos approach, on the other hand, retains the approximately factored matrix for reuse. This approach has the potential to extend the encouraging results presented in this report to three dimensions.

Appendix A

Nomenclature

Roman

$[\mathbf{A}], [\mathbf{B}], [\mathbf{C}]$	Steady block matrices
$[\mathrm{a}], [\mathrm{b}], [\mathrm{c}]$	Unsteady block matrices
$[\tilde{\mathrm{a}}], [\tilde{\mathrm{b}}], [\tilde{\mathrm{c}}]$	Unsteady block matrices in periodic region
$[\breve{\mathrm{a}}], [\breve{\mathrm{b}}], [\breve{\mathrm{c}}]$	Unsteady block matrices in wake region
a_0	$-(\partial\lvert\nabla\Phi\rvert/\partial n)_{SP}^{-1}$
C	Speed of sound
c	Blade chord
c_1, c_2	Coefficients in Goldstein rotational velocity
$[\mathbf{D}]$	Matrix operator for ϕ_D
$\mathbf{d}$	Vector of Fourier coefficients
$\mathbf{E}$	Steady force vector
$\mathbf{e}$	Unsteady force vector
$[\mathbf{F}_1]$	Discrete Fourier transform matrix in far field
$[\mathbf{F}_2]$	Filter and propagation matrix in far field
$[\mathbf{F}_3]$	Discrete inverse Fourier transform matrix in far field
F	Fractional arc length array
$\mathbf{f}$	Vector of grid motion
f	x-coordinate of grid motion
G	Blade-to-blade gap
G_r	Blade-to-blade gap in rotated coordinate system
g	y-coordinate of grid motion
H	y-computational coordinate for grid generation
$[\mathbf{I}]$	Identity matrix
I	Number of computational nodes in axial direction
$[\tilde{\mathbf{I}}]$	Modified identity matrix for periodic boundary conditions
$[\mathbf{J}]$	Jacobian of coordinate transformation
$[\tilde{\mathbf{J}}]$	$[\mathbf{J}]^T[\mathbf{J}] - [\mathbf{I}]$
J	Number of computational nodes in circumferential direction
J_m	Bessel function of the first kind

j	$\sqrt{-1}$
$\mathbf{K}$	Steady stiffness matrix
K_1, K_2	"Wave numbers" in Goldstein rotational velocity
$\mathbf{k}$	Unsteady stiffness matrix
k_p	Penalty number
L	Grid motion distribution array
$\mathbf{M}$	Vector of grid equations
M	Mach number
m	Circumferential mode number
$\mathbf{N}$	Vector of steady flow equations
$[\mathbf{N}]$	Row vector of interpolation functions
N_R	Number of rotor blades
N_V	Number of stator vanes
$\mathbf{n}$	Unit normal to surface
n	Normal direction
P	Steady pressure
p	Unsteady pressure
Q	Steady prescribed mass flux
q	Unsteady prescribed mass flux
R	Steady density
R_u	Universal gas constant
r	Wake displacement
r^*	Radial coordinate in three-dimensional analysis
r_H	Hub radius
r_T	Tip radius
S	Arc length of points in airfoil definition
$\mathbf{s}$	Unit tangent to surface
s	Tangential dirction
s_f	Entropy of fluid
$[\mathbf{T}]$	Transition matrix in far-field analysis
T_f	Temperature of fluid
t	Time
U	Steady velocity in x-direction
V	Steady velocity in y-direction
V_r	Steady free stream velocity in rotated coordinate system
V_g	Group velocity
$\mathbf{v}$	Velocity
$\mathbf{v}^G$	Goldstein rotational velocity
$\mathbf{v}^R$	Rotational velocity
$[\mathbf{W}]$	Global matrix of discretized unsteady flow equations
X	x-component of points in airfoil definition
$\mathbf{x}$	Vector of computational grid coordinates
x	First physical coordinate
x_r	Rotated x-coordinate for far-field analysis
x^*	Axial coordinate in three-dimensional analysis

Y	y-component of points in airfoil definition
Y_m	Bessel function of the second kind
y	Second physical coordinate
y_r	Rotated y-coordinate for far-field analysis
$\mathbf{Z}$	Vector of cascade geometry definition
z	Coefficient of propagation in far field

Greek

$\overline{\alpha}, \overline{\beta}, \overline{\gamma}, \overline{\delta}$	Coefficients of grid generation equations
α	Axial wave number
α_r	Axial wave number in rotated coordinate system
α_p	Axial wave number of $\boldsymbol{\phi}^P$
β	Circumferential wave number
β_r	Circumferential wave number in rotated coordinate system
β_p	Circumferential wave number of $\boldsymbol{\phi}^P$
Γ	Surface in variational principle
γ	Ratio of specific heats c_p/c_v
Δ	Drift function
δ	Variational symbol
ε	Coefficient of smoothing in wake
η	y computational coordinate
Θ	Stagger angle
Θ_G	Angular gap in three-dimensional analysis
θ	Angle of rotation for discontinuous potential analysis
θ^*	Circumferential coordinate in three-dimensional analysis
κ	Blade number
Λ	Period in variational principle
Ξ	x-computational coordinate for grid generation
Ξ_B	Aerodynamic damping due to plunging vibration
Ξ_T	Aerodynamic damping due to torsional vibration
ξ	x-computational coordinate
Π	Variational functional
π	$\cos^{-1}(-1)$
ρ	Density
Σ	Domain in variational principle
σ	Interblade phase angle
τ	t-computational coordinate
$\boldsymbol{\Phi}$	Vector of nodal values of Φ
Φ	Steady potential
$\tilde{\Phi}$	Coefficient of potential in rapid distortion theory
$\boldsymbol{\phi}$	Vector of nodal values of ϕ
$\boldsymbol{\phi}^H$	Homogeneous part of vector of nodal values of ϕ
$\boldsymbol{\phi}^P$	Particular part of vector of nodal values of ϕ

$\tilde{\phi}$	Reduced form of ϕ in periodic boundary conditions
$\breve{\phi}$	Form of ϕ in wake boundary conditions
ϕ	Unsteady potential
$\overline{\phi}$	Complex conjugate of ϕ
$\tilde{\phi}$	Potential in rapid distortion theory
ϕ^u	Unsteady potential on upper surface of comp. domain
ϕ^ℓ	Unsteady potential on lower surface of comp. domain
ϕ_c	Continuous part of far-field potential
ϕ_d	Discontinuous part of far-field potential
ϕ'_d	Discontinuous part of far-field potential in rotated sys.
Ψ	Stream function
Ψ_0	Stream function value on stagnation streamline
ψ	Distance in streamwise direction
Ω	Wheel speed of rotor in three-dimensional analysis
$\Omega_{-\infty}$	Inlet flow angle
Ω_∞	Exit flow angle
ω	Frequency

Script

$\mathcal{A}$	Constant in stagnation point analysis
$\mathcal{B}$	Constant in rapid distortion theory analysis
$\mathcal{C}$	Constant in Bernoulli's equation
$\mathcal{D}, \mathcal{E}$	Coefficients in discontinuous far field analysis
$\mathcal{P}$	Grid spacing function for Ξ grid generation equation
$\mathcal{Q}$	Grid spacing function for H grid generation equation

Superscripts

x	x-grid equation
y	y-grid equation

Subscripts

$-\infty$	Upstream far field
∞	Downstream far field
i	Associated with grid i-station
j	Associated with grid j-station
0	Reference value
T	Total or stagnation quantity

Appendix B

Sensitivity of the NACA Modified Four-Digit Airfoil Definition

As an example of how airfoil shapes and their perturbations are calculated, the NACA modified four-digit series of airfoils will be examined [61]. The NACA four-digit definition allows the specification of five variables to determine the airfoil shape: the magnitude of maximum thickness, m_t, the magnitude of the maximum camber, m_c, the chordwise location of the maximum thickness, ℓ_t, the chordwise location of the maximum camber, ℓ_c, and the leading edge radius, r_t.

The thickness distribution is defined by the following two equations:

$$\pm y_t = a_0\sqrt{x} + a_1 x + a_2 x^2 + a_3 x^3 \tag{B.1}$$

ahead of the location of maximum thickness, and

$$\pm y_t = d_0 + d_1(1-x) + d_2(1-x)^2 + d_3(1-x)^3 \tag{B.2}$$

aft of the maximum thickness location, where lengths have been nondimensionalized by the blade chord, c. The positive sign of y_t corresponds to the upper surface of the airfoil, while the negative sign refers to the lower surface.

The four coefficients d_0, d_1, d_2, and d_3 are determined from four boundary conditions. The first is that the thickness at the maximum thickness location is one-half the magnitude of the maximum thickness. Second, the thickness at the trailing edge is zero. Third, the slope of the thickness distribution at the maximum thickness location is zero. Fourth, the slope of the thickness distribution at the trailing edge is specified, so that the airfoil has a finite wedge angle at the trailing edge. The specified slope may be determined from the following curve fit:

$$\left.\frac{dy_t}{dx}\right|_{\text{TE}} = -m_t\left(0.775 + 2.51667x - 13.625x^2 + 35.8333x^3 - 12.5x^4\right) \tag{B.3}$$

where TE refers to the trailing edge of the airfoil.

The four coefficients a_0, a_1, a_2, and a_3 are also determined from four boundary conditions. First, as before, the magnitude of the thickness at the maximum thickness location is specified. Second, the slope of the thickness distribution at the maximum

thickness location is zero. The third condition is that the curvature (or second derivative) of the thickness distribution at the maximum thickness location is the same as that computed from the aft coefficients. Fourth, the leading edge radius is specified, i.e., the thickness at the leading edge radius location is the leading edge radius ($y_t = x$). According to the definition, the leading edge radius is

$$r_t = 1.1019 \left(\frac{m_t I}{6} \right)^2 \tag{B.4}$$

where I is the first digit following the dash in the designation and the value of I does not exceed 8.

For each set of coefficients, a linear matrix equation may be constructed. The solution of these two equations results in the coefficients. Functionally, it is clear that

$$\mathbf{d} = \mathbf{d}(m_t, \ell_t) \tag{B.5}$$

and

$$\mathbf{a} = \mathbf{a}(m_t, \ell_t, r_t) \tag{B.6}$$

where $\mathbf{d}$ and $\mathbf{a}$ are vectors containing the defining coefficients.

The specification of the mean line is considerably more straightforward. The mean line is defined by two equations:

$$y_m = \frac{m_c}{\ell_c^2} \left(2\ell_c x - x^2 \right) \tag{B.7}$$

ahead of the maximum camber location, and

$$y_m = \frac{m_c}{(1-\ell_c)^2} \left[(1 - 2\ell_c) + 2\ell_c x - x^2 \right] \tag{B.8}$$

aft of the maximum camber location. Note that the shape of the mean line is simply two parabolas connected together with C^1 continuity.

The actual airfoil definition is the superposition of the mean line and the thickness distribution, i.e.,

$$y_{\text{AIR}} = y_m \pm y_t \tag{B.9}$$

where the surface is determined by the sign of y_t. In practice, the airfoil definition points are calculated at some finite number of locations, N. This set of (x, y) locations is then rotated through the stagger angle, Θ, about a specified rotation point (x_r, y_r), so that

$$\left.\begin{aligned} X_i &= (x_{\text{AIR}_i} - x_r)\cos\Theta - (y_{\text{AIR}_i} - y_r)\sin\Theta \\ Y_i &= (x_{\text{AIR}_i} - x_r)\sin\Theta + (y_{\text{AIR}_i} - y_r)\cos\Theta \end{aligned}\right\} i = 1, 2, \ldots, N \tag{B.10}$$

where X_i and Y_i are the airfoil defining shape points discussed in Chapter 3. The arc length, S_i, is then computed at each point, and the X and Y locations are splined

as a function of S. The X and Y locations may be used to form the airfoil shape portion of the vector $\mathbf{Z}$ in the grid and steady flow equations, Eqs. (3.8) and (3.9).

Now that the airfoil definition and spline generation procedure has been explained, the perturbation of the airfoil defining points, $\mathbf{Z}'$, may be computed. Consider the effect of a small change in the magnitude of the airfoil camber, m'_c. The perturbation of the unrotated points defining the airfoil shape is

$$y'_{\text{AIR}} = \frac{m'_c}{\ell_c^2}\left(2\ell_c x - x^2\right) \tag{B.11}$$

ahead of the maximum camber location, and

$$y'_{\text{AIR}} = \frac{m'_c}{(1-\ell_c)^2}\left[(1-2\ell_c) + 2\ell_c x - x^2\right] \tag{B.12}$$

aft of the maximum camber location. Because the x-locations of the defining points do not change, x'_{AIR} is zero.

In general, then, the perturbation of the y-locations of the defining points may be written as:

$$y'_{\text{AIR}} = \frac{\partial y_m}{\partial m_c}m'_c + \frac{\partial y_m}{\partial \ell_c}\ell'_c \pm \left(\frac{\partial y_t}{\partial m_t}m'_t + \frac{\partial y_t}{\partial \ell_t}\ell'_t + \frac{\partial y_t}{\partial r_t}r'_t\right) \tag{B.13}$$

This perturbation at each point is then rotated through the stagger angle, so that

$$\begin{aligned} X'_i = \quad & (x'_{\text{AIR}_i} - x'_r)\cos\Theta \quad - \quad (y'_{\text{AIR}_i} - y'_r)\sin\Theta \\ & -(x_{\text{AIR}_i} - x_r)\Theta'\sin\Theta \quad + \quad (y_{\text{AIR}_i} - y_r)\Theta'\cos\Theta \end{aligned} \tag{B.14}$$

$$\begin{aligned} Y'_i = \quad & (x'_{\text{AIR}_i} - x'_r)\sin\Theta \quad + \quad (y'_{\text{AIR}_i} - y'_r)\cos\Theta \\ & +(x_{\text{AIR}_i} - x_r)\Theta'\cos\Theta \quad - \quad (y_{\text{AIR}_i} - y_r)\Theta'\sin\Theta \end{aligned} \tag{B.15}$$

where Θ' is the perturbation in the stagger angle, and x'_r and y'_r are the perturbations in the x- and y-location of the rotation point, which are included here for completeness. The perturbation in the arc length at each point, S', may also be computed. The perturbations are then cubic splined as a function of arc length.

In summary, then, this appendix has shown how the vector of defining points that form part of the vector $\mathbf{Z}$ could be calculated for an actual airfoil shape. The perturbation in these points, $\mathbf{Z}'$, due to small changes in airfoil defining parameters may be calculated by perturbing the analytical expressions that define the airfoil.

Bibliography

[1] Groeneweg, J. F., Sorfin, T. G., Rice, E. J., and Gliebe, P. R., "Turbomachinery Noise," *Aeroacoustics of Flight Vehicles: Theory and Practice*, Volume 1: Noise Sources, H. H. Hubbard (ed.), NASA Reference Publication 1258, August 1991.

[2] Gliebe, P. R., "Aeroacoustics in Turbomachines and Propellers — Future Research Needs," *Unsteady Aerodynamics, Aeroacoustics, and Aeroelasticity of Turbomachines and Propellers*, H. M. Atassi (ed.), Springer-Verlag, New York, 1993.

[3] Dowell, E. H. (ed.), Curtiss, H. C., Scanlan, R. H., and Sisto, F., *A Modern Course in Aeroelasticity*, Second Revised and Enlarged Edition, Kluwer Academic Publishers, Dordrecht, The Netherlands, 1989.

[4] Snyder, L. E., and Burns, D. W., "Forced Vibration and Flutter Design Methodology," Chapter 22 in AGARD Manual on Aeroelasticity in Axial-Flow Turbomachines, Structural Dynamics and Aeroelasticity, Vol. 2, M. F. Platzer and F. O. Carta (eds.), AGARD-AG-298, March 1987.

[5] Verdon, J. M., "Unsteady Aerodynamics for Turbomachinery Aeroelastic Applications," *Unsteady Transonic Aerodynamics*, D. Nixon (ed.), AIAA, Washington, DC, 1989.

[6] Whitehead, D. S., "Force and Moment Coefficients for Vibrating Aerofoils in Cascade," Aeronautical Research Council, London, Reports and Memoranda 3254, February 1960.

[7] Whitehead, D. S., "Bending Flutter of Unstalled Cascade Blades at Finite Deflection," Aeronautical Research Council, London, Reports and Memoranda 3386, October 1962.

[8] Atassi, H., and Akai, T. J., "Aerodynamic Force and Moment on Oscillating Airfoils in Cascade," ASME Paper 78–GT–181, 1978.

[9] Whitehead, D. S., "Vibration and Sound Generation in a Cascade of Flat Plates in Subsonic Flow," Aeronautical Research Council, Reports and Memoranda 3685, 1970.

[10] Smith, S. N., "Discrete Frequency Sound Generation in Axial Flow Turbomachines," Aeronautical Research Council, Reports and Memoranda 3709, March 1972.

[11] Adamczyk, J. J., and Goldstein, M. E., "Unsteady Flow in a Supersonic Cascade with Subsonic Leading-Edge Locus," *AIAA Journal*, Vol. 16, December 1978, pp. 1248–1254.

[12] Verdon, J. M., and McCune, J. E., "Unsteady Supersonic Cascades in Subsonic Axial Flow," *AIAA Journal*, Vol. 13, No. 2, February 1975, pp. 193–201.

[13] Nagashima, T., and Whitehead, D. S., "Linearized Supersonic Unsteady Flow in Cascades," Aeronautical Research Council, Reports and Memoranda 3811, 1977.

[14] Bendiksen, O. O., "Bending-Torsion Flutter in Supersonic Cascades," *AIAA Journal*, Vol. 19, No. 6, June 1981, pp. 774–781.

[15] Goldstein, M. E., Braun, W., and Adamczyk, J. J., "Unsteady Flow in a Supersonic Cascade With Strong In-Passage Shocks," *Journal of Fluid Mechanics*, Vol. 83, 1977, pp. 569–604.

[16] Bendiksen, O. O., "Role of Shocks in Transonic/Supersonic Compressor Flutter," *AIAA Journal*, Vol. 24, July 1986, pp. 1179–1186.

[17] Namba, M., "Three-Dimensional Flows," Chapter 4 in AGARD Manual on Aeroelasticity in Axial-Flow Turbomachines, Unsteady Turbomachinery Aerodynamics, Vol. 1, M. F. Platzer and F. O. Carta (eds.), AGARD-AG-298, March 1987.

[18] Giles, M. B., "Calculation of Unsteady Wake/Rotor Interaction," *AIAA Journal of Propulsion*, Vol. 4, No. 4, July-August, 1988, pp. 356–362.

[19] Ni, R. H., and Sharma, O., "Using Three-Dimensional Euler Flow Simulations to Assess Effects of Periodic Unsteady Flow Through Turbines," AIAA Paper 90–2357.

[20] Saxer, A. P., and Giles, M. B., "Inlet Radial Temperature Redistribution in a Transonic Turbine Stage," AIAA Paper 90–1543.

[21] Rai, M. M., "Three-Dimensional Navier-Stokes Simulations of Turbine Rotor-Stator Interaction, Part I — Methodology," *Journal of Propulsion and Power*, Vol. 5, May-June 1989, pp. 305–311; "Part II — Results," pp. 312–319.

[22] Verdon, J. M., and Caspar, J. R., "Subsonic Flow Past an Oscillating Cascade With Finite Mean Flow Deflection," *AIAA Journal*, Vol. 18, No. 5, May 1980, pp.l 540–548.

[23] Whitehead, D. S., and Grant, R. J., "Force and Moment Coefficients of High Deflection Cascades," Proceedings of the 2nd International Symposium on Aeroelasticity in Turbomachines, P. Suter (ed.), Juris-verlag Zurich, 1981, pp. 85–127.

[24] Hall, K. C., "Deforming Grid Variational Principle for Unsteady Small Disturbance Flows in Cascades," *AIAA Journal*, Vol. 31, No. 5, 1993, pp. 891–900.

[25] Verdon, J. M., and Caspar, J. R., "A Linearized Unsteady Aerodynamic Analysis for Transonic Cascades," *Journal of Fluid Mechanics*, Vol. 149, December 1984, pp. 403–429.

[26] Goldstein, M. E., "Unsteady Vortical and Entropic Distortions of Potential Flows Round Arbitrary Obstacles," *Journal of Fluid Mechanics*, Vol. 93, Part 3, Dec. 1978, pp. 433–468.

[27] Atassi, H. M., and Grzedzinski, J., "Unsteady Disturbances of Streaming Motions Around Bodies," *Journal of Fluid Mechanics*, Vol. 209, Dec. 1989, pp. 385–403.

[28] Hall, K. C., and Verdon, J. M., "Gust Response Analysis for Cascades Operating in Nonuniform Mean Flows," *AIAA Journal*, Vol. 29, No. 9, 1991, pp. 1463–1471.

[29] Hall, K. C., and Crawley, E. F., "Calculation of Unsteady Flows in Turbomachinery Using the Linearized Euler Equations," *AIAA Journal*, Vol. 27, June 1989, pp. 777–787.

[30] Hall, K. C., and Clark, W. S., "Linearized Euler Prediction of Unsteady Aerodynamic Loads in Cascades", *AIAA Journal*, Vol. 31, No. 3, 1993, pp. 540–550.

[31] Holmes, D. G., and Chuang, H. A., "2D Linearized Harmonic Euler Flow Analysis for Flutter and Forced Response," *Unsteady Aerodynamics, Aeroacoustics, and Aeroelasticity of Turbomachines and Propellers*, H. M. Atassi (ed.), Springer-Verlag, New York, 1993.

[32] Hall, K. C., Clark, W. S., and Lorence, C. B., "A Linearized Euler Analysis of Unsteady Transonic Flows in Turbomachinery," *Transactions of the ASME: Journal of Turbomachinery*, Vol. 116, No. 3, July 1994, pp. 477–488.

[33] Lindquist, D. R., and Giles, M. B., "Validity of Linearized Unsteady Euler Equations with Shock Capturing," *AIAA Journal*, Vol. 32, No. 1, January 1994, pp. 46–53.

[34] Clark, W. S., and Hall, K. C., "A Numerical Model of Stall Flutter in Cascades," To be presented at the ASME 40th Gas Turbine and Aeroengine Congress and Exposition, Houston, TX, 1995.

[35] Hall, K. C., and Lorence, C. B., "Calculation of Three-Dimensional Unsteady Flows in Turbomachinery Using the Linearized Harmonic Euler Equations," *Transactions of the ASME: Journal of Turbomachinery*, Vol. 115, No. 4, 1993, pp. 800–809.

[36] Lighthill, M. J., "A New Method of Two-Dimensional Aerodynamic Design," Aeronautical Research Council, Reports and Memorandum 2112, 1945.

[37] Giles, M. B., and Drela, M., "Two-Dimensional Transonic Aerodynamic Design Method," *AIAA Journal*, Vol. 25, 1987, pp. 1199–1206.

[38] Bock, K. W., "Aerodynamic Design by Optimization," in AGARD, Computational Methods for Aerodynamic Design (Inverse) and Optimization, AGARD–CP–463.

[39] Jameson, A., "Aerodynamic Design via Control Theory," NASA Contract Report CR–181749.

[40] Crawley, E. F., and Hall, K. C., "Optimization and Mechanisms of Mistuning in Cascades," *Transactions of the ASME: Journal of Engineering for Gas Turbines and Power*, Vol. 107, No. 2, 1985, pp. 418–426.

[41] Adelman, H. M., and Haftka, R. T., "Sensitivity Analysis of Discrete Structural Systems," *AIAA Journal*, Vol. 24, No. 5, 1986, pp. 823–832.

[42] Haug, E. J., Choi, K. K., and Komkov, V., *Design Sensitivity Analysis of Structural Systems*, Academic Press, Orlando, 1986.

[43] Taylor, A. C., III, Hou, G. W., and Korivi, V. M., "Methodology for Calculating Aerodynamic Sensitivity Derivatives," *AIAA Journal*, Vol. 30, No. 10, 1992, pp. 2411–2419.

[44] Baysal, O., and Eleshaky, M. E., "Aerodynamic Design Optimization Using Sensitivity Analysis and Computational Fluid Dynamics," *AIAA Journal*, Vol. 30, No. 3, 1992, pp. 718–725.

[45] Sadrehaghighi, I., Smith, R. E., and Tiwari, S. N., "Grid and Design Variables Sensitivity Analyses for NACA Four-Digit Wing-Sections," Presented at the AIAA 31st Aerospace Sciences Meeting, Reno, NV, January 11–14, 1993. AIAA Paper 93–0195.

[46] Murthy, D. B., and Kaza, K. R. V., "Semianalytical Technique for Sensitivity Analysis of Unsteady Aerodynamic Computations," *Journal of Aircraft*, Vol. 28, No. 8, 1991, pp. 481–488.

[47] Bateman, H., "Irrotational Motion of a Compressible Fluid," Proc. National Academy of Sciences, Vol. 16, 1930, p. 816.

[48] Batchelor, G. K., *An Introduction to Fluid Dynamics*, Cambridge University Press, Cambridge, 1967.

[49] Lane, F, "System Mode Shapes in the Flutter of Compressor Blade Rows," *Journal of the Aeronautical Sciences*, Vol. 23, No. 1, January, 1956, pp. 54–66.

[50] Verdon, J. M., Adamczyk, J. J., and Caspar, J. R., "Subsonic Flow Past an Oscillating Cascade With Steady Blade Loading — Basic Formulation," Unsteady Aerodynamics, R. B. Kinney (ed.), University of Arizona, Tuscon, AZ, July, 1975, pp. 827–851.

[51] Hall, K. C., Lorence, C. B., and Clark, W. S., "Nonreflecting Boundary Conditions for Linearized Unsteady Aerodynamic Calculations," Presented at the AIAA 31st Aerospace Sciences Meeting, Reno, NV, January 11–14, 1993. AIAA Paper 93–0882.

[52] Thompson, J. F., Thames, F. C., and Mastin, C. W., "Automatic Numerical Generation of Body-Fitted Curvilinear Coordinate System for Field Containing Any Number of Arbitrary Two-Dimensional Bodies," *Journal of Computational Physics*, Vol. 15, July 1974, pp. 299–319.

[53] Cook, R. D., Malkus, D. S., and Plesha, M. E., *Concepts and Applications of Finite Element Analysis*, Third Edition, John Wiley and Sons, New York, 1989.

[54] Anderson, D. A., Tannehill, J. C., and Pletcher, R. H., *Computational Fluid Mechanics and Heat Transfer*, Hemisphere Publishing Corporation, New York, 1984.

[55] Verdon, J. M., "Linearized Unsteady Aerodynamic Theory," Chapter 2 in AGARD Manual on Aeroelasticity in Axial-Flow Turbomachines, Unsteady Turbomachinery Aerodynamics, Vol. 1, M. F. Platzer and F. O. Carta (eds.), AGARD–AG–298, March 1987.

[56] Lorence, C. B., "An Investigation of Three-Dimensional Unsteady Flows in Turbomachinery Using the Linearized Euler Equations," M. S. Thesis, Duke University, Durham, NC, December 1991.

[57] Carta, F. O., "Unsteady Aerodynamics and Gapwise Periodicity of Oscillating Cascaded Airfoils," *Transactions of the ASME: Journal of Engineering for Power*, Vol. 105, No. 3, July 1983, pp. 565–574.

[58] Ventres, C. S., Theobald, M. A., and Mark, W. D., "Turbofan Noise Generation, Volume 1: Analysis", NASA Contract Report CR–167952, July 1982.

[59] Kerrebrock, J. L., "Small Disturbances in Turbomachine Annuli with Swirl," *AIAA Journal*, Vol. 15, No. 6, June 1977, pp. 794–803.

[60] Plaut, R. H., and Huseyin, K., "Derivatives of Eigenvalues and Eigenvectors in Non-Self-Adjoint Systems," *AIAA Journal*, Vol. 11, No. 2, February, 1973.

[61] Abbott, I. H., and von Doenhoff, A. E., *Theory of Wing Sections*, Dover Publications, New York, 1959.

[62] Tyler, J. M., and Sofrin, T. G., "Axial Flow Compressor Noise Studies," *SAE Transactions*, Vol. 79, 1962, pp. 309–332.

[63] Gill, P. E., Murray, W., and Wright, M. H., *Practical Optimization*, Academic Press, San Diego, CA, 1981.

[64] Hall, K. C., and Silkowski, P. D., "The Influence of Neighboring Blade Rows on the Unsteady Aerodynamic Response of Cascades," To be presented at the ASME 40th Gas Turbine and Aeroengine Congress and Exposition, Houston, TX, 1995.

[65] Hanson, D. B., "Mode Trapping in Coupled 2D Cascades — Acoustic and Aerodynamic Results," AIAA Paper 93–4417.

[66] Saad, Y., and Schultz, M. H., "GMRES: A Generalized Minimum Residual Algorithm for Solving Nonsymmetric Linear Systems," *SIAM Journal of Scientific Statistical Computing*, Vol. 7, No. 3, July 1986, pp. 856–869.

[67] Burgreen, G. W., and Baysal, O., "Three-Dimensional Aerodynamic Shape Optimization of Wings Using Sensitivity Analysis," Presented at the 32nd AIAA Aerospace Sciences Meeting, Reno, NV, Jan. 10–13, 1994. AIAA Paper 94–0094.

[68] Eleshaky, M. E., and Baysal, O., "Preconditioned Domain Decomposition Scheme for Three-Dimensional Aerodynamic Sensitivity Analysis," Presented at the 12th AIAA Computational Fluid Dynamics Conference, July 1993. AIAA Paper 93–3392.

[69] Golub, G. H., and Van Loan, C. F., *Matrix Computations*, Second Edition, Johns Hopkins University Press, Baltimore, MD, 1989.